Near–Infrared Absorbing Cyanine Dyes and Organic–Inorganic Perovskites for Electronic Applications

---

Dissertation
zur
Erlangung der naturwissenschaftlichen Doktorwürde
(Dr. sc. nat.)

vorgelegt der
Mathematisch–naturwissenschaftlichen Fakultät
der
Universität Zürich
von
Anna C. Véron
von Winterthur ZH

Promotionskommission
Prof. Dr. Kim K. Baldridge (Vorsitz)
Prof. Dr. Frank A. Nüesch (Leitung der Dissertation)
Prof. Dr. Jay S. Siegel
Prof. Dr. Anthony Linden

Zürich, 2017

„Man sieht oft etwas hundertmal, tausendmal,
ehe man es zum allerersten Male wirklich sieht.“

„Sometimes you regard a subject a hundred or a thousand times
before you actually see it for the very first time.”

Christian Morgenstern (1871–1914)

ABSTRACT OF THE DISSERTATION

Near–Infrared Absorbing Cyanine Dyes and Organic–Inorganic Perovskites for Electronic Applications

by Anna C. Véron

University of Zurich, 2017

Light-absorbing materials with excellent semiconducting properties are of great importance for the application in solar cells, transistors or light-emitting devices, which are emerging technologies. This thesis encompasses the synthesis and analysis of new materials for this purpose.

Heptamethine cyanine dyes are strong absorbers of light in the near–infrared (NIR) energy regime with synthetically tunable absorption and redox properties, making them excellent candidates as light harvesters in organic solar cells. In particular, the absorption of sunlight invisible to the human eye allows for the fabrication of visibly transparent solar cells. In here, the exchange of counterions from cyanine iodide salts to PF_6^- and Δ–TRISPHAT$^-$ is presented and the effect of the counterion on the material properties of the dye is discussed. While the counterion had little to no influence on the optical and electrochemical properties in solution, a tremendous effect on the properties in the solid state was found. Thin films of the dyes with varying counterions showed differently shaped absorption bands indicating alterations in the dye aggregation behavior. Tendencies in the solid state packing of the salts with different counterions are further highlighted by X–ray crystal structures. Also the formation of bulk heterojunction blend films with [60]PCBM was strongly affected by the counterion. With the PF_6^- counterion large fully phase–separated domains were obtained, whereas the Δ–TRISPHAT$^-$ counterion gave a fully intermixed dye–fullerene phase. These findings will stimulate the further development of cyanine bulk heterojunction solar cells. When the heptamethine dyes were applied in semitransparent bilayer organic solar cells together with C_{60}, a power conversion efficiency of 2.2% was achieved while maintaining a high average visible transparency of 66%.

Organic–inorganic hybrid perovskites are an uprising class of compounds which have recently attracted tremendous attention due to the rapid increase in power conversion efficiency of perovskite solar cells (PSCs), reaching more than 20% in 2016. This work aimed at the enhancement of photon–to–current generation of PSCs into the NIR energy regime by utilizing heptamethine dyes as co–sensitizers. For this purpose, new heptamethine dyes with electron–donating substituents were synthesized and characterized in order to tune their redox levels to be compatible with the perovskite

material. While the cyanine dyes were able to perform reasonably well as hole–transporting materials – supporting high short–circuit currents of up 15 mA cm^{-2}, co–sensitization beyond 800 nm was not successful. Further synthetic adaptations of the dyes and improvements of the perovskite/cyanine interface might be necessary.

Further investigations on organic–inorganic hybrid materials addressed the incorporation of large organic cations into low–dimensional inorganic networks. Such systems allow for the combination of desirable properties from both components, such as the structural and functional versatility of organic compounds with the stability and electrical properties of inorganic materials. Two–dimensional lead halide perovskite materials with the general formula $(R\text{-}NH_3)_2PbX_4$ contain layers of PbX_4 sheets alternating with layers of organic cations $R\text{-}NH_3$ and have interesting properties such as room–temperature photo– and electroluminescence as well as high charge carrier mobilities, making them promising candidates for the application in devices such as light emitting diodes or field–effect transistors (FET). In this thesis, a method to synthesize 2D–perovskite films consisting of highly ordered crystallites is presented. In XRD spectra of the thin films very intense (00ℓ) reflexes were found from ℓ=2 up to ℓ=20, suggesting that the alternating layers of inorganic sheets and organic cations are perfectly arranged in parallel to the substrate plane. This structure is promising especially for the application in FET devices as the inorganic sheets are aligned in the direction of charge transport from source to drain electrode.

Finally, an original hybrid material is presented, which incorporates NIR–heptamethine cations in an inorganic network consisting of infinite chains of face–sharing lead iodide octahedra. The structure of this hybrid was solved using X–ray crystal structure analysis and structural aspects are discussed. This “cyanine perovskite” represents the first one–dimensional lead halide perovskite incorporating a functional NIR–absorbing dye as the organic cation, which is predicted to lead to unusual optical and electrical properties through the synergistic interaction between the components.

ZUSAMMENFASSUNG

Cyanin–Farbstoffe mit Nah–Infrarot Absorption und Organisch–Anorganische Perowskite für Elektronische Anwendungen

von Anna C. Véron

Universität Zürich, 2017

Lichtabsorbierende Materialien mit ausgezeichneten Halbleitungseigenschaften sind unersetzlich für viele aufstrebende moderne Technologien, wie Solarzellen, Transistoren oder lichtemittierende Bauelemente. Diese Arbeit umfasst die Synthese und Untersuchung von neuen Materialien mit solchen Eigenschaften.

Heptamethin–Cyanin–Farbstoffe sind intensive Absorber von Licht im nahinfraroten (NIR) Energiebereich, und ihre Absorptions– sowie Redoxeigenschaften können synthetisch angepasst werden. Daher sind sie hervorragend geeignet um in organischen Solarzellen Sonnenlicht einzufangen, das für das menschliche Auge unsichtbar ist, und erlauben somit die Herstellung von optisch transparenten Solarzellen. Diese Arbeit beschreibt den Austausch des Gegenions in Cyanin–Salzen von Iodid zu PF_6^- und Δ–TRISPHAT$^-$ und untersucht den Einfluss dieser Gegenionen auf die Materialeigenschaften der Farbstoffe. Während das optische und elektrochemische Verhalten der Farbstoffe in Lösung nur gering vom Gegenion beeinflusst wurden, konnte ein beachtlicher Effekt auf die Eigenschaften im Feststoff demonstriert werden. Unter anderem war die Form der Absorptionsbanden von dünnen Filmen je nach Gegenion unterschiedlich, was darauf hinweist, dass die Farbstoffe unterschiedliches Aggregationsverhalten zeigen. Im Weiteren wurden Tendenzen zur Packung der Moleküle im Feststoff mittels Röntgenstrukturanalyse hervorgehoben. Auch bei der Bildung von schleuderbeschichteten Kompositfilmen von Cyanin–Farbstoffen und [60]PCBM für Bulk–Heteroübergang–Solarzellenanwendungen spielte das Gegenion eine bedeutsame Rolle. Mit PF_6^- als Gegenion trat eine vollständige Phasensegregation unter der Bildung von großen Domänen der beiden Komponenten ein, während das Gegenion Δ–TRISPHAT$^-$ zu einer Farbstoff–Fulleren–Mischphase führte. Diese Ergebnisse sind entscheidend für die weitere Entwicklung von Bulk–Heteroübergang–Solarzellen mit Cyanin–Farbstoffen. Die NIR–Heptamethin–Farbstoffe wurden außerdem zusammen mit C_{60} in halbdurchsichtigen organischen Doppelschicht–Solarzellen angewandt, wobei eine Energieumwandlungseffizienz von 2.2% und gleichzeitig eine hohe durchschnittliche Transparenz für sichtbares Licht von 66% erreicht wurden.

Organisch–anorganische Perowskite sind eine aufstrebende Klasse von Verbindungen, welche aufgrund des raschen Anstiegs der Energieumwandlungseffizienz

von Perowskit-Solarzellen, die 2016 über 20% erreicht hat, in letzter Zeit große Aufmerksamkeit auf sich gezogen hat. Eines der Ziele dieser Arbeit war die Erweiterung der Photostromerzeugung in den Bereich der NIR–Strahlung durch zusätzliche Sensibilisierung mit Heptamethin–Farbstoffen. In dieser Absicht wurden neue Heptamethin–Farbstoffe mit Elektronendonor–Substituenten synthetisiert und charakterisiert, um ihre Energieniveaus für eine optimale Kompatibilität mit dem Perowskit–Material anzupassen. In der Solarzelle konnten die Cyanin–Farbstoffe erfolgreich als Lochleiterschichten eingesetzt, und hohe Kurzschlussphotostromdichten von bis zu 15 mA cm^{-2} erreicht werden. Jedoch konnte keine zusätzliche Sensibilisierung durch den Farbstoff im Bereich über 800 nm festgestellt werden, und somit werden weitere synthetische Adaptionen der Farbstoffe oder Verbesserungen der Perowskit–Cyanin–Grenzfläche notwendig sein.

Weitere Untersuchungen im Bereich der organisch–anorganischen Hybridmaterialien befassten sich mit dem Einbau von großen organischen Kationen in niedrigdimensionale Netzwerke von anorganischen Salzen. Solche Systeme erlauben die Kombination erwünschter Eigenschaften von beiden Komponenten, wie die strukturelle und funktionelle Vielfältigkeit von organischen Verbindungen mit der Stabilität und den elektronischen Eigenschaften von anorganischen Materialien. Zweidimensionale Bleihalogenid–Perowskite mit der Summenformel $(R\text{-}NH_3)_2PbX_4$ bestehen aus im Wechsel übereinander gestapelten Schichten aus PbX_4 und organischen Kationen $R\text{-}NH_3$ und besitzen interessante Eigenschaften, wie Photo– und Elektrolumineszenz bei Raumtemperatur sowie hohe Ladungsträgerbeweglichkeit. Daher eignen sie sich ausgezeichnet für die Anwendung in elektronischen Bauteilen, wie z.B. Leuchtdioden, oder Feldeffekttransistoren (FET). In dieser Arbeit wird eine Methode zur Herstellung von 2D–Perowskitfilmen präsentiert, die aus hoch angeordneten Kristalliten bestehen. XRD–Spektren dieser Filme zeigen intensive (00ℓ)–Reflexe, von $\ell=2$ bis zu $\ell=20$, was darauf hinweist, dass die alternierenden Schichten parallel zur Substratebene angeordnet sind. Diese Struktur ist besonders vielversprechend für die Anwendung in FET–Bauteilen, da die anorganischen Schichten in der Richtung des Ladungstransports zwischen Source– und Drain–Elektrode angeordnet sind.

Schliesslich wird ein neues Hybridmaterial präsentiert, welches aus NIR–Heptamethin–Kationen und unendlichen Ketten aus flächenverknüpften Bleiiodid–Oktaedern besteht. Seine Kristallstruktur wurde mittels Röntgenkristallstrukturanalyse bestimmt und strukturelle Aspekte werden diskutiert. Dieser „Cyanin–Perowskit" ist der erste eindimensionale Bleihalogenid–Perowskit der NIR–absorbierende Kationen beinhaltet. Durch synergistische Wechselwirkung der beiden Komponenten werden ungewöhnliche optische und elektrische Eigenschaften erwartet.

ACKNOWLEDGEMENTS

When I was 14 years old and had my first chemistry lessons at school, I dreamed of growing up to become a chemist and to do exciting research. Pursuing a PhD project that involved colorful molecules and their interaction with light was a great way to realize that dream. This is why I am deeply grateful to everybody who made this journey possible and accompanied me along the way.

First of all I would like to thank Frank A. Nüesch (Empa, EPFL) for giving me the possibility to pursue my PhD research project in his group, for letting me work independently and dedicating his time to detailed discussions when needed.

Jay S. Siegel and Kim K. Baldridge (UZH, TJU) have been interacting with me on numerous occasions since I started my first semester at UZH in 2006. I am fortunate to have been taught, guided and criticized by them throughout the process of my BSc and MSc studies, and am grateful that it was them who came to take the lead on my graduation committee.

I would like to express special thanks also to all other professors and lecturers at UZH, who excellently taught us in different fields of chemistry – especially Stefan Bienz, Roger Alberto, and Nathaniel Finney – many of the "tools" I needed to accomplish my PhD work successfully I have acquired from them during my undergraduate studies.

For their help and assistance with cyanine dye synthesis I would like to thank Nicole Pfeiffer, Yulia Schoger, and Matthias Nagel, as well as Thomas Geiger for his supervision during that part of the project. For measuring numerous samples of mine and for their helpful tips and discussions I thank Laurent Bigler and the MS service team at UZH, as well as Michael Schneider and his team at the laboratory for microelemental analysis at ETH Zurich and Beatrice Fischer (Lab 209, Empa) for thermal analysis and IR spectroscopy.

For the fruitful collaboration on the topics of organic solar cells and blend films I am very grateful to the "device group" of our lab at Empa: Frank Nüesch, Roland Hany, Jakob Heier, Hui Zhang, Sandra Jenatsch, Mohammed Makha, Roland Steim, Jean–Nicolas Tisserant and Chuyao Peng. Thank you for applying my dyes in numerous devices and for involving me in various different projects. I am also thankful to have gained deeper knowledge about device physics and photophysical processes and that I could always find answers when I had questions about these topics.

It was a great experience to be able to travel to Brazil during my PhD to visit our project partners of the Brazilian Swiss Joint Research Program (BSJRP). "Muito obrigada" for welcoming me there and for the interesting collaboration to Carlos F.O. Graeff and his group at UNESP Bauru, especially Hagos Tesfay, Marcus Vismara and Augusto Batagin–Neto.

When I started to work with perovskite solar cells and fabricating my first devices and thin films, I was truly fortunate to have Adriana Paracchino at my side who diligently and patiently taught me all the important steps. For their help and collaboration on the topic of perovskite solar cells I would like to thank also Aswani Yella, Fabrizio Giordano and Jiyoun Seo from LPI at EPFL. It was very generous of Michael Grätzel to let me visit his group and learn from them. Furthermore I would like to thank Silvia Fernandes (UNESP Araraquara, Brazil) who visited our lab as a guest PhD student for several months to work on perovskites with me. It was a very productive and stimulating time in the lab with her. For introducing me to powder XRD and allowing me to measure numerous samples on their instrument, I am deeply grateful to Arndt Remhof and Steve Landsmann, (Lab 501 at Empa). Arndt always found time for answering my questions, he was curious and excited about what I was working on and I was even invited to talk in his group seminar.

I am thankful to Daniel Schreier and Michael Stiefel for introducing me to scanning electron microscopy and for their help and assistance with the measurements. For giving me access to the IPCE setup in their lab and their help with the characterization of solar cells as well as fluorescence measurements I would like to thank Fan Fu, Stephan Bücheler and Benjamin Bissig (Lab 207, Empa). Thomas Schmaltz and Holger Frauenrath were very helpful and generous in our collaboration on FET devices.

For determining the crystal structures of several of my compounds, but especially of the "cyanine perovskite", which was only a tiny needle and not even a single crystal, I am deeply indebted to Anthony Linden. Also he was very helpful in numerous discussions and patiently answered my questions about crystallography. Finally I am thankful that he agreed to be on my PhD committee.

I am also deeply grateful to Dani Rentsch, not only for his assistance with NMR spectroscopy but also for his valuable input on many other topics of my project, also for fixing my bike when it was broken and of course, for his friendship.

Finally, I would like to thank all my colleagues from Lab 209 who I had the pleasure to work with during the past years: Mihaela Alexandru, Surendra Anantharaman, Philip Caspari, Micha Bajic, Etienne Berner, Matia Bulloni, Monica Circu, Simon Dünki, Silvia Fernandes, Beatrice Fischer, Isabella Gartmann, Donatas Gesevicius, Sandra Jenatsch, Yeesong Ko, Mohammed Makha, Fahimeh Nafezarefi, Dorina Opris, Adriana Paracchino, Elena Perju, José Quinsaat, René Schneider, Yulia Schoger, Philippe Schwaller, Roland Steim, Christian Walder, Lei Wang, Gaëtan Wicht, Hui Zhang. I enjoyed a great and funny time with them, in the lab, during coffee breaks and also after work. Especially thankful I am to Nicolas Leclaire for all his support and discussions that kept me motivated even in difficult times, as well as his efforts to improve my French in our tandems after work.

During my studies, I was really fortunate to meet a great number of fantastic people at UZH, who have often supported and inspired me and many of them have become close friends. Especially grateful I am to Aleksandra Djekic, Bernadette Vogler, Nicolas Baumann, Alexander Szentkuti, Rafael Ackermann, Henrik Neugebauer, Alois Degonda, Jeannine Hess, Daniel Hurschler, Miriam Oberholzer, Silvan Bosshard, Dario Bosshard, Fiona Gaggia, Lucas Waser, Daphne Diemer, Ana Stojanovic, Roman Maag, Derik Frantz, Silvia Rocha, Karla Arias, Eoin Quinlan, Fitore Kasumaj, Angela Steinauer, Helen Seifert, Imke Schubert, Matthias Ziller, Christian Marti, and Kristoffer Beham.

Finally I would like to thank my father Richard for his endless support and encouragement during my studies and my mother Christina for teaching me to look at the world full of curiosity and fascination already as a little child. Both of my parents and my siblings Marcel, Pascal and Jasmin I want to thank for always believing in me.

For his constant love, his patience and compassion especially during the challenging times of my PhD I am deeply grateful to Gabriel Furlan.

TABLE OF CONTENTS

LIST OF TABLES

LIST OF FIGURES

LIST OF SCHEMES

LIST OF ABBREVIATIONS AND SYMBOLS

[60]PCBM	2a-phenyl-1,2(2a)-homo[5,6]fullerene-C60-Ih-2a-butanoic acid methyl ester
Alq$_3$	tris(8-hydroxyquinolinato)aluminium
BLA	bond length alternation
CB	conduction band
CBM	conduction band minimum
COSY	correlation spectroscopy
δ	chemical shift (NMR)
DCM	dichloromethane
DDA$^+$	dodecylammonium
DDAI	dodecylammonium iodide
DDAP	dodecylammonium lead iodide perovskite $(C_{12}H_{25}NH_3)_2PbI_4$
DFT	density functional theory
DMAP	4-dimethylaminopyridine
DMF	dimethylformamide
DMSO	dimethylsulfoxide
d.p.	decomposition point (temperature)
DSC	differential scanning calorimetry
ε	molar extinction coefficient
EA	elemental analysis
E_{el}	electrochemical bandgap
E_{opt}	optical bandgap
E_{ox}	oxidation potential
EQE	external quantum efficiency
E_{red}	reduction potential
ESI	electrospray ionization
FA$^+$	formamidinium
FAI	formamidinium iodide
FB	forward bias
Fc / Fc$^+$	ferrocene / ferrocinium
FF	fill factor
FTO	fluorine–doped tin oxide
fwd	forward scan (from SC to FB)
FWHM	full width at half maximum
GBL	γ-butyrolactone
η	power conversion efficiency
HMBC	heteronuclear multiple–bond correlation
HOMO	highest occupied molecular orbital
HR–MS	high resolution mass–spectrometry
HSQC	heteronuclear single quantum coherence
HTM / HTL	hole transporting material / layer
IAC	integrated absorption coefficient
IPS	ideal polymethine state
IR	infrared

ITO	indium tin oxide
J	coupling constant (NMR)
J–V	current–voltage
J_{sc}	short–circuit current
λ	wavelength
LiTFSI	bis(trifluoromethane)sulfonimide lithium salt
λ_{max}	absorption maximum
LUMO	lowest unoccupied molecular orbital
MA$^+$	methylammonium
MAI	methylammonium iodide
MO	molecular orbital
m.p.	melting point (temperature)
NHE	normal hydrogen electrode
NIR	near infrared
NMP	*N*-Methyl-2-pyrrolidone
NMR	nuclear magnetic resonance
OSC	organic solar cell
PAH	polyaromatic hydrocarbon
PSC	perovskite solar cell
rev	reverse scan (from FB to SC)
RH	relative humidity
S_0	electronic ground state
S_1	first electronic excited state
SC	short circuit
SEM	scanning electron microscopy
TBACl	tetrabutylammonium chloride
FET	Field–effect transistor
TGA	thermogravimetric analysis
THF	tetrahydrofurane
TLC	thin layer chromatography
UV	ultraviolet
VB	valence band
VBM	valence band maximum
Vis	visible light
V	voltage
V_{oc}	open–circuit voltage
XRD	X-ray diffraction

1 GENERAL CONTEXT AND STRUCTURE

During the past decades major concerns have risen regarding the impact of human civilization on the environment of planet earth. The consumption of coal, oil, or natural gas for energy harvesting causes CO_2–emissions which lead to global warming and climate change.[1,2] At the same time fossil fuel resources are becoming scarce as predicted by Hubbert's peak oil theory.[3] In addition to this, the demand for electrical energy of the world's population is steadily growing as the digital revolution is boosting rapid technological development and the implementation of electronic devices in our everyday lives.[4] The growing awareness of these concerns has recently enabled a great amount of research towards the cost–effective and sustainable harvesting of renewable sources of energy, such as wind, biomass, ocean, hydrogen, geothermal, hydropower and the sun.[5] Especially the latter represents a powerful source of energy, which can be harvested and converted to electrical energy in photovoltaic (PV) cells. The percentage of PV contributing to the total amount of energy production is yearly increasing all around the world.[6] Another concern besides renewable energy conversion is the development of modern electrical devices and components, as e.g. light–emitting devices (LEDs) or field–effect transistors (FETs) which are useful in display applications, in sensors or electronic circuits. Further innovation of all these technologies requires investigating on new materials with tailored properties, which will be the subject of this thesis.

Specifically, the focus lies on organic compounds that absorb light in the near–infrared (NIR) region (chapter 2). This property is useful for a wide variety of applications, such as photography, laser printers and digital copy technology, for information storage in optical disks (CD–R), as heat filters, in solar cells and photodetectors, and even in medical applications as photosensitizers for photodynamic cancer therapy.[7] Additionally, compounds with NIR–emission are receiving attention for their application in telecommunication, laser, night–vision technology, information security displays, sensors, and, very importantly, bioimaging.[7] The class of organic compounds studied in this thesis is the one of cyanine dyes, which contains a large number of representatives with great structural diversity and strong light absorption tunable all over the spectrum, from the ultraviolet (UV) to the NIR region. A detailed introduction to NIR–absorption in organic compounds and especially cyanine dyes is given in chapter 2.1. In the following chapters 2.2 and 2.3 the synthesis and counterion exchange of heptamethine cyanine dyes is presented and discussed, along with their photophysical and electrochemical characterization and evaluation for device application.

In here, the main application of these dyes relates to the role as active semiconductors in solar cells (chapter 3). However, further implementation in photodetectors or as emitters in light-emitting electrochemical cells (LECs) is adressed. The theoretical background as well as results and discussions of solar cell devices based on cyanine dyes are presented in chapters 3.1 and 3.2 for organic and perovskite solar cells, respectively. Organic solar cells (OSCs) based on organic compounds bring several advantages such as low cost and solution processability of the materials. They are particularly attractive for architectural integration due to their aesthetic appearance and the possibility to design solar cells in many colors – including transparent and semitransparent – for façade and window applications.[8] On the other hand, perovskite solar cells (PSCs) are one of the most promising classes of emerging solar cell technologies. Their efficiencies under laboratory conditions have increased strikingly, from 3.8 % at the time of their discovery in 2009 to 22.1% in 2016.[9,10] While reaching efficiencies of other benchmark solar cell technologies (such as CIGS or crystalline silicon) their production costs are lower, mainly due to the employment of cheap materials and solution processability.[11,12]

In a second part of this thesis further attention is given to organic–inorganic hybrid perovskite materials, especially their low–dimensional analogues (chapter 4). After a detailed introduction on this class of compounds in chapter 4.1, the results and discussions on the fabrication of highly ordered 2D–perovskite thin films suitable for FET applications are summarized in chapter 4.2.

Finally, the different aspects of this thesis are combined in chapter 4.3, in which the crystal structure of a novel “cyanine perovskite” material is presented and discussed. This new material consists of infinite inorganic chains and NIR–absorbing cyanine cations and possible scenarios for the interaction of these components are evaluated together with possible applications.

Conclusive remarks and perspectives for the future development of the individual fields are summarized in chapter 5, while the experimental procedures for all chapters are detailed chapter 7.

2 NIR–ABSORBING CYANINE DYES AND COUNTERION EXCHANGE

2.1 Introduction

Synthetic organic dyes have been known and produced since the middle of the 19th century, with their main purpose being to dye textiles for clothing and houseware. The fascination of humans with colored objects caused the development many different dye structures which led to a steady improvement of their absorption properties and stability during the last 150 years.

Nowadays there still is a great demand for colored molecules, not only for decorative or cosmetic purposes, but for all kinds of technologies which require strong absorption or emission of light. Among them are the labelling and visualization of biological compounds and tissue (fluorescence microscopy, tumor imaging, photodynamic therapy), chemical sensors, light-emitting devices, and harvesting sun light and transforming it into electrical energy in a solar cell, or into chemical energy by photochemical water splitting.

2.1.1 Light–Absorbing Organic Molecules

Light is electromagnetic radiation of certain energy within the electromagnetic spectrum shown in **Figure 2.1**. Visible light is the part of the spectrum detectable by the human eye, and typically has energies between ≈ 3.1 and 1.8 eV, which correspond to wavelengths λ between 400 and 700 nm. Near–infrared radiation (NIR), which is not detectable by the human eye, is found adjacent to the visible range in the spectrum at lower energies down to ≈ 0.9 eV corresponding to wavelengths up to 1400 nm.

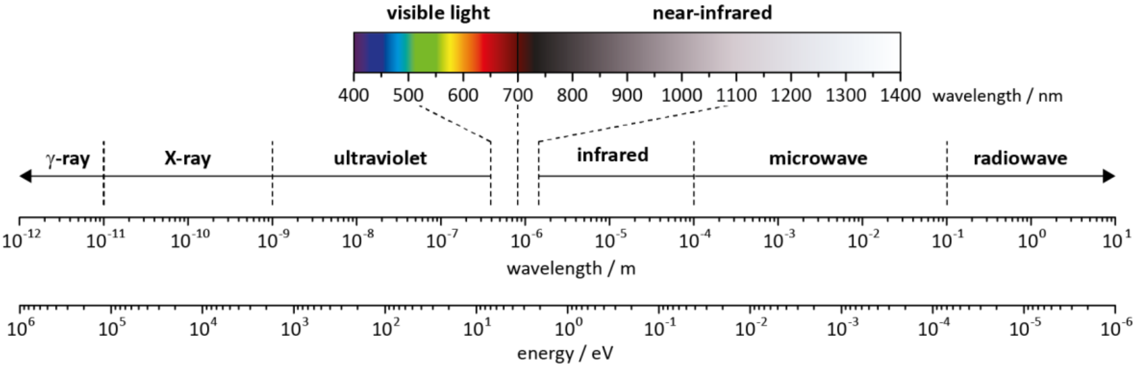

Figure 2.1. The electromagnetic spectrum shows different types of radiation with respect to their wavelength and energy scales. The regions of visible light and near–infrared radiation are highlighted.

In order to understand and describe the absorption of light by a molecule, its molecular orbitals (MOs) have to be considered. If the energy difference ΔE between an occupied and an unoccupied orbital of a molecule equals the energy $\Delta E = h\nu$ of a photon, the photon can be absorbed, which goes in parallel with the promotion of an electron to the unoccupied orbital (**Figure 2.1**). Quantum mechanically the probability of absorbing a photon is proportional to the transition dipole moment to the square. The latter includes symmetry considerations of the orbitals, nuclear wavefunction overlap and spin conservation. The smaller the energy difference between the highest occupied molecular orbital (HOMO) and the lowest unoccupied molecular orbital (LUMO), the more the absorption is shifted to longer wavelengths, from UV to the visible light, blue to red and finally into the NIR region > 700 nm.

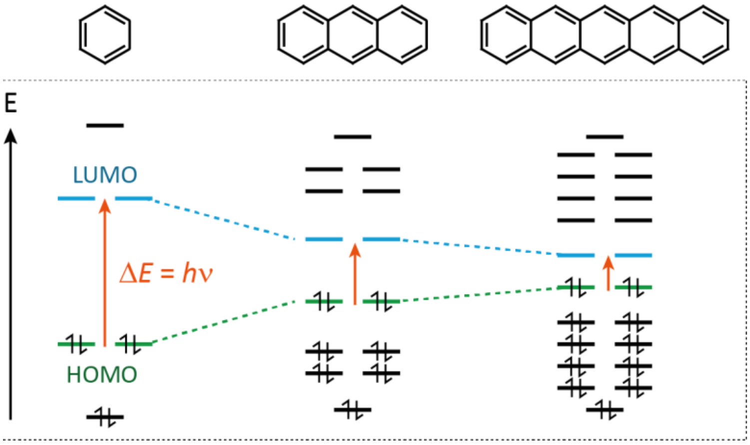

Figure 2.2. Illustration of the decreasing HOMO–LUMO energy gap with increasing conjugation length. Frontier molecular orbital diagrams for benzene, anthracene and pentacene (from left to right).

Organic molecules containing conjugated π–electrons typically have MO levels that allow for the absorption of light. Quantum mechanically the π–electrons in a conjugated system can be described by the one–dimensional particle in a box model.[13] The energy difference ΔE between the HOMO and the LUMO in a linear conjugated system is given by equation **(1)** where *h* is Planck's constant, *L* is the length of the box (i.e. length of the conjugated system), *m* is the mass of an electron and *n* is the number of electrons in the box (i.e. the number of π–electrons in the conjugated system).

$$\Delta E = \frac{h^2(n+1)}{8mL^2} \tag{1}$$

The two parameters *n* and *L* are are both related to the number of carbon atoms N in the system, and thus the HOMO–LUMO energy difference is decreasing with increasing size of the conjugated system: $\Delta E \sim 1/N$. **Figure 2.1** illustrates the decrease in bandgap for increasing conjugation length when going from benzene over anthracene to pentacene. From the particle in a box model, the energy gap could become infinitesimal for an infinite number of conjugated double bonds, e.g. in a conjugated polymer. In practice, however, this is not the case and organic molecules with a small bandgap and sharp absorption band in the NIR region are rather uncommon. Such compounds are of great interest for different kinds of applications and the strategies to design structures with NIR absorbing properties will be illustrated in the following chapter 2.1.2.

2.1.2 Strategies to Obtain NIR–Absorbing Organic Compounds

In order to reduce the HOMO–LUMO gap of organic molecules, several approaches are known today.[7,14–16] These strategies, their advantages and challenges will be highlighted in the following.

i. Extended π–systems
ii. Donor–acceptor systems
iii. Minimization of bond length alternation
iv. Intermolecular interactions

i. *Extended π–systems*: As introduced in chapter 2.1.1 the bandgap of conjugated π–systems decreases when their size is increased. Extended π–systems are large molecules typically consisting of linked or fused benzene units. Several groups have investigated on the synthesis, functionalization and characterization of such compounds during the last decades. Especially the studies of K. Müllen and coworkers are well known and several extensive reviews on the topic can be found.[17–19] In the recent years also graphene and carbon nanotubes have been a research highlight in the field of extended π–systems[19], but in here the focus will be on non–polymeric compounds with a defined molecular weight.

Scheme 2.1 shows a polyphenylene derivative (**1**) which consists of linked benzene units and can be oxidized to obtain its benzenoid polycyclic aromatic hydrocarbon (PAH) analogue **2** in which the benzene units are fused together.[20,21] In polyphenylene derivative **1** the conjugation is strongly reduced due to twisting of the neighboring benzene units, leading to a poor overlap of the π–orbitals, so that despite its large size, this compound is a colorless solid.[20] Rigidization and planarization of this system leads to a strong extension of the π–conjugation, and compound **2**, with 222 carbon atoms, 37 “full” benzene units and a diameter of 3 nm is considered one of the largest fully condensed aromatic system that has actually been prepared to this day (when considering only “small” molecules with a defined molecular weight and neither graphite, graphene, carbon nanotubes, or conjugated polymers). The absorption band of **2** (in the solid state) is very broad due to a great number of possible electronic transitions in this large system; it spans all over the visible range into the NIR with an absorption maximum λ_{max} at 765 nm.[21]

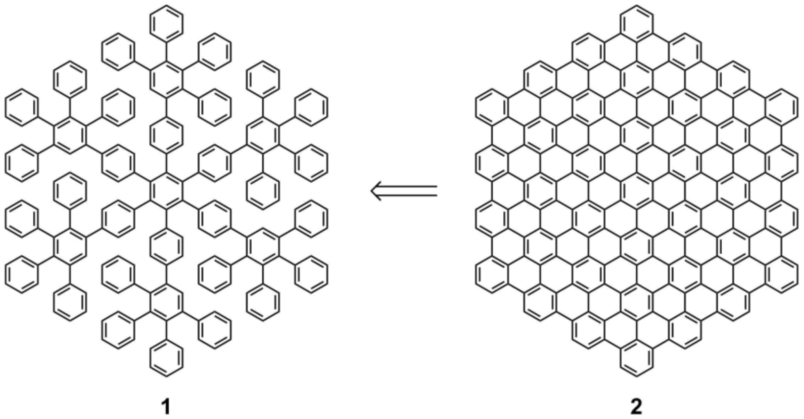

Scheme 2.1. Structure of a polyphenylene (**1**) and its benzenoid PAH analogue (**2**).[20,21]

While PAH compounds and their functionalized derivatives are strong absorbers and have potential applications in organic electronics,[18,22] they have several disadvantages. Their synthesis is complicated and as they are practically insoluble in any solvent, high purities (which are required for the application in devices) are difficult to achieve, and spectroscopic characterization in solution is impossible. Due to this it is also not possible to process them using solution–deposition techniques, so that other more costly methods must be used to fabricate thin films for organic electronic devices. The addition of functional groups (e.g. alkyl chains, methoxy groups) is able to improve the solubility of PAHs[23,24] but to reach a satisfying processability remains difficult. Furthermore, the extension of their absorption into the NIR is rather limited compared to other approaches discussed later in this chapter. Theoretically, if size of benzenoid PAH compounds is increased, the decrease in bandgap reaches saturation, so that a utopic compound with a bandgap of 0.6 eV ($\lambda_{max} \approx 2000$ nm), would have to contain more than 120 full benzene rings[17], and apart from being very difficult to synthesize, it would not have the desired processing properties, as discussed above. To conclude, pure benzenoid PAH compounds are not very promising candidates as light harvesters with a small bandgap in organic electronic devices. If a benzenoid framework of naphtalene units linked in *peri*–positions is flanked between two imide functional groups, however, an interesting class of compounds is obtained. They are called Rylene dyes and have the general structure shown in **Scheme 2.2**. Rylene diimides have sharp absorption bands tunable from blue to the NIR, are easily functionalizable and possess good solubility in various solvents.[25,26] They show strong electron accepting properties making them interesting for the application in organic solar cells[27].

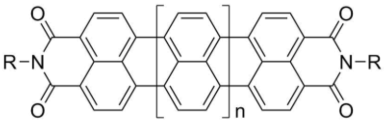

Scheme 2.2. General structure of the rylene dye family.

Also in the case of rylene dyes, the decreased bandgap is an effect mainly of the increasing conjugation length and it can only be lowered to a certain value, as the overall π–system is governed by the effective conjugation length.[28]

ii. *Donor–acceptor systems:* A further approach to obtain low–bandgap chromophores is the coupling of electron–rich (donor, D) and electron–poor (acceptor, A) moieties in a molecule. As illustrated in **Figure 2.3**, hybridization of the HOMO and LUMO orbitals of a donor and acceptor moiety leads to splitting in energy. The resulting HOMO is increased whereas the resulting LUMO is decreased in energy, and thus the gap between them is smaller compared to a system containing only either the donor or the acceptor moieties.

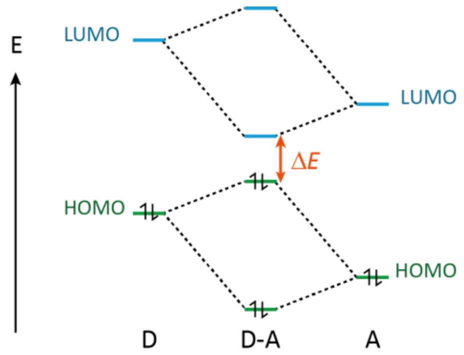

Figure 2.3. Mixing of donor and acceptor frontier molecular orbitals leads to a decreased bandgap (ΔE) of a donor–acceptor system.

This concept was described theoretically for polysquaraines in 1996,[29,30] and finds popular use in the design of low bandgap polymers[16,31,32] as well as oligomers and small molecules[33–35] today.

iii. *Minimization of bond length alternation:* As mentioned at the end of chapter 2.1.1, the HOMO–LUMO gap of a π–conjugated system does not decrease to become infinitesimal with the extension of its size to infinity, but rather it approaches a saturation value. The particle in a box model is valid only under several approximations, one of which is that the potential energy of the electrons is constant over the length L of the box. In reality there is a fluctuation of the potential over the length of a conjugated chain, with valleys around the nuclei (attraction of the electrons by the positive nuclei) and peaks in between (electronic repulsion within the bonds) as illustrated in Figure 2.4.

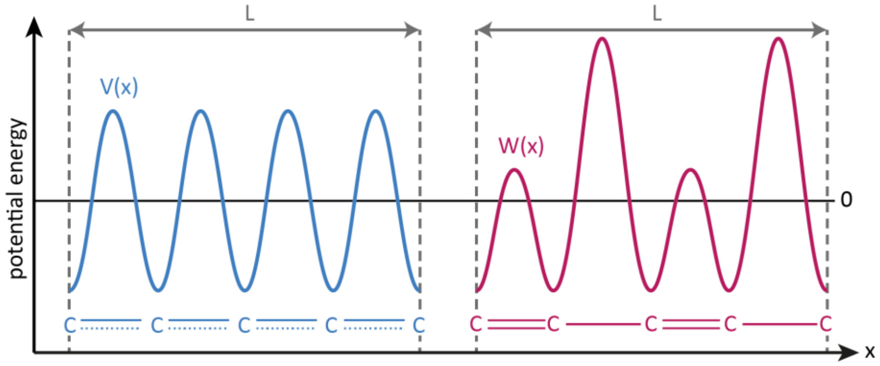

Figure 2.4. Potential energy fluctuation in two fragments of conjugated systems. V(x) is the potential for a fragment without any BLA (in blue on the left side), W(x) is the potential for a fragment with alternating double and single bonds.[36]

The potential fluctuation for two theoretical fragments of π–conjugated chains of carbon atoms is shown: On the left side (in blue) is a chain where all bonds are equally long "1.5x" bonds and the system is perfectly delocalized, which gives a potential energy of the electrons V(x). On the right side (in red) is a chain where double bonds and single bonds are alternating, so that there is bond length alternation (BLA), and the potential energy of the electrons is W(x). If this potential fluctuation is used as the perturbing potential in a first order correction of the particle in a box potential, one finds that the perturbation is zero for V(x), and thus the particle in a box model gives realistic orbital energy values for systems where no BLA occurs.[36] For W(x) however, the perturbation affects the potential and thus also the orbital energy levels: the energy of the HOMO is lowered by a constant magnitude independent of the chain length, whereas the LUMO is not affected.[36] This leads to a notable increase of the HOMO–LUMO gap with respect to the one predicted by equation **(1)** using the particle in a box model.

In fact, most polyenes possess significant bond length alternation because the bonds cannot be represented as both single and double bonds in equivalent resonance structures. In **Scheme 2.3** this can be seen easily: The mesomeric resonance structure of the polyene with separated charges on the right side is unfavorable, the π–electrons are not fully delocalized and the structure is rather confined in alternating single and double bonds. This is why the unperturbed particle in a box model gives an inaccurate prediction of the energy levels and the HOMO–LUMO gap of polyenes.

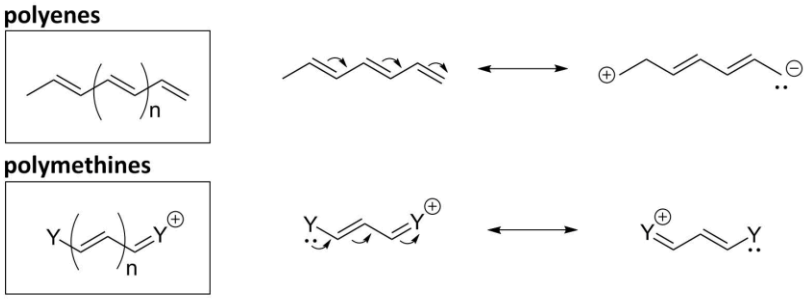

Scheme 2.3. Mesomeric resonance structures of conjugated polyenes (top) and polymethines flanked by heteroatom–containing end groups Y (bottom).

There are, however, also linear conjugated π–systems which show only very little bond length alternation, namely polymethines.[37] Unlike polyenes, they consist of an odd number of π–conjugated methine units (–CH=), and thus require to be flanked by heteroatoms to balance the charge, as shown in the general structure in **Scheme 2.3** (bottom left). It can be seen that both mesomeric resonance structures of polymethines are identical, and the π–electrons can be perfectly delocalized, so that all the bonds are equal in length. As a consequence, compounds containing polymethine units have remarkably smaller bandgaps compared to polyenes with a similar number of carbon atoms in the π–conjugated chain.

Cyanine dyes are a prominent class of synthetic polymethine compounds, with many different structures known today. They consist of polymethine chains flanked by *N*–heterocyclic rings (typically indole or benzindoles, but also imidazole, pyridine, pyrrole, quinoline and thiazole).[38] Their absorption bands are sharp and tunable all over the visible spectrum and into the NIR. By each additional double bond in the chain, typically a red–shift of ≈100 nm is obtained, as can be seen from the absorption spectra of indole trimethines (Cy3, n=1), pentamethines (Cy5, n=2) and heptamethines (Cy7, n=3) in **Figure 2.5**.

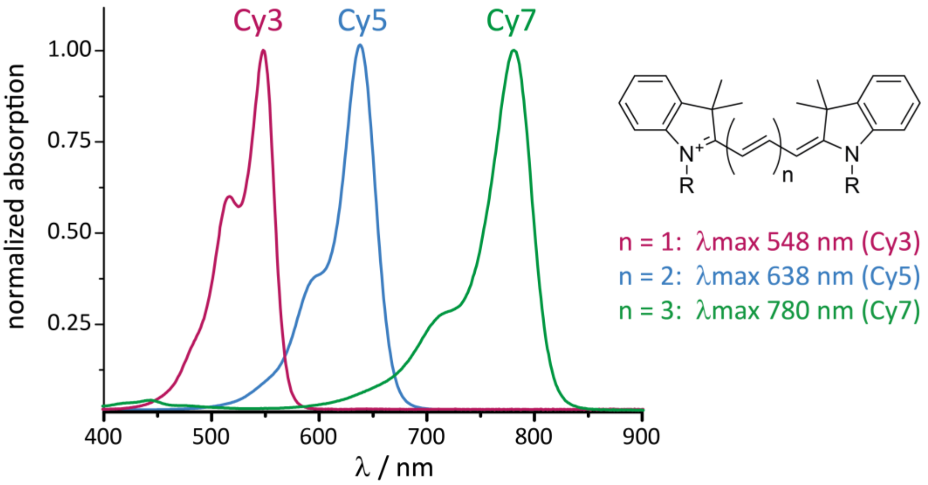

Figure 2.5. Normalized absorption spectra in solution of three indole cyanine dyes with different polymethine chain lengths (Cy3, Cy5 and Cy7) and their general structure.[a]

It is possible to get even longer chains (nonamethines, Cy9, n=4), which possess even lower HOMO–LUMO gaps; however they are very instable towards oxidation of the double bonds[39] and in longer cyanine chains symmetry breaking with disruption of the ideal polymethine state (IPS) are known to occur.[40] For these reasons heptamethine dyes are the most suitable NIR dyes in the cyanine family. Their structural varieties and properties will be discussed in chapter 2.1.3.

iv. *Intermolecular interactions*: A further approach to obtain NIR–absorbance in organic materials is different from the previously discussed ones, in that it is not the property of a single molecule, but the interaction of the π–systems of several molecules that leads to a decreased optical bandgap. Attractive interactions between π–electrons of two or more molecules lead to π–π–stacking in the solid state. Delocalization of the electrons over the π–systems of several molecules leads to band formation, similar to π–conjugated polymers. Another effect, which is of particular relevance for cyanine dyes, is the dipolar coupling of the transition dipoles of π–stacked molecules. Cyanines are known to form two kinds of aggregates: head–to–head or ladder–like aggregates (H) and head–to–tail or staircase–like aggregates (J),[41–43] as illustrated on the right side in **Figure 2.6**. In both kinds of aggregates, a splitting of the excited state is caused by the coupling of the transition dipole moments. The splitting is slightly larger in J– than in H–aggregates, but in both cases only one of the two excited states is accessible by an allowed transition. In H–aggregates, this results in a larger bandgap and thus a blue–shifted absorption, in J–aggregates the bandgap is lowered and thus the absorption is red–shifted (illustrated in the energy diagram in **Figure 2.6**).

---

[a] The structure of the heptamethine dye Cy7 showing this absorption spectrum is slightly modified: it contains a central cyclohexene moiety for increased stability. See chapter 2.1.3.

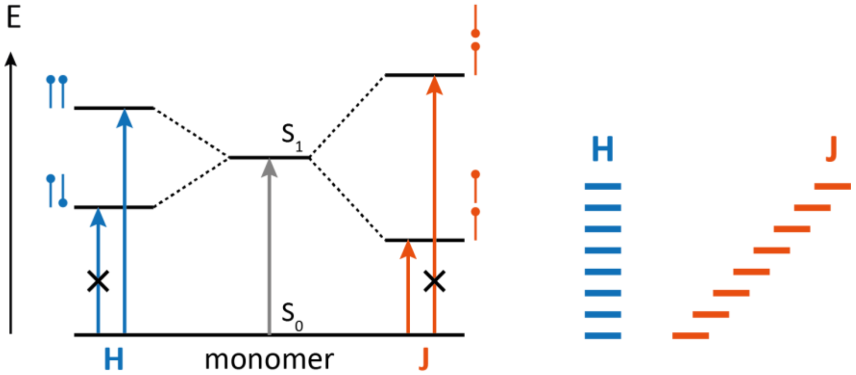

Figure 2.6. Dipolar coupling of the transition dipole leads to a splitting of the excited state (S_1) in H– and J–aggregated dimers. Forbidden S_0–S_1 transitions are marked with a cross. The stacking sequence in H–aggregates (ladder) and J–aggregates (staircase) is shown on the right.

This shows that J–aggregates allow for shifting the absorption of a NIR–absorbing cyanine dye even further to longer wavelengths in the solid state. To control the aggregation of cyanine dyes however, is not trivial and requires careful engineering of both the dye structure as well as deposition conditions (such as solvents, substrates etc.)[44]

To summarize this chapter, there are several approaches to obtain organic materials with NIR absorbing properties, both using structural features within a molecule (extended π–systems, D–A systems, minimized BLA) and intermolecular interactions in the solid state (J–aggregates). The NIR–chromophores studied in this thesis are heptamethine cyanine dyes which will be introduced in more detail in the following chapter.

2.1.3 Heptamethine Cyanine Dyes

Already more than a century ago, heptamethines and other cyanine dyes have been used to enhance the spectral sensitivity of silver halide in photographic emulsions.[45] They exhibit unique optical properties, such as high molar extinction coefficients ($\varepsilon \approx 2 \times 10^5$ M^{-1} cm^{-1}) and tunable absorption wavelengths in the NIR (from the visible to over 1200 nm). At the same time they are easy to synthesize (many structures are even commercially available) and offer great possibilities for structural modifications, so that heptamethine dyes can be tailored to reach desired properties.[46,47] Substituents at various positions in the structure allow for the tuning of solubility, optical and electrochemical properties, as well as the introduction of functional groups that react with specific targets (e.g. biomolecules or surfaces of materials).[48,49]

Nowadays, heptamethine cyanine dyes are being investigated for all kinds of applications that require strong NIR absorption and/or fluorescence. Water–soluble heptamethine dyes are extensively used as fluorescent probes in biomolecular labelling due to the low autofluorescence of biological tissue in the NIR spectrum and good biological compatibility compared to other NIR dyes.[50] It is also notable that heptamethine dyes are being investigated for tumor diagnostics and theranostic cancer treatment (targeted drug delivery and photodynamic therapy).[51] Apart from the biological and medical fields, heptamethine dyes are applied as laser dyes[52,53] and in optical recording media.[54] Finally, and most relevant for this thesis, their strong NIR absorbing properties are of great interest for the field of organic electronics. They are used as light harvesters both in dye–sensitized solar cells (DSSC)[55] and organic solar cells (OSC),[56,57] where their strong NIR absorption could allow for the fabrication of visibly transparent solar cells. Also for other devices, such as NIR photodetectors or NIR light–emitting devices, heptamethine cyanine dyes are ideal candidates.

2.1.3.1 Synthesis of Heptamethine Dyes

Structurally, most heptamethine dyes used and studied today carry a central cyclohexene moiety (structure **7** in **Scheme 2.4**) in order to avoid *cis–trans* isomerization of the double bonds and to stabilize the conjugated chain towards oxidative degradation; furthermore this moiety leads to a lower tendency of aggregation of the molecules in solution and the increased rigidity of the system enhances the fluorescence quantum yield.[39]

Scheme 2.4 illustrates the synthesis of a symmetric heptamethine dye **7** by Knoevenagel condensation of an alkyl–indolium cation carrying an activated methyl group (**4**) with a pentamethine dianil compound (**6**); this procedure was first described by Makin et al in 1977.[58] The condensation reaction can be carried out in anhydrous ethanol under reflux using sodium acetate as a base.[59] These conditions have several advantages: Not only are they mild and environmentally friendly but they allow the heptamethine salt to crystallize out of the cooled reaction mixture in high purity, so that no further purification steps are required. Depending on the substituents, however, other solvents (e.g. acetic anhydride)[60] and/or bases (e.g. triethylamine)[61] might have to be employed in order to obtain the product in good yields. Salon et al. have reported improved yields for the synthesis of heptamethines with C–substituents at the *meso*–position (R^2 = alkyl, aryl) by using pyridine both as a base and solvent.[62]

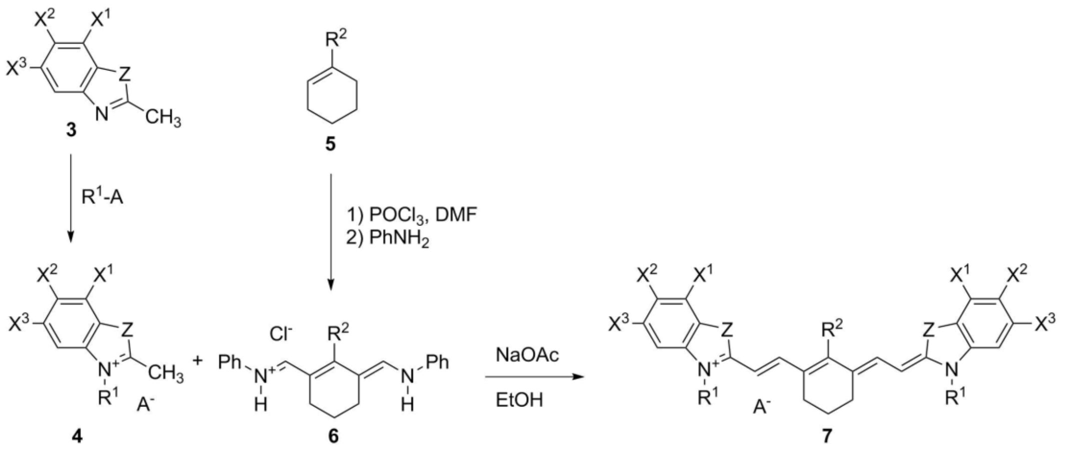

Scheme 2.4. General synthetic strategy towards symmetric heptamethine dyes **7**. Typical substituents: R^1 = alkyl group; R^2 = Ph, Cl or others; A^- = leaving group (e.g. halides, $R–SO_3^-$); X^1, X^2, X^3, = various substitutions possible, eg.. fused benzene ring(s). Z = $C(CH_3)_2$, S, or fused benzene ring.

Quarternary indolenium salts **4** are obtained by alkylation of the corresponding indole carrying a methyl group at the 2–position (**3**).[63] If the choice of counteranion in the final heptamethine salt is of importance, the alkylation reagent R^1–A has to be chosen carefully. It is not only influencing the reactivity of the alkylation step but also its leaving group A^- is preserved as the counteranion of the final heptamethine cation. Good leaving groups for the alkylation are the halides I^- and Br^- or sulfonates $R–SO_3^-$,[61] while the halides are more versatile for subsequent counterion exchanges to other anions in the heptamethine salt.[64] Indole precursors **3** are synthesized via *Fischer* indole synthesis[65] and various substitutions at the heterocycle X^1, X^2, X^3 (**Scheme 2.4**) can be introduced at this initial step.[60] Several indole derivatives with a 2–methyl group are also commercially available today.

Dianil compounds **6** are the Schiff bases of their corresponding dialdehydes which are synthesized by reaction of cyclohexene **5** with a Vilsmeier–Haack reagent, generated from *N*,*N*–dimethylformamide and phosphorus oxychloride. These dialdehydes are very reactive and cannot be stored; thus they are protected with phenylamine to form dianils **6** for easier handling. In some procedures heptamethines are also synthesized directly by *in–situ* treatment of the reactive dialdehyde with the corresponding heterocycles **4**.[60] By choosing suitably substituted cyclohexene derivatives **5** various groups can be introduced at the *meso*–position (R^2) of the heptamethine dye. Dianil compounds with R^2 =Ph or Cl are commercially available. A post–synthetic strategy to introduce different *meso*–substituents to the heptamethine chromophore will be described in chapter 2.1.3.2.

It is also possible to synthesize unsymmetrical heptamethine dyes with different substitutions on each side; however the loss in symmetry is detrimental for the optical properties of the polymethine (hypsochromic shift, lowered molar extinction coefficient).[66]

2.1.3.2 Modifications of Heptamethine Salts

As can be seen from above, the possibilities for introducing different substituents into heptamethine dyes are nearly unlimited and a vast number of derivatives are described in the literature. In this work, the focus lies on NIR heptamethine dyes suitable for application in organic electronic devices. The structural modifications which are of particular interest for this purpose will be highlighted in the following. The N–alkyl group R^1 should be chosen to ensure good solubility in organic solvents, which is necessary for processing the dyes into thin films (e.g. by spin–coating).

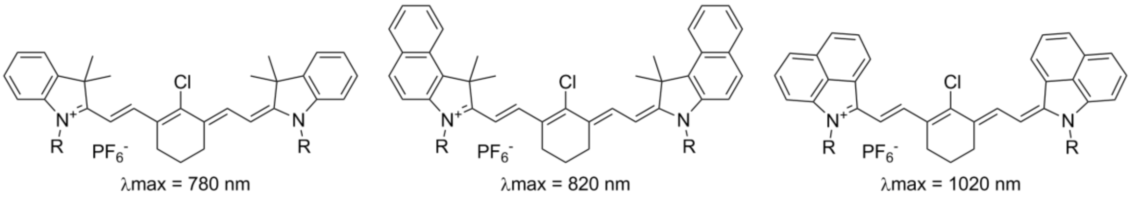

Scheme 2.5. Heptamethines with different indole heterocycles and their absorption maxima (in ethanol). Heterocycles from left to right: Indole, benz[*e*]indole, benz[*cd*]indole.

Different indole heterocycles are able to alter the absorption maximum of the dye (**Scheme 2.5**), while a bathochromic shift is obtained when the conjugation in the heterocycle is increased. It has been shown that the use of the benz[*cd*]heterocycle gives absorption maxima above 1000 nm.[67,68]

An attractive location for the post–synthetic modification of heptamethine dyes is the *meso*–position (R^2 in **Scheme 2.4**). Chloro substituted dyes (R^2 = Cl) have been shown to undergo aromatic substitution reactions with nucleophiles, which can happen by an $S_{RN}1$ mechanism (unimolecular radical nucleophilic substitution), which is initiated by single–electron transfer from the nucleophile to the π–system under formation of two neutral radical species,[69,70] as shown below in (1). Upon loss of the nucleofugal chloride group in the neutral cyanine radical $[Cy–Cl]^{\bullet}$, a cationic cyanine radical is formed (2) which can then react with a nucleophile Nu^- to form the radical adduct $[Cy–Nu]^{\bullet}$ (3). Radical transfer from this adduct to a cyanine cation $[Cy–Cl]^+$ gives the substituted product $[Cy–Nu]^+$ along with a neutral cyanine radical (4), which can undergo steps (2)–(4) again.

$$[Cy–Cl]^+ + Nu^- \rightarrow [Cy–Cl]^{\bullet} + Nu^{\bullet} \quad (1)$$

$$[Cy–Cl]^{\bullet} \rightarrow Cy^{\bullet +} + Cl^- \quad (2)$$

$$Cy^{\bullet +} + Nu^- \rightarrow [Cy–Nu]^{\bullet} \quad (3)$$

$$[Cy–Nu]^{\bullet} + [Cy–Cl]^+ \rightarrow [Cy–Nu]^+ + [Cy–Cl]^{\bullet} \quad (4)$$

The combination of two radical species in this pathway has to be avoided, as it would not lead to the desired substitution product. The solvent used for this reaction needs to allow for electron transfer and should not be a radical quencher; polar aprotic solvents such as DMF or DMSO have been described as suitable.[71] Various substituents (e.g. amines, thiolates[70] and barbiturates[61]) can be introduced to the *meso*–position of heptamethine cyanine dyes in this way. Electron–donating or electron–withdrawing substituents at the π–system are able to alter the redox levels of the molecule.[72,73] It is reported that the substituent at the *meso*–position of a heptamethine dye influences mainly its reduction potential (LUMO), and only slightly the oxidation potential (HOMO). Electron–donating groups are raising the energy levels, whereas electron–withdrawing groups are lowering them.[74, page 71] For the application in solar cells the tuning of these levels is of particular interest as electron transfer from the LUMO of the absorber to an electron–accepting material and/or hole transport from the HOMO of the absorber to a hole–transporting material has to be possible. This subject will be further discussed in chapters 2.3.1 and 3.2.2.

As cyanine dyes are cations, their properties can not only be tuned by modification of the chromophore, but also by the choice of different counterions. Bouit et al. have shown that the counterion has an important effect on the chromophore.[64] An undisturbed cyanine cation, in which all polymethine carbon bonds are equally long, is called to be in the ideal polymethine state (IPS). By pairing the cation with a counterion, however, this IPS can be disturbed. Strongly coordinating counterions tend to push the electron density to one side of the π–system and break the symmetry in the chromophore. This leads to bond length alternation and loss of the unique optical properties of the cyanine cation.[64] The counterion was shown to have a strong influence also on the solid state properties of a cyanine salt, such as the compatibility with other materials in molecular blends.[75] For electronic applications, where the cyanine salts are applied in their solid state form, the choice of ideal counterions is thus crucial.

2.2 Synthesis of Cyanine Dyes with Different Counterions

2.2.1 Aim: Counterion Exchange for Optimized Interfaces

In organic solar cells (OSC) exciton splitting occurs at the donor–acceptor interface (see chapter 3.1.1.1 for the working principle of OSC). Thus it is essential to achieve smooth interfaces providing good contact between the two materials. When cyanine dyes are used as electron donors together with fullerenes as electron acceptors, the formation of optimized interfaces can be challenging. There is a strong difference in hydrophilicity between the polar cyanine salts and the apolar carbon compounds. Mobile ions have also been shown to be able to alter the energy levels at the interface and thus the thermodynamics of electron transfer reactions.[76,77]

As introduced in the previous chapter, the choice of counterion can have a tremendous effect on the properties of cyanine salts, particularly in their solid state. Bouit et al. have intensively investigated the influence of different counterions on the photophysical properties of heptamethine dyes.[64] Small, hard counterions polarize the cationic dye core, leading to bond length alternation (BLA) and disruption of the ideal polymethine state (IPS)[64] (which is manifested as a blue shift of λ_{max} and a decreased ε). They could show that soft, bulky anions, such as the TRISPHAT− anion,[78] are the most suitable for reaching IPS. Furthermore, large anions containing aromatic moieties could allow for favorable interactions between the cyanine salt and fullerenes at the heterojunction and thus optimized interfaces.[b]

In this work, two simple and well–known cyanine chromophores are used in order to investigate the influence of the counterion on the properties of a cyanine salt: a NIR absorbing heptamethine dye (λ_{max} = 780 nm) and a trimethine dye (λ_{max} = 550 nm). The counterions are exchanged from iodide to hexafluorophosphate (PF_6^-) and Δ–TRISPHAT$^-$, respectively, and the resulting four cyanine dye salts are purified and fully characterized. The structures of the dyes and the Δ–TRISPHAT$^-$ counterion are shown in **Scheme 2.6**. The main focus in this work lies on NIR heptamethine dyes **Cy7P** and **Cy7T**, but also the trimethine analogues **Cy3P** and **Cy3T** are included, as they are useful e.g. for fundamental studies of blend films. In chapter 2.2.2 the optical and electrochemical properties of these four compounds, as well as the crystal structures of NIR dyes **Cy7P** and **Cy7T** obtained by single crystal X–ray diffraction are discussed and compared. The properties of these compounds in thin films and bulk heterojunction blends together with C_{60}, as well as their application in OSC devices are reported in chapter 3.

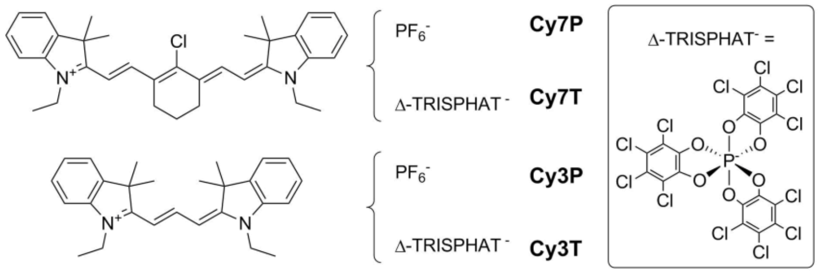

Scheme 2.6. Structures of standard heptamethine **Cy7**$^+$ and trimethine **Cy3**$^+$ chromophores with different counterions. PF$_6$ (**Cy7P** and **Cy3P**) and Δ–TRISPHAT (**Cy7T** and **Cy3T**).

2.2.2 Results and Discussion

2.2.2.1 Synthesis and Counterion Exchange[79,80]

The cyanine iodide salts (**Cy3I**, **Cy7I**) serving as precursors in the counterion exchange reactions have been prepared according to literature procedures.[59,63,81]

---

[b] See chapter 3.1.1 for a more detailed introduction on the state of the art of cyanine-fullerene interfaces in bilayer and bulk-heterojunction architectures for organic solar cells.

Synthesis of the heptamethine dye core was achieved via Knoevenagel condensation of an alkylated indolium precursor carrying an activated methyl group and a dianil compound with chloro–cyclohexene moiety (see chapter 2.3.2.1.2, **Scheme 2.9**, page 30).

In order to exchange I^- for PF_6^-, an aqueous solution of sodium hexafluorophosphate ($NaPF_6$) was added to an alcoholic solution of the cyanine iodide (**Cy3I**, **Cy7I**) leading to a precipitation of the corresponding cyanine PF_6^- salt (**Cy3P**, **Cy7P**).[64] The compounds were easily obtained in high purity by washing and recrystallization of the precipitate. Exchange from I^- to Δ–TRISPHAT$^-$ was carried out by stirring a solution of cyanine iodide (**Cy3I**, **Cy7I**) and Δ–TRISPHAT tetrabutylammonium salt in DCM at room temperature overnight. First, purification was achieved by column chromatography to remove residual cyanine iodide salts. Tetrabutylammonium salt impurities could only be removed after recrystallization and the salts **Cy3T** and **Cy7T** were obtained in high purity and good yields. The yield for **Cy3P** (56%) was lower than for **Cy7P** (94%) due to losses during repeated recrystallizations to reach the final purity suitable for device application.

Table 2.1. Summary of reaction conditions and yields for counterion exchanges.

	counterion	***conditions***	***cyanine cation***	***yield***
Cy3P	PF_6^-	$NaPF_6$, MeOH /H_2O	**Cy3⁺** 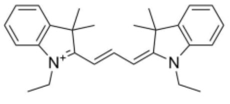	56%
Cy7P			**Cy7⁺** 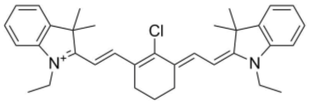	94%
Cy3T	Δ–TRISPHAT$^-$	NBu_4^+ Δ–TRISPHAT$^-$, DCM, rt, 20 h	**Cy3⁺** 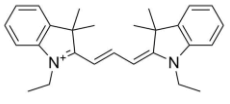	50%
Cy7T			**Cy7⁺** 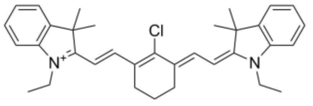	57%

Structures and purity of all compounds were confirmed by ^1H– and ^{13}C–NMR (correlations obtained from HSQC and HMBC and COSY experiments), elemental analysis (EA) and high resolution mass spectrometry (HR–MS). The reaction conditions and yields for the counterion exchanges are summarized in **Table 2.1**.

2.2.2.2 Optical and Electrochemical Characterization[79]

In order to evaluate the influence of the counterion on the optical properties of the cyanine dyes, absorption and emission spectra in different solvents were recorded.

UV–Vis–NIR absorption spectra of the compounds in solution normalized to their molar extinction coefficient ε at λ_{max} are shown in **Figure 2.7** and a summary of the optical properties is given in **Table 2.2**. The solvents were, in order of decreasing polarity:[c] DMF, acetonitrile, ethanol, chlorobenzene, chloroform and cyclohexane. Only the TRISPHAT salts were soluble in cyclohexane (at concentrations ≈ 2×10^{-5} M) which indicates that this counterion is able to lower the overall polarity of the cyanine salt.

The heptamethine dyes show a narrow absorption band between 650 and 850 nm. The value of λ_{max} is equal for **Cy7P** and **Cy7T** in each solvent, suggesting that the ions dissociate in solution and the absorption of the dye cation is not influenced by the anions. With decreasing polarity of the solvent a slight bathochromic shift of λ_{max} can be observed (positive solvatochromism). However, the change in λ_{max} is so small that it can be assumed that the nature of the ground state and excited state remain similar. The solvent has an influence on the molar extinction coefficient ε as well as on the peak shape. In the case of **Cy7T**, extraordinarily high values for ε are found in the chlorinated solvents chloroform and chlorobenzene (375×10^{3} and 360×10^{3} M^{-1} cm^{-1}, respectively, compared to an average value of 240×10^{3} M^{-1} cm^{-1} in the other solvents). When comparing the integrated absorption coefficient (IAC), however, it can be seen that the area under the absorption band is very similar (IAC = 9×10^{18} to 1×10^{19} M^{-1} cm^{-1} s^{-1} in all solvents), indicating an absorption of similar intensity in all solvents. The difference in ε arises from much narrower peak shapes in the chlorinated solvents. This could be due to a better solubilization of the dyes in these solvents, leading to less dimerization/aggregation. Oscillator strengths greater than one have been found for the heptamethine dyes, indicating that apart from the HOMO and LUMO orbitals additional molecular orbitals participate in the $S_0 \rightarrow S_1$ transition. The optical bandgap of the heptamethine dyes calculated from the absorption onset was found to be ≈ 1.52 eV (average from all solvents).

The trimethine dyes show a narrow absorption band between 450 and 580 nm. As for the heptamethines a slight positive solvatochromism of a few nanometers is observed; however also for the trimethines it is small enough to assume that the nature of the excited state is similar to the ground state. The absorption intensity also varies slightly depending on the solvent. A peak narrowing as found for **Cy7T** in chlorinated solvents, however, was not observed, as the solvents that give a higher ε also show a higher IAC. The optical bandgap of the trimethine dyes calculated from the absorption onset was found to be ≈ 2.17 eV (average from all solvents).

---

[c] Polarity of solvents classified by value of relative permittivity.

Overall the counterion seems to have very little to no influence on the absorption properties of the cyanine dyes in solution, as the ions are well solubilized and dissociated from each other.

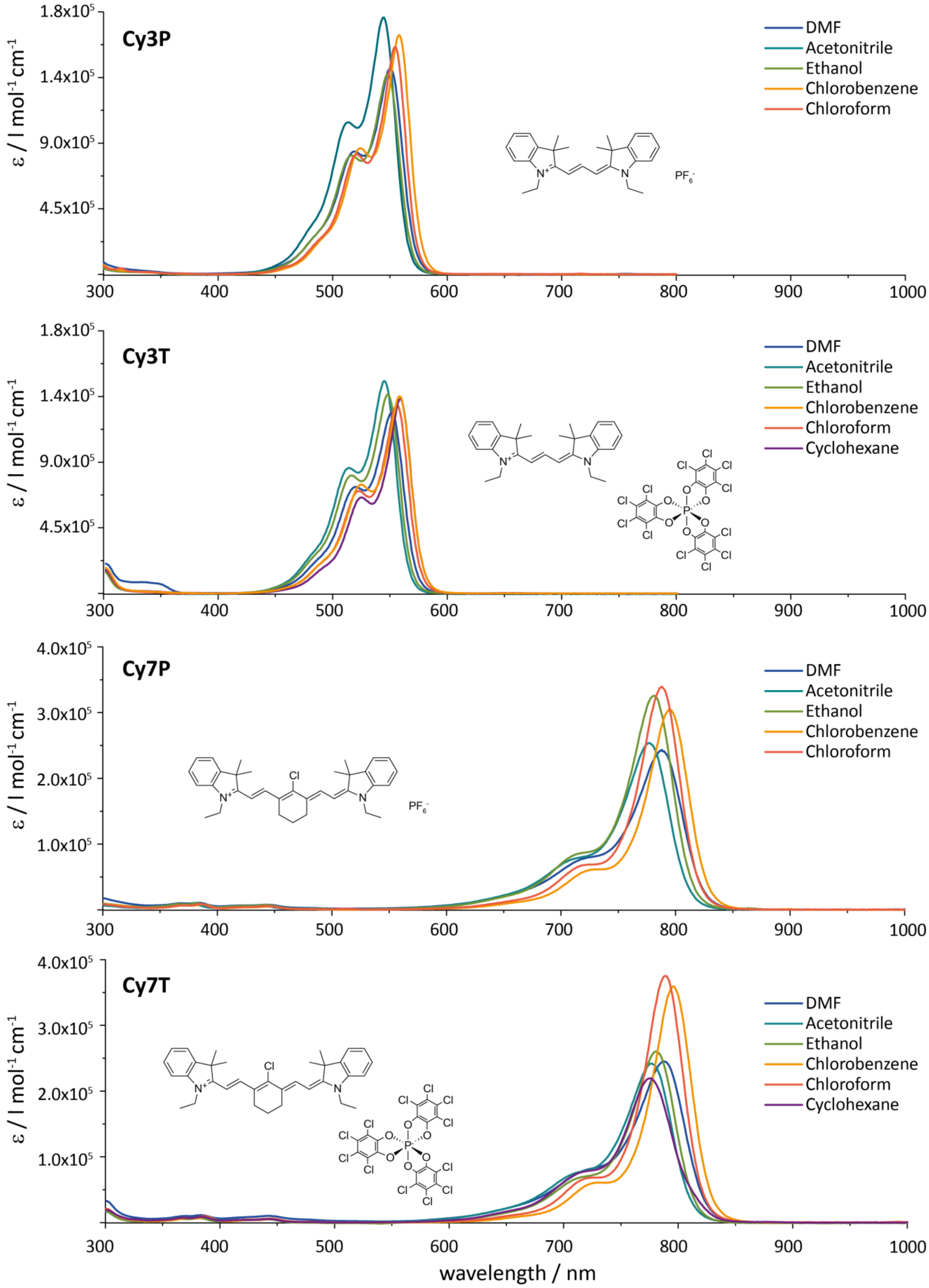

Figure 2.7. UV–Vis–NIR absorption spectra of **Cy3P**, **Cy3T**, **Cy7P** and **Cy7T** in different solvents normalized to their molar extinction coefficient ε at λ_{max}. PF_6^- salts were not soluble in cyclohexane.

Table 2.2. Optical properties of cyanine dyes with different counterions in different solvents.

dye	*solvent*	λ_{max}[a] *nm*	ε[b] $M^{-1}\,cm^{-1}$	*IAC × 10^18*[c] $M^{-1}\,cm^{-1}\,s^{-1}$	*f*[d]
Cy3P	DMF	550	141'000	8.1	1.16
	ACN	544	176'000	9.8	1.40
	EtOH	548	137'000	7.6	1.09
	PhCl	558	164'000	8.1	1.16
	$CHCl_3$	555	156'000	7.8	1.11
Cy3T	DMF	550	124'000	6.9	0.99
	ACN	544	146'000	8.0	1.15
	EtOH	548	136'000	7.5	1.08
	PhCl	557	135'000	7.0	1.01
	$CHCl_3$	555	129'000	6.7	0.95
	cyclohexane	558	133'000	6.3	0.91
Cy7P	DMF	788	243'000	10.1	1.46
	ACN	777	254'000	10.0	1.44
	EtOH	781	325'000	11.5	1.66
	PhCl	795	305'000	9.2	1.32
	$CHCl_3$	788	340'000	10.3	1.48
Cy7T	DMF	787	245'000	10.3	1.47
	ACN	777	242'000	9.7	1.40
	EtOH	781	260'000	9.1	1.31
	PhCl	796	360'000	9.8	1.41
	$CHCl_3$	789	375'000	10.8	1.55
	cyclohexane	775	219'000	8.9	1.27

[a] Absorption maximum. [b] Molar extinction coefficient at λ_{max}. [c] Integrated absorption coefficient. [d] Oscillator strength. Details about the determination of these values are given in the experimental part, chapter 0.

Emission spectra of the dyes with PF_6^- and TRISPHAT$^-$ counterions in different solvents show a fluorescence band between 540 and 650 nm for trimethines and between 760 and 850 nm for the heptamethines. The Stokes shifts are small (12–19 nm), which is typical for cyanine dyes.[82] As for the absorption properties in solution, little to no influence of the counterion was observed. Emission spectra are shown in the experimental chapter (**Figure 7.1**, page 113).

Cyclic voltammetry (CV) measurements were carried out in electrolyte solution (0.1M TBACl in DMF) to determine the redox potentials of the dyes. Again, it was found that the counterion does not have an influence on the electrochemical properties of the cation, neither the trimethine nor the heptamethine. For both **Cy7P** and **Cy7T**, the oxidation potential vs vacuum E_{ox} was found to be −5.37 eV, and the reduction potential E_{red} was at −4.20 eV. The electrochemical band gap of the heptamethine dyes is 1.17 eV.

For the trimethine dyes no anodic peak was observed around E_{ox}, which indicates that the oxidation is irreversible. A possible explanation is that the dyes dimerize irreversibly upon oxidation. It has been described in the literature that such a dimer can form a stable bis–dye upon loss of two protons and two electrons.[83] When the measurement was performed in TFE (trifluoroethanol), however, the oxidation of the trimethines was reversible, so that E_{ox} could be determined. For both **Cy3P** and **Cy3T**, the oxidation potential vs vacuum E_{ox} was found to be −5.91 eV, and the reduction potential E_{red} was at −3.78 eV. The electrochemical band gap of the heptamethine dyes is 2.13 eV.

The counterions PF_6^- and TRISPHAT$^-$ themselves are not redox active in the potential range of the cation or C_{60}, which makes them suitable for their application in solar cells, as they are not able to trap charges. The difference between the optical and electrochemical gap observed here follows the general trend known for cyanine dyes (E_{opt}–E_{el} ≈ 0.35 V).[73]

2.2.2.3 X–ray Crystal Structures[79]

Single crystals of **Cy7P** and **Cy7T** suitable for X–ray crystal structure analysis could be grown by vapor diffusion of Et_2O into DCM solutions of each compound. The packing of the heptamethine cations in the crystal structures is influenced to a large extent by the counterion.

With the PF_6^- counterion a monoclinic solvent–free crystal structure in the space group *Pn* (#7) was obtained. The asymmetric unit (**Figure 2.8 a**) contains four symmetry–independent cations and anions. The independent cations generally have very similar conformations with only small differences in most torsion angles. The major differences are that one cation has the terminal methyl group of one ethyl substituent rotated by approximately 180° relative to its orientation in the other three cations and that another cation has the opposite half–chair puckering of the central six–membered ring compared with the other cations. No additional crystallographic symmetry could be found in the structure, although the structure is pseudocentrosymmetric with an 83% fit of the atoms to the additional symmetry element; the differences between the conformations of the cations are breaking the additional symmetry. No obvious interactions, such as π–π stacking, could be found in the crystal packing (**Figure 2.8b**).

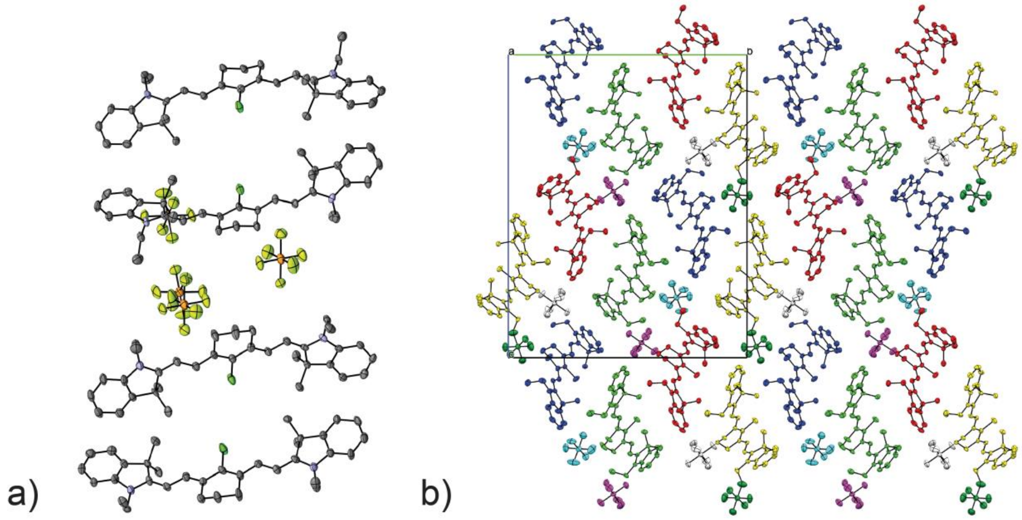

Figure 2.8. Crystal structure of **Cy7P**. (a) asymmetric unit, (b) crystal packing viewed along the a–axis, colored by symmetry equivalence.[79]

With Δ–TRISPHAT⁻ as the counterion, a triclinic crystal structure in the space group P—1 (#2) was obtained. In contrast to the structure with PF_6^-, only one cation and anion is found in the asymmetric unit (**Figure 2.9 a**) alongside some highly disordered solvent molecules which are assumed to be diethyl ether. In the crystal packing (**Figure 2.9 b**), the cations and anions form layers parallel to the a–axis. However, the distances between the π–systems of the cyanine cations are on the order of 10 Å, and thus no π–π stacking occurs.

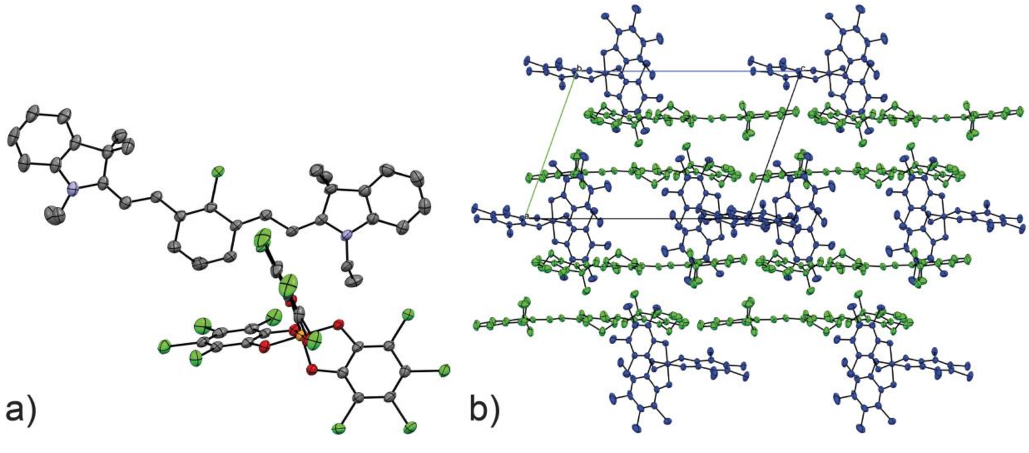

Figure 2.9. Crystal structure of **Cy7T**. (a) asymmetric unit, (b) crystal packing viewed along the b–axis, colored by symmetry equivalence.[79]

When comparing the crystal structures of **Cy7P** and **Cy7T**, it is found that the TRISPHAT counterion associates more weakly with the heptamethine cation, as expected due to sterical hindrance. The Δ–TRISPHAT⁻ counterion leads to a more ordered packing structure of the cations, which are found at larger spacing from each other than in the crystal structure with PF_6^-. It is difficult however to draw direct conclusions from this on the packing structure of the cations in spin–coated thin films used for organic solar cells, as these are thought to be amorphous.

2.3 Synthesis of Heptamethines with Different *meso*–Substitution

2.3.1 Aim: Tuning of the Redox Levels of Heptamethine Dyes

As mentioned in the introductory chapter, there is a vast number of differently substituted heptamethine with various dyes known in the literature, while most investigations target at biological applications. Specific studies on how to obtain chromophores with suitable electron levels for application solar cell devices, however, are absent.

The target of this work is the synthesis of various NIR absorbing heptamethine dyes which can act as hole–transporting layers (HTL) and co–sensitizers in methylammonium lead halide ($CH_3NH_3PbI_3$) perovskite solar cells (see chapter 3.2.2) using the following considerations: In order for hole–injection from the perovskite to the heptamethine to occur, the HOMO level of the dye must be higher in energy than the valence band maximum (VBM) of the perovskite. In order for co–sensitization to occur, an electron must be injected from the LUMO of the dye into the conduction band of the perovskite, and thus the LUMO should be higher in energy than the conduction band minimum (CBM) of the perovskite. In **Figure 2.10** the energy levels of $CH_3NH_3PbI_3$[84] and the heptamethine cation **Cy7⁺**[79] (which was used previously in the counterion study, see chapter 2.2) are depicted. Both, E_{ox} and (E_{ox} + E_{opt}) of **Cy7⁺** are indicated for the following reason: The redox potentials obtained from cyclic voltammetry measurements (E_{ox} and E_{red}) are usually not identical with the real orbital energy levels (HOMO and LUMO) in the molecule.[85] In cyanine dyes, the opticap bandgap (E_{opt}) is usually larger than the electrochemical bandgap (E_{el}).[73,86] An approximate value for the energy of the first excited state S_1 of a cyanine dye is obtained by adding the optical bandgap to the first oxidation potential (E_{ox} + E_{opt}).[73]

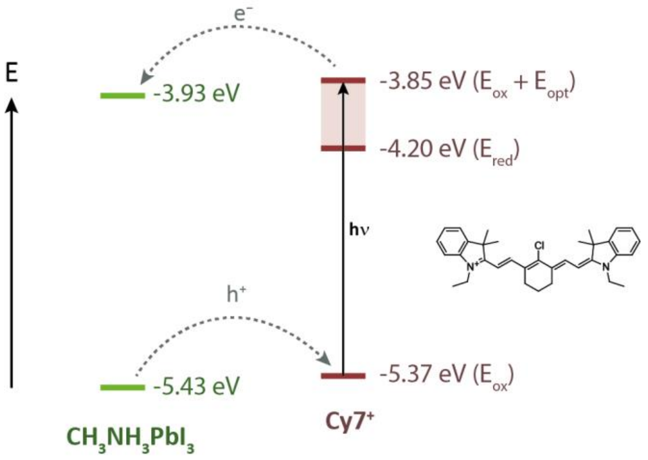

Figure 2.10. Energy level diagram of VBM and CBM of $CH_3NH_3PbI_3$ and redox potentials of the **Cy7**$^+$ cation.[79,84] The dotted lines indicate the targeted hole or electron injection processes in the solar cell, which are not very favored when using **Cy7**$^+$.

As can be seen in **Figure 2.10**, the HOMO and LUMO levels of **Cy7**$^+$ are only slightly offset in energy compared to the VBM and CBM of $CH_3NH_3PbI_3$. It is apparent, that both the HOMO and the LUMO level of a cyanine HTL should ideally be slightly higher in energy (than for **Cy7**$^+$) in order for efficient electron / hole transfer to occur in the solar cell. It was introduced in chapter 2.1.3.2 that *meso*–substitution at the heptamethine chromophore allows for fine–tuning of these levels.[72] The introduction of electron–donating substituents at this position is predicted to raise both energy levels, while the LUMO should be affected stronger than the HOMO.[74] At the same time it is of interest to extend the absorption of the heptamethine dye further into the NIR, which can be achieved by introducing benzindole heterocycles (see chapter 2.1.3.2).[68]

Given this motivation, heptamethine dyes with different (benz)indole flanking groups as well as various electron–donating substituents in *meso*–substitution are synthesized and fully characterized and the influence of these substituents on their properties is studied. Finally their compatibility with the $CH_3NH_3PbI_3$ perovskite layer is evaluated. The creation of a library of NIR heptamethine dyes with varying redox levels is also beneficial for other types of organic electronic applications.

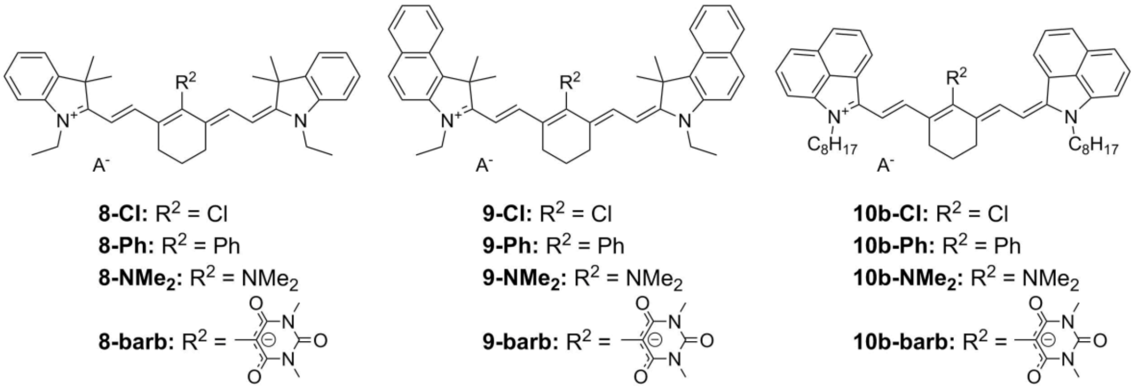

Scheme 2.7. Target structures of heptamethine dyes flanked by different indole heterocycles with varying *meso*–substitution.[d] Dyes with the barb–substituent are internal salts, all other dyes carry $A^- = I^-$ or PF_6^- as the counterion.

The target molecules are shown in **Scheme 2.7**. Various substituents with inductive or mesomeric electron–donating properties have been chosen, which are expected to be achieved by straightforward synthesis or by post–synthetic modification of the chloro–heptamethine dye. All dyes are synthesized as the iodide salts and then counterion exchange to PF_6^- is performed, except for the structures with the barbiturate (**barb**) substituent, which are internal salts and thus do not require a counterion.

2.3.2 Results and Discussion

2.3.2.1 Synthesis

2.3.2.1.1 Benz[cd]indolium heterocycle

In order to obtain heptamethine dyes that absorb above 1000 nm, the benz[cd]indolium heterocycle was synthesized as shown in **Scheme 2.8** according to an adapted literature procedure.[87] First, lactam **11** was *N*–alkylated with the respective alkylbromide (R^1–Br) in sulfolane using potassium iodide (KI) and 4–dimethylaminopyridine (DMAP) as catalysts and potassium hydroxide (KOH) as a base. The resulting intermediate was further treated with methyl magnesium chloride in THF; after aqueous work–up and precipitation with KI the alkylated benz[cd]indolium heterocycle with a methyl group in 2–position (**12a** or **12b**) was obtained as the iodide salt. Heptamethine dyes containing the benz[cd]indolium heterocycle are expected to be less soluble than their indolium and benz[e]indolium analogues (which carry methyl groups in 3–position of the indole), and thus require to be substituted in a way to increase their solubility. Branched alkyl chains like 2–ethylhexyl are known to improve the

---

[d] Dye **8-Cl** is identical with the **Cy7⁺** cation from the previous chapter 2.2. The structure will be named **8-Cl** here in analogy to the other dyes discussed in this chapter.

solubility and thermal properties of polymethine dyes.[88,89] 2–Pentyl was chosen because it can be expected to have similar properties and the alkylation and subsequent reduction of lactam **11** with 2–bromopentane is already described.[87] The obtained yield of 71% over two steps is in good agreement with the literature. As will be mentioned later, the solubility and aggregation behavior of heptamethine dye **10a–Cl** with the 2–pentyl side chain was not satisfying. Thus the 1–octyl chain was chosen as a long alkyl chain expected to improve the solubility of compounds with large π–systems. The alkylation of lactam **11** with 1–bromooctane was carried out using the same reaction condition and work–up as for 2–bromopentane, however the yield was lower (45% over both steps). Attempts were made to introduce a hexadecyl alkyl chain using the same alkylation and reduction procedure starting from lactam **11**, however no product could be isolated.

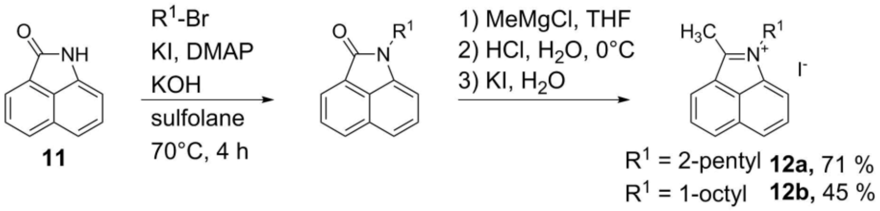

Scheme 2.8. Synthesis of *N*–alkylated benz[cd]indolium heterocycle.

2.3.2.1.2 Knoevenagel Coupling to Heptamethine Dyes

Heptamethine dyes were synthesized as shown in **Scheme 2.9.**[59] Indolium and benz[e]indolium heterocycles (**13** and **14**) with an ethyl group as the *N*–alkyl chain were prepared according to literature procedures[63] and coupled with a dianil compound carrying a Ph– or a Cl–substituent at the *meso*–position to give indole heptamethines (**8**) and benz[e]indolium heptamethines (**9**).

The synthesis of benz[cd]indolium heptamethines (**10**) was carried out in a similar fashion. **10a–Cl** with 2–pentyl as the *N*–alkyl chain showed strong broadening of NMR signals in various solvents, which was attributed to aggregation. This is an unwanted property for the purpose of this thesis and thus 1–octyl was examined as an alternative. **10b–Cl** with 1–octyl as the *N*–alkyl chain did not show the NMR line broadening and so the 1–octyl chain was chosen for further synthesis and study of the dyes containing the benz[*cd*]indolium heterocycle. **10b–Cl** could not be synthesized using NaOAc as a base in ethanol like the other heptamethine dyes; an alternative route with triethylamine (NEt_3) as a base in acetic anhydride (Ac_2O) was successful.

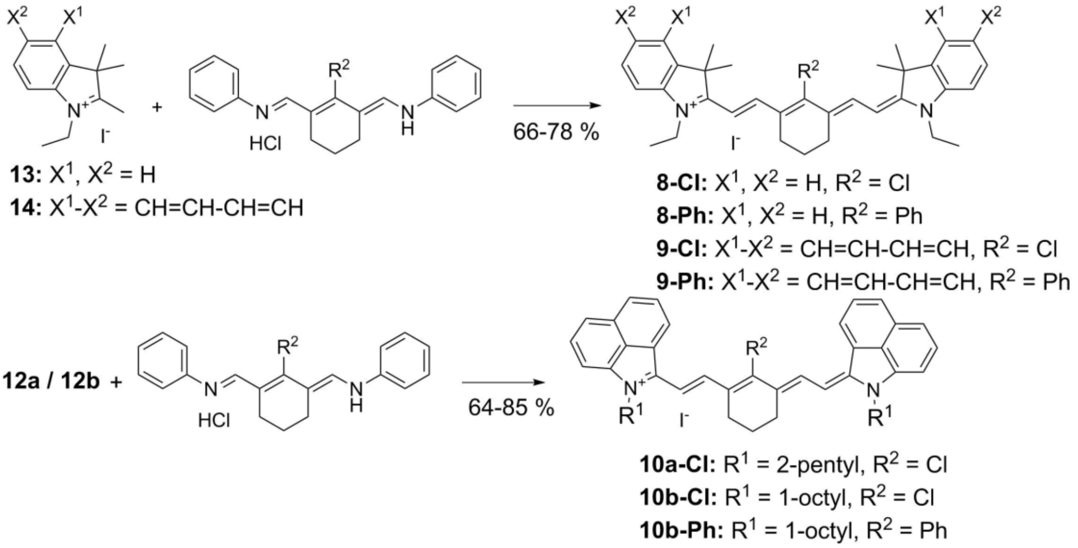

Scheme 2.9. Synthesis of heptamethine iodide salts by Knoevenagel coupling of a heterocycle with the respective dianil. Reaction conditions: NaOAc, EtOH, reflux, 1–16 h. **7b–Cl** was synthesized using an alternative route: NEt_3, Ac_2O, AcOH, 65 °C, 30 min

All heptamethines were first obtained as iodides and then precipitated as PF_6^- salts as described in chapter 2.2.2.1, so that the final products have PF_6^- as their counterion.

2.3.2.1.3 $S_{RN}1$ substitution in *meso*–position

Heptamethine dyes with a chloro–substituent in the *meso*–position (**8–Cl**, **9–Cl**, and **10b–Cl**) were further subjected to nucleophilic substitution conditions ($S_{RN}1$).[90] 1,3–Dimethylbarbituric acid and dimethyl amine and were used as nucleophiles to obtain the respective *meso*–barbiturate (**8/9–barb**) and *meso*–NMe_2 analogues (**8/9–NMe₂**) as shown in **Scheme 2.10**. The *meso*–NMe_2 analogues were first obtained as iodides and then precipitated as PF_6^- salts. The *meso*–barbiturate dyes form an inner salt and are thus “counterion–free”. **9–barb** (**Scheme 2.7**) is commercially available and was purchased for optical and electrochemical analysis and for comparison with the synthesized dyes.

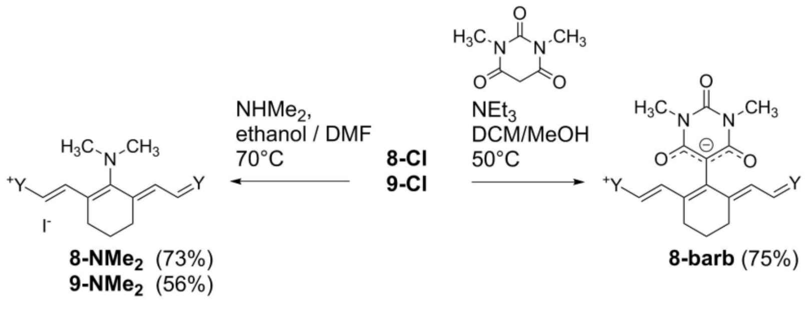

Scheme 2.10. Nucleophilic substitution reactions to obtain dyes with electron–donating substituents in *meso*–position. Y stands for the respective heterocycle (**8**: indole, **9**: benz[e]indole). Yields are given in parentheses.

Efforts were made to synthesize also the benz[cd]indolium heptamethine dyes with electron donors in the *meso*–position by $S_{RN}1$ substitution. It was found however, that they are difficult to obtain by using the same reaction conditions as given in **Scheme 2.10**.

Both cations **10b–NMe₂** and **10b–barb** (**Scheme 2.7**) could be detected by ESI–MS in the reaction mixtures and in the crude products. During purification attempts by chromatography or recrystallization in ambient atmosphere, however, decomposition of the products was observed. UV–Vis absorption spectra showed absorption bands in the region 400–600 nm and mass/charge ratios corresponding to the heterocyclic precursor **12b** were identified by ESI–MS, indicating a decomposition of the heptamethine chromophore. A possible explanation for this decomposition might be that the large π–system of benz[*cd*]indolium heptamethine dyes becomes particularly sensitive towards oxidation by air as it becomes more electron rich when substituted with stronger electron donors. Synthesis and purification under strict exclusion of oxygen, e.g. in a nitrogen–filled glovebox, could be a way to circumvent this problem.

2.3.2.1.4 Benz[*cd*]indolium Squaraine Dye

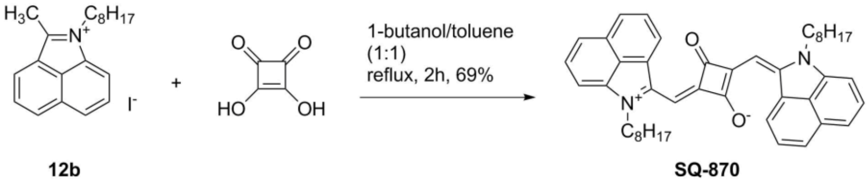

Scheme 2.11. Synthesis of NIR squaraine dye SQ–870.

A squaraine dye flanked by the benz[*cd*]indolium heterocycle (**SQ–870**) was prepared according to a literature procedure as shown in **Scheme 2.11**.[91]

2.3.2.2 Optical and Electrochemical Characterization

2.3.2.2.1 Heptamethine Dyes

UV–Vis–NIR absorption spectra of the heptamethine dyes with different *meso*–substitution are shown in **Figure 2.11** and a summary of the optical properties in solution is given in **Table 2.3**.

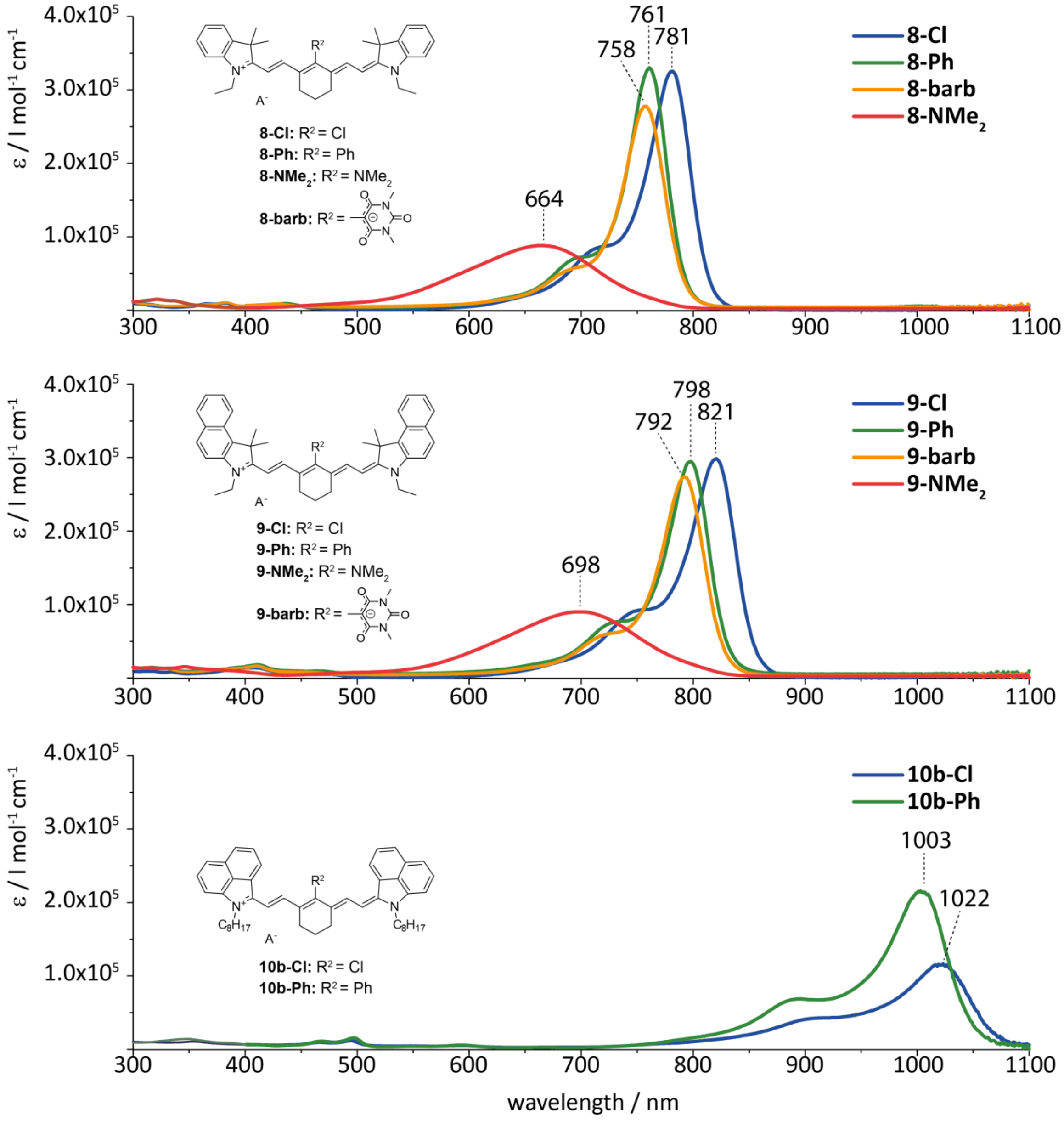

Figure 2.11. UV–Vis–NIR absorption spectra of heptamethines with different *meso*–substitution in ethanol (normalized to their molar extinction coefficient ε at λ_{max}). Counterion A= PF_6^-, except for the barbiturate dyes.

As expected, there is a red–shift in the absorption when the conjugation in the heterocyclic flanking group is increased. Between the indolium and benz[*e*]indolium analogues the absorption maxima differ by ≈ 35 nm; when changing the heterocyclic flanking group from benz[*e*]indolium to benz[*cd*]indolium, however, a remarkable red shift of ≈ 200 nm is found. This can be attributed to the increased rigidity as the carbon at the 3–position of benz[*cd*]indolium is sp^2–hybridized and involved in the conjugated π–system instead of being sp^3–hybridized and carrying two methyl groups (1–position of benz[*e*]indolium).

Table 2.3. Optical properties of heptamethines with different *meso*–substitution in ethanol.

dye	λ_{max} [a] *nm*	ε [b] $M^{-1}\,cm^{-1}$	$IAC \times 10^{18}$ [c] $M^{-1}\,cm^{-1}\,s^{-1}$	*f* [d]
8–Cl	781	325'000	11.5	1.66
8–Ph	761	330'000	11.3	1.64
8–NMe$_2$	664	88'000	10.06	1.53
8–barb	758	278'000	9.99	1.45
9–Cl	821	298'000	12.0	1.65
9–Ph	798	295'000	10.9	1.59
9–NMe$_2$	698	90'000	9.95	1.44
9–barb	792	274'000	9.55	1.46
10b–Cl	1022	116'000	4.83[e]	0.69[e]
10b–Ph	1003	216'000	7.65	1.10

[a] Absorption maximum. [b] Molar extinction coefficient at λ_{max}. [c] Integrated absorption coefficient. [d] Oscillator strength. Details about the determination of these values are given in the experimental part, chapter 0. [e] IAC and *f* are lower for **10b–Cl** because the absorption peak exceeds the scanning range of the instrument (300-1100 nm).

When exchanging the *meso*–substituent from –Cl to the electron–donating groups –Ph, –barb, and –NMe$_2$, a hypsochromic shift of the absorption is observed. It is notable that the tertiary amines **8–NMe$_2$** and **9–NMe$_2$** show a very broad absorption peak with low molar extinction coefficients ε at λ_{max} and the most pronounced blue shift of ≈ 120 nm with respect to the chloro dyes. This is attributed to loss of the ideal polymethine state and formation of a charge–centered "bis–dipole" state in the presence of strong electron donors, as illustrated in **Scheme 2.12**. This effect has been demonstrated by S. Pascal et. al. for a series of different secondary and tertiary amines in the *meso*–position of heptamethine dyes.[92]

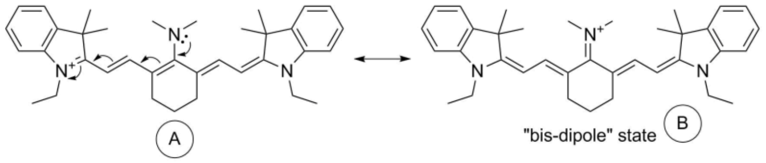

Scheme 2.12. Resonance structures of **8–NMe$_2$** illustrating the charge–centered "bis–dipole" state.

When comparing the –Cl dyes with their respective –Ph and –barb analogues, only a slight blue shift is found. This is expected for the –Ph group which is only a weak electron donor. For the barbiturate substituent, however, this is surprising, as it is a much stronger electron donating group and the heptamethine can form a similar "bis–dipole" structure as for the $-NMe_2$ derivatives, as illustrated in **Scheme 2.13** (resonance structure (B)).

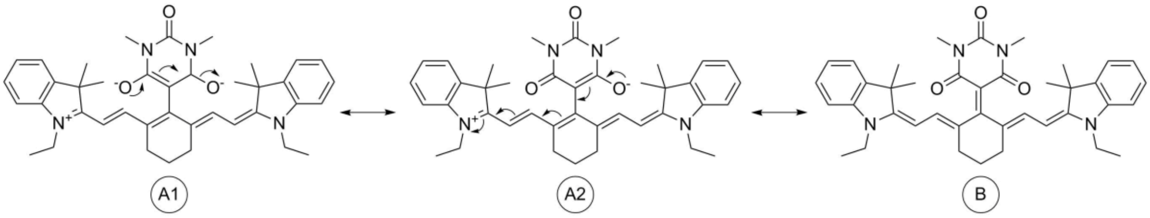

Scheme 2.13. Resonance structures of **8–barb**.

S. Pascal et. al. have reported that neutral heptamethines (with a central double bond, e.g. carbonyls and imines) show very pronounced hypso– and hypochromic shifts, with absorption maxima between 350 and 500 nm, which indicates an even stronger loss of the cyanine state than in the corresponding secondary amines.[92] The resonance structure (B) of barbiturate heptamethine dyes (**Scheme 2.13**) is similar to the neutral oxo– and imino–polymethines, and thus it could be expected that they should also show a strong blue shift and peak broadening. But their absorption maxima are only slightly blue–shifted with respect to the Cl–derivatives and they show very high extinction coefficents ($> 270\times10^3$ M^{-1} cm^{-1}) indicating that their ideal polymethine state remains undisturbed by the barbiturate substituent. Two possible explanations for this are proposed. One is the delocalization within the barbiturate, as shown for resonance structures (A1) and (A2) in **Scheme 2.13**, which is able to stabilize the negative charge within the substituent so that the "bis–dipole" state (B) is less pronounced. Secondly, the formation of a central double bond is hindered due to sterical reasons, as the bulky barbiturate substituent is tilted out of the cyanine plane.[61]

Cyclic voltammetry (CV) measurements were carried out in electrolyte solution (0.1M TBACl in DMF) to determine the influence of the *meso*–substitution on the redox potentials of the heptamethine dyes which are given in **Figure 2.12**. The oxidation potential (E_{ox}) can be considered as an estimate of the electronic ground state of S_0 a dye, whereas the addition of the optical bandgap to the oxidation potential ($E_{ox} + E_{opt}$) can be considered an approximation for the first excited state S_1.[e] Comparing these levels to the LUMO/CB of other materials (e.g. the fullerene acceptors C_{60} and [60]PCBM or the solar cell material $CH_3NH_3PbI_3$) allows to roughly estimate whether electron transfer from the dye to these materials is feasible.

---

[e] The redox levels obtained by CV involve oxidation/reduction of the compounds, and are thus not equal to their HOMO and LUMO levels.[85] In this work, the redox potentials of different dyes obtained by CV are compared to each other and the influence of the substituents on the redox levels can be considered similar to the influence on the molecular orbital levels.

The reduction potentials (E_{red} in **Figure 2.12**) show a clear rise in energy along with the electron donating strength of the substituent in *meso*–position, i. e. in the order –Cl, –Ph, –NMe$_2$, –barb. The oxidation potentials show a similar trend, with exception of the –NMe$_2$ dyes, which have oxidation potentials in the same range as the –Cl dyes. This can be attributed to the formation of the "bis–dipolar" state mentioned previously (**Scheme 2.12**), which leads to an enlarged bandgap. When comparing the S_1 levels ($E_{ox} + E_{opt}$) of dyes within the **8**– and **9**–series to the conduction band of $CH_3NH_3PbI_3$, it can be concluded that the incorporation of electron–donating groups at *meso*–position (while maintaining the ideal polymethine state) gives dyes with suitable levels for electron injection into the $CH_3NH_3PbI_3$ perovskite. Thus the barbiturate dyes **8–barb** (–3.59 eV) and **9–barb** (–3.62 eV) are the most promising candidates to act as co–sensitizers in $CH_3NH_3PbI_3$ perovskite solar cells. Also the positions of the oxidation potentials (HOMOs) of **8–barb** (–5.15 eV) and **9–barb** (–5.11 eV) are ideal for acting as hole–transporting materials in a perovskite solar cell.

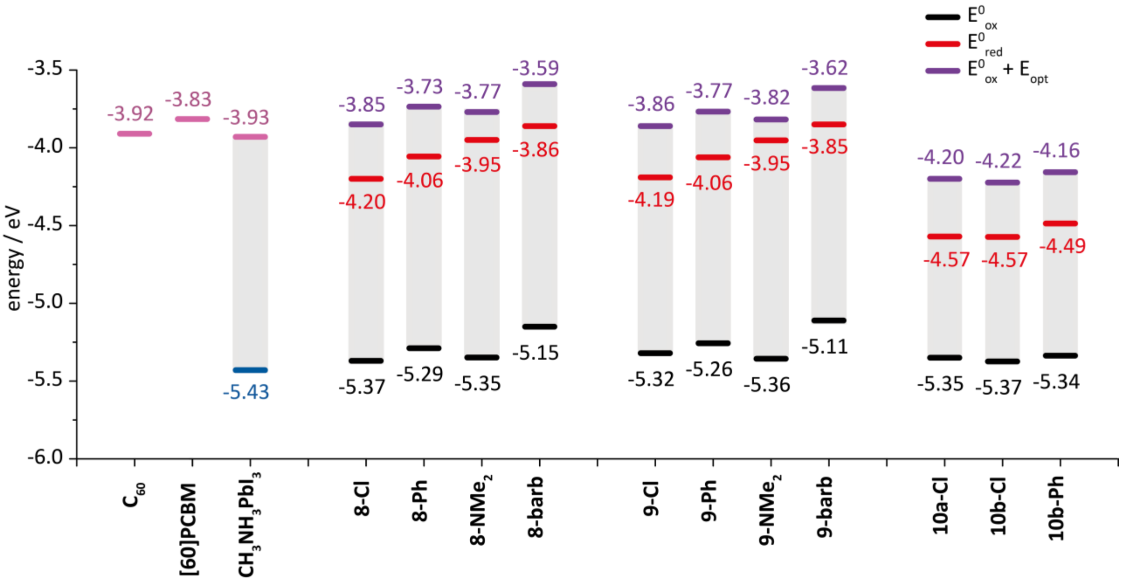

Figure 2.12. Redox energy levels of heptamethine dyes **8–10** obtained by cyclic voltammetry in solution (DMF, 0.1M TBACl) vs. vacuum level. First oxidation potential (E^0_{ox} in black), first reduction potential (E_{red} in red) and sum of and optical bandgap ($E_{ox} + E_{opt}$) as an estimate of S_1 (purple). For comparison: VBM (blue) and CBM (pink) of $CH_3NH_3PbI_3$[84] and LUMO levels of fullerenes C_{60} and [60]PCBM (pink).[93]

Benz[*cd*]indolium heptamethine dyes of the **10**–series show very small electrochemical bandgaps. It is notable, that the oxidation potentials (E_{ox}) are in the same range as for the corresponding dyes of the **8**– and **9**–series. The very small bandgap is almost solely caused by the strong lowering of the reduction potential (E_{red}) of these dyes. This means, that their S_1 levels are very low, and electron transfer from these dyes to fullerenes or $CH_3NH_3PbI_3$ is most likely not possible. Also it is interesting that dyes **10a–Cl** and **10b–Cl**, which only differ in their *N*–alkyl chain, have nearly identical redox levels, which shows that the effect of the *N*–alkyl chain on the electrochemical properties can be neglected. The reduction potential (E_{red}) of **10b–Ph** is higher in energy compared to the –Cl analogue, which is in agreement with the trends observed for the **8**– and **9**–series of heptamethine dyes.

2.3.2.2.2 Squaraine Dye

The UV–Vis–NIR absorption spectrum of benz[*cd*]indolium squaraine dye **SQ–870** is shown in **Figure 2.13** as well as the redox levels E_{ox} (–3.91), E_{red} (–4.20) and $E_{ox} + E_{opt}$ (–5.26) in eV. The bandgap of the squaraine dye is larger than the one of the heptamethine dyes with the same heterocycle due to a shorter polymethine chain in the squaraine system. The absorption maximum of 867 nm is slightly more shifted towards the NIR region compared to benz[*e*]indolium heptamethines of the **9–**series, and the molar extinction coefficient ($\varepsilon = 142\times10^3$ M^{-1} cm^{-1}) is remarkably lower compared to heptamethine dyes with a similar bandgap ($\varepsilon = 298\times10^3$ M^{-1} cm^{-1} for **9–Cl**). The redox energy levels however, are slightly higher in energy compared to the heptamethine dyes, making squaraine dye **SQ–870** a promising NIR–absorber suitable for photovoltaic applications.

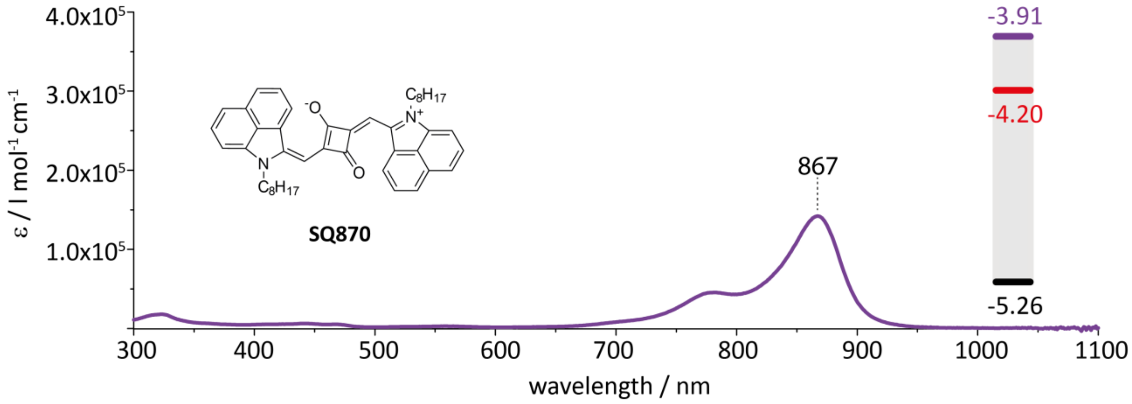

Figure 2.13. UV–Vis–NIR absorption spectrum of squaraine dye **SQ–870** in ethanol. Energy levels of E_{ox} (black), E_{red} (red) as well as $E_{ox} + E_{opt}$ (purple) in eV are given.

3 SOLAR CELL DEVICES: ORGANIC AND PEROVSKITE SOLAR CELLS

The growing awareness that our civilization needs to develop efficient alternative energy technologies in order to replace fossil fuels has boosted various fields of research during the last decade. Conversion of sun light into electrical energy is particularly attractive and thus the development of efficient, low-cost and stable solar cells is of great interest. This thesis contributes findings to two classes of solar cells — organic and perovskite solar cells, which will be reported in the following.

3.1 Organic Solar Cells

3.1.1 Introduction

Organic solar cells (OSCs) belong to the third generation of solar cell types, also called emerging solar cell technologies. Their aim is to further reduce the production costs of solar cells, compared to the first (crystalline silicon solar cells) and second generation (thin film inorganic semiconductors, such as amorphous silicon, copper indium gallium selenide, and cadmium telluride) of solar cell technologies. OSCs employ organic semiconductors for solar energy conversion. Organic materials have several advantages, such as low cost, solution processability, and their properties are adjustable by molecular engineering. In addition they possess high molar extinction coefficients, allowing for the application of very thin films (in the range of 100 nm), which further lowers the cost due to low material consumption and allows for fabrication of light–weight devices.[94,95] OSCs are attractive for architectural integration due to their aesthetic appearance and the possibility to design solar cells in many colors – including transparent and semitransparent – for façade and window applications.[8]

3.1.1.1 Working Principle and Device Architecture

In general, OSC devices consist of two organic materials which form the active layers: a donor and an acceptor. The working principle of an organic solar cell is briefly summarized in **Figure 3.1 b** and **c**. Absorption of a photon ($h\nu \geq E_g$) by the donor material leads to the promotion of an electron to the LUMO. The "electron gap" left behind in the HOMO is called a hole (h^+). Electron–hole pairs are called excitons and are strongly bound by coulomb forces in materials with a low relative permittivity (such as organic compounds). In order for the exciton to be splitted, it needs to diffuse to the donor–acceptor interface (**Figure 3.1 d**) and the energy difference between the LUMO levels of donor and acceptor must be larger than the exciton binding energy.[f] The separated charges can move to the respective electrodes where they are collected and led to recombine after being put to work in an external circuit. Here, light absorption and charge generation are only illustrated in the donor material; however the same principle is also valid for excitons generated by light absorption in the acceptor layer.

In **Figure 3.1**, two common device architectures are illustrated. The bilayer architecture **(a)** involves a layer of each material sandwiched between the two electrodes. A hole–transporting layer (HTL) between the donor and the anode creates an electron barrier in order to avoid charges from flowing to the wrong electrodes. In some cases additional interface materials can be added on both sides of the active layers in order to facilitate charge transport or optimize other properties of the solar cell. The diffusion of excitons to the interface is a critical factor for the performance of OSCs. Typically excitons in organic materials cannot travel distances larger than a few tens of nanometers before they recombine,[96] and thus all photons absorbed at a greater distance from the donor–acceptor interface do not lead to electrical current generation. Thus the bilayer architecture is not optimal for efficient charge generation, as only the region close to the interface can contribute to current generation, and film thicknesses have to be chosen to be very thin. This makes the layers susceptible for defects and decreases their absorptivity.

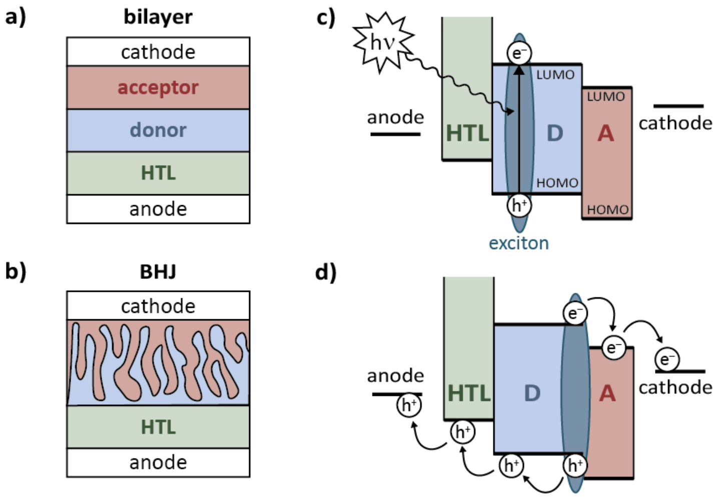

Figure 3.1. Left: Typical device architectures of OSC. **a)** Bilayer solar cell with a planar interface between donor and acceptor. **b)** Bulk heterojunction (BHJ) with a blend of donor and acceptor materials. **Right:** Working principle of an organic solar cell. **c)** Absorption of a photon and exciton generation. **d)** Exciton splitting at the donor-acceptor interface leads to the generation of charges. D = donor, A = acceptor, HTL = hole transporting layer.

---

[f] This is the traditionally assumed model for exciton splitting.[263] Recent findings indicate that the splitting can also occur if there is no energy level difference as a driving force, and thus the exact mechanism for charge transfer from donor to acceptor is still not fully understood.[101]

An attempt to avoid the problems associated with short exciton diffusion lengths is presented in the bulk–heterojunction (BHJ) architecture **Figure 3.1 (b)**, in which donor and acceptor materials are blended together in order to form small domains (on the order of the exciton diffusion length). Ideally the structure should consist of “comb”–like features of both donor and acceptor to maximize the interface between them (as drawn in **Figure 3.1 (b)**). The formation of islands of one material within the other should be avoided, as photogenerated charge carriers in those islands are trapped and cannot be collected at the electrodes. BHJ blends are fabricated by deposition of a mixture of both compounds from solution. The formation of phase-separated domains is thus influenced by many factors and it is of great interest to optimize these in order to optimize the performance of OSCs.

3.1.1.2 Characterization of a Solar Cell

The efficiency of solar cells is generally assessed by measuring their current–voltage (*J*–*V*) characteristics. **Figure 3.2** shows the typical shape of a solar cell *J*–*V* curve indicating the parameters determining the performance of the cell: open–circuit voltage (V_{OC}), short–circuit current density (J_{SC}), and fill factor (FF). V_{m} and J_{m} are the voltage and current at the maximum power point. The efficiency η is defined as the ratio of maximum power output P_{out} to power input P_{in}.[97]

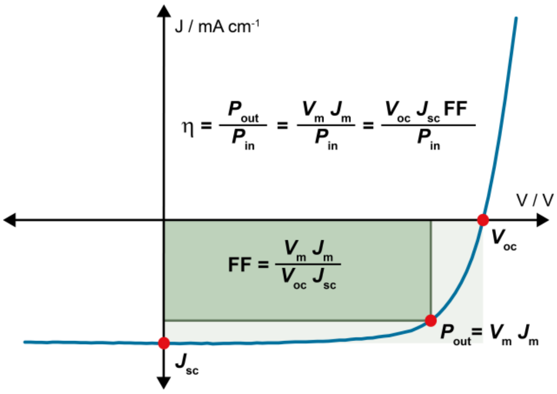

Figure 3.2. *J*–*V* characteristics of a solar cell under illumination with light and important parameters determining its performance.

3.1.1.3 State of the Art

The p–type donor materials employed in organic solar cells are typically conjugated polymers, such as polythiophene derivatives, the most famous example being poly(3–hexylthiophene) (P3HT). Other frequently used polymers are derivatives with phenylene–vinylene or fluorene backbones.[94] Apart from polymers, also many small organic molecules (such as phtalocyanine) are commonly used for the light–absorbing donor layers.[97] The n–type acceptor layers typically consist of fullerenes, such as C_{60} and its derivatives, e.g. [60]PCBM. Other compounds which possess high reduction potentials, such as rylene derivatives, can be used as acceptor materials.[98]

Apart from the active layers the solar cell stack involves a substrate, i.e. glass or plastic foils coated with ITO or other transparent conductive layers to form a bottom electrode[99] and a top electrode (thermally evaporated metals or laminated conductive foils). Between the active layers and the electrodes several kinds of transport layers have been shown to be useful. Commonly applied hole transporting layers (HTLs) such as PEDOT:PSS or molybdenum oxide (MoO_x) form an excellent contact for holes and act as an electron barrier between the active layers and the anode, whereas electron transport layers such as lithium fluoride, calcium, or metal oxides (ZnO or TiO_x) are employed to ensure efficient electron transport to the cathode.[100]

During the last 15 years of research on OSCs their efficiencies have increased from < 4% to 11.5% (certified)[g] for single heterojunction cells by H. Yan and coworkers. Their latest developments involve BHJ solar cells with perylenediimides as non–fullerene acceptors and controlled morphology by temperature dependent aggregation of the p-type polymers leading to a record efficiency of 11.5%.[101,102]

In comparison with inorganic semiconductors, which typically feature bandlike absorption, organic molecules possess structured absorption spectra with distinct maxima and minima. This allows for specific absorption of only part of the solar spectrum, e.g. in the UV or NIR and thus for the fabrication of transparent solar cells which can be incorporated into windows of buildings and cars.[103–105] In this area, the work of Bulovic et al. is especially notable, who have employed a NIR–absorbing phtalocyanine dye as an electron donor together with C_{60} to achieve a solar cell with an efficieny of 1.7% and an average visible transmission of 55%.[103]

3.1.1.4 Cyanine Dyes in Organic Solar Cells

Due to their outstanding photophysical properties, cyanine dyes are promising candidates for the application as sensitizers in solar energy conversion. As introduced previously (chapter 2.1.3.1, page 15) the synthesis of these compounds is easy and cost–effective and many structures are commercially available on a large scale. Being readily soluble in various solvents, cyanine dyes can be deposited from solution and are compatible with industrial processing techniques.

It was introduced in chapter 2.1.3 (page 14) that heptamethine cyanine dyes possess a single sharp absorption maximum above 750 nm. This property is not frequently found in organic chromophores, which often have several or broad absorption bands. NIR absorbing dyes are particularly interesting for solar cell applications, as they allow more

---

[g] NREL efficiency chart for best research cell efficiencies, September 2016. http://www.nrel.gov/ncpv/images/efficiency_chart.jpg

low energy photons to be harvested, which is required for multijunction cells, for example. Additionally it offers the possibility to fabricate (semi)transparent solar cells with high visible light transparency.[106]

Cyanine dyes were shown to be able to act as electron–donors as well as electron–acceptors in OSCs.[107] In the last years the group of F. Nüesch achieved considerable improvements in the performance of cyanine/C_{60} bilayer solar cells. Devices with good efficiencies (η = 3%) and high fill factors (FF = 60%) were reported.[108] Based on these findings the adaptation of the BHJ architecture with ideal domain sizes of cyanine and [60]PCBM (on the order of the exciton diffusion length) would be a promising strategy for further improving the efficiency of cyanine OSCs. One limiting factor in cyanine solar cells is the low charge carrier mobility which has to be addressed urgently to make further progress.

3.1.2 Aim

Previous studies showed that trimethine dyes can be blended with [60]PCBM to form phase separated structures and that the phase morphology strongly depends on the nature of the counterion.[75] The lateral dimensions of the domains vary greatly depending on the counterion. With many of them (iodide, perchlorate and hexafluorophosphate) very large domains of several micrometers were obtained, that are not suitable for photovoltaic applications, given the small exciton diffusion lengths.

Further investigations on this topic are necessary in order to find optimal counterions for improved BHJ morphologies. The TRISPHAT$^-$ counterion was introduced in chapter 2.2 as a soft and bulky anion that showed to be weakly coordinating to the cyanine chromophore.[64] TRISPHAT$^-$ contains aromatic moieties which could form van–der–Waals interactions with fullerenes. This could lead to a better mixing of the otherwise polar cyanine salt with the hydrocarbon compounds and thus to improved domain sizes in the blend film.

Apart from controlling the BHJ phase separation morphology, mobile counterions were found to also have an important effect on the performance of bilayer cyanine solar cells.[76,109]

In this work, two cyanine chromophores with different counterions are used: a trimethine and a NIR absorbing heptamethine cyanine dye with the counterions PF_6^- (**Cy3P** and **Cy7P**) and TRISPHAT$^-$ (**Cy3T** and **Cy7T**). Structures of the compounds are shown in **Scheme 2.6** (page 19). The influence of these two counterions on the performance of bilayer solar cells as well as BHJ blends is examined.

3.1.3 Results and Discussion: Semi–transparent Organic Solar Cells

Bilayer organic solar cells were fabricated with heptamethine salts **Cy7P** or **Cy7T** as the electron donor and C_{60} as the electron acceptor. The cathode was either composed of an 80 nm thick reflective Ag layer; alternatively, semitransparent cells were fabricated with an Ag (12 nm)/Alq_3 (60 nm) electron-collecting electrode (**Figure 3.3 a**).[79] Therefore, highly transparent devices were obtained with average (450–670 nm) visible transmittance values of 62% (for **Cy7P**) and 66% (for **Cy7T**) and maximum transparencies of over 75% (**Figure 3.3 b**).[106] For semitransparent OPV cells, best performances were (for **Cy7P**) J_{SC} = 3.6 mA cm^{-2}, V_{oc} = 0.38 V, FF = 64.8%, η = 0.9% and (for **Cy7T**) J_{SC} = 6.4 mA cm^{-2}, V_{oc} = 0.63 V, FF = 54.0%, η = 2.2% (**Figure 3.3 c**). For nontransparent devices, η = 1.8% for **Cy7P** and η = 2.8% for **Cy7T** were measured. In general, semitransparent devices have a lower performance compared to devices that use a highly reflective back metal contact, since more light can be absorbed in the latter case. Average performance values are given in the Experimental Part.

The influence of the counterion on solar cell performance is notable. The decreased J_{SC} for **Cy7P**, despite its broader absorption spectrum (**Figure 3.3 b**), indicates a lower charge generation yield at the dye/C_{60} heterojunction. Also, V_{oc} for **Cy7P** is considerably lower as compared to **Cy7T**. It has been shown that V_{oc} is correlated to the redox energy levels of the active donor and acceptor materials,[100,110] and specific factors have been identified that limit V_{oc}, such as morphology, bimolecular charge recombination, or shunt conduction.[111,112] Indeed, reverse dark current densities for cells using **Cy7P** (−2 mA cm^{-2} at −1 V) were considerably higher than for **Cy7T** (−0.04 mA cm^{-2}), resulting in a lowered V_{oc} and eroding the device efficiency partly. Also the packing of the ions in the film, the formation of dipole layers, and potential shifts at the dye/C_{60} interface could have a strong influence on the energetics of the relevant redox levels. The redox levels as measured by CV in solution are the same for **Cy7P** and **Cy7T**, and E_{red} (−4.20 eV) is in principle unfavorable for electron transfer after dye excitation to C_{60} (LUMO= −3.92 eV).[93] Therefore, we must assume that the redox potentials of individual molecules in solution do not reflect the energetic situation in the solid film and hence in the actual OPV cells.

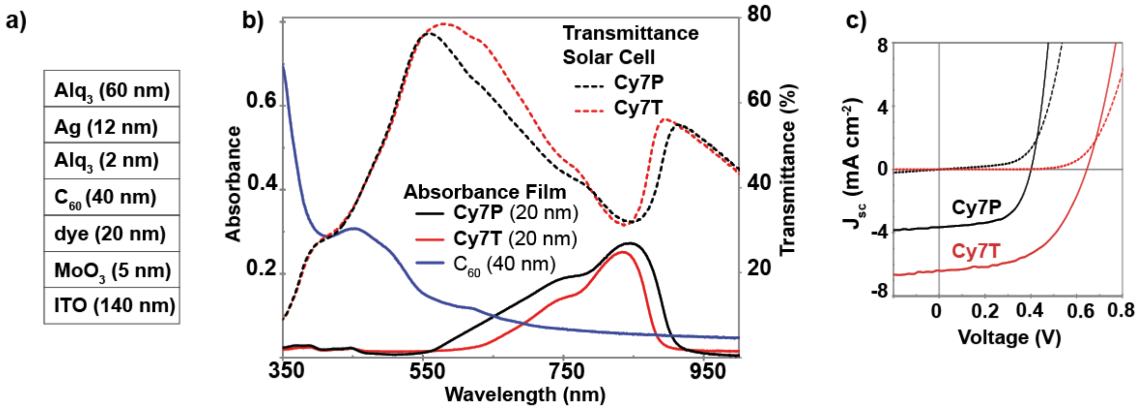

Figure 3.3. (a) Schematic of the optimized semitransparent cyanine/C$_{60}$ cell architecture. **(b)** Absorbance spectra of thin films of C$_{60}$, **Cy7P**, and **Cy7T**; transmittance spectra of solar cells. **(c)** White light (solid lines) and dark (dotted lines) solar cell *J*–*V* characteristics for solar cells with **Cy7P** (black) and **Cy7T** (red).

It is interesting to note that the properties of heptamethine dyes **Cy7P** and **Cy7T** in the solid state are greatly influenced by the counterion. The thin film absorption spectra of the two salts show very different peak shapes; the absorption band of **Cy7T** is much narrower, due to reduced aggregation in the presence of the large TRISPHAT$^-$ counterion.

Recently, the group around R. R. Lunt has published a detailed study on the effects of various counterions in heptamethine salts on their photovoltaic properties.[113] They could confirm the strong increase in V_{oc} and device performance when going from small hard counterions to larger counterions containing halogenated aromatic moieties. Further experiments in order to elucidate the mechanism behind V_{oc} enhancement in these systems lead to their conclusion that it arises from changes in the interface gap (defined as the difference between the donor HOMO and acceptor LUMO) induced by the counterion. This hypothesis is confirmed by ion mixing experiments which lead to a linear increase in V_{oc} when the ratio between two counterions is varied. Finally, they report a strong effect of the counterion on the oxidation potential of the cyanine dye measured by ultraviolet photoelectron spectroscopy (UPS) in the solid state.[113]

3.1.4 Optimized Domain Size in Cyanine/[60]PCBM Blends

In collaboration with coworkers,[114–116] cyanine dyes with different counterions synthesized within the scope of this thesis have been studied in bulk heterojunction (BHJ) blends together with [60]PCBM. Spin–coated thin films of blends of **Cy7P** (PF_6^- counterion) or **Cy7T** (TRISPHAT$^-$ counterion) were characterized by atomic force microscopy (AFM) and dissolution experiments, which revealed striking differences in the morphology depending on the choice of counterion. With the PF_6^- counterion, the films were found to form fully phase–separated bilayers with a rough interfacial layer, which had detrimental effects on solar cell device performances. With the TRISPHAT$^-$ counterion, however, a smooth blend of [60]PCBM and dye was obtained and it was not possible to selectively dissolve the components, indicating that they had formed a blend on the molecular level.[114] In fact, this morphology was also not found to be optimal for application in solar cells, as the great miscibility of the dye and [60]PCBM did not give any phase separation. Solar cell efficiencies of **Cy7T**/[60]PCBM blends were at 1.1%, which is half the performance obtained from bilayer devices of **Cy7T**/C_{60} (chapter 3.1.3).[114,116] The increased miscibility of **Cy7T** with fullerenes could additionally be confirmed by ESR and photo–ESR studies conducted by Vismara et al., who found a significant increase in photogenerated spins in blends of **Cy7T**/C_{60} as compared to **Cy7P**/C_{60}.[115]

In conclusion, it was demonstrated that the counterion can tremendously influence the morphology of BHJ blends between cyanine salts and [60]PCBM. Especially the large anion TRISPHAT$^-$ containing aromatic moieties can undergo attractive interactions with the fullerenes, possibly by π–π interactions. Further studies with counterions containing aromatic moieties could lead to the desired blend morphology with domain sizes on the order of the exciton diffusion length, as would be required for efficient BHJ solar cells.

3.2 Perovskite Solar Cells

3.2.1 Introduction

Perovskite solar cells (PSCs) are a relatively new branch of emerging photovoltaic technologies. They have evolved out of dye-sensitized solar cells (DSSCs) by replacement of the organic dye with an organic–inorganic hybrid material as the sensitizer. Only a few years after their discovery, the power conversion efficiency of PSCs has increased strikingly, from 3.8 % in 2009 to 22.1% in 2016.[9,10] This rapid development sparked excitement in the scientific community and a great number of researchers is currently focused on obtaining deeper understanding in this promising branch of photovoltaic technology. Additional to high efficiencies, PSC devices hold several other advantages, such as low cost and solution processability of the components.[11] Furthermore, the scope of hybrid organic–inorganic hybrid materials has extended to other applications, such as lasing,[117] light–emitting devices,[118] photodetectors[119] and X-ray detection.[120]

While several different device architectures for PSCs are being investigated, the highest efficiencies to date are obtained using a compact TiO_2 hole–blocking layer, a mesoporous TiO_2 layer infiltrated with the organic–inorganic perovskite $CH_3NH_3PbI_3$, and the organic hole–transporting material (HTM) Spiro-OMeTAD, sandwiched between the cathode, typically fluorine-doped tin oxide (FTO) on glass, and thermally evaporated gold as the anode (**Figure 3.4a**).[121,122]

The organic–inorganic hybrid material adapts a perovskite crystal structure with the general formula AMX_3, where A is an organic cation, M is a bivalent post–transition metal and X is a halide. The perovskite framework consists of a three–dimensional network of corner–sharing MX_6^{2-} octahedra, in which the cations A are occupying the 12–fold coordinated gaps in the structure to balance the charge (**Figure 3.4b**).[123,124] The most well–known member of this family is methylammonium lead triiodide (A = $CH_3NH_3^+$, M = Pb^{2+}, X = I^-) which is widely applied in solar cells.[9,122]

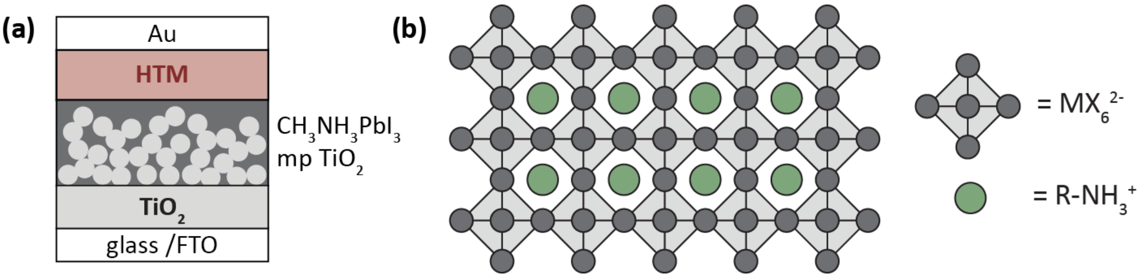

Figure 3.4. (a) Typical architecture of a PSC from bottom to top: glass/FTO cathode, compact layer of TiO_2, mesoporous (mp) TiO_2, perovskite $CH_3NH_3PbI_3$, hole–transport material (HTM), gold (Au) anode. **(b)** Schematic of crystal structure of organic–inorganic perovskites composed of corner–sharing MX_6^{2-} octahedra (grey) and organic cation (green).

An overview over different procedures available for the fabrication of hybrid perovskite thin films is given in chapter 4.1.3 (page 59). Recent advances have been made by tuning the composition of organic cations in lead iodide perovskites. A mixture of formamidinium (FA^+) and methylammonium (MA^+) led to an improved efficiency of 14.9% compared to the perovskites containing only one of these two cations (12.5% for MA^+, 10.5% for FA^+).[125] Additional improvements were reported with a new spin–coating deposition technique of the perovskite layer and further fine tuning of the composition of the halides (X = I, Br), providing efficiencies of 18–20%.[126,127] Efficiencies over 20% and remarkable improvement of the long-term stability of solar cells were achieved when a small amount of Cs^+ was mixed with FA^+ and MA^+ cations in a lead iodide/bromide perovskite.[10]

While the composition and nature of organic cations in the perovskite structure seems to be an attractive point for fine–tuning of the material properties, the selection of organic molecules for the A site in the crystal structure of AMX_3 lead halide perovskites is limited by size constraints.[124,128] Cations larger than ≈ 2.6 Å cannot be incorporated into a three–dimensional lead halide network, but instead, structures with lower dimensionality of the inorganic network can be formed.[129] This subject will be highlighted in more detail in chapter 4.

3.2.2 Enhancing the Spectral Sensitivity of PSCs into the NIR

3.2.2.1 Aim

The organic–inorganic perovskite material $CH_3NH_3PbI_3$ is a strong absorber, able to convert photons over the whole visible region into electric current with great efficiency. **Figure 3.5** shows the external quantum efficiency (EQE, black line)[h] of a PSC in a standard architecture (as shown in **Figure 3.4a**) using Spiro-OMeTAD as the hole–transporting material. It can be seen that lower energy photons (> 800 nm) are not harvested and converted into electricity, as they are not absorbed by the perovskite material. Heptamethine cyanine dyes are strong absorbers in the NIR, with a sharp absorption band > 800 nm (as introduced in detail in chapter 2.1.3). **Figure 3.5** shows the normalized absorbance of a thin film of heptamethine dye **9–barb**, which possesses redox levels compatible with the valence band (VB) / conduction band (CB) of the perovskite material. Details about structure and optical / electrochemical properties of **9–barb** are found in chapter 2.3.2.

---

[h] The EQE is the ratio of the number of charge carriers collected by the solar cell to the number of photons of a given energy shining on the solar cell.

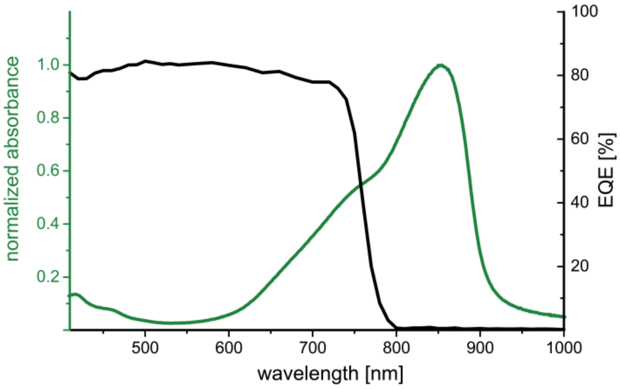

Figure 3.5. EQE of a standard PSC (black line) and normalized absorbance of NIR absorbing heptamethine dye **9–barb** in a thin film (green line).

In order to enhance the spectral sensitivity of PSCs into the NIR beyond 800 nm, cyanine dyes are tested as HTMs and co–sensitizers in the solar cell. Considerations about tuning the redox levels of cyanine dyes to be suitable for this purpose are discussed in detail in chapter 2.3.1. The synthesis and characterization of the proposed heptamethine target structures is described in chapter 2.3.2 and their redox levels are summarized and compared to $CH_3NH_3PbI_3$ in **Figure 2.12** (page 35). The preparation and characterization of PSCs with cyanine dye HTMs is described in the following.

3.2.2.2 Results and Discussion

3.2.2.2.1 Sequential Deposition: Rough Perovskites

In first experiments cyanine dye **9–Cl** was examined as a hole transporting material. The solar cells were fabricated according to a standard literature procedure by Burschka et al.,[121] with the following layer stack: glass / FTO / TiO_2 blocking layer (30–50 nm) / TiO_2 mesoporous layer infiltrated with $CH_3NH_3PbI_3$ (300–400 nm)/ HTM / Au (80 nm). The sequential deposition method involved a first step of spin–casting lead iodide (PbI_2) from DMF solution onto the substrate with mesoporous TiO_2, followed by dip–coating in a methylammonium iodide (MAI) solution which leads to conversion to the perovskite. HTM Spiro-OMeTAD or **9–Cl** was then applied by spin–coating from chlorobenzene solutions. Spiro-OMeTAD contained a dopant (cobalt complex FK209) and additives (LiTFSI and 4-*tert*-butylpyridine) as described in the literature.[121] As a reference, solar cells without any HTM were fabricated, in which the Au electrode was directly evaporated onto the perovskite. According to the literature, Spiro-OMeTAD is applied in a thickness of > 200 nm and its conductivity is enhanced by dopants and additives. Cyanine dyes suffer from low charge carrier mobilities and even though conductivity can be improved by the addition of dopants to some extent,[56] they can be only applied in thicknesses of less than 100 nm in solar cells. In this experiment, **9–Cl** was applied without the addition of dopants in a thickness of 20–30 nm.

Table 3.1. Average performance of PSCs with $CH_3NH_3PbI_3$ prepared by sequential deposition. Cyanine **9–Cl** is compared to the standard HTM Spiro-OMeTAD and solar cells without HTM. All cells were measured from SC to FB (forward scan).

HTM	V_{oc} *V*	J_{sc} *mA cm^{-2}*	***FF*** *%*	η *%*
Spiro-OMeTAD	0.912 ± 0.047	18.35 ± 2.60	62.1 ± 4.9	10.38 ± 1.71
9–Cl	0.488 ± 0.058	5.86 ± 0.51	42.1 ± 8.0	1.23 ± 0.40
no HTM	0.593 ± 0.102	6.46 ± 1.57	45.6 ± 6.3	1.78 ± 0.68

Average solar cell parameters (from at least 10 cells) of PSCs with different HTMs are summarized in **Table 3.1** and *J*–*V* characteristics of the best cells are shown in **Figure 3.6**. Here, only standard "forward" scans from short circuit (SC) to forward bias (FB) were measured, as this work was performed previous to the issue of hysteresis in PSCs coming into focus of the scientific community.[130]

While the reference solar cells using Spiro-OMeTAD have efficiencies > 10%, cyanine dye **9–Cl** as the HTM gives poor performing solar cells with < 2% efficiency. In fact, the performance is very similar to the solar cells containing no HTM at all, in which the Au anode is in direct contact with the perovskite. Thus it can be assumed, that this is also the case in the devices with cyanine as the HTM. The mesoporous TiO_2 layer infiltrated with perovskite crystals is characterized by a high roughness and it might not be possible to fully cover it with the thin cyanine dye film.

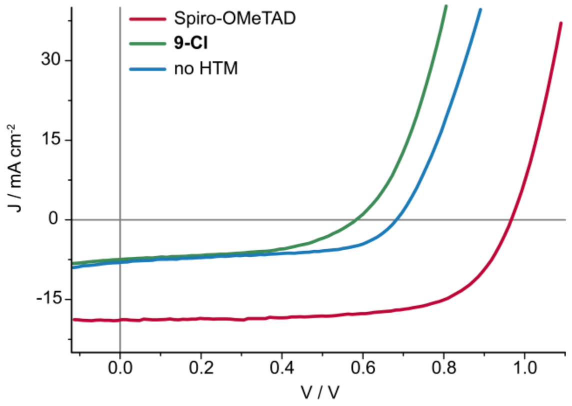

Figure 3.6. *J*–*V* characteristics of the best cells from **Table 3.1** measured from SC to FB (forward scan). Cyanine **9–Cl** (green) is compared to the standard HTM Spiro-OMeTAD (red) and solar cells without HTM (blue).

In order to overcome this problem, studies on p–type doping of the cyanine layers were performed by Jenatsch et al.[131] While the conductivity could be improved, it is still not possible to apply cyanine films at a thickness of 200 nm, as it would be required to cover the rough perovskite prepared by sequential deposition.

3.2.2.2.2 Antisolvent Deposition: Smooth Perovskites

During the course of this project, new perovskite deposition techniques were published, making the fabrication of flat and uniform perovskite films possible. Specifically the “antisolvent” deposition technique is able to provide smooth perovskite films of low roughness.[126,132,133] In contrast to the sequential deposition, both precursors (MAI and PbI_2) are dissolved in the same solvent or solvent mixture that retards crystallization of the perovskite, due to complexation of the Pb^{2+} ions. During the spin–coating process of this precursor solution, an antisolvent (which does not dissolve the perovskite) is added to wash the film and induce crystallization. Solar cells with a low roughness perovskite layer were prepared in collaboration with F. Giordano and J.–Y. Seo: glass / FTO / TiO_2 blocking layer (30–50 nm) / TiO_2 mesoporous layer infiltrated with perovskite / perovskite overlayer / HTM / Au (80 nm). This perovskite layer consisted of mixed organic cations (FA^+ and MA^+) and mixed halides (I^- and Br^-) and was prepared by an antisolvent method.[134] The bandgap of this mixed perovskite material is supposed to be very similar to that of $CH_3NH_3PbI_3$.[127] Cyanine dyes **9–Cl** and **9–barb** were tested as HTMs and compared to the standard Spiro-OMeTAD; average solar cell characterization parameters (of at least 2 cells) are listed in **Table 3.2**, *J*–*V* curves of the best cells are shown in **Figure 3.7**. The yield of working devices was 100% for all HTMs, no short–circuited cells were obtained in a batch of nine devices. Solar cells without any HTM gave only short–circuited or shunted devices, which is why they are not shown.

Table 3.2. Average performance of PSCs with low roughness mixed perovskite. Cyanine dyes **9–Cl** and **9–barb** are compared to the standard HTM Spiro-OMeTAD. **9–Cl + additives** was doped with the same additives as Spiro-OMeTAD in the standard recipe.[133] Scan direction is indicated as fwd (forward scan, SC to FB) or rev (reverse scan, FB to SC).

HTM	***scan***	V_{oc} *V*	J_{sc} *mA cm^{-2}*	***FF*** *%*	η *%*
Spiro-OMeTAD	fwd	1.029 ± 0.019	18.08 ± 0.65	73.72 ± 3.07	13.69 ± 0.27
	rev	1.015 ± 0.020	17.85 ± 0.41	74.03 ± 4.54	13.40 ± 0.71
9–Cl	fwd	0.993 ± 0.001	12.70 ± 0.80	48.02 ± 2.95	6.03 ± 0.02
	rev	0.911 ± 0.003	13.90 ± 0.98	58.65 ± 0.06	7.43 ± 0.55
9–Cl + additives	fwd	0.992 ± 0.013	11.38 ± 0.21	51.96 ± 8.94	5.83 ± 0.82
	rev	0.886 ± 0.007	13.60 ± 1.32	61.38 ± 4.70	7.34 ± 0.09
9–barb	fwd	1.021 ± 0.001	12.90 ± 1.46	45.67 ± 0.62	6.03 ± 0.75
	rev	0.909 ± 0.003	15.22 ± 1.57	54.33 ± 0.45	7.53 ± 0.87

Solar cells with the standard HTM Spiro-OMeTAD performed very well with the best efficiency at 14.12% and high fill factors > 70% independent of the scan direction.[130] With cyanine dye **9–Cl** as the HTM the best efficiency was 7.44%, the lowered performance compared to the standard is mainly due to a loss in *FF* and J_{sc}. When dopant and additives (cobalt complex FK209, 4-*tert*-butylpyridine and LiTFSI) were added to cyanine dye **9–Cl** no significant effect on the solar cell performance was found. With cyanine dye **9–barb** as the HTM the best efficiency was 8.39%; J_{sc} and V_{oc} were slightly increased, while the *FF* was similar as compared to **9–Cl**. For both **9–Cl** and **9–barb** J_{sc} was well above 11 mA cm^{-2}, which is rather high for undoped cyanine dye films compared to what is known from their performance in OSCs.[79] For all PSCs with cyanine HTMs a pronounced difference between the forward (fwd) and reverse (rev) *J*–*V* scan was observed. The origins of *J*–*V* hysteresis in PSCs are still not fully elucidated, as recently summarized in a review by Chen et al.[135] They highlight the following four possible mechanisms: slow transient capacitive current,[136] dynamic trapping and detrapping processes of charge carriers,[130,137] band bending due to ion migration,[138,139] and band bending due to ferroelectric polarization.[140] In this work an influence of the scan direction on photovoltaic performance was only observed with cyanine salts as HTMs, but not with Spiro-OMeTAD. This favors mechanisms which involve traps or band bending caused by mobile ions for the explanation of *J*–*V* hysteresis.

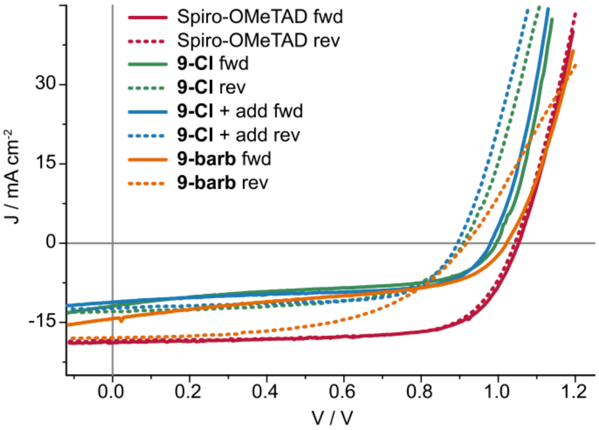

Figure 3.7. *J*–*V* characteristics of the best cells from **Table 3.2** measured from SC to FB (fwd, solid lines) and FB to SC (rev, dotted lines).The different HTMs are: cyanine **9–Cl** (green), **9–Cl** with additives (blue), **9–barb** (orange) compared to the standard Spiro-OMeTAD (red).

EQE spectra of the best performing solar cells are shown in **Figure 3.8** (left). The current generation in the range of 400–800 nm is lowered with cyanine HTMs compared to the Spiro-OMeTAD standard, as is expected from the lower J_{sc} of these cells. No conversion of photons > 800 nm could be observed, indicating that the cyanine dyes are not acting as co–sensitizers in these solar cells. Transmission spectra of the solar cell stacks (**Figure 3.8**, right) demonstrate that the cyanine films have a reasonable thickness for the absorption of light (30–35 %T) and that the chromophores are intact.

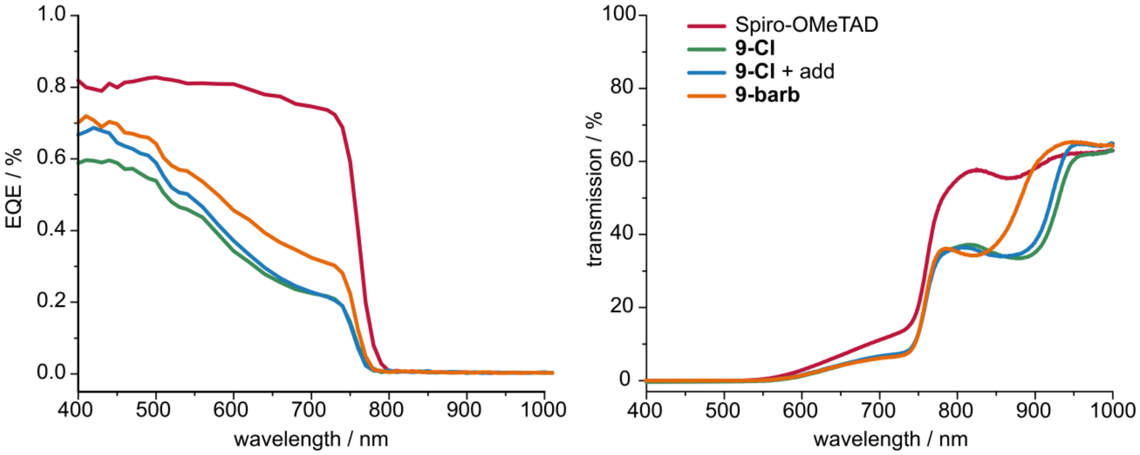

Figure 3.8. EQE (left) and transmission spectra (right) of the best solar cells from **Table 3.2**.The different HTMs are: cyanine **9–Cl** (green), **9–Cl** with additives (blue), **9–barb** (orange) compared to the standard Spiro-OMeTAD (red).

In summary, cyanine dyes have been found to act as HTMs in PSCs, achieving high currents $J_{sc} > 11$ mA cm^{-2}, but not as NIR co–sensitizers. A possible reason for this might be the mismatch of orbital energies, so that the electrons cannot be injected from the cyanine LUMO into the CB of the perovskite. Synthetic modifications of the cyanine dyes to further raise the energy of their LUMO, as well as compositional modification of the perovskite to lower its CB could be strategies to avoid this mismatch.

3.2.3 Further Advancements in the Field of PSCs

Within the scope of this thesis additional studies in the field of PSCs have been carried out together with coworkers.

In collaboration with S. Fernandes (UNESP Araraquara, SP, Brazil) et al., niobium oxide was investigated as a hole-blocking material in order to replace TiO_2 which is known to be unstable under exposure to UV irradiation.[141] Compact Nb_2O_5 layers were applied in varying thicknesses together with mesoporous TiO_2 and $CH_3NH_3PbI_3$ prepared by sequential deposition, which gave PSCs with similar efficiencies to TiO_2–only devices (12.3%). PSCs with 50 nm Nb_2O_5 blocking layer gave hysteresis–free solar cells together with improved short term stability of the solar cells.[142]

In collaboration with M. Makha et al., a transparent laminated top electrode for PSCs was investigated to provide a low-cost and roll-to-roll compatible alternative to a gold evaporated contact. The electrode was composed of a mesh-like silver network on polyethylene terephthalate (PET), coated with a PEDOT:PSS/sorbitol film and could achieve stabilized power conversion efficiencies of over 7%.[143]

4 LOW–DIMENSIONAL ORGANIC–INORGANIC HYBRID PEROVSKITES

4.1 Introduction

4.1.1 Background and Structures

Organic–inorganic hybrid materials containing inorganic and organic structural components are able to combine the advantages from both sides – structural versatility and tunable properties of organic molecules as well as stability, crystallinity and outstanding electrical properties of inorganic compounds.[144,145] Furthermore, new properties arise as a result of the synergistic combination of the components making organic–inorganic hybrids and nanocomposites extremely versatile materials with intriguing properties for various purposes and applications.[145–148] Prominent compound classes based on the hybrid material concept are e.g. metal–organic frameworks (MOFs) and silica-based mesoporous hybrids which find application in the controlled storage and release of certain compounds, as well as in catalysis, sorption, chromatography, sensors, etc.[149,150] Organic–inorganic perovskites are receiving tremendous attention by various research groups in the past years due to their exceptional photophysical and electronic properties. Particularly three–dimensional (3D) perovskites consisting of lead halides and small organic cations are able to achieve high performances in perovskite solar cells (PSCs), as introduced in chapter 3.2.1.[122,151]

The family of compounds called perovskites adapts the same crystal structure as $CaTiO_3$, which was named after Russian mineralogist L. A. Perovski.[123] Thus the general formula of three–dimensional perovskites is AMX_3, where A is usually a large cation, M is a medium–sized cation and X is an anion, forming an extended three–dimensional network of corner-sharing MX_6 octahedra.[123] In organic–inorganic hybrid perovskites, one of these components is organic. Even fully organic structures are known, so–called "molecular perovskites".[152] In organic–inorganic halide perovskites, which are the subject of this thesis, A is an organic cation, M is a bivalent metal (Pb^{2+}, Sn^{2+}, etc.) and X is a halogen (Cl, Br, or I). Especially the lead halide perovskites possess intriguing optical and electrical properties,[153] and will be the focus of this thesis.

The toxicity of lead is a major concern for the commercialization of lead–based perovskite solar cells,[154] and efforts are made towards its replacement with less toxic elements.[155] Unfortunately, lead–free analogues were not able to keep up to the outstanding properties of lead halide perovskites so far.[154,156–158] Some studies found that the amount of lead typically employed in PSCs (in thin films of ≈ 200 nm) is low enough to keep the impact on the lead content of soil at a negligible level in case of breakage of a panel.[159]

The most recent advances in PSCs raising photovoltaic power conversion efficiencies to > 20% have been realized by compositional fine–tuning of the organic cations incorporated in the inorganic network.[10,127] This indicates that the composition and nature of the organic cations in lead halide perovskites are an attractive point for modification and optimization of their structure and properties. In 3D–perovskites of the general structure AMX_3 the cation A is constrained in size in order to fit into the voids within the corner–sharing network of MX_6 octahedra. In order to predict the possibility for a set of ions A^+, M^{2+} and X^-, to form a perovskite structure, a tolerance factor t is defined by *Goldschmidt's rule* **(2)**,[124,128] where R_A, R_X and R_M are the ionic radii of the respective ions (treating all ions as rigid spheres and considering close packing).

$$\boldsymbol{R_A + R_X = t\sqrt{2}(R_M + R_X)} \tag{2}$$

For a 3D–perovskite structure, t needs to take a value of 0.8–1.0, and $t \approx 1.0$ for the cubic crystal structure. Outside of this range 3D–perovskite–like structures can still be found, but distortions are predicted to occur.[160,161] It needs to be noted that the determination of t is not straightforward for systems containing organic cations, because they are not spherically symmetric like inorganic ions and thus it can be difficult to assign their ionic radii.[162] For lead iodide perovskites, assuming $R_{Pb^{2+}}$ = 1.19 Å and R_{I^-}= 2.20 Å[163] and t = 1, the maximum size of the organic cation A is found to be ≈ 2.6 Å.[164] Given that C–C bond lengths are between 120–154 pm,[165] only very small organic cations, such as methylammonium and formamidinium are able to form three–dimensional $APbI_3$ perovskites.[124,129]

These considerations only allow for a narrow choice of organic cations to be incorporated, and thus the options for structural versatility are strongly limited in 3D–perovskite structures. These restrictions, however, are lifted gradually if the dimensionality of the inorganic network is reduced to two–dimensional (2D), one–dimensional (1D), or even zero–dimensional (0D) structures.[129]

The dimensionality stated here reflects the connectivity of the MX_6 octahedra, which can form sheets (2D) or linear chains (1D) as illustrated in **Figure 4.1**. While sheets are usually formed of corner-sharing octahedra, linear chains can be built up in different ways from corner–, edge–, or face–sharing octahedra. In 0D–structures the inorganic part is present as isolated MX_6 octahedral clusters (0D).[124,164] Even though their crystal structures do not directly resemble the perovskite mineral $CaTiO_3$, the low–dimensional structures are often still referred to as "perovskites", as they can be described as slices of the parent 3D–perovskite AMX_3.[129]

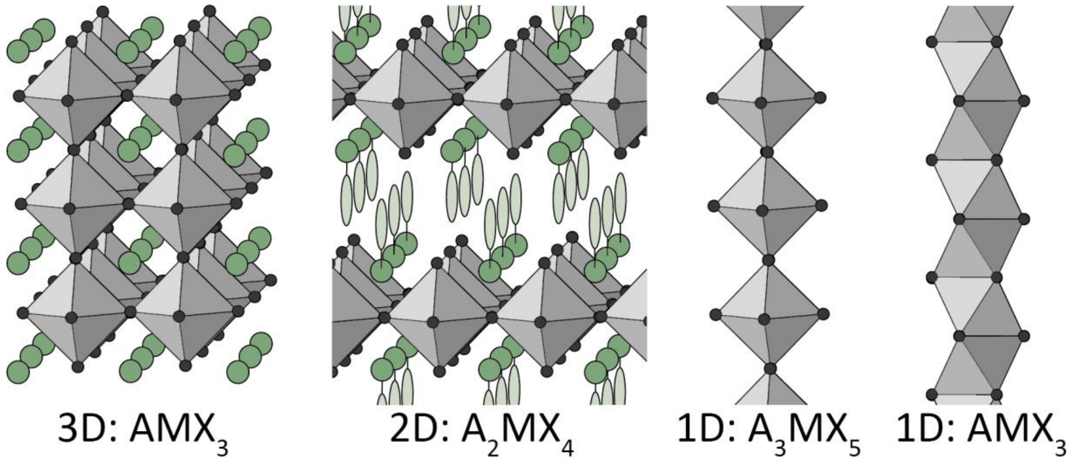

Figure 4.1. Illustration of perovskite structures with different dimensionality and their general formula. Corner–sharing octahedra (grey) forming a 3D–network (AMX_3) with small organic cations (green) or sheets in a layered 2D–structure (A_2MX_4) with larger cations.[164] Polyanionic 1D–chains of corner–sharing (A_3MX_5)[166] or face–sharing octahedra (AMX_3);[167–169] cations omitted, as their position can vary.

In low–dimensional perovskites there are in principle no size restrictions for the organic cation, as the connectivity and the spacing between the inorganic components can vary and adapt to the steric demands of the cation.[124,129] Besides steric constraints, there are also electronic effects governing the formation of these hybrid structures, as it is necessary to balance the charges between the polyanionic inorganic structure and the organic cations.[129]

2D–perovskites with alternating layers of inorganic sheets and organic cations are analogues of the all–inorganic (n=1) *Ruddlesden–Popper* phases[123] with the general formula A_2MX_4.[170] The spacing between the inorganic sheets is determined by the length of the organic cation, which is demonstrated in a series 2D–perovskites incorporating alkylammonium cations $C_nH_{2n+1}NH_3^+$ of varying chain length (n = 4, 6, 8, ...18).[171,172] The stoichiometry of these layered systems, however, requires that there are two cations A^+ or one bivalent cation A^{2+} per inorganic moiety MX_4^{2-}.[164] Again, this leads to size constraints in the width of the cations, as they need to be able to pack sufficiently dense in order to balance the charge of the inorganic sheets. Furthermore, it is thought that the organic cations must contain a terminal ammonium group in order to interact with the inorganic components in layered 2D–perovskites by hydrogen bonding.[164,173–175]

With organic cations that are even more sterically demanding or lack specific functional groups for the ionic interaction with the inorganic substructure (e.g. if the positive charge is delocalized over a π–system), it is possible to lower the dimensionality further to 1D– or 0D–perovskite structures.[176] These systems offer a great structural versatility due to the fact that MX_6 octahedra can form chains by corner–, edge– or face–sharing (**Figure 4.1**). These chains can be interrupted into clusters of several octahedra of varying stoichiometry. An overview of the large number of structural possibilities in low–dimensional perovskites can be found in a recent review by B. Saparov and D.B. Mitzi.[129]

In most organic–inorganic hybrid perovskites (with higher dimensionality) simple organic cations are employed with mainly a templating function and only an indirect influence on the material properties. However, there is also the possibility to incorporate photoactive cations into the inorganic networks, which can play a more active role in the resulting optical and electrochemical properties of the hybrid material. For example, polythiophenes,[177] oligothiophenes,[173] polydiacetylenes,[178] fullerenes[174] as well as naphthalene or pyrene chromophores[179–181] (functionalized with alkylammonium chains) have been successfully incorporated into 2D–perovskites. Large cations without ammonium groups based on Schiff bases,[182] methylviologen,[183] tropylium,[167] and naphthalene diimides[184] have been described to form 1D–perovskites with chains of face–sharing MX_6 octahedra; other hybrid materials with sterically demanding cations incorporated into inorganic networks of varying connectivity have been reported.[176,185,186]

The incorporation of large functional cations – which can be tailored by the tools of organic synthesis – into polyanionic inorganic networks allows for the design of new materials with great structural diversity and functional tunability as well as promising optical and electronic properties.

4.1.2 Properties and Applications

Lower dimensional organic–inorganic perovskites show several distinct differences in their electronic structure and properties compared to their three–dimensional parents.[187] While 3D–perovskites like $CH_3NH_3PbI_3$ typically behave like inorganic semiconductors with low exciton binding energies and band–to–band absorption,[188,189] layered 2D–perovskites are characterized by excitonic absorption and high oscillator strengths.[175,190] This effect is attributed to both quantum confinement by the dimensional reduction[191] and dielectric confinement due to the layered structure forming a "quantum well" semiconductor.[190,192] The relative permittivity is much lower in the organic cation layer, so that the effective Coulomb interaction between electrons and holes is enhanced in the inorganic layer leading to an increased exciton binding energy.[171,193,194]

Depending on the nature of the organic cations and inorganic layers, the excitons in 2D organic–inorganic perovskites can have properties of both *Wannier–Mott* excitons (which have large radii 30–100 Å, small binding energies 10–30 meV, and typically occur in inorganic materials) and/or *Frenkel* excitons (which have small radii ~5 Å, large binding energies 500–1000 meV and typically occur in organic materials).[129,195,196] The measured exciton binding energies (60–540 meV) and radii (6.2–22.9 Å) in different layered organic–inorganic hybrids are reported to vary over a large region,[187] and there are controversies whether they are *Wannier–Mott* or *Frenkel* type excitons.[129,171,197] Some studies suggest that with appropriately chosen organic cations and inorganic layers, both types of excitons could be generated in the separate layers and coupling of the excitons could lead to *Frenkel–Wannier* hybrid excitons.[129,195,198] This could give rise to unusual properties, such as optical nonlinearity.[129,199]

The orbitals involved in the absorption of light in organic–inorganic perovskites are solely based on the inorganic component (for cations that are not photoactive). In the case of lead halide perovskites the top of the VB is composed of mainly p–orbitals of the halide mixed with 6s–orbitals of Pb^{2+}, while the bottom of the CB is formed by 6p–orbitals of Pb^{2+}.[200] It follows that the value of the VB can be altered by the choice of halide (VB decreases in energy from I^- to Br^- to Cl^-), while the CB remains unaffected.[200]

The bandwidth of the CB and VB decreases with the dimensionality of the inorganic network from 3D to 2D, 1D and 0D structures, leading to an increased bandgap.[201] **Figure 4.2** illustrates the absorption spectra of lead iodide based hybrid perovskites with different dimensionality: 3D–perovskite $CH_3NH_3PbI_3$ shows a broad absorption band all over the visible; for the lower dimensional analogues a sharp absorption peak is observed which is gradually shifted to lower wavelengths λ from 2D to 0D.[187]

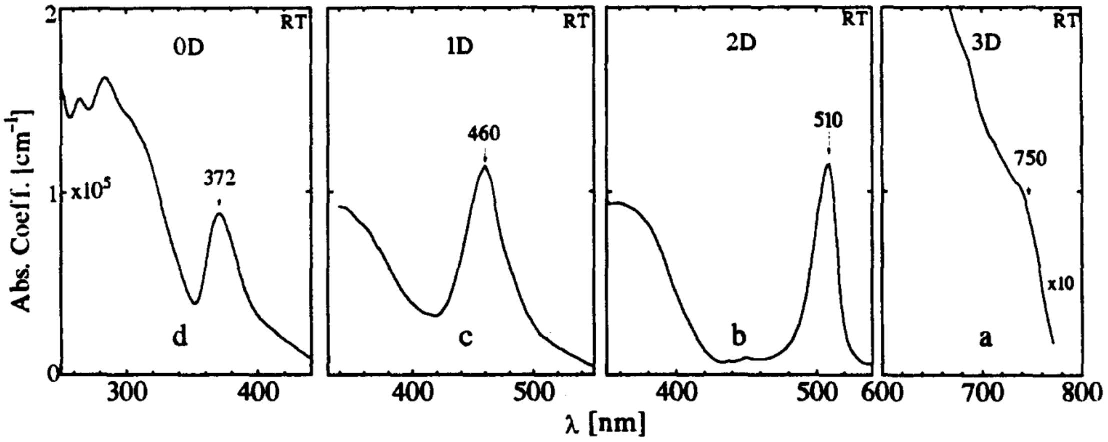

Figure 4.2. Absorption spectra of lead iodide based hybrid perovskites with different dimensionality. From right to left: (a) 3D: $CH_3NH_3PbI_3$; (b) 2D: $(C_9H_{19}NH_3)_2PbI_4$; (c) 1D: $(NH_2C(I)=NH_2)_3PbI_5$; (d) 0D: $(CH_3NH_3)_4PbI_6 \cdot 2H_2O$. Reprinted from *Progr. Sol. St. Chem., Vol. 25*, G.C. Papavassiliou, *Three– and low–dimensional inorganic semiconductors*, page 198, Copyright (1997), with permission from Elsevier.

As mentioned above, most cations have only a templating effect and determine the dimensionality of the hybrid crystal, but their orbitals do not directly contribute to the optical properties of the material. When comparing a series of organic cations with increasing alkyl chain lengths *n* in a series of layered 2D perovskites $(C_nH_{2n+1}NH_3)_2PbI_4$, it is found that while the spacing of the layers increases with *n*, this does not influence the bandgap for all chains $n \geq 4$, as the distances between the inorganic sheets do not allow for electronic interactions.[171,172] A notable property of this family of compounds is their thermal behavior, as they undergo reversible phase transitions. The first transition is reported to be associated with conformational changes within the alkyl chain,[171] while a second transition is described as a complete melting of the longer alkylammonium cations.[172] The phase transition temperatures increase with increasing chain length n; from 250 K (n = 4) to 346 K (n = 18) for the first transition, which is accompanied by a visual color change of the crystal from yellow to orange; and from 313 K (n = 7) to 373 K (n = 18) for the melting transition, which leads to a distinct loss of the crystallinity.[171,172]

In lower dimensional perovskites the effective masses of electrons and holes are higher than in their 3D analogues, leading to lowered charge carrier mobilities.[158,202] The confinement of charge carriers in a two–dimensional sheet, as in layered A_2MX_4 perovskites, however, could be useful for applications where charge transport in a certain direction is required, as for instance in thin–film field–effect transistors (FETs). The inorganic sheets of 2D–perovskites could act as semiconducting channels when aligned between the source and drain electrodes.[203] Further areas of application for lower dimensional perovskites are light-emitting devices,[204–207] solar cells,[208] photodetectors,[209,210] nonlinear optical applications,[211,212] or as battery cathodes.[213]

4.1.3 Synthesis and Preparation of Thin Films

For the synthesis of organic–inorganic hybrid perovskites various different approaches are available which can be chosen or combined depending on the properties of the desired organic and inorganic precursors. For both 3D– and lower dimensional compounds similar procedures can be applied, as the dimensionality of the resulting hybrid is usually determined by the size of the ions and/or the employed stoichiometry. The most common preparation procedure is the co–crystallization of an organic salt (e.g. alkylammonium iodide) with an inorganic salt (e.g. lead iodide) from solution.[124,170] By slow evaporation or cooling of solutions containing both precursors in the right stoichiometry single crystals suitable for X–ray analysis can be obtained.[124] This obviously requires sufficient solubility of both precursors in the same solvent. Typically employed solvents are water, aqueous solutions of hydrohalic acids (HI, HBr or HCl depending on the desired halide in the perovskite), alcohols and other polar organic solvents (DMF, DMSO, GBL or NMP).[124,126,132,170,214] If the bivalent oxidation state of the chosen metal is unstable (e.g. Ge^{2+} or Sn^{2+}), the crystallization has to be carried out under inert atmosphere to avoid oxidation – for lead halide perovskites, however, this is usually not a concern, as Pb^{2+} is a stable oxidation state.[215] When employing structurally more advanced organic cations (than simple alkylammonium halides) it is often difficult to find a congruent solvent for both precursors. Alternatively, hybrid crystals can be grown by slow diffusion of two separate solutions – one containing the organic salt and the other the inorganic halide – by layering or gel diffusion techniques.[171,216] Another route to prepare organic–inorganic hybrid perovskites is by solid–state reaction or melt processing.[217] These processes are limited due to the large difference in thermal properties between the organic and inorganic precursors. The rather low decomposition points of organic compounds (< 300°C) require mild processing temperatures, which are often not sufficient to melt the inorganic salts, including lead halides.[124,215]

Also for the preparation of thin films of organic–inorganic hybrid perovskites, which are typically needed for their application in optoelectronic devices, a variety of methods is known. During recent years special attention was given to the optimization of crystal size, grain boundaries and homogeneity of thin films of 3D–perovskites (especially $CH_3NH_3PbI_3$) for photovoltaic applications.[218] For each set of organic and inorganic precursor, however, the crystallization and film forming properties can vary and need to be optimized individually. Thin films on various substrates can be fabricated by spin–coating from solution, either in a one–step procedure using a solution containing both precursors,[126,214,219,220] or by two–step procedures, which involve sequential spin–coating or dip–coating of the two components.[121,221–223] Typically, films of the inorganic component are prepared first, followed by exposure to a solution containing the organic halide. This leads to intercalation of the organic cation into the inorganic structure, e.g. to form a layered 2D–perovskite.[224,225] Few examples are known where the organic compound is deposited first and then subjected to a solution of the metal halide.[177]

Thin films of organic–inorganic layered perovskites have been described to have a strong tendency for preferential orientation of the perovskite sheets parallel to the substrate plane.[124,221] This can be observed in powder XRD–diffraction patterns as a strong enhancement of the intensity of the c–axis reflections (00ℓ) compared to the other peaks, an effect also known from all–inorganic layered perovskites.[226]

Apart from solution coating techniques, organic–inorganic perovskites can also be deposited by thermal evaporation.[124,224,227–230] Also here, procedures have been developed for co–evaporation of both the inorganic and organic salt using a dual–source system[227,230] or sequential deposition of the two precursors. Two–step procedures which combine solution– and vapor–deposition techniques or thermal evaporation have also been reported.[228,229]

4.2 Highly Ordered 2D–Perovskite Films

4.2.1 Aim

As introduced above, 2D layered organic–inorganic hybrid perovskites have a tendency to form thin films with a preferential orientation of the inorganic sheets with respect to the substrate plane. Such films could be of great interest for field–effect transistors (FETs) as the inorganic sheets are aligned in the direction of charge transport between source and drain electrodes.

Thin films of dodecylammonium lead iodide (DDAP) which has the formula $(C_{12}H_{25}NH_3)_2PbI_4$ can be fabricated *via* an intercalation procedure which has been studied in detail by Ahmad et al.[224] This procedure involves deposition of a PbI_2 film followed by dip–coating in a solution of dodecylammonium iodide (DDAI) which leads to intercalation of the cation into the inorganic sheets. Ahmad et al. have studied and optimized several aspects of this procedure, namely the PbI_2 film thickness as well as the solvent and concentration of the organic cation used in the intercalation step. Preliminary experiments to prepare thin films of DDAP based on the optimized conditions reported by Ahmad et al. have been carried out; it was found that slight variations of the experimental conditions had a great impact on the crystallinity and preferential orientation of the perovskite crystallites in the thin film.

Figure 4.3 shows powder X–ray diffraction (XRD) patterns of two thin films of DDAP. The first pattern (top) corresponds to an incompletely converted film with a random orientation of the crystallites, as the peaks can be correlated to the pattern of DDAP powder. In the second pattern (bottom), only the (00ℓ) reflexes up to (00 20) are visible, indicating that the film consists of highly ordered crystallites with a preferential orientation of the inorganic sheets in parallel to the substrate plane.

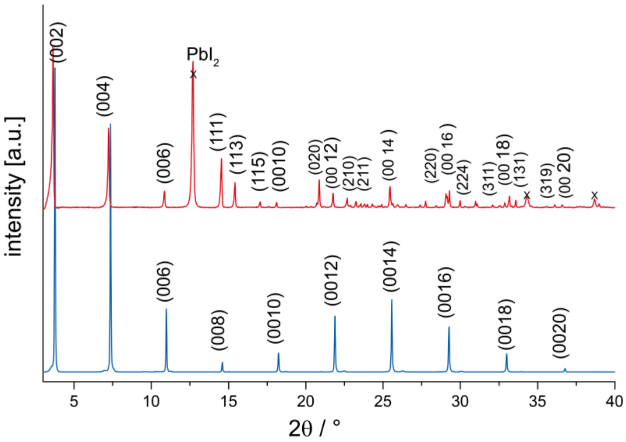

Figure 4.3. XRD patterns of two different films of DDAP.Top: Incompletely converted film with random orientation of crystallites, peaks labelled with "x" correspond to leftover PbI_2. Bottom: Highly ordered crystallites with only (00ℓ) reflexes visible.

The following study aims at the elucidation of further factors influencing the formation of the 2D–perovskite during the intercalation process, in addition to the ones investigated by Ahmad et al.,[224] with focus on the fabrication of highly ordered films. In particular, the influence of the morphology of the PbI_2 precursor films, of the intercalation temperature and atmosphere are highlighted.

4.2.2 Spin–Coated Lead Iodide Films with Controlled Morphology

PbI_2 films were spin–cast on glass slides from warm DMF solution (70 °C). The concentration of the solution was near saturation at this temperature (29% w/w). Freshly prepared films were light yellow and turned dark yellow as they were drying. It was found that the drying conditions right after spin–coating have a remarkable effect on the final morphology of the PbI_2 films, which is even visible by eye. **Figure 4.4** shows a photograph of PbI_2 films which were subjected to different drying temperatures right after spin–coating; films dried at low temperatures (5–25 °C) gave opaque yellow films, while when dried at higher temperatures (70 °C) the films were found to be transparent. The observed visible transparency differences indicate that these films have different roughness and / or crystal sizes leading to different scattering properties.

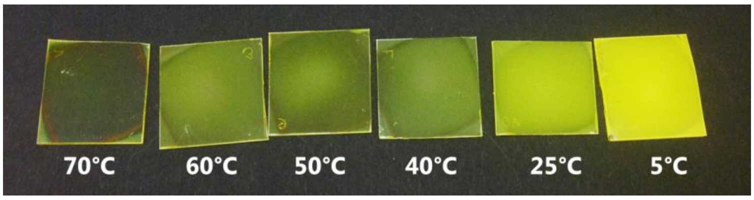

Figure 4.4. Photograph of spin–coated PbI_2 films dried at different temperatures.

The PbI_2 films shown in **Figure 4.4** were analyzed by scanning electron microscopy (SEM) and XRD. When regarding the SEM images (**Figure 4.5**) a clear trend towards the formation of compact films consisting of small crystallites was observed when the drying temperature was increased. When dried at room temperature (25 °C), the PbI_2 film consisted of disk–shaped crystallites, which do not fully cover the substrate forming a porous structure. If the film was cooled at 5 °C during drying, the platelets were considerably larger, and the porosity of the film was increased. The films dried at 40–70 °C , however, were homogeneously covered with thin platelets forming a compact structure. The thickness of all PbI_2 films, determined from the cross–sectional SEM images, was found to be ≈ 100 nm, while the porous films were slightly thicker than the compact ones. XRD patterns of the PbI_2 films (**Figure 4.6**) confirmed the trends observed in the SEM images. Notably, in all films the intensity of the (00ℓ) reflexes was enhanced, when compared to the standard XRD pattern of PbI_2 powder.[231] This is typical for thin films of PbI_2 due to the arrangement of platelet shaped crystals on the substrate.[221,228]

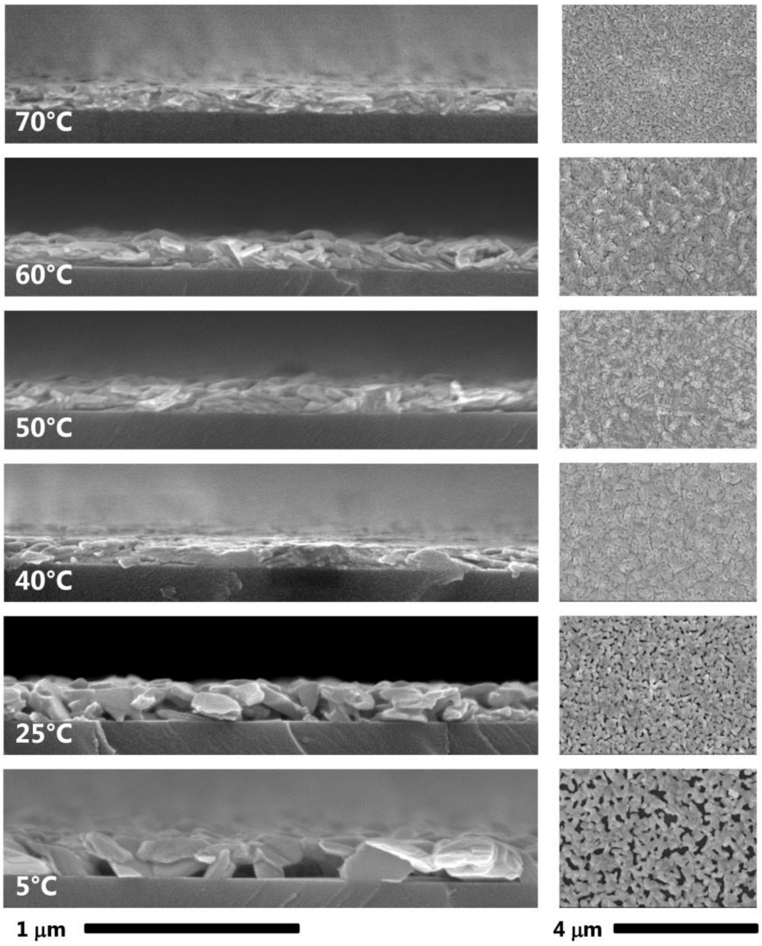

Figure 4.5. SEM images of spin–coated PbI_2 films dried at different temperatures.From top to bottom: 70 °C, 60 °C, 50 °C, 40 °C, 25 °C and 5 °C. View of film cross–sections (left) and surfaces (right).

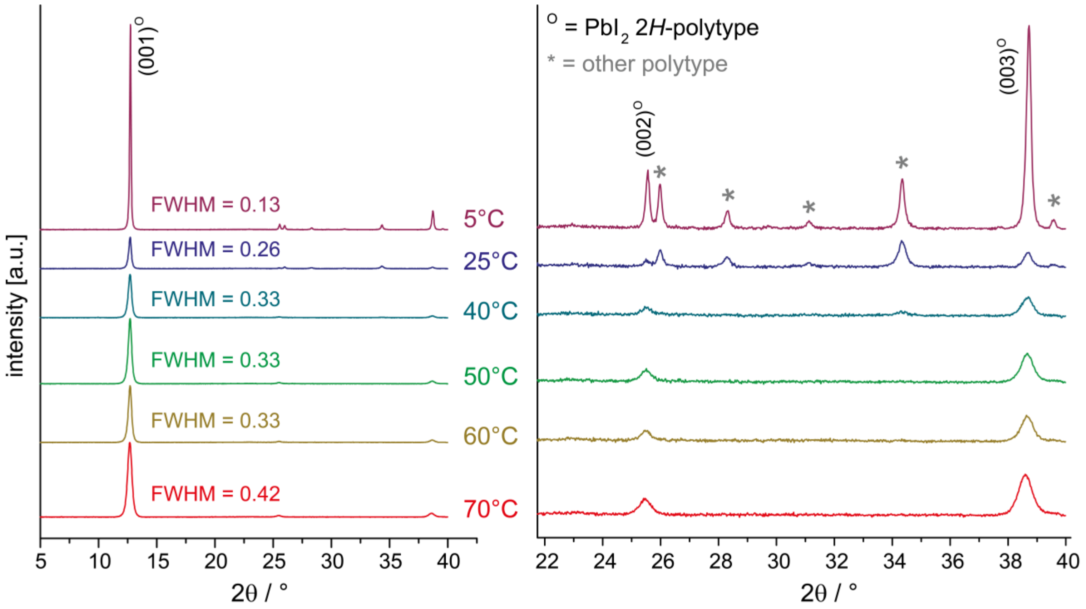

Figure 4.6. XRD patterns of spin–coated PbI_2 films dried at different temperatures. Full spectrum from 5–40° 2θ (left), and zoom on the region 22–40°2θ (right). FWHM for (001) peak of each spectrum is given, peaks were indexed according to literature.[231] Peaks labelled with an asterisk (*) correspond to a different polytype than the standard 2*H*.

The full width at half maximum (FWHM) of the (001) peak of each XRD pattern was determined, as it is related to the crystallite size.[232,233] The film dried at 70 °C gave the largest FWHM value (0.42) in the series, indicating that its crystals are smallest in size. For the films dried at 40–60 °C FWHM had the same value (0.33), which is in agreement with the SEM images, where these films are very similar. The film dried at 25 °C showed a lower FWHM (0.26), and in the film dried at 5 °C it was even remarkably lower (0.13), confirming that these films are composed of larger crystallites.[234]

For the films dried at 40–70 °C, only the (00ℓ) reflexes referring to the $2H$–polytype of PbI_2 were observed.[231,235] For the films dried at lower temperatures additional reflexes were observed, corresponding to a different polytype of PbI_2 – presumably $6R$. A comparison of the pattern from the film at 5 °C with the five most common polytypes of PbI_2 is shown in **Figure 7.2** (page 123). The presence of an additional polytype to $2H$ in the other films (40–70 °C) can however not be excluded, as it might be not visible in their patterns due to the broadness of the peaks. To our knowledge, the presence of other polytypes than $2H$ in thin films of PbI_2 has not been described in the literature so far.

The change in morphology at different drying temperatures can be explained by the complexation of PbI_2 with the solvent DMF. The light yellow color of the freshly spin–coated films indicates that they consist of a $PbI_2{\cdot}DMF$ complex, as described by Wakamiya et al.[236] The rapid decomposition of this complex was found to start at 70 °C, which explains the formation of small compact crystallites in films dried at this temperature, due to fast crystallization of PbI_2. It can be assumed that this complex also decomposes at lower temperatures, as also the thin films dried at lower temperatures undergo a color change to dark yellow, albeit much slower. Allowing more time for the crystallization, larger crystallites are able to grow which consume the precursor film around them and form a porous PbI_2 film.

Experiments on different storage conditions of spin–coated PbI_2 films showed that the films were reasonably stable in air over several days, but converted to Pb(OH)I over a course of 8 months. More information is given in the experimental chapter (**Figure 7.3** and **Figure 7.4**, page 123).

In summary, the variation of the drying temperature of spin–coated $PbI_2{\cdot}DMF$ precursor films allows for tuning of the morphology of the final PbI_2 layers from compact to porous. Fan et al. have reported a strategy to fabricate PbI_2 films with controlled morphology by thermal evaporation by optimizing the choice of substrate and deposition rate.[228] To our knowledge, control of the morphology of for spin–cast PbI_2 films has not been reported in the literature so far. The controlled morphology of these films is useful not only for the intercalation process to prepare 2D–perovskites (as demonstrated in chapter 4.2.3), but also for fabrication of solar cell absorbers such as $CH_3NH_3PbI_3$, for which PbI_2 films are frequently employed as precursors.[121,228,229]

4.2.3 Intercalation of Dodecylammonium Cations into PbI_2 Films

In order to form the 2D–perovskite DDAP, PbI_2 films were dip–coated in a solution of dodecylammonium iodide (DDAI) leading to intercalation of the organic cation into the PbI_2 sheets. Factors that influence the intercalation process have been described by Ahmad et al. to be the thickness of the PbI_2 films, as well as the solvent and concentration of the organic cation.[224] They also found that the dipping time is of importance, as the films need to be removed from the solution once they are fully converted, otherwise abrasion occurs and the films are damaged.[224] In this study, for the conversion of PbI_2 into DDAP, a PbI_2 film thickness of ≈ 100 nm and a DDAI solution in toluene (0.58% w/w) were used, as were the optimized conditions reported by Ahmad et al, with the exception that their precursor films were prepared by thermal evaporation.[224]

It was found that the morphology of the PbI_2 precursor film has a great influence on the intercalation speed. **Figure 4.7** shows the XRD spectra of a porous (dried at 25 °C) and a compact PbI_2 film (dried at 70 °C), which have both been subjected to the same dip–coating conditions.[i] The porous precursor film converted to a highly crystalline film of DDAP with preferential orientation of the crystallites (pattern shows only (00ℓ) reflexes), while the compact film did not fully convert to DDAP and gave a random distribution of DDAP crystallites (for peak assignment see **Figure 4.3**).

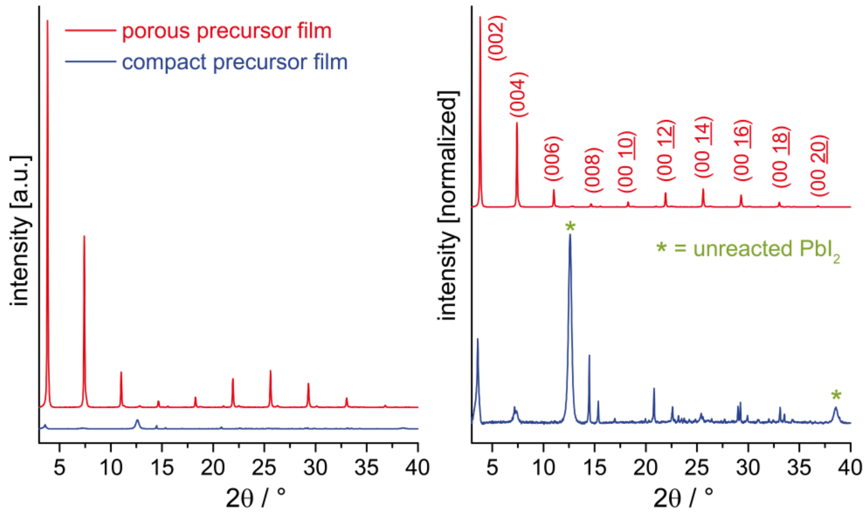

Figure 4.7. XRD patterns of thin films of DDAP prepared from PbI_2 precursor films with different morphologies.Left: Intensities as measured, right: Normalized intensities. Porous precursor film (red) with reflexes assigned.[172] Compact precursor film (blue) with unreacted PbI_2 (marked with *).

---

[i] Dip–coating temperature and reaction time: 30 °C, 60 sec; intercalation under ambient atmosphere.

The faster conversion of porous PbI_2 films can be explained by the fact that the reaction solution can permeate the films more efficiently by entering the pores during the dipping process.[228] Compact films were also not fully converted at longer reaction times (> 100 sec), at which point they started to be damaged via abrasion by the solvent.

Another experimental factor which was found to have an important effect on the final DDAP film was the temperature during intercalation. **Figure 4.8** shows the XRD patterns of two DDAP thin films both prepared at 40 °C or 50 °C, while all other experimental conditions were identical.[j] At 40 °C there was still a small amount of unreacted PbI_2 left. At 50 °C the intercalation proceeded faster to fully converted DDAP films and films were of higher crystallinity with strong preferential orientation of the crystallites. It is important to note that DDAP undergoes a phase transition from phase III to phase II at 42 °C.[172] This means that at 50 °C films are formed in phase II followed by thermal relaxation to phase III at room temperature, while films prepared at 40 °C directly form phase II. Billing et al. reported on the thermal hysteresis of 2D–perovskites; the relaxation from phase II to phase III upon cooling occurs at a lower temperature than the transition from phase III to phase II upon heating.[172] In our work, it was found that in thin films of DDAP the relaxation to the room temperature phase III occurs very slowly and even after two weeks it is not fully completed (peaks marked with * in **Figure 4.8**). Additionally, intercalation of water is observed when the films are stored over several days and exposed to ambient air for XRD analysis (peaks marked with † in **Figure 4.8**). Further information on the relaxation from phase III to phase II and the intercalation of water is given in the experimental chapter 7.2.3.1 (page 121). The faster conversion and subsequent slow relaxation and recrystallization process are likely to be reasons for the improved crystallinity and preferential orientation of films prepared at 50 °C.

The film thickness of the optimized DDAP thin films was ≈ 1 μm, as determined from cross–sectional SEM images (shown in the experimental chapter 7.2.3.1, **Figure 7.5**, page 124) and profilometry.

---

[j] porous PbI_2 films (dried at 25 °C); reaction time: 45 sec; intercalation under ambient atmosphere.

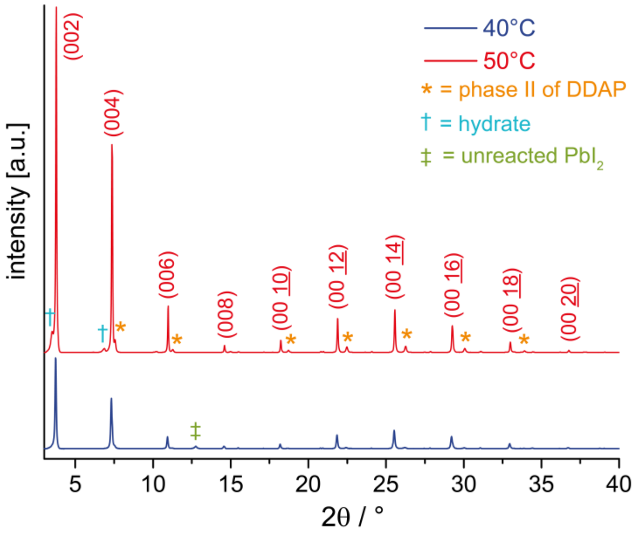

Figure 4.8. XRD patterns of thin films of DDAP prepared at different intercalation temperatures, intensities as measured. 40 °C (blue line), 50 °C (red line) stored for two weeks. * = phase II of DDAP; † = hydrate; [k] ‡ = unreacted PbI_2.

To conclude, it was found that conditions supporting a fast conversion of PbI_2 films to DDAP, such as porous precursor films and increased temperature of the solution (50 °C) are beneficial for the formation of films with highly ordered crystallites. When considering that PbI_2 films already consist of preferentially (00ℓ) oriented crystals (**Figure 4.6**), a fast conversion allows for preservation of this order, while the longer reaction times under slow conversion conditions seem to disturb it. Furthermore, DDAP films prepared at higher temperatures (> 42 °C) are formed in phase II, followed by slow thermal relaxation to the room temperature phase III, which leads to the formation of highly crystalline films.

4.2.4 Optimization of Highly Ordered DDAP Films for FET Devices

In order to characterize the electrical properties of DDAP layers with highly ordered crystallites, thin films on standardized organic field effect transistor (OFET) substrates from *Fraunhofer*[237] were prepared using the optimized intercalation conditions described above.[l] These substrates are pre–patterned with Au contacts forming channels of varying width (2.5 µm, 5.0 µm, 10 µm, and 20 µm) for the fabrication of bottom contact transistors. The spin–coated PbI_2 precursor films crystallized in a different morphology on different areas of the substrate, as can be seen on the SEM images in **Figure 4.9**. On the SiO_2 surface (top left), the film was porous and identical to the films grown on glass substrates under the same conditions (**Figure 4.5**). On top of the Au contacts of the OFET substrate (top right), however, a compact morphology of the PbI_2 film was found. This dense

---

[k] additional information on phase II and intercalated H_2O is given in chapter 7.2.3.1 (page 120).

[l] PbI_2 films dried at 25 °C; dip–coating at 50 °C; under ambient atmosphere.

arrangement of crystals seems to grow also over the edges of the Au contacts into the FET channels (bottom left: 5μm channel, bottom right: 10 μm channel).[m] It is apparent that the nature of the substrate influences the growth of the crystals to a large extent, which is in agreement with what Fan et al. reported on thermally evaporated PbI_2 films.[228]

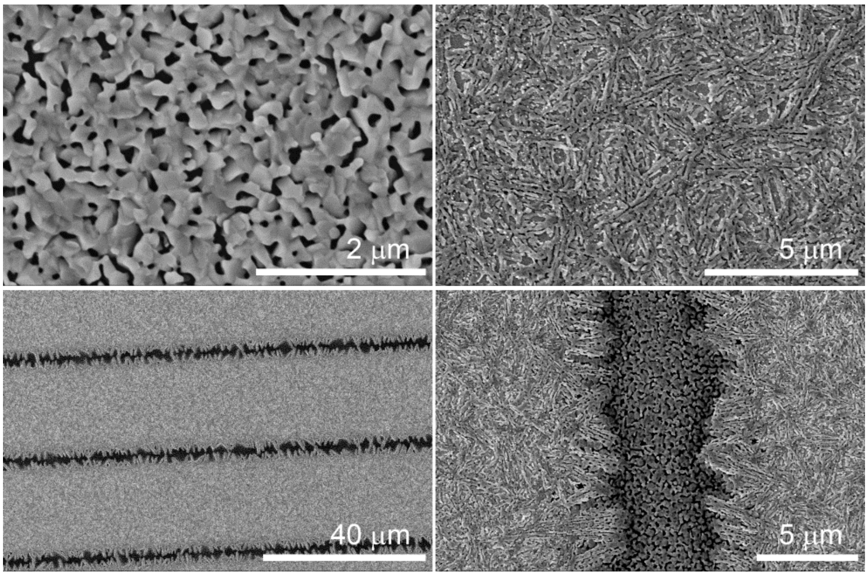

Figure 4.9. SEM images of spin–coated PbI_2 thin films on *Fraunhofer* standard OFET substrates, different areas of the substrate. Top left: on SiO_2 surface; top right: on a gold contact; bottom left: 5 μm channel; bottom right: 10 μm channel.

In the subsequent intercalation step, the inhomogeneity of the PbI_2 precursor films on OFET substrates also affected the growth of the final DDAP film. SEM images revealed large inhomogeneous DDAP crystallites on the Au contacts, while there were defects and holes in the channels and the films were also disrupted on the plain SiO_2 surface around the channels (**Figure 4.10**).[m] In short, the patterning of *Fraunhofer* standard OFET substrates was found to be unfavorable for the preparation of smooth and continuous DDAP films by the intercalation procedure.

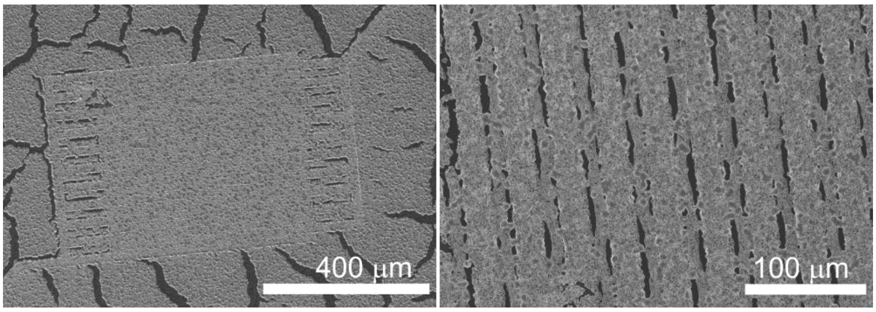

Figure 4.10. SEM images of a DDAP film on *Fraunhofer* standard OFET substrate prepared by intercalation procedure. Left: overview of a block of channels shows disruptions of the film. Right: closer view shows defects and holes in the channels.

---

[m] XRD patterns of PbI_2 and DDAP films on OFET substrates shown here were the same as for the films on glass, showing (00ℓ) reflexes only.

As an alternative to bottom–contact FET devices, the electrical properties of thin semiconducting films could also be characterized in a top–contact geometry.[238] The advantage of the latter is that films can be fabricated on plain Si–wafers that do not contain any pre–patterning, which might adversely affect their morphology. In the following, experiments towards optimizing the film thickness and continuity of DDAP layers for top–contact FET devices were carried out.

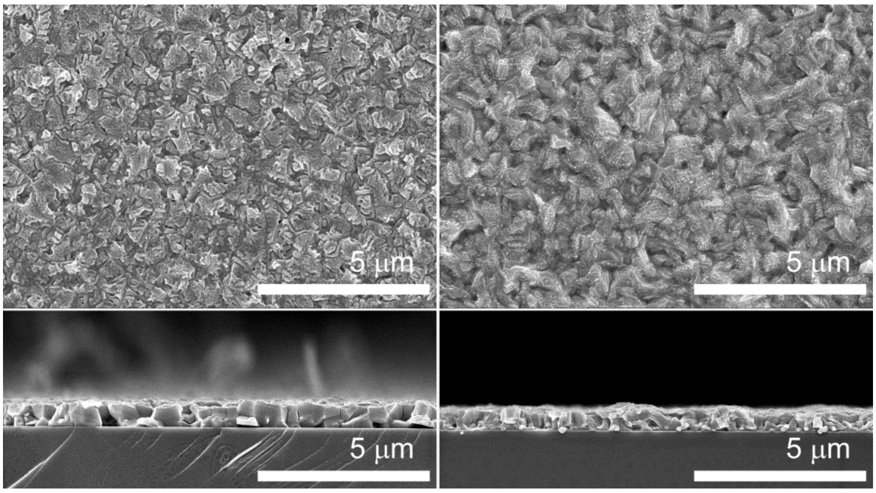

Figure 4.11. SEM images of surfaces (top) and cross–sections (bottom) of a DDAP film on Si–SiO$_2$ wafer before (left) and after annealing (right).

For application in devices films are required to be compact and smooth with minimal gaps (grain boundaries) between the crystallites. In order to improve these properties annealing experiments of DDAP films[n] were carried out. **Figure 4.11** shows SEM images illustrating the morphology differences of a film before (left) and after annealing at 100 °C, followed by slow cooling to room temperature (right). After annealing the film is more compact and homogeneous, as compared to before annealing, where well–defined crystallites separated by grain boundaries are found. As introduced previously, DDAP undergoes two phase transitions, a first one (associated with a conformational change of the organic cations) at 42 °C, and a second one (associated with a quasi–melting of the organic layer) at 70 °C.[172] The quasi–melting of the organic cations allows for the morphology change observed in the annealed films. XRD spectra showed that the desired preferential orientation of the crystallites was preserved after annealing (**Figure 7.7**, page 126).

A further improvement for the application of DDAP films in devices was achieved by reducing their film thickness. As described previously, PbI$_2$ films with a thickness of

---

[n] on Si–SiO$_2$ wafer substrates; prepared from porous PbI$_2$ film at a dip–coating temperature of 50 °C inside nitrogen–filled glovebox.

≈ 100 nm resulted in a thickness of ≈ 1000 nm of DDAP film after intercalation. Thus, in order to reduce the thickness of DDAP films to ≈ 100 nm, the thickness of PbI_2 precursor films had to be adjusted to ≈ 10 nm, which was achieved straightforwardly by lowering the concentration of the spin–coating solution. **Figure 4.12** (top left) shows that the thin PbI_2 films still have the desired porous morphology. For the intercalation of DDAI into these very thin PbI_2 films also the concentration of the dip–coating solution had to be adjusted, as the conversion is completed much faster. The very short reaction times (on the order of a few seconds) would be difficult to control manually and, as described before, films are known to suffer from damage by abrasion when remaining in the dip–coating solution after conversion is completed.[224] When the dip–coating solution was diluted by a factor of 10, the conversion rate could be slowed down to achieve homogeneous DDAP films with a thickness of ≈ 100 nm (**Figure 4.12**). XRD patterns of these films showed intense (00ℓ) reflexes indicating a highly ordered arrangement of crystallites (**Figure 7.7**, page 126).

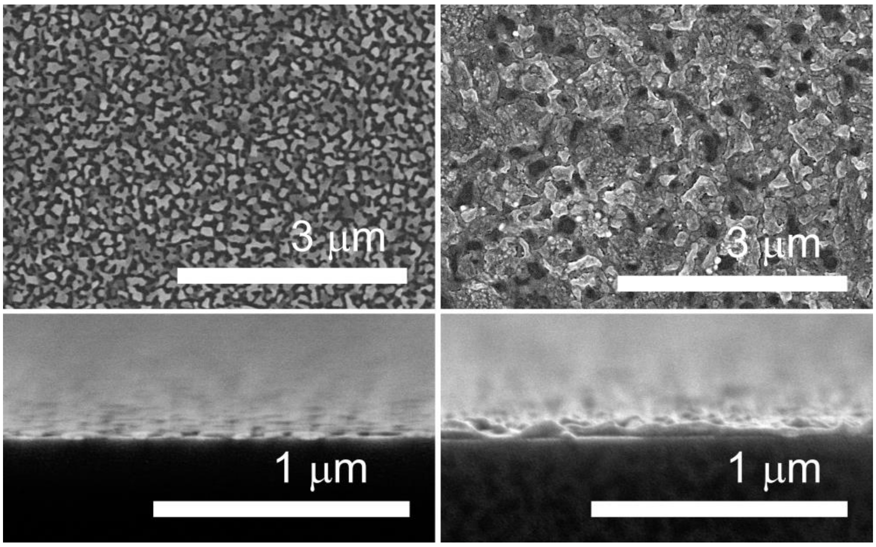

Figure 4.12. SEM images of surfaces (top) and cross–sections (bottom) of PbI_2 films (left) and DDAP films (right) with reduced film thickness for device application.

To summarize, DDAP films were optimized for the fabrication of bottom–contact FET devices. The film morphology could be considerably improved by annealing and the thickness was reduced to ≈ 100 nm by adjusting the concentrations of the precursor solutions. Fabrication of FET devices is currently ongoing.

4.3 NIR–Cyanine Cations in Organic–Inorganic Hybrid Perovskites

4.3.1 Aim

As described in the introductory chapter 4.1, the incorporation of functional organic cations into organic–inorganic lead halide perovskites could be a promising strategy for obtaining new materials with unusual photophysical properties. There are several examples in the literature reporting on the synergistic interplay of organic chromophores with the inorganic framework in a hybrid structure, such as an oligothiophene incorporated in a 2D–perovskite[173] or a naphthalene diimide dye in a 1D–structure.[184,202] Cyanine dyes are organic chromophores with high extinction coefficients and excellent tunability of the absorption wavelength and redox properties, as introduced and discussed in detail in chapter 2. Most organic compounds require functionalization with a cationic moiety, such as an ammonium group, to make them suitable for forming hybrid perovskites in a polyanionic inorganic framework.[164,173,174] Such modifications are not required for cyanine dyes, as most of them are already cationic in their native form. Based on these considerations, this work aimed at the incorporation of NIR–absorbing heptamethine dyes as functional organic cations into lead halide perovskite structures.

4.3.2 Results and Discussion

From a solution of a heptamethine iodide salt (**8–Cl**) and PbI_2 in DMF thin green needles were grown by slow evaporation. X–ray crystal structure determination revealed that both precursors co–crystallized into a monoclinic hybrid crystal (**Cy7–PbI₃**) with the general formula $(C_{34}H_{40}ClN_2^{+})_n[PbI_3^{-}]_n\cdot 2n(DMF)$ in the space group $P2_1/c$. The inorganic component $[PbI_3^{-}]$ forms polyanionic chains of face–sharing octahedra running parallel to the c–axis, with the cyanine cations and solvent molecules dispersed between them. The asymmetric unit consisting of one cyanine cation $[Cy7^{+}]$, one $[PbI_3^{-}]$ fragment and two molecules of DMF is depicted in **Figure 4.13** (left), together with the unit cell containing four asymmetric units (right).

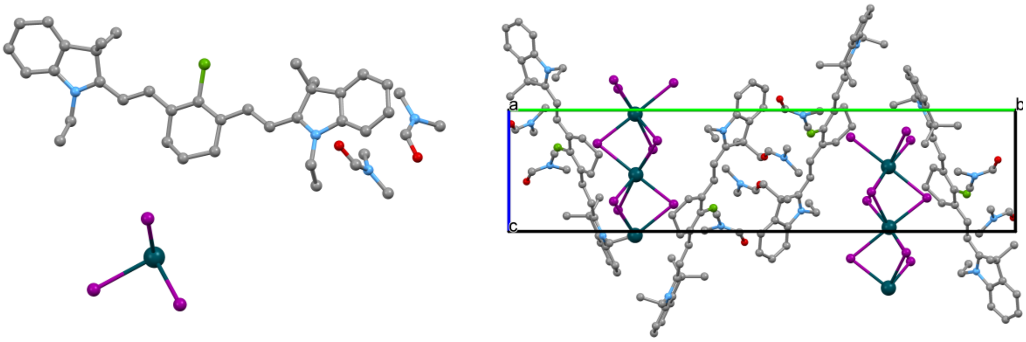

Figure 4.13. Crystal structure of **Cy7–PbI₃**. Left: asymmetric unit; right: unit cell, view along a–axis.

The packing of the crystal structure viewed along the c–axis is shown in **Figure 4.14** (top). There are two sets of cyanine cations arranged around each $[PbI_3^-]_n$ chain, with DMF molecules dispersed in between. Each set of cyanine cations is stacked into columns in a herringbone–like arrangement, at an average distance of 3.9–4.1 Å, indicating weak van der Waals interactions between them. The arrangement of one set of cations along a $[PbI_3^-]_n$ chain is shown in **Figure 4.14** (bottom).

When analyzing the bond lengths in the polymethine chain of the cation, very little to no bond length alternation (BLA) is found with an average C–C bond length of 1.39±0.01 Å. As can be seen in **Figure 7.12** (chapter 7.3.7, page 140), the BLA in **Cy7–PbI$_3$** is only slightly larger than with the TRISPHAT$^-$ counterion, which is known as one of the best counterions for reaching the ideal polymethine state (IPS) in the solid phase.[64,79] The fact that the $[PbI_3^-]_n$ counterion is weakly coordinating and not disturbing the ideal polymethine state allows for the chromophore to preserve its excellent optical properties, such as low band gap and high molar extinction coefficient.[64,92] Furthermore, the closely packed herringbone structure of the dye molecules could allow for the formation of spectroscopic *J*–aggregates.[43]

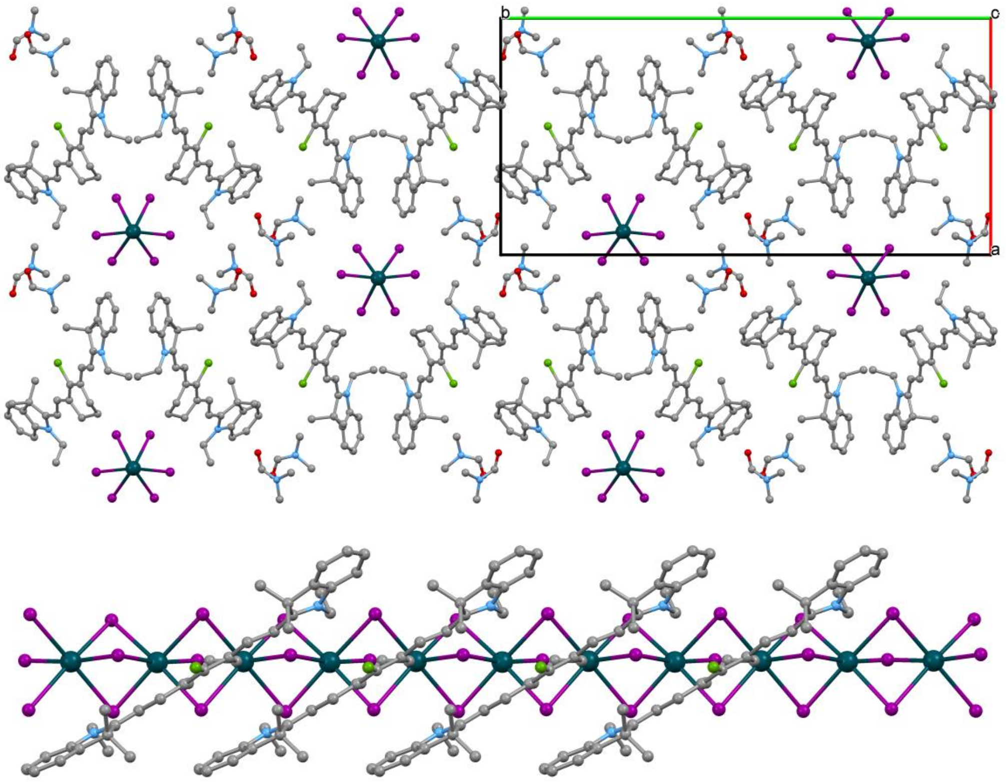

Figure 4.14. Crystal structure of **Cy7–PbI$_3$** (hydrogen atoms omitted for clarity). Top: Crystal packing viewed along the c–axis; bottom: view of one set of cyanine cations arranged along a $[PbI_3^-]_n$ chain.

Cy7–PbI$_3$ does not contain any hydrogen bonding interactions between the organic and inorganic component, as has been described for examples of similar organic–inorganic hybrid structures in the literature.[173,184] The co–crystallization of the precursor compounds into of a hybrid involves the transfer of the iodide ion from the cyanine salt to PbI_2 to form PbI_3^- which then arranges in polyanionic chains of face–sharing octahedra that are counterbalanced by the cyanine cations.

This structure is the first example of the incorporation of a strong NIR–absorber into an inorganic framework to form an organic–inorganic perovskite. From the interaction of both components in such a hybrid interesting properties are predicted to arise, which will need to be studied by detailed characterization of this new material in future work. A few examples of these interactions and possible energy level scenarios will be discussed in the following.

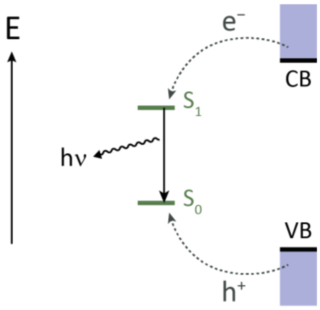

Figure 4.15. Energy level configuration and possible charge transfer processes in a hybrid material where the HOMO–LUMO gap of the organic component is smaller than the bandgap of the inorganic network. The relevant energy levels include the singlet S_0 and S_1 states of the chromophore and the VB and CB of the inorganic component. The energy level offset is chosen arbitrarily. Adapted with permission from Saparov, B.; Mitzi, D. B. *Chem. Rev.* **2016**, *116* (7), 4558–4596.[129] Copyright (2016) American Chemical Society.

The incorporation of optically active organic cations into organic–inorganic perovskites has been first described in 1999, both by Braun et al. reporting on energy transfer between the organic and inorganic components of layered perovskites containing small aromatic chromophores,[180,181] and by Mitzi et al. with a 2D–perovskite containing a quaterthiophene (AEQT).[173] The latter was substituted with two terminal ammonium groups and incorporated into inorganic frameworks with varying halides (X=Cl, Br, I) to form $(AEQT)PbX_4$. As the halides alter the bandgap of the framework, different energy level alignments between the two components were obtained, which affected the optical properties of the hybrid. In all compounds the emission from the excitons in the inorganic layer was found to be quenched in the presence of the quaterthiophene. Only with the chloride analogue, in which the inorganic layer has a larger bandgap than the chromophore, strong photoluminescence from the quaterthiophene was observed. The proposed scenario in this system is an electron transfer from the CB (of the lead halide network) to the S_1 (of the organic chromophore) together with a hole transfer from the VB to the S_0. The resulting excited state of the chromophore will then decay by emission of a photon, as illustrated in **Figure 4.15**.[129,173] The relative position of the energy levels of the organic and inorganic components in **Cy7–PbI$_3$** is likely to be similar to $(AEQT)PbCl_4$, because on the one hand the HOMO–LUMO gap of the NIR–heptamethine chromophore is considerably narrower than the one of AEQT[239] (see compound **8–Cl** in **Figure 2.12**, page 35), and the bandgap of the one–dimensional $[PbI_3^-]_n$ chains is widened compared to the 2D–sheets (see **Figure 4.2**, page 58). Based on these considerations, hybrid compound **Cy7–PbI₃** could have similar properties as described in the literature for $(AEQT)PbCl_4$, but with strong NIR–emission from the heptamethine chromophore, which could be employed in light–emitting devices.[204]

More recently, further studies focusing on the properties of low–dimensional perovskites with photoactive cations have been reported. Maughan et al. have demonstrated a compound composed of tropylium cations and similar chains of face–sharing lead iodide octahedra as in **Cy7–PbI₃**.[167] The tropylium lead iodide hybrid was found to exhibit broad spectral absorption and reduced bandgap (2.15 eV) as compared to the individual components which was attributed to charge–transfer absorption behavior.[158,167] In a similar 1D–perovskite system recently reported by Liu et al. the bandgap of the hybrid material could be further reduced by employing a naphthalene diimide dye as the organic component.[184] This compound exhibited an indirect bandgap of 1.26 eV and long–lived charge–separated excited states associated with a spatial separation of the VB and CB, as revealed by DFT calculations.[202] **Cy7–PbI₃** could have similar properties to this material, with a further lowering of the bandgap due to the very small HOMO–LUMO gap of the heptamethine dye. Such hybrid compounds with low bandgap and panchromatic absorption are promising candidates as absorbers in solar cells.[158]

In order to evaluate the engagement of the NIR–absorbing heptamethine dye and the $[PbI_3^-]_n$ chains in **Cy7–PbI₃** in synergistic interactions, such as electron / energy transfer or charge–transfer absorption processes, further characterization of the material is necessary. Ongoing and future work on this subject aims at the fabrication of highly pure and crystalline thin films as well as bulk powder of **Cy7–PbI₃** for optical and electrochemical characterization. In order to detect unpaired electrons in possible charge–separated excited states, ESR and photo–ESR measurements could be useful, while DFT calculations could reveal the position of energy levels of the individual components and their respective alignment.

This is the first demonstration of cyanine iodide salts forming a hybrid perovskite together with PbI_2, which might pave the way for a new class of materials. Cyanines are a versatile class of cationic dyes with great structural and functional tunability – and depending on the desired interaction with the inorganic network appropriate dyes can be chosen. The vast number of available cyanine dyes with sharp absorption peaks all over the visible and into the NIR will allow for a great diversity of different hybrid materials.

5 CONCLUSIONS AND OUTLOOK

5.1 Synthesis of Heptamethine Dyes and Counterion Exchange

NIR absorbing heptamethine dyes with different heterocyclic flanking groups (indolium, benz[*e*]indolium and benz[*cd*]indolium) and different substituents in *meso*–position (–Cl, –Ph, –NMe_2 and 1,3–dimethylbarbiturate "–barb") were synthesized in straightforward procedures. The influence of the heterocyclic flanking group and the *meso*–substituent on the optical and electrochemical properties was evaluated.

Indolium and benz[*e*]indolium heterocycles gave NIR heptamethine dyes with absorption maxima in the range of 760–820 nm and very high extinction coefficients ($270–330 \times 10^3$ M^{-1} cm^{-1}). With the benz[*cd*]indolium heterocycle heptamethine dyes with absorption maxima > 1000 nm and high extinction coefficients ($120–220 \times 10^3$ M^{-1} cm^{-1}) could be obtained.

It could be shown that electron donating substituents in *meso*–position are able to raise the redox levels of of heptamethine dyes, making electron transfer from the dyes to different solar cell electron acceptors (such as C_{60}, [60]PCBM or $CH_3NH_3PbI_3$) possible. The electron donating group –NMe_2 showed pronounced hypso– and hypochromic shifts, indicating loss of the ideal cyanine state and formation of a bis–dipolar state. With the 1,3–dimethylbarbiturate substituent, which is also an electron donating group, the cyanine state was found to remain intact. This is explained by additional delocalization within the barbiturate substituent and by sterical reasons avoiding the formation of a central double bond. Dyes carrying this group at the *meso*–position showed the strongest rise in energy of the redox levels while maintaining a sharp NIR absorption peak typical for heptamethines and are thus very promising candidates for the application as electron donors in solar cells.

Counterion exchange from iodide to PF_6^- and $TRISPHAT^-$ was performed and the influence of the counterion on the properties of a heptamethine salt was evaluated. It was found that the optical and electrochemical properties in solution were not affected by the counterion due to dissociation and solubilization of the ions. In the solid state, however, the counterion influences the properties of the heptamethine salt to a great extent. The large and bulky counterion Δ–$TRISPHAT^-$ was found to reduce dimerization and aggregation of the dyes compared to the PF_6^- counterion, which is reflected in a narrower absorption peak in the solid state. Packing tendencies of the PF_6^- and Δ–$TRISPHAT^-$ salts were also highlighted by X–ray crystal structure analysis.

Future work in this field will have to address the charge carrier mobility of cyanine dye thin films, which will need to improve substantially in order to achieve high solar cell efficiencies. Additionally, the stability of the dyes remains an issue for reliable solar cell performances. An interesting starting point to tackle both problems would be the evaluation of the influence of the cyanine counterion on the charge carrier mobility and long–term stability of thin films, as it was found to have a great effect also on other solid state properties. A new counterion with promising properties could be the polyanionic $[PbI_3^-]_n$–chains in a "cyanine perovskite" (see chapters 4.3 and 5.5). This material is likely to form crystalline thin films, which could lead to improved properties as compared to the amorphous thin films obtained with other counterions. The presence of inorganic conductive channels is likely to improve the charge carrier mobility and the closely packed herringbone structure of the chromophores could lead to interesting optical properties, such as spectroscopic aggregates.

5.2 Semi–Transparent Organic Solar Cells Using Cyanine Salts

Semi–transparent bilayer organic solar cells using two NIR heptamethine dyes with different counterions (PF_6^- and TRISPHAT$^-$) were fabricated and characterized. A notable influence of the counterion on the solar cell performance, mainly on the open circuit voltage (V_{oc}) was found. By changing the counterion from PF_6^- to TRISPHAT$^-$ an increase in V_{oc} from 0.38 V to 0.63 V and an increase in efficiency from 0.9% to 2.2% was achieved while maintaining a high transparency of 66% in the visible.[79] This is the first time that the tremendous influence of the counterion on cyanine solar cell performance has been illustrated and in the meantime the topic has inspired also other research groups to further investigate on this topic.[113]

Additionally, studies on bulk–heterojunction blends of the cyanine salts with different counterions (PF_6^- and TRISPHAT$^-$) and fullerenes showed a strongly increased miscibility of the two components. While the PF_6^- counterion yielded films with fully phase–separated bilayer morphology, the TRISPHAT$^-$ counterion showed perfect miscibility of the cyanine salt and [60]PCBM. Both morphologies were still not optimal for solar cell application (best efficiency at 1.1%), but future studies on different counterions with aromatic moieties could lead to the desired blend morphology with domain sizes on the order of the exciton diffusion length.[114]

Apart from organic solar cells, future work will involve the investigation of NIR photodetectors based on cyanine dyes. In these, the low charge carrier mobility can be compensated by the application of a reverse bias, which facilitates the extraction of electrons. Such devices are interesting in surveillance of machinery and quality control, as well as NIR scanners for medical applications.

5.3 Perovskite Solar Cells with Cyanine HTMs

Perovskite solar cells with NIR heptamethine dyes as the HTMs were fabricated, characterized and compared to the standard HTM Spiro-OMeTAD. It was found that the cyanine dyes have hole–transporting properties, maintaining high short circuit currents of J_{sc} = 11–15 mA cm^{-2} and power conversion efficiencies of η = 6.0–8.0% in PSCs with smooth perovskite layers. EQE measurements, however, showed no current generation for photons > 800 nm and thus no NIR–cosensitization by the heptamethine dyes. The reasons for this could be a mismatch of the electron levels; i.e. that hole injection from the perovskite to cyanine is possible, but electron injection from cyanine to the perovskite is hindered. Further work on this subject should aim at the synthesis of new NIR dyes with higher LUMO levels or alternatively at altering the perovskite/dye interface e.g. by employing dipoles at the interface which could be able to shift the respective energy levels.[80,240]

5.4 Highly Ordered Organic–Inorganic 2D–Perovskite Films

Layered organic–inorganic hybrid perovskite films of $(C_{12}H_{25}NH_3)_2PbI_4$ (DDAP) were fabricated from solution using a two–step procedure.[224] In a first step, PbI_2 films were spin–coated from DMF solution and an efficient method of controlling their morphology from compact to porous by varying the drying temperature of the precursor film was developed. The morphology of PbI_2 films was shown to have an important influence on the subsequent intercalation step. During dip–coating in a solution of the organic cation, porous PbI_2 precursor films underwent rapid conversion to form DDAP films with highly ordered crystallites, which was not possible to achieve with compact precursor films. Additional experimental factors for controlling the crystallinity of the final DDAP film were found to be the intercalation temperature and atmosphere. At temperatures slightly above room temperature (> 42 °C), DDAP was found to form in phase II, which then slowly converted to room temperature phase III over time. This slow crystallization process allowed for a higher crystallinity of the DDAP film.

In conclusion, careful fine–tuning of the experimental conditions enabled the reliable fabrication of 2D–perovskite thin films consisting of highly ordered crystallites. XRD spectra of such films showed very intense (00ℓ) reflexes from ℓ=2 up to ℓ=20, suggesting that the alternating layers of inorganic sheets and organic cations are perfectly arranged in parallel to the substrate plane. This highly ordered structure is very promising for the application in FET devices as the inorganic sheets are aligned in the direction of charge transport. For the electrical characterization, such films were prepared on pre–patterned OFET substrates. It was found however that the pre–patterning influenced the crystal growth substantially and device–quality films could not be obtained. As an alternative, films were optimized for producing top–contact FET devices. The film morphology of DDAP on Si–SiO_2 wafers could be considerably improved by annealing and by adjusting the concentrations of precursor solutions, very thin films of ≈ 100 nm could be achieved.

The fabrication of top–contact FET devices for the characterization of the electrical properties of thin DDAP films with highly ordered inorganic sheets is currently ongoing.

5.5 A Novel 1D–Perovskite Incorporating NIR–Cyanine Cations

The co–crystallization of a NIR–heptamethine salt and PbI_2 into a new organic–inorganic hybrid compound was demonstrated. The structure of the hybrid was determined by X–ray crystal structure analysis, which revealed a monoclinic crystal in the space group $P2_1/c$, consisting of polyanionic $[PbI_3^-]_n$ chains of face–sharing octahedra running parallel to the c–axis. This structure represents the first one–dimensional lead halide perovskite incorporating a functional NIR–absorbing dye as the organic cation, which is predicted to lead to unusual optical and electrical properties through the synergistic interaction between the components.

Further work on this topic will aim at the systematic characterization and evaluation of the properties of this new hybrid material. Investigation by means of ESR and fluorescence spectroscopy could reveal a possible energy transfer between the components. DFT calculations will additionally be able to predict and model the electronic interactions between the inorganic structures and cyanine molecules.

Furthermore, a great number of cyanine cations with varying bandgaps and redox properties is available, which might be suitable for the incorporation into organic–inorganic hybrid compounds. This first demonstration of a “cyanine perovskite” could lead to a new class of materials with interesting photophysical properties for various applications such as light–emitting devices and solar cells.

6 REFERENCES

(1) Dimento, J. F. C.; Doughman, P.; Levesque, S. In *Climate Change: What it Means for Us, Our Children, and Our Grandchildren*; MIT Press, 2015; pp 295–317.

(2) Cook, J.; Oreskes, N.; Doran, P. T.; Anderegg, W. R. L.; Verheggen, B.; Maibach, E. W.; Carlton, J. S.; Lewandowsky, S.; Skuce, A. G.; Green, S. A.; Nuccitelli, D.; Jacobs, P.; Richardson, M.; Winkler, B.; Painting, R.; Rice, K. *Environ. Res. Lett.* **2016**, *11* (4), 48002.

(3) Bentley, R. W. In *Introduction to Peak Oil*; Springer International Publishing, 2016; pp 9–55.

(4) *Handbook of Research on Comparative Approaches to the Digital Age Revolution in Europe and the Americas*; Passarelli, B., Straubhaar, J., Cuevas-Cerveró, A., Eds.; IGI Global, 2016.

(5) Learning About Renewable Energy | NREL https://www.nrel.gov/workingwithus/learning.html (accessed Nov 11, 2016).

(6) Overview of installed PV in 2013 - Solar Energy - Renewables International http://www.renewablesinternational.net/overview-of-installed-pv-in-2013/150/452/75985/ (accessed Nov 11, 2016).

(7) Qian, G.; Wang, Z. Y. *Chem. - An Asian J.* **2010**, *5* (5), 1006–1029.

(8) Nagy, Z.; Svetozarevic, B.; Jayathissa, P.; Begle, M.; Hofer, J.; Lydon, G.; Willmann, A.; Schlueter, A. *Front. Archit. Res.* **2016**, *5* (2), 143–156.

(9) Kojima, A.; Teshima, K.; Shirai, Y.; Miyasaka, T. *J. Am. Chem. Soc.* **2009**, *131* (17), 6050–6051.

(10) Saliba, M.; Matsui, T.; Seo, J.-Y.; Domanski, K.; Correa-Baena, J.-P.; Nazeeruddin, M. K.; Zakeeruddin, S. M.; Tress, W.; Abate, A.; Hagfeldt, A.; Grätzel, M. *Energy Environ. Sci.* **2016**, *9* (6), 1989–1997.

(11) Snaith, H. J. *J. Phys. Chem. Lett.* **2013**, *4* (21), 3623–3630.

(12) Major advance in solar cells made from cheap, easy-to-use perovskite: Physicists boost efficiency of material that holds promise as base for next-generation solar cells. https://www.sciencedaily.com/releases/2016/11/161108153323.htm (accessed Nov 11, 2016).

(13) Davies, J. *The Physics of Low-Dimensional Semiconductors*; 1998; Vol. 6.

(14) Roncali, J. *Chem. Rev.* **1997**, *97* (1), 173–206.

(15) Roncali, J. *Macromol. Rapid Commun.* **2007**, *28* (17), 1761–1775.

(16) van Mullekom, H. *Mater. Sci. Eng. R Reports* **2001**, *32* (1), 1–40.

(17) Watson, M. D.; Fechtenkötter, A.; Müllen, K. *Chem. Rev.* **2001**, *101* (5), 1267–1300.

(18) Li, C.; Liu, M.; Pschirer, N. G.; Baumgarten, M.; Müllen, K. *Chem. Rev.* **2010**, *110* (11), 6817–6855.

(19) Grimsdale, A. C.; Müllen, K. *Angew. Chem. Int. Ed. Engl.* **2005**, *44* (35), 5592–5629.

(20) Iyer, V. S.; Wehmeier, M.; Brand, J. D.; Keegstra, M. A.; Müllen, K. *Angew. Chemie Int. Ed. English* **1997**, *36* (15), 1604–1607.

(21) Simpson, C. D.; Brand, J. D.; Berresheim, A. J.; Przybilla, L.; Räder, H. J.; Müllen, K. *Chem. Eur. J.* **2002**, *8* (6), 1424–1429.

(22) Seyler, H.; Purushothaman, B.; Jones, D. J.; Holmes, A. B.; Wong, W. W. H. *Pure Appl. Chem.* **2012**, *84* (4), 1047–1067.

(23) Wang, Z.; Watson, M. D.; Wu, J.; Müllen, K. *Chem. Commun.* **2004**, No. 3, 336–337.

(24) Wu, J.; Watson, M. D.; Tchebotareva, N.; Wang, Z.; Müllen, K. *J. Org. Chem.* **2004**, *69* (24), 8194–8204.

(25) Herrmann, A.; Müllen, K. *Chem. Lett.* **2006**, *35* (9), 978–985.

(26) Weil, T.; Vosch, T.; Hofkens, J.; Peneva, K.; Müllen, K. *Angew. Chem. Int. Ed. Engl.* **2010**, *49* (48), 9068–9093.

(27) Lv, X.; Li, Z.; Li, S.; Luan, G.; Liang, D.; Tang, S.; Jin, R. *Int. J. Mol. Sci.* **2016**, *17* (5), 721.

(28) Bredas, J. L.; Silbey, R.; Boudreaux, D. S.; Chance, R. R. *J. Am. Chem. Soc.* **1983**, *105*, 6555–6559.

(29) Brocks, G.; Tol, A. *J. Phys. Chem.* **1996**, *100* (5), 1838–1846.

(30) Brocks, G.; Tol, A. *Synth. Met.* **1996**, *76* (1–3), 213–216.

(31) Griffiths, J.; Millar, V.; Bahra, G. S. *Dye. Pigment.* **1995**, *28* (4), 327–339.

(32) Kularatne, R. S.; Magurudeniya, H. D.; Sista, P.; Biewer, M. C.; Stefan, M. C. *J. Polym. Sci. Part A Polym. Chem.* **2013**, *51* (4), 743–768.

(33) Dufresne, S.; Bourgeaux, M.; Skene, W. G. *J. Mater. Chem.* **2007**, *17* (12), 1166–1177.

(34) Rocha, S. V.; Finney, N. S. *Org. Lett.* **2010**, *12* (11), 2598–2601.

(35) Kohl, C.; Becker, S.; Müllen, K. *Chem. Commun.* **2002**, *2002* (23), 2778–2779.

(36) Autschbach, J. *J. Chem. Educ.* **2007**, *84* (11), 1840–1845.

(37) König, W. *J. für Prakt. Chemie* **1926**, *112* (1), 1–36.

(38) McNaught, A. D.; Wilkinson., A. *IUPAC Compendium of Chemical Terminology, 2nd ed. (the "Gold Book")*; IUPAC: Oxford, 1997; Vol. 2.

(39) L. Strekowski. *Top. Heterocycl. Chem.* **2008**, *14*, 1–241.

(40) Lepkowicz, R. S.; Przhonska, O. V.; Hales, J. M.; Fu, J.; Hagan, D. J.; Van Stryland, E. W.; Bondar, M. V.; Slominsky, Y. L.; Kachkovski, A. D. *Chem. Phys.* **2004**, *305* (1–3), 259–270.

(41) Chowdhury, A.; Wachsmann-Hogiu, S.; Bangal, P. R.; Raheem, I.; Peteanu, L. A. *J. Phys. Chem. B* **2001**, *105* (48), 12196–12201.

(42) Wang, M.; Silva, G. L.; Armitage, B. A. *J. Am. Chem. Soc.* **2000**, *122* (41), 9977–9986.

(43) Würthner, F.; Kaiser, T. E.; Saha-Möller, C. R. *Angew. Chemie Int. Ed.* **2011**, *50* (15), 3376–3410.

(44) Steiger, R.; Pugin, R.; Heier, J. *Colloids Surfaces B Biointerfaces* **2009**, *74* (2), 484–491.

(45) Vogel, H. *Ber. Dtsch. Chem. Ges.* **1873**, *6* (2), 1302–1306.

(46) Strekowski, L.; Lipowska, M.; Patonay, G. *Synth. Commun.* **1992**, *22* (17), 2593–2598.

(47) Bricks, J. L.; Kachkovskii, A. D.; Slominskii, Y. L.; Gerasov, A. O.; Popov, S. V. *Dye. Pigment.* **2015**, *121*, 238–255.

(48) Lipowska, M.; Patonay, G.; Strekowski, L. *Synth. Commun.* **1993**, *23* (21), 3087–3094.

(49) Funabiki, K.; Mase, H.; Hibino, A.; Tanaka, N.; Mizuhata, N.; Sakuragi, Y.; Nakashima, A.; Yoshida, T.; Kubota, Y.; Matsui, M. *Energy Environ. Sci.* **2011**, *4* (6), 2186–2192.

(50) Guo, Z.; Park, S.; Yoon, J.; Shin, I. *Chem. Soc. Rev.* **2014**, *43* (1), 16–29.

(51) Shi, C.; Wu, J. B.; Pan, D. *J. Biomed. Opt.* **2016**, *21* (5), 50901.

(52) Snavely, B. B. *Opt. Eng.* **1970**, *8* (4), 119–125.

(53) Webster, F. Cyanine dye infrared lasers. 3831105, August 20, 1974.

(54) Dai, Z.; Qun, L.; Peng, B. *Dye. Pigment.* **1998**, *36* (3), 243–248.

(55) Park, J.; Viscardi, G.; Barolo, C.; Barbero, N. *Chim. Int. J. Chem.* **2013**, *67* (3), 129–135.

(56) Fan, B.; de Castro, F. A.; Heier, J.; Hany, R.; Nüesch, F. *Org. Electron.* **2010**, *11* (4), 583–588.

(57) Bouit, P. A.; Rauh, D.; Neugebauer, S.; Delgado, J. L.; Piazza, E. Di; Rigaut, S.; Maury, O.; Andraud, C.; Dyakonov, V.; Martin, N. *Org. Lett.* **2009**, *11* (11), 4806–4809.

(58) Makin, S. M.; Boiko, I. I.; Shavrygina, O. A. *Zhurnal Org. Khimii* **1977**, *13* (11), 2440–2443.

(59) Encinas, C.; Miltsov, S.; Otazo, E.; Rivera, L.; Puyol, M.; Alonso, J. *Dye. Pigment.* **2006**, *71* (1), 28–36.

(60) Li, Q.; Tan, J.; Peng, B.-X. *Molecules* **1997**, *2* (6), 91–98.

(61) Nagao, Y.; Sakai, T.; Kozawa, K.; Urano, T. *Dye. Pigment.* **2007**, *73* (3), 344–352.

(62) Salon, J.; Ska, E. W.; Raszkiewicz, A.; Patonay, G.; Strekowski, L. *J. Heterocycl. Chem.* **2005**, *42* (5), 959–961.

(63) Pardal, A.; Ramos, S.; Santos, P.; Reis, L.; Almeida, P. *Molecules* **2002**, *7*, 320–330.

(64) Bouit, P. A.; Aronica, C.; Toupet, L.; Guennic, B. Le; Andraud, C.; Maury, O. *J. Am. Chem. Soc.* **2010**, *132* (12), 4328–4335.

(65) Fischer, E.; Hess, O. *Ber. Dtsch. Chem. Ges.* **1884**, *17* (1), 559–568.

(66) Geiger, T.; Schoger, I.; Rentsch, D.; Véron, A. C.; Oswald, F.; Meyer, T.; Nüesch, F. *Int. J. Photoenergy* **2014**, *2014*, 1–10.

(67) Callant, P.; Gueuens, I.; Waumans, B.; Van Aert, H. Colour Laser Marking of Articles and Security Documents Precursors. WO2012076493A1, 2012.

(68) Fabian, J.; Nakazumi, H.; Matsuoka, M. *Chem. Rev.* **1992**, *92* (6), 1197–1226.

(69) Bunnett, J. F. *Acc. Chem. Res.* **1978**, *11* (1962), 413–420.

(70) Strekowski, L.; Lipowska, M.; Patonay, G. *J. Org. Chem.* **1992**, *57* (17), 4578–4580.

(71) Bunnett, J. F.; Scamehorn, R. G.; Traber, R. P. *J. Org. Chem.* **1976**, *41* (23), 3677–3682.

(72) Matichak, J. D.; Hales, J. M.; Barlow, S.; Perry, J. W.; Marder, S. R. *J. Phys. Chem. A* **2011**, *115* (11), 2160–2168.

(73) Loutfy, R. O.; Sharp, J. H. *Photogr. Sci. Eng.* **1976**, *20* (4), 165–174.

(74) Tyutyulkov, N. *Polymethine dyes: structure and properties*; St. Kliment Ohridski University Press, 1991.

(75) Heier, J.; Groenewold, J.; Huber, S.; Nüesch, F.; Hany, R. *Langmuir* **2008**, *24* (14), 7316–7322.

(76) Benmansour, H.; Castro, F. A.; Nagel, M.; Heier, J.; Hany, R.; Nüesch, F. *Chim. Int. J. Chem.* **2007**, *61* (12), 787–791.

(77) Bernards, D. A.; Flores-Torres, S.; Abruna, H. D.; Malliaras, G. G. *Science (80-.).* **2006**, *313* (5792), 1416–1419.

(78) Lacour, J.; Ginglinger, C. *Angew. Chem. Int. Ed. Engl.* **1997**, *36* (6), 608–610.

(79) Véron, A. C.; Zhang, H.; Linden, A.; Nüesch, F.; Heier, J.; Hany, R.; Geiger, T. *Org. Lett.* **2014**, *16* (4), 1044–1047.

(80) Jenatsch, S.; Wang, L.; Bulloni, M.; Véron, A. C.; Ruhstaller, B.; Altazin, S.; Nüesch, F.; Hany, R. *ACS Appl. Mater. Interfaces* **2016**, *8* (10), 6554–6562.

(81) Peng, Z.-H.; Qun, L.; Zhou, X.-F.; Carroll, S.; Geise, H. J.; Peng, B.; Dommisse, R.; Carleer, R. *J. Mater. Chem.* **1996**, *6* (4), 559–565.

(82) Zhang, Z.; Achilefu, S. *Org. Lett.* **2004**, *6* (12), 2067–2070.

(83) Lenhard, J. R.; Cameron, a. D. *J. Phys. Chem.* **1993**, *97* (19), 4916–4925.

(84) Kim, H.-S.; Lee, C.-R.; Im, J.-H.; Lee, K.-B.; Moehl, T.; Marchioro, A.; Moon, S.-J.; Humphry-Baker, R.; Yum, J.-H.; Moser, J. E.; Grätzel, M.; Park, N.-G. *Sci. Rep.* **2012**, *2* (7436), 591.

(85) Bredas, J.-L. *Mater. Horiz.* **2014**, *1* (1), 17–19.

(86) Geiger, T.; Benmansour, H.; Fan, B.; Hany, R.; Nüesch, F. *Macromol. Rapid Commun.* **2008**, *29* (8), 651–658.

(87) Waumans, B.; Callant, P. Colour laser marking of articles and security documents. WO2012171728 A1, 2012.

(88) Tong, L.; Bixian, P. *Dye. Pigment.* **1998**, *39* (4), 201–209.

(89) Makowski, B. T.; Valle, B.; Singer, K. D.; Weder, C. *J. Mater. Chem.* **2012**, *22* (7), 2848–2850.

(90) Henary, M.; Mojzych, M. In *Topics in Heterocyclic Chemistry*; 2008; Vol. 14, pp 221–238.

(91) Dust, M.; Neumann, P.; Hauser, P.; Wagenblast, G.; Benthack-Thoms, Heidi Barzynski, Helmut Kuppelmaier, H. Naphtholactam quadratic-acid dyes and optical registration materials containing them. DE3631843, 1988.

(92) Pascal, S.; Haefele, A.; Monnereau, C.; Charaf-eddin, A.; Jacquemin, D.; Guennic, B. Le; Andraud, C.; Maury, O. *J. Phys. Chem. A* **2014**, *118*, 4038–4047.

(93) Zhang, X.; Li, X.-D.; Ma, L.-X.; Zhang, B. *RSC Adv.* **2014**, *4* (104), 60342–60348.

(94) Günes, S.; Neugebauer, H.; Sariciftci, N. S. *Chem. Rev.* **2007**, *107* (4), 1324–1338.

(95) Wang, Q.; Xie, Y.; Soltani-Kordshuli, F.; Eslamian, M. *Renew. Sustain. Energy Rev.* **2016**, *56*, 347–361.

(96) Peumans, P.; Yakimov, A.; Forrest, S. R. *J. Appl. Phys.* **2003**, *93* (7), 3693–3723.

(97) Mishra, A.; Bäuerle, P. *Angew. Chem. Int. Ed. Engl.* **2012**, *51* (9), 2020–2067.

(98) Hudhomme, P. *EPJ Photovoltaics* **2013**, *4*, 40401.

(99) Kaltenbrunner, M.; White, M. S.; Głowacki, E. D.; Sekitani, T.; Someya, T.; Sariciftci, N. S.; Bauer, S. *Nat. Commun.* **2012**, *3*, 770.

(100) Steim, R.; Kogler, F. R.; Brabec, C. J. *J. Mater. Chem.* **2010**, *20* (13), 2499–2512.

(101) Liu, J.; Chen, S.; Qian, D.; Gautam, B.; Yang, G.; Zhao, J.; Bergqvist, J.; Zhang, F.; Ma, W.; Ade, H.; Inganäs, O.; Gundogdu, K.; Gao, F.; Yan, H. *Nat. Energy* **2016**, *1* (7), 16089.

(102) Zhao, J.; Li, Y.; Yang, G.; Jiang, K.; Lin, H.; Ade, H.; Ma, W.; Yan, H. *Nat. Energy* **2016**, *1* (2), 15027.

(103) Lunt, R. R.; Bulovic, V. *Appl. Phys. Lett.* **2011**, *98* (11), 113305.

(104) Colsmann, A.; Puetz, A.; Bauer, A.; Hanisch, J.; Ahlswede, E.; Lemmer, U. *Adv. Energy Mater.* **2011**, *1* (4), 599–603.

(105) Chen, C. C.; Dou, L.; Zhu, R.; Chung, C. H.; Song, T. Bin; Zheng, Y. B.; Hawks, S.; Li, G.; Weiss, P. S.; Yang, Y. *ACS Nano* **2012**, *6* (8), 7185–7190.

(106) Zhang, H.; Wicht, G.; Gretener, C.; Nagel, M.; Nüesch, F.; Romanyuk, Y.; Tisserant, J.-N.; Hany, R. *Sol. Energy Mater. Sol. Cells* **2013**, *118*, 157–164.

(107) Meng, F.; Chen, K.; Tian, H.; Zuppiroli, L.; Nuesch, F. *Appl. Phys. Lett.* **2003**, *82* (21), 3788–3790.

(108) Hany, R.; Fan, B.; de Castro, F. A.; Heier, J.; Kylberg, W.; Nüesch, F. *Prog. Photovoltaics Res. Appl.* **2011**, *19* (7), 851–857.

(109) Nüesch, F.; Faes, A.; Zuppiroli, L.; Meng, F.; Chen, K.; Tian, H. *J. Mater. Sci.* **2005**, *40* (6), 1353–1357.

(110) Rand, B. P.; Burk, D. P.; Forrest, S. R. *Phys. Rev. B - Condens. Matter Mater. Phys.* **2007**, *75* (11), 1–11.

(111) Dolores Perez, M.; Borek, C.; Forrest, S. R.; Thompson, M. E. *J. Am. Chem. Soc.* **2009**, *131* (26), 9281–9286.

(112) Maurano, A.; Hamilton, R.; Shuttle, C. G.; Ballantyne, A. M.; Nelson, J.; O'Regan, B.; Zhang, W.; McCulloch, I.; Azimi, H.; Morana, M.; Brabec, C. J.; Durrant, J. R. *Adv. Mater.* **2010**, *22* (44), 4987–4992.

(113) Suddard-Bangsund, J.; Traverse, C. J.; Young, M.; Patrick, T. J.; Zhao, Y.; Lunt, R. R. *Adv. Energy Mater.* **2016**, *6* (1), 1501659.

(114) Heier, J.; Peng, C.; Véron, A. C.; Hany, R.; Geiger, T.; Nüesch, F. A.; Vismara, M. V. G.; Graeff, C. F. O. *Proc. SPIE* **2014**, *9184*, 918408.

(115) Vismara, M. V. G. Estudo dos Processos de Geração e Transferência de Cargas em Corantes Cianinas, PhD Thesis, Universidade Estadual Paulista "Júlio de Mesquita Filho," 2015.

(116) Peng, C. Thin Film Solar Cells and Photophysical Processes Based on Cationic Cyanine Dyes, Master Thesis, Swiss Federal Institute of Technology Lausanne (EPFL), 2013.

(117) Xing, G.; Mathews, N.; Lim, S. S.; Yantara, N.; Liu, X.; Sabba, D.; Grätzel, M.; Mhaisalkar, S.; Sum, T. C. *Nat. Mater.* **2014**, *13* (5), 476–480.

(118) Tan, Z.-K.; Moghaddam, R. S.; Lai, M. L.; Docampo, P.; Higler, R.; Deschler, F.; Price, M.; Sadhanala, A.; Pazos, L. M.; Credgington, D.; Hanusch, F.; Bein, T.; Snaith, H. J.; Friend, R. H. *Nat. Nanotechnol.* **2014**, *9* (9), 687–692.

(119) Dong, R.; Fang, Y.; Chae, J.; Dai, J.; Xiao, Z.; Dong, Q.; Yuan, Y.; Centrone, A.; Zeng, X. C.; Huang, J. *Adv. Mater.* **2015**, *27* (11), 1912–1918.

(120) Yakunin, S.; Sytnyk, M.; Kriegner, D.; Shrestha, S.; Richter, M.; Matt, G. J.; Azimi, H.; Brabec, C. J.; Stangl, J.; Kovalenko, M. V; Heiss, W. *Nat. Photonics* **2015**, *9* (7), 444–449.

(121) Burschka, J.; Pellet, N.; Moon, S.-J.; Humphry-Baker, R.; Gao, P.; Nazeeruddin, M. K.; Grätzel, M. *Nature* **2013**, *499* (7458), 316–319.
(122) Park, N.-G.; Gratzel, M.; Miyasaka, T. *Organic-Inorganic Halide Perovskite Photovoltaics*; Springer International Publishing: Cham, 2016.
(123) Tilley, R. J. D. *Perovskites: Structure-Property Relationships*; John Wiley & Sons, Ltd: Chichester, UK, 2016.
(124) Mitzi, D. B. *Prog. Inorg. Chem.* **1999**, *48*, 1–121.
(125) Pellet, N.; Gao, P.; Gregori, G.; Yang, T. Y.; Nazeeruddin, M. K.; Maier, J.; Grätzel, M. *Angew. Chem. Int. Ed. Engl.* **2014**, *53* (12), 3151–3157.
(126) Jeon, N. J.; Noh, J. H.; Kim, Y. C.; Yang, W. S.; Ryu, S.; Seok, S. Il. *Nat. Mater.* **2014**, *13* (9), 897–903.
(127) Jeon, N. J.; Noh, J. H.; Yang, W. S.; Kim, Y. C.; Ryu, S.; Seo, J.; Seok, S. Il. *Nature* **2015**, *517* (7535), 476–480.
(128) Goldschmidt, V. M. *Naturwissenschaften* **1926**, *14* (21), 477–485.
(129) Saparov, B.; Mitzi, D. B. *Chem. Rev.* **2016**, *116* (7), 4558–4596.
(130) Snaith, H. J.; Abate, A.; Ball, J. M.; Eperon, G. E.; Leijtens, T.; Noel, N. K.; Stranks, S. D.; Wang, J. T.-W.; Wojciechowski, K.; Zhang, W. *J. Phys. Chem. Lett.* **2014**, *5* (9), 1511–1515.
(131) Jenatsch, S.; Geiger, T.; Heier, J.; Kirsch, C.; Nüesch, F.; Paracchino, A.; Rentsch, D.; Ruhstaller, B.; Véron, A. C.; Hany, R. *Sci. Technol. Adv. Mater.* **2015**, *16* (3), 35003.
(132) Xiao, M.; Huang, F.; Huang, W.; Dkhissi, Y.; Zhu, Y.; Etheridge, J.; Gray-Weale, A.; Bach, U.; Cheng, Y. B.; Spiccia, L. *Angew. Chem. Int. Ed. Engl.* **2014**, *53* (37), 9898–9903.
(133) Abate, A.; Paek, S.; Giordano, F.; Correa-Baena, J.-P.; Saliba, M.; Gao, P.; Matsui, T.; Ko, J.; Zakeeruddin, S. M.; Dahmen, K. H.; Hagfeldt, A.; Grätzel, M.; Nazeeruddin, M. K. *Energy Environ. Sci.* **2015**, *8* (10), 2946–2953.
(134) Saliba, M.; Orlandi, S.; Matsui, T.; Aghazada, S.; Cavazzini, M.; Correa-Baena, J.-P.; Gao, P.; Scopelliti, R.; Mosconi, E.; Dahmen, K.-H.; De Angelis, F.; Abate, A.; Hagfeldt, A.; Pozzi, G.; Graetzel, M.; Nazeeruddin, M. K. *Nat. Energy* **2016**, *1* (2), 15017.
(135) Chen, B.; Yang, M.; Priya, S.; Zhu, K. *J. Phys. Chem. Lett.* **2016**, *7* (5), 905–917.
(136) Sanchez, R. S.; Gonzalez-Pedro, V.; Lee, J.; Park, N.; Kang, Y. S.; Mora-Sero, I.; Bisquert, J. *J. Phys. Chem. Lett.* **2014**, *5* (13), 2357–2363.
(137) Shao, Y.; Xiao, Z.; Bi, C.; Yuan, Y.; Huang, J. *Nat. Commun.* **2014**, *5* (8), 5784.
(138) Eames, C.; Frost, J. M.; Barnes, P. R. F.; O'Regan, B. C.; Walsh, A.; Islam, M. S. *Nat. Commun.* **2015**, *6* (5), 7497.
(139) Haruyama, J.; Sodeyama, K.; Han, L.; Tateyama, Y. *J. Am. Chem. Soc.* **2015**, *137* (32), 10048–10051.
(140) Chen, H.-W.; Sakai, N.; Ikegami, M.; Miyasaka, T. *J. Phys. Chem. Lett.* **2015**, *6* (1), 164–169.
(141) Leijtens, T.; Eperon, G. E.; Pathak, S.; Abate, A.; Lee, M. M.; Snaith, H. J. *Nat. Commun.* **2013**, *4*, 2885.
(142) Fernandes, S. L.; Véron, A. C.; Neto, N. F. A.; Nüesch, F. A.; Dias da Silva, J. H.; Zaghete, M. A.; Graeff, C. F. de O. *Mater. Lett.* **2016**, *181*, 103–107.

(143) Makha, M.; Fernandes, S. L.; Jenatsch, S.; Offermans, T.; Schleuniger, J.; Tisserant, J.-N.; Véron, A. C.; Hany, R. *Sci. Technol. Adv. Mater.* **2016**, *17* (1), 260–266.

(144) Chujo, Y. *Curr. Opin. Solid State Mater. Sci.* **1996**, *1* (6), 806–811.

(145) Takada, J.; Awaji, H.; Koshioka, M.; Nakajima, A.; Nevin, W. A. *Appl. Phys. Lett.* **1992**, *61* (18), 2184.

(146) Nalwa, H. S. *Handbook of Organic-Inorganic Hybrid Materials and Nanocomposites*; American Scientific Publishers, 2003; Vol. 2.

(147) Kickelbick, G. *Hybrid Materials: Synthesis, Characterization, and Applications*; Kickelbick, G., Ed.; Wiley-VCH Verlag GmbH & Co. KGaA: Weinheim, Germany, 2007.

(148) Judeinstein, P.; Sanchez, C. *J. Mater. Chem.* **1996**, *6* (4), 511–525.

(149) Zhou, H.-C. "Joe"; Kitagawa, S. *Chem. Soc. Rev.* **2014**, *43* (16), 5415–5418.

(150) Hoffmann, F.; Cornelius, M.; Morell, J.; Fröba, M. *Angew. Chemie Int. Ed.* **2006**, *45* (20), 3216–3251.

(151) Chen, Q.; De Marco, N.; Yang, Y.; Song, T. Bin; Chen, C. C.; Zhao, H.; Hong, Z.; Zhou, H.; Yang, Y. *Nano Today* **2015**, *10* (3), 355–396.

(152) Bremner, C. A.; Simpson, M.; Harrison, W. T. A. *J. Am. Chem. Soc.* **2002**, *124* (37), 10960–10961.

(153) Ishihara, T. *J. Lumin.* **1994**, *60–61* (C), 269–274.

(154) Jacobsson, T. J.; Pazoki, M.; Hagfeldt, A.; Edvinsson, T. *J. Phys. Chem. C* **2015**, *119* (46), 25673–25683.

(155) Boix, P. P.; Agarwala, S.; Koh, T. M.; Mathews, N.; Mhaisalkar, S. G. *J. Phys. Chem. Lett.* **2015**, *6* (5), 898–907.

(156) Noel, N. K.; Stranks, S. D.; Abate, A.; Wehrenfennig, C.; Guarnera, S.; Haghighirad, A.-A.; Sadhanala, A.; Eperon, G. E.; Pathak, S. K.; Johnston, M. B.; Petrozza, A.; Herz, L. M.; Snaith, H. J. *Energy Environ. Sci.* **2014**, *7* (9), 3061.

(157) Stoumpos, C. C.; Malliakas, C. D.; Kanatzidis, M. G. *Inorg. Chem.* **2013**, *52* (15), 9019–9038.

(158) Ganose, A. M.; Savory, C. N.; Scanlon, D. O. *Chem. Commun.* **2017**, *53*, 20–44.

(159) Hailegnaw, B.; Kirmayer, S.; Edri, E.; Hodes, G.; Cahen, D. *J. Phys. Chem. Lett.* **2015**, *6* (9), 1543–1547.

(160) Glazer, A. M. *Acta Crystallogr. Sect. A* **1975**, *31* (6), 756–762.

(161) Glazer, A. M. *Acta Crystallogr. Sect. B Struct. Crystallogr. Cryst. Chem.* **1972**, *28* (11), 3384–3392.

(162) Kieslich, G.; Sun, S.; Cheetham, T. *Chem. Sci.* **2015**, *6* (6), 3430–3433.

(163) Shannon, R. D. *Acta Crystallogr. Sect. A* **1976**, *32* (5), 751–767.

(164) Mitzi, D. B. *J. Chem. Soc. Dalt. Trans.* **2001**, No. 1, 1–12.

(165) Haynes, W. M. *CRC Handbook of Chemistry and Physics, 95th Edition, 2014-2015*; 2014; Vol. 54.

(166) Wang, S.; Mitzi, D. B.; Feild, C. a.; Guloy, A. *J. Am. Chem. Soc.* **1995**, *117* (19), 5297–5302.

(167) Maughan, A. E.; Kurzman, J. A.; Neilson, J. R. *Inorg. Chem.* **2015**, *54* (1), 370–378.

(168) Zhao, H. R.; Li, D. P.; Ren, X. M.; Song, Y.; Jin, W. Q. *J. Am. Chem. Soc.* **2010**, *132* (1), 18–19.

(169) Chen, Y.; Yang, Z.; Guo, C.-X.; Ni, C.-Y.; Li, H.-X.; Ren, Z.-G.; Lang, J.-P. *CrystEngComm* **2011**, *13* (1), 243.

(170) Arend, H.; Huber, W.; Mischgofsky, F. H.; Richter-Van Leeuwen, G. K. *J. Cryst. Growth* **1978**, *43* (2), 213–223.

(171) Ishihara, T.; Takahashi, J.; Goto, T. *Phys. Rev. B* **1990**, *42* (17), 11099–11107.

(172) Billing, D. G.; Lemmerer, A. *New J. Chem.* **2008**, *32*, 1736–1746.

(173) Mitzi, D. B.; Chondroudis, K.; Kagan, C. R. *Inorg. Chem.* **1999**, *38* (26), 6246–6256.

(174) Kikuchi, K.; Takeoka, Y.; Rikukawa, M.; Sanui, K. *Colloids Surfaces A Physicochem. Eng. Asp.* **2005**, *257–258*, 199–202.

(175) Pedesseau, L.; Sapori, D.; Traoré, B.; Robles, R.; Fang, H.-H.; Loi, M. A.; Tsai, H.; Nie, W.; Blancon, J.-C.; Neukirch, A. J.; Tretiak, S.; Mohite, A. D.; Katan, C.; Even, J.; Kepenekian, M. *ACS Nano* **2016**, acsnano.6b05944.

(176) Kamminga, M. E.; Fang, H.-H.; Filip, M. R.; Giustino, F.; Baas, J.; Blake, G. R.; Loi, M. A.; Palstra, T. T. M. *Chem. Mater.* **2016**, *28* (13), 4554–4562.

(177) Era, M. *Chem. Lett.* **2003**, *32* (3), 272–273.

(178) Takeoka, Y.; Asai, K.; Rikukawa, M.; Sanui, K. *Chem. Commun.* **2001**, No. 24, 2592–2593.

(179) Era, M.; Maeda, K.; Tsutsui, T. *Chem. Phys. Lett.* **1998**, *296* (3–4), 417–420.

(180) Braun, M.; Tuffentsammer, W.; Wachtel, H.; Wolf, H. C. *Chem. Phys. Lett.* **1999**, *303* (1–2), 157–164.

(181) Braun, M.; Tuffentsammer, W.; Wachtel, H.; Wolf, H. C. *Chem. Phys. Lett.* **1999**, *307* (5–6), 373–378.

(182) Duan, H.-B.; Zhao, H.-R.; Ren, X.-M.; Zhou, H.; Tian, Z.-F.; Jin, W.-Q. *Dalt. Trans.* **2011**, *40* (8), 1672.

(183) Tang, Z.; Guloy, A. M. *J. Am. Chem. Soc.* **1999**, *121* (2), 452–453.

(184) Liu, J.-J.; Guan, Y.-F.; Jiao, C.; Lin, M.-J.; Huang, C.-C.; Dai, W. *Dalt. Trans.* **2015**, *44* (13), 5957–5960.

(185) Evans, H. A.; Lehner, A. J.; Labram, J. G.; Fabini, D. H.; Barreda, O.; Smock, S. R.; Wu, G.; Chabinyc, M. L.; Seshadri, R.; Wudl, F. *Chem. Mater.* **2016**, *28* (11), 3607–3611.

(186) Wang, G.-E.; Jiang, X.-M.; Zhang, M.-J.; Chen, H.-F.; Liu, B.-W.; Wang, M.-S.; Guo, G.-C. *CrystEngComm* **2013**, *15* (47), 10399.

(187) Papavassiliou, G. C. *Prog. Solid State Chem.* **1997**, *25* (3–4), 125–270.

(188) Miyata, A.; Mitioglu, A.; Plochocka, P.; Portugall, O.; Wang, J. T.-W.; Stranks, S. D.; Snaith, H. J.; Nicholas, R. J. *Nat. Phys.* **2015**, *11* (7), 582–587.

(189) Lin, Q.; Armin, A.; Nagiri, R. C. R.; Burn, P. L.; Meredith, P. *Nat Phot.* **2015**, *9* (2), 106–112.

(190) Hong, X.; Ishihara, T.; Nurmikko, A. V. *Phys. Rev. B* **1992**, *45* (12), 6961–6964.

(191) Elleuch, S.; Dammak, T.; Abid, Y.; Mlayah, A.; Boughzala, H. *J. Lumin.* **2010**, *130* (4), 531–535.

(192) Ishihara, T. In *Optical Properties of Low-Dimensional Materials*; Ogawa, T., Kanemitsu, Y., Eds.; World Scientific Publishing Co. Pte. Ltd., 1995.

(193) Tanaka, K.; Takahashi, T.; Kondo, T.; Umebayashi, T.; Asai, K.; Ema, K. *Phys. Rev. B - Condens. Matter Mater. Phys.* **2005**, *71* (4), 1–6.

(194) Hirasawa, M, Ishihara, T. Goto, T. *Journal of the Physical Society of Japan*. 1994, pp 3870–3879.

(195) Agranovich, V. M.; Gartstein, Y. N.; Litinskaya, M. *Chem. Rev.* **2011**, *111* (9), 5179–5214.

(196) Manser, J. S.; Christians, J. A.; Kamat, P. V. *Chem. Rev.* **2016**, *116* (21), 12956–13008.

(197) Kataoka, T.; Kondo, T.; Ito, R.; Sasaki, S.; Uchida, K.; Miura, N. *Phys. B Condens. Matter* **1993**, *184* (1–4), 132–136.

(198) Ema, K.; Inomata, M.; Kato, Y.; Kunugita, H.; Era, M. *Phys. Rev. Lett.* **2008**, *100* (25), 1–4.

(199) Blumstengel, S.; Sadofev, S.; Xu, C.; Puls, J.; Henneberger, F. *Phys. Rev. Lett.* **2006**, *97* (23), 8–11.

(200) Ishihara, T.; Hirasawa, M.; Goto, T. *Jpn. J. Appl. Phys.* **1995**, *34* (S1), 71.

(201) Umebayashi, T.; Asai, K.; Kondo, T.; Nakao, A. *Phys. Rev. B* **2003**, *67* (15), 155405.

(202) Savory, C. N.; Palgrave, R. G.; Bronstein, H.; Scanlon, D. O. *Sci. Rep.* **2016**, *6*, 20626.

(203) Kagan, C. R.; Mitzi, D. B.; Dimitrakopoulos, C. D. *Science (80-.).* **1999**, *286* (5441), 945–947.

(204) Chondroudis, K.; Mitzi, D. B. *Chem. Mater.* **1999**, *11* (11), 3028–3030.

(205) Mitzi, D. B.; Chondroudis, K.; Kagan, C. R. *IBM J. Res. Dev.* **2001**, *45* (1), 29–45.

(206) Dohner, E. R.; Hoke, E. T.; Karunadasa, H. I. *J. Am. Chem. Soc.* **2014**, *136* (5), 1718–1721.

(207) Vassilakopoulou, A.; Papadatos, D.; Koutselas, I. *Appl. Mater. Today* **2016**, *5*, 128–133.

(208) Smith, I. C.; Hoke, E. T.; Solis-Ibarra, D.; McGehee, M. D.; Karunadasa, H. I. *Angew. Chem. Int. Ed. Engl.* **2014**, *53* (42), 11232–11235.

(209) Ahmad, S.; Kanaujia, P. K.; Beeson, H. J.; Abate, A.; Deschler, F.; Credgington, D.; Steiner, U.; Prakash, G. V.; Baumberg, J. J. *ACS Appl. Mater. Interfaces* **2015**, *7* (45), 25227–25236.

(210) Zhou, J.; Chu, Y.; Huang, J. *ACS Appl. Mater. Interfaces* **2016**, acsami.6b09489.

(211) Kondo, T.; Iwamoto, S.; Hayase, S.; Tanaka, K.; Ishi, J.; Mizuno, M.; Ema, K.; Ito, R. *Solid State Commun.* **1998**, *105* (8), 503–506.

(212) Papagiannouli, I.; Maratou, E.; Koutselas, I.; Couris, S. *J. Phys. Chem. C* **2014**, *118* (5), 2766–2775.

(213) Jaffe, A.; Karunadasa, H. I. *Inorg. Chem.* **2014**, *53* (13), 6494–6496.

(214) Zhang, S.; Audebert, P.; Wei, Y.; Al Choueiry, A.; Lanty, G.; Bréhier, A.; Galmiche, L.; Clavier, G.; Boissière, C.; Lauret, J.-S.; Deleporte, E. *Materials (Basel).* **2010**, *3* (5), 3385–3406.

(215) Mitzi, D. B. *Chem. Mater.* **1996**, *8* (3), 791–800.

(216) Mitzi, D. . *J. Solid State Chem.* **1999**, *145* (2), 694–704.

(217) Mitzi, D. B.; Liang, K. *Chem. Mater.* **1997**, *9* (12), 2990–2995.

(218) Habibi, M.; Zabihi, F.; Ahmadian-Yazdi, M. R.; Eslamian, M. *Renew. Sustain. Energy Rev.* **2016**, *62*, 1012–1031.

(219) Zhang, S.; Lanty, G.; Lauret, J.-S.; Deleporte, E.; Audebert, P.; Galmiche, L. *Acta Mater.* **2009**, *57* (11), 3301–3309.

(220) Carnie, M. J.; Charbonneau, C.; Davies, M. L.; Troughton, J.; Watson, T. M.; Wojciechowski, K.; Snaith, H.; Worsley, D. A. *Chem. Commun.* **2013**, *49* (72), 7893–7895.

(221) Liang, K.; Mitzi, D. B.; Prikas, M. T. *Chem. Mater.* **1998**, *10* (1), 403–411.

(222) Schlipf, J.; Docampo, P.; Schaffer, C. J.; Körstgens, V.; Bießmann, L.; Hanusch, F.; Giesbrecht, N.; Bernstorff, S.; Bein, T.; Müller-Buschbaum, P. *J. Phys. Chem. Lett.* **2015**, *6* (7), 1265–1269.

(223) Shi, J.; Luo, Y.; Wei, H.; Luo, J.; Dong, J.; Lv, S.; Xiao, J.; Xu, Y.; Zhu, L.; Xu, X.; Wu, H.; Li, D.; Meng, Q. *ACS Appl. Mater. Interfaces* **2014**, *6* (12), 9711–9718.

(224) Ahmad, S.; Kanaujia, P. K.; Niu, W.; Baumberg, J. J.; Vijaya Prakash, G. *ACS Appl. Mater. Interfaces* **2014**, *6* (13), 10238–10247.

(225) Pradeesh, K.; Baumberg, J. J.; Prakash, G. V. *Appl. Phys. Lett.* **2009**, *95* (3), 33309.

(226) Chon, U.; Jang, H. M.; Kim, M. G.; Chang, C. H. *Phys Rev Lett* **2002**, *89* (8), 87601.

(227) Liu, M.; Johnston, M. B.; Snaith, H. J. *Nature* **2013**, *501* (7467), 395–398.

(228) Fu, F.; Kranz, L.; Yoon, S.; Löckinger, J.; Jäger, T.; Perrenoud, J.; Feurer, T.; Gretener, C.; Buecheler, S.; Tiwari, A. N. *Phys. status solidi* **2015**, *212* (12), 2708–2717.

(229) Chen, Q.; Zhou, H.; Hong, Z.; Luo, S.; Duan, H.-S.; Wang, H.-H.; Liu, Y.; Li, G.; Yang, Y. *J. Am. Chem. Soc.* **2014**, *136* (2), 622–625.

(230) Era, M.; Hattori, T.; Taira, T.; Tsutsui, T. *Chem. Mater.* **1997**, *9* (1), 8–10.

(231) Mitchell, R. S. *Zeitschrift für Krist.* **1959**, *111* (1–6), 372–384.

(232) Scherrer, P. In *Nachrichten von der Gesellschaft der Wissenschaften zu Göttingen, Mathematisch-Physikalische Klasse*; 1918; Vol. 2, pp 98–100.

(233) Patterson, A. L. *Phys. Rev.* **1939**, *56* (10), 978–982.

(234) Langford, J. I.; Wilson, A. J. C. *J. Appl. Crystallogr.* **1978**, *11* (2), 102–113.

(235) Beckmann, P. A. *Cryst. Res. Technol.* **2010**, *45* (5), 455–460.

(236) Wakamiya, A.; Endo, M.; Sasamori, T.; Tokitoh, N.; Ogomi, Y.; Hayase, S.; Murata, Y. *Chem. Lett.* **2014**, *43*, 711–713.

(237) Organic Field Effect Transistors (OFET) - Fraunhofer IPMS http://www.ipms.fraunhofer.de/en/research-development/end-of-line-test-substrates/ofet.html (accessed Nov 1, 2016).

(238) Cosseddu, P.; Bonfiglio, A. *Thin Solid Films* **2007**, *515* (19), 7551–7555.

(239) Rentsch, S.; Yang, J. P.; Paa, W.; Birckner, E.; Schiedt, J.; Weinkauf, R. *Phys. Chem. Chem. Phys.* **1999**, *1* (8), 1707–1714.

(240) Abate, A.; Saliba, M.; Hollman, D. J.; Stranks, S. D.; Wojciechowski, K.; Avolio, R.; Grancini, G.; Petrozza, A.; Snaith, H. J. *Nano Lett.* **2014**, *14* (6), 3247–3254.

(241) E.N. Maslen, A.G. Fox, M.A. O'Keefe, in 'International Tables for Crystallography', Ed. A.J.C. Wilson, Kluwer Academic Publishers, Dordrecht, 1992, Vol. C, Table 6.1.1.1, pp. 477-486; b) D.C. Creagh, W.J. McAuley, *ibid*. Table 4.2.6.8, pp. 219-222; c) D.C. Creagh, J.H. Hubbell, *ibid*. Table 4.2.4.3, pp. 200-206.

(242) Fulmer, G. R.; Miller, A. J. M.; Sherden, N. H.; Gottlieb, H. E.; Nudelman, A.; Stoltz, B. M.; Bercaw, J. E.; Goldberg, K. I. *Organometallics* **2010**, *29* (9), 2176–2179.

(243) Descalzo, A. B.; Rurack, K. *Chem. Eur. J.* **2009**, *15* (13), 3173–3185.

(244) Shrotriya, V.; Li, G.; Yao, Y.; Chu, C.-W.; Yang, Y. *Appl. Phys. Lett.* **2006**, *88* (7), 73508.

(245) Etgar, L.; Gao, P.; Xue, Z.; Peng, Q.; Chandiran, A. K.; Liu, B.; Nazeeruddin, M. K.; Grätzel, M. *J. Am. Chem. Soc.* **2012**, *134*, 17396–17399.

(246) Siidra, O. I.; Zenko, D. Y.; Suknotova, A. N.; Krivovichev, S. V. *Mineral. Mag.* **2013**, *77* (8), 3239–3248.

(247) Császár, A. G.; Czakó, G.; Furtenbacher, T.; Tennyson, J.; Szalay, V.; Shirin, S. V.; Zobov, N. F.; Polyansky, O. L. *J. Chem. Phys.* **2005**, *122* (21), 214305.

(248) CrysAlisPro, Version 1.171.38.43c, Rigaku Oxford Diffraction: Abingdon, Oxfordshire, England 2015.

(249) Coppens, P.; Leiserowitz, L.; Rabinovich, D. *Acta Crystallogr.* **1965**, *18* (6), 1035–1038.

(250) Sheldrick, G. M. *Acta Crystallogr. Sect. A Found. Adv.* **2015**, *71* (1), 3–8.

(251) Parsons, S.; Flack, H. D.; Wagner, T. *Acta Crystallogr. Sect. B Struct. Sci. Cryst. Eng. Mater.* **2013**, *69* (3), 249–259.

(252) Stewart, R. F.; Davidson, E. R.; Simpson, W. T. *J. Chem. Phys.* **1965**, *42* (9), 3175–3187.

(253) Ibers, J. A.; Hamilton, W. C. *Acta Crystallogr.* **1964**, *17* (6), 781–782.

(254) Sheldrick, G. M. *Acta Crystallogr. Sect. C Struct. Chem.* **2015**, *71* (1), 3–8.

(255) C.K. Johnson. ORTEPII, Report ORNL-5138, Oak Ridge National Laboratory: Oak Ridge, Tennessee 1976.

(256) CrysAlisPro, Version 1.171.36.28, Agilent Technologies: Yarnton, Oxfordshire, England 2013.

(257) Sheldrick, G. M. *Acta Crystallogr. Sect. A* **2008**, *64* (1), 112–122.

(258) Flack, H. D.; Bernardinelli, G. *Acta Crystallogr. Sect. A* **1999**, *55* (5), 908–915.

(259) Flack, H. D.; Bernardinelli, G. *J. Appl. Crystallogr.* **2000**, *33* (4), 1143–1148.

(260) van der Sluis, P.; Spek, A. L. *Acta Crystallogr. Sect. A* **1990**, *46* (3), 194–201.

(261) Spek, A. L. PLATON, Program for the Analysis of Molecular Geometry, University of Utrecht: The Netherlands 2009.

(262) Spek, A. L. *Acta Crystallogr. Sect. C Struct. Chem.* **2015**, *71* (1), 9–18.

(263) Deibel, C.; Dyakonov, V. *Reports Prog. Phys.* **2010**, *73* (9), 96401.

7 EXPERIMENTAL PROCEDURES AND ANALYTICAL DATA

7.1 Synthesis and Characterization of Cyanine Dyes

7.1.1 General

All chemicals and solvents were purchased from commercial sources (*Aldrich, VWR, FEW* or *ABCR*) and used as received, unless otherwise stated. Reactions were carried out under inert atmosphere (argon) in oven-dried glassware. TLC chromatography was performed using *Macherey Nagel POLYGRAM® SIL G/UV254* silica plates; the developed plates were visualized by exposure to UV-light (254 nm) or by staining with anisaldehyde reagent. ^{1}H-NMR spectra were recorded on a *Bruker AV-400* spectrometer at 400 MHz. Chemical shifts (δ) are reported in ppm (parts per million) with the solvent residual signal (2.50 for DMSO-d$_6$, 2.05 for acetone-d$_6$, 7.26 for CDCl$_3$)[242] as the reference. *J* coupling constants are given in Hz. Multiplicities are reported as *s* (singlet), *bs* (broad singlet), *d* (doublet), *t* (triplet), *q* (quartet), *quint* (quintet), *sext* (sextet), *m* (multiplet) or *td* (triplet of doublets). ^{1}H–decoupled–^{13}C–NMR spectra were recorded on a *Bruker AV-400* spectrometer at 100 MHz. Chemical shifts (*δ*) are reported in ppm with the solvent residual signal as the reference (39.52 for DMSO-d$_6$, 29.84 for acetone-d$_6$, 77.16 for CDCl$_3$)[242]. Correlations of ^{1}H–NMR and ^{13}C–NMR signals with the compound structure were derived from 2D–NMR experiments (HSQC, HMBC and COSY). High resolution electrospray ionization mass spectra (HR–ESI–MS) were measured on a *Bruker maXis* UHPLC-HR-MS instrument by the MS–service team of the University of Zurich; masses are reported as m/z (mass to charge ratio). Elemental analysis data were obtained by the micro-laboratory of ETH Zurich. The determination of the elements C, H, N and O was carried out with instruments of the company *LECO*; halogens (Cl, I, F) were determined according to the Schöninger method; determination of P was achieved in a pressure digestion device and photometrical quantification. IR spectroscopy was carried out on a *Bruker TENSOR 27* FT-IR spectrometer, relative peak intensities are noted as *s* (strong), *m* (medium) or *w* (weak). Melting points (m.p.) and decomposition points (d.p.) were obtained from differential scanning calorimetry (*Differential Scanning Calorimeter DSC 8000* by *Perkin Elmer*) and thermogravimetric analysis (*TG 209 F1* by *NETZSCH*).

7.1.2 Synthesis

7.1.2.1 Precursors

Structures of starting materials **S1-S8** are given in **Scheme 7.1**. Indolium iodide precursors **S1** and **S2** were prepared according to literature procedures.[63] Lactam **S3** was purchased from *TCI Chemicals*. Chloro-substituted dianil salt **S4** was purchased from ORGANICA Feinchemie GmbH Wolfen; phenyl–substituted dianil salt **S5** was prepared according to the literature procedure.[62] Δ-TRISPHAT tetrabutylammonium salt **S7** and 1,3–dimethylbarbituric acid **S8** were purchased from Sigma-Aldrich.

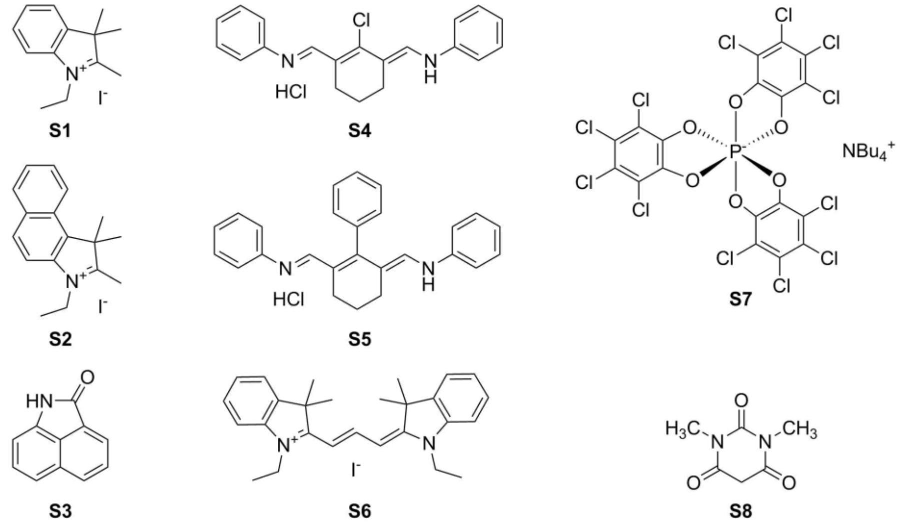

Scheme 7.1: Precursors **S1**–**S8** used for the synthesis and counterion exchange.

7.1.2.2 Benz[cd]indolium Heterocycle

2-Methyl-1-(1-methylbutyl)-benz[*cd*]indolium iodide (12a)

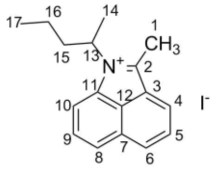

Chemical Formula: $C_{17}H_{20}IN$
Molecular Weight: 365.26

1st step: 1-(1-Methylbutyl)- (1*H*)-benz[*cd*]indol-2-one

S3 (5.03 g, 29.50 mmol) was dissolved in sulfolane (20 ml) and KI (0.98 g, 5.90 mmol) and DMAP (0.48 g, 3.98 mmol) were added to the solution. Then a first portion of KOH (0.99 g, 17.70 mmol, 0.60 eq) and 2-bromopentane (1.90 ml, 14.75 mmol, 0.50 eq) was added. The reaction mixture was stirred at 70–75 °C for 5 h, and every hour another portion of KOH (0.99 g, 17.70 mmol, 0.60 eq) and 2-bromopentane (1.90 ml, 14.75 mmol, 0.50 eq) was added (in total five portions, 3.00 eq KOH and 2.50 eq 2-bromopentane). After cooling to room temperature the reaction mixture was diluted with MTBE (400 ml) and transferred to a separating funnel. The MTBE soln. was washed with water (3x), the water phase was extracted with fresh MTBE (3x). The combined ether phases were washed consecutively with a solution of 15% NaCl, 15% NaCl containing 4% HCl, 15% NaCl containing 1% $NaHCO_3$ and 25% NaCl. The ether phase was dried over Na_2SO_4 and concentrated to give 6.88 g of 1-(1-Methylbutyl)-(1*H*)-benz[*cd*]indol-2-one as a yellow solid. The product was used for the next step without further purification.

2nd step: 2-Methyl-1-(1-methylbutyl)-benz[*cd*]indolium iodide

Crude 1-(1-methylbutyl)-(1*H*)-benz[*cd*]indol-2-one (6.70 g, 28.00 mmol) was dissolved in dry THF (20 ml) under argon. A solution of MeMgCl (12 ml, 3.0 M in THF) was added drop-wise over a period of 15 minutes. After complete addition, the solution was heated to 55 °C for 60 min. After cooling to room temperature the reaction mixture was poured slowly into 100 ml of an ice/water mixture containing 12 ml of 32% HCl. The resulting suspension was filtered and the clear filtrate was added to a stirred solution of KI (9.30 g, 56.00 mmol) in water (100 ml). The formed precipitate was filtered, washed with water and EtOAc and dried under vacuum to obtain **12a** (7.65 g, 20.90 mmol, 71% yield over two steps) as a red solid. d. p. < 100 °C, λ_{max} (EtOH) = 333, 358, 374 nm.

^{1}H-NMR ($CDCl_3$): 9.04 (*d*, *J*=7.2, 1H, H-4); 8.63 (*d*, *J*=8.0, 1H, H-6); 8.37 (*d*, *J*=7.5, 1H, H-10); 8.29 (*d*, *J*=8.2, 1H, H-8); 8.10 (*t*, *J*=7.7, 1H, H-5); 7.92 (*t*, *J*=7.9, 1H, H-9); 5.26 (*sext*, *J*=7.3, 1H, H-13); 3.56 (*s*, 3H, H-1); 2.28-2.16 (*m*, 2H, H-15); 1.96 (*d*, *J*=6.8, 3H, H-14); 1.55-1.46 (*m*, 1H, H-16); 1.29-1.20 (*m*, 1H, H-16); 1.96 (*t*, *J*=7.3, 3H, H-17). ^{13}C-NMR ($CDCl_3$): 171.3 (C-2), 139.4 (C-6), 137.0 (C-11), 136.4 (C-4), 131.4 (C-8), 131.3 (C-5), 129.8 (C-9), 129.08 (C-3 or C-7), 129.05 (C-3 or C-7), 123.4 (C-12), 122.8 (C-10), 58.1 (C-13), 38.8 (C-15), 21.7 (C-14), 20.0 (C-16), 17.5 (C-1), 13.7 (C-17).

HR-MS (pos. ESI): m/z for [$C_{17}H_{20}N^+$]; calculated 238.15903, found 238.15863. IR (cm^{-1}): 3377*w*, 2961*w*, 2932*w*, 2863*w*, 2724*w*, 1697*w*, 1637*w*, 1584*w*, 1498*s*, 1478*m*, 1467*m*, 1366*m*, 1354*s*, 1341*s*, 1226*m*, 1215*m*, 1187*m*, 1147*m*, 1127*w*, 1053*w*, 1041*m*, 999*w*, 887*w*, 867*w*, 826*s*, 805*w*, 782*w*, 756*s*, 668*w*, 632*w*, 620*w*.

2-Methyl-1-octyl-benz[*cd*]indolium iodide (12b)

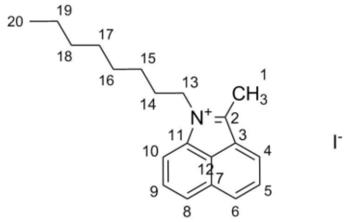

Chemical Formula: $C_{20}H_{26}IN$
Molecular Weight: 407.34

1st step: 1-Octyl- (1*H*)-benz[*cd*]indol-2-one

S3 (5.1 g, 30.15 mmol, 1.00 eq) was dissolved in sulfolane (20 ml) and KI (0.99 g, 6.02 mmol, 0.2eq) and DMAP (0.50 g, 4.06 mmol, 0.14 eq) were added to the solution. Then a first portion of KOH (1.01 g, 18.06 mmol, 0.60 eq) and 1-bromooctane (2.60 ml, 15.02 mmol, 0.50 eq) was added. The reaction mixture was stirred at 70–75 °C for 3 h, whereas every hour another portion of KOH (1.01 g, 18.06 mmol, 0.60 eq) and 1-bromooctane (2.60 ml, 15.02 mmol, 0.50 eq) was added. In total, three portions (1.80 eq KOH and 1.50 eq 1-bromooctane) were added.

After cooling to room temperature the reaction mixture was diluted with EtOAc (400 ml) and transferred to a separating funnel. The EtOAc soln. was washed with water, then the water phase was extracted 3x with fresh EtOAc. The combined organic phases were washed consecutively with a solution of 15% NaCl, 15% NaCl containing 4% HCl, 15% NaCl containing 1% $NaHCO_3$ and finally a solution of 25% NaCl. The organic phase was dried over Na_2SO_4 and concentrated to give 11.17 g of crude intermediate product as a yellow solid. The crude product was used for the next step without further purification.

2nd step: 2-Methyl-1-octyl-benz[*cd*]indolium iodide

Crude 1-octyl-(1*H*)-benz[*cd*]indol-2-one (9.23 g, 32.80 mmol, 1.00 eq) was dissolved in dry THF (30 ml) under argon in a dried 2-neck flask. A solution of MeMgCl (13.9 ml, 3.0 M in THF, 1.28 eq) was added drop-wise over a period of 10 minutes. After complete addition, the brown solution was heated to 55 °C for 60 min. After cooling to room temperature the reaction mixture was poured slowly into 150 ml of an ice/water mixture containing 12.3 ml of 32% HCl. This biphasic mixture was distilled on a rotary evaporator to remove THF. The remaining aqueous mixture was filtered and the clear filtrate was added to a stirred solution of KI (10.80 g, 65.50 mmol, 2.00 eq) in water (ca. 150 ml). The formed precipitate was filtered, washed with water and EtOAc and dried under vacuum to obtain 2-Methyl-1-octyl-benz[*cd*]indolium iodide (4.60 g, 11.29 mmol, 45% yield over two steps) as a red solid. m.p. 157 °C, d.p. 216 °C; λ_{max} (EtOH) = 332, 359, 373 nm.

^{1}H-NMR (CDCl$_3$): 8.95 (*d*, *J*=7.2, 1H, H-4); 8.59 (*d*, *J*=8.0, 1H, H-6); 8.37 (*d*, *J*=7.4, 1H, H-10); 8.26 (*d*, *J*=8.2, 1H, H-8); 8.03 (*t*, *J*=7.7, 1H, H-5); 7.87 (*t*, *J*=7.8, 1H, H-9); 4.83 (*t*, *J*=7.5, 2H, H-13); 3.44 (*s*, 3H, H-1); 2.00 (*m*, 2H, H-14); 1.46 (*m*, 2H, H-15); 1.31 (*m*, 2H, H-15); 1.25-1.13 (*m*, 6H, H-17, H-18, H-19); 0.80 (*t*, *J*=6.9, 3H, H-20). ^{13}C-NMR (CDCl$_3$): 170.2 (C-2), 139.2 (C-6), 138.4 (C-11), 135.9 (C-4), 131.5 (C-8), 131.1 (C-5), 129.8 (C-9), 128.9 (C-3), 128.7 (C-7), 122.6 (C-12), 121.4 (C-10), 48.7 (C-13), 31.5 (C-18), 30.4 (C-14), 29.0 (C-16), 28.9 (C-17), 26.9 (C-15), 22.4 (C-19), 16.3 (C-1), 13.9 (C-20). HR-MS (pos. ESI): m/z for [$C_{20}H_{26}N^+$]; calculated 280.20598, found 280.20549. IR (cm^{-1}): 3038*w*, 2989*w*, 2952*w*, 2921*m*, 2850*m*, 2726*w*, 1697*w*, 1640*w*, 1629*w*, 1585*w*, 1507*m*, 1498*m*, 1480*w*, 1467*w*, 1456*w*, 1433*m*, 1373*m*, 1342*s*, 1221*m*, 1196*w*, 1183*w*, 1145*m*, 1105*w*, 1008*w*, 998*w*, 952*w*, 924*w*, 891*w*, 879*w*, 831*m*, 825*m*, 804*w*, 784*w*, 768*w*, 752*s*, 725*w*, 672*w*, 631*w*, 612*w*.

7.1.2.3 Heptamethine Dyes: Knoevenagel Coupling

For Knoevenagel coupling to obtain the iodide salts of heptamethine dyes **8-Cl**, **8-Ph**, **9-Cl** and **9-Ph** the following general procedure was used. Heterocycle precursor **S1** or **S2** (2.1 eq), dianil precursor **S4** or **S5** (1.0 eq) and NaOAc (2.3 eq; dried in high vacuum at 80 °C for 12 h) were weighed in a 1–neck flask equipped with a reflux condenser under argon. EtOH (anhydrous) was added to obtain a solution with the following concentration of the dianil precursor: ≈ 55 mM (for the chloro-dianil **S4**) or ≈ 30 mM (for the phenyl-dianil **S5**). The solution was heated to reflux (80 °C) under argon for 16h, then let cool to room temperature and placed in a refridgerator (4 °C) for 2 days. After filtration and washing with cold EtOH, the iodide salts of the title compounds were obtained as crystalline solids.

Counterion exchange to from I^- to PF_6^- was performed by precipitation in aqueous solutions of $NaPF_6$ or KPF_6.

2-[2-[2-chloro-3-[2-(1-ethyl-1,3-dihydro-3,3-dimethyl-2*H*-indol-2-ylidene)ethylidene]-1-cyclohexen-1-yl]ethenyl]-1-ethyl-3,3-dimethyl-3*H*-indolium iodide (8–Cl)

Using the general procedure described above, **S1** (7.25 g, 23.00 mmol) **S4** (3.94 g, 10.95 mmol) and NaOAc (2.07 g, 25.19 mmol) in 200 mL EtOH gave the iodide salt of **8-Cl** as green cubic crystals (4.36 g, 62% yield). Counterion exchange to PF_6^- and analytical data of the PF_6^- salt are found in chapter 7.1.2.4 for **Cy7P**.

1-ethyl-2-[2-[3-[2-(1-ethyl-1,3-dihydro-3,3-dimethyl-2*H*-indol-2-ylidene) ethylidene]-2-phenyl-1-cyclohexen-1-yl]ethenyl]-3,3-dimethyl-3*H*-indolium hexafluorophosphate

(8–Ph)

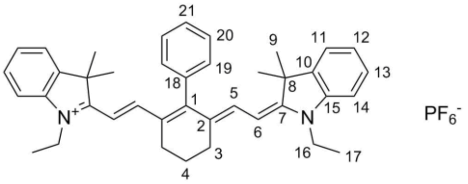

Chemical Formula: $C_{40}H_{45}F_6N_2P$
Molecular Weight: 698.78

Using the general procedure described above, **S1** (1.52 g, 4.82 mmol) **S5** (0.97 g, 2.42 mmol) and NaOAc (0.40 g, 4.84 mmol) in 70 mL EtOH gave the iodide salt of **8-Ph** as a crystalline green powder (1.50 g, 89% yield).

For the counterion exchange to PF_6^- the iodide salt of **8-Ph** (1.50 g, 2.204 mmol, 1 eq) was dissolved in MeOH (80 ml) and added dropwise to a solution of KPF_6 (16.22 g, 88.142 mmol, 40 eq) in water (150 ml). The resulting suspension was stirred for 10 min and filtered over celite. The precipitate was then treated as described for **Cy7P** and recrystallized from MeOH to give the PF_6^- salt of **8-Ph** as green crystals (0.97 g, 63%). d.p. 290 °C.

^{1}H-NMR (acetone-d$_6$): 7.67 (*m*, 2H, H-20); 7.63 (*m*, 1H, H-21); 7.45 (*d*, *J*=7.4, 2H, H-11); 7.34–7.29 (*m*, 2H, H-14, H-19); 7.32 (*d*, *J*=14.1; 2H, H-5); 7.22 (*td*, *J*=7.4, 0.9; 2H, H-12); 6.31 (*d*, *J*=14.1, 2H, H-6); 4.23 (*q*, *J*=7.2, 4H, H-16); 2.74 (*t*, *J*=6.2, 4H, H-3); 2.01 (*m*, 2H, H-4); 1.36 (*t*, *J*=7.2, 6H, H-17); 1.22 (*s*, 12H, H-9). Signal for H-5 appears within multiplett 7.34–7.29. Chem. shift determined from COSY. ^{13}C-NMR (acetone-d$_6$): 129.6 (C-20), 172.4 (C-7), 163.3 (C-1), 149.1 (C-5), 143.0 (C-15), 141.9 (C-10), 140.0 (C-18), 132.0 (C-2), 130.4 (C-19), 129.5 (C-13), 129.1 (C-21), 125.6 (C-12), 123.2 (C-11), 111.4 (C-14), 100.4 (C-6), 49.5 (C-8), 39.7 (C-16), 27.7 (C-9), 25.3 (C-3), 22.1 (C-4), 12.4 (C-17).

HR-MS (pos. ESI): m/z for [$C_{40}H_{45}N_2^+$]; calculated 553.35773, found 553.35759. Elemental Analysis: Calculated: [C] 68.75% [H] 6.49% [N] 4.01% [F] 16.31% [P] 4.43%; Found: [C] 68.81% [H] 6.42% [N] 3.93% [F] 16.21% [P] 4.52%. IR (cm^{-1}): 3052*w*, 2974*w*, 2952*w*, 2930*w*, 2871*w*, 2847*w*, 1539*s*, 1511*m*, 1482*m*, 1467*w*, 1452*m*, 1444*m*, 1435*m*, 1398*m*, 1366*s*, 1337*m*, 1288*w*, 1250*m*, 1229*m*, 1210*m*, 1179*m*, 1167*m*, 1151*s*, 1125*w*, 1099*s*, 1074*s*, 1058*s*, 1037*s*, 1018*s*, 937*m*, 921*m*, 870*w*, 824*s*, 805*w*, 776*w*, 756*s*, 715*m*, 703*m*, 672*m*, 631*w*, 612*w*.

2-[2-[2-chloro-3-[2-(3-ethyl-1,3-dihydro-1,1-dimethyl-2*H*-benz[*e*]indol-2-ylidene) ethylidene]-1-cyclohexen-1-yl]ethenyl]-3-ethyl-1,1-dimethyl-1*H*-benz[*e*]indolium hexafluorophosphate

(9–Cl)

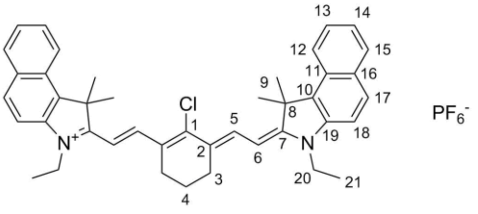

Chemical Formula: $C_{42}H_{44}ClF_6N_2P$
Molecular Weight: 757.24

Using the general procedure described above, **S2** (4.14 g, 11.4 mmol) **S4** (1.94 g, 5.4 mmol) and NaOAc (1.02 g, 12.4 mmol) in 100 mL EtOH gave the iodide salt of **9-Cl** as shiny orange crystals (1.63 g, 41% yield) after recrystallization from methanol.

For the counterion exchange to PF_6^- the iodide salt of **9-Cl** (1.00 g, 1.353 mmol, 1 eq) was dissolved in MeOH (60 ml) and added dropwise to a solution of $NaPF_6$ (11.36 g, 67.643 mmol, 50 eq) in water (25 ml). The precipitate was then treated as described for **Cy7P** and recrystallized from MeOH to give the PF_6^-salt of **9-Cl** as green crystals (0.74 g, 72%). d.p. 266 °C.

^{1}H-NMR (DMSO-d$_6$): 8.38 (*d*, *J*=14.2, 2H, H-5); 8.30 (*d*, *J*=8.5, 2H, H-12); 8.11 (*d*, *J*=8.8, 2H, H-17); 8.08 (*d*, *J*=8.1, 2H, H-15); 7.78 (*d*, *J*=8.9, 2H, H-18); 7.67 (*dd*, *J*=7.81, 7.68, 2H, H-13); 7.53 (*dd*, *J*=7.64, 7.62, 2H, H-14); 6.37 (*d*, *J*=14.3, 2H, H-6); 4.39 (*q*, *J*=7.0, 4H, H-20); 2.77 (*t*, *J*=5.9, 4H, H-3); 1.96 (*s*, 12H, H-9); 1.90 (*quint*, *J*=5.8, 2H, H-4); 1.38 (*t*, *J*=7.1, 6H, H-21).

^{13}C-NMR (DMSO-d$_6$): 173.0 (C-7), 147.4 (C-1), 142.1 (C-5), 139.4 (C-19), 133.7 (C-10), 131.5 (C-16), 130.5 (C-17), 129.9 (C-15); 127.8 (C-13), 127.5 (C-11), 126.1 (C-2), 125.0 (C-14), 122.3 (C-12), 111.6 (C-18), 100.9 (C-6), 50.7 (C-8), 39.2 (C-20), 26.9 (C-9), 25.9 (C-3), 20.4 (C-4), 12.5 (C-21). Signal for C-20 is hidden under solvent peak. Chem. shift determined from HSQC. HR-MS (pos. ESI): m/z for [$C_{42}H_{44}ClN_2^+$]; calculated 611.31875, found 611.31841. HR-MS (neg. ESI): m/z for [F_6P^-]; calculated 144.96473, found 144.96500. Elemental Analysis: Calculated: [C] 66.62% [H] 5.86% [N] 3.70% [F] 15.05% [P] 4.09% [Cl] 4.68; Found: [C] 66.62% [H] 5.97% [N] 3.79% [F] 14.89% [P] 3.89% [Cl] 4.87. IR (cm^{-1}): 2974*w*, 2932*w*, 1624*w*, 1584*w*, 1546*s*, 1520*w*, 1502*m*, 1478*w*, 1466*w*, 1431*m*, 1415*m*, 1387*w*, 1352*w*, 1286*w*, 1269*m*, 1231*m*, 1180*m*, 1158*s*, 1124*m*, 1091*s*, 1051*m*, 1005*m*, 963*m*, 926*m*, 910*m*, 874*m*, 854*s*, 827*s*, 811*s*, 785*m*, 737*m*, 717*m*, 684*w*, 670*m*, 633*w*, 615*w*.

3-ethyl-2-[2-[3-[2-(3-ethyl-1,3-dihydro-1,1-dimethyl-2*H*-benz[*e*]indol-2-ylidene) ethylidene]-2-phenyl-1-cyclohexen-1-yl]ethenyl]-1,1-dimethyl-1*H*-Benz[*e*]indolium hexafluorophosphate
(9–Ph)

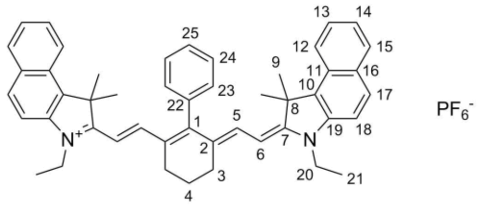

Chemical Formula: $C_{48}H_{49}F_6N_2P$
Molecular Weight: 798.90

Using the general procedure described above, **S2** (2.00 g, 5.48 mmol) **S5** (1.05 g, 2.61 mmol) and NaOAc (0.49 g, 6.00 mmol) in 80 mL EtOH gave the iodide salt of **9-Ph** as green crystals (1.58 g, 78% yield).

For the counterion exchange to PF_6^- the iodide salt of **9-Ph** (0.80 g, 1.024 mmol, 1 eq) was dissolved in MeOH (200 ml, heated to 35–40 °C) and added dropwise to a solution of KPF_6 (7.54 g, 40.981 mmol, 40 eq) in water (100 ml). The resulting suspension was stirred for 1 h and filtered over celite. The precipitate was then treated as described for **Cy7P** and recrystallized from MeOH to give the PF_6^-salt of **9-Ph** as green crystals (0.72 g, 88%). d. p. 255 °C

^{1}H-NMR (acetone-d$_6$): 8.10 (*d*, *J*=8.6, 2H, H-12); 8.05 (*d*, *J*=8.9, 2H, H-17); 8.02 (*d*, *J*=8.6, 2H, H-15); 7.78–7.69 (*m*, 3H, H-24, H-25); 7.65 (*d*, *J*=8.8, 2H, H-18); 7.63–7.59 (*m*, 2H, H-13); 7.50–7.46 (*m*, 2H, H-14); 7.43 (*d*, *J*=14.2, 2H, H-5); 7.40–7.38 (*m*, 2H, H-23); 6.37 (*d*, *J*=14.2, 2H, H-6); 4.36 (*q*, *J*=7.2, 4H, H-20); 2.79–2.78 (*m*, 4H, H-3); 2.09–2.07 (*m*, 2H, H-4); 1.55 (*s*, 12H, H-9); 1.42 (*t*, *J*=7.2, 6H, H-21). ^{13}C-NMR (acetone-d$_6$): 173.7 (C-7), 162.8 (C-1), 148.2 (C-5), 140.6 (C-19), 140.1 (C-22), 134.2 (C-10), 132.8 (C-16), 132.0 (C-2), 131.4 (C-17), 130.9 (C-15), 130.4 (C-23), 129.7 (C-24), 129.2 (C-25), 129.0 (C-11), 128.5 (C-13), 125.7 (C-14), 123.0 (C-12), 111.8 (C-18), 100.0 (C-6), 51.4 (C-8), 40.0 (C-20), 27.3 (C-9), 25.3 (C-3), 22.2 (C-4), 12.7 (C-21).

HR-MS (pos. ESI): m/z for [$C_{48}H_{49}N_2^+$]; calculated 653.38903, found 653.38903. Elemental Analysis: Calculated: [C] 72.17% [H] 6.18% [N] 3.51% [F] 14.27% [P] 3.88%; Found: [C] 72.29% [H] 6.10% [N] 3.34% [F] 14.35% [P] 3.87%;

IR (cm^{-1}): 3055*w*, 2969*w*, 2932*w*, 2870*w*, 2850*w*, 1624*w*, 1583*w*, 1574*w*, 1538*m*, 1518*m*, 1504*m*, 1478*w*, 1439*m*, 1429*m*, 1410*m*, 1386*m*, 1372*m*, 1353*s*, 1277*m*, 1268*w*, 1224*m*, 1181*m*, 1159*m*, 1146*m*, 1092*s*, 1049*m*, 1003*m*, 963*m*, 935*m*, 918*m*, 874*m*, 846*s*, 825*s*, 812*s*, 783*m*, 762*m*, 734*m*, 716*m*, 708*m*, 685*w*, 671*m*, 612*w*.

2-[2-[2-Chloro-3-[2-[1-(1-methylbutyl)benz[*cd*]indol-2(1*H*)-ylidene]ethylidene]-1-cyclohexen-1-yl]ethenyl]-1-(1-methylbutyl)-benz[*cd*]indolium hexafluorophosphate (10a–Cl)

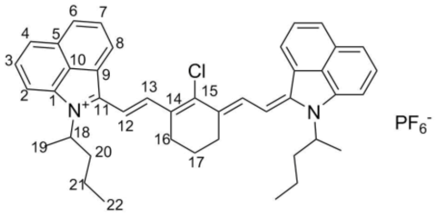

Chemical Formula: $C_{42}H_{44}ClF_6N_2P$
Molecular Weight: 757.24

12a (5.00 g, 13.69 mmol, 2.1 eq), **S4** (2.34 g, 6.52 mmol, 1.0 eq) and anhydrous sodium acetate (1.23 g, 14.99 mmol, 2.3 eq) were dissolved in 100 ml dry ethanol and heated to reflux. After 30 min the reaction mixture was filtered hot (Note: at longer reaction times decomposition of the product was found). The precipitate was washed with ethanol and dried under vacuum to give the iodide salt of **10a-Cl** as a fine black powder (3.13 g, 4.25 mmol, 65% yield). m.p. 142 °C; d.p. 225 °C.

^{1}H-NMR ($CDCl_3$): 8.82 (*d, J*=11.7, 2H, H-12); 8.39 (*d, J*=6.0, 2H, H-8); 8.10 (*d, J*=7.6, 2H, H-6); 7.85 (*t, J*=7.7, 2H, H-7); 7.68 (*broad d, J*=6.1, 2H, H-4); 7.59 (*t, J*=7.8, 2H, H-3); 7.46 (*broad d, J*=6.0, 2H, H-2); 6.93 (*broad d, J*=12.7, 2H, H-13); 4.97 (*bs*, 2H, H-18); 2.94 (*bs*, 4H, H-16); 2.25-2.16 (*m*, 2H, H-20); 2.11-2.07 (*m*, 2H, H-17); 2.06-2.00 (*m*, 2H, H-20); 1.77 (*d, J*=6.7, 6H, H-19); 1.51-1.38 (*m*, 2H, H-21); 1.22-1.18 (*m*, 2H, H-21); 0.92 (*t, J*=7.3, 6H, H-22). ^{13}C-NMR ($CDCl_3$): 142.9 (C-12); 139.5 (C-1); 132.8 (C-14); 131.3 (C-6); 130.3 (C-5); 129.8 (C-7); 129.3 (C-3); 128.1 (C-8); 125.9 (C-10); 123.2 (C-4); 112.2 (C-2); 108.8 (C-13); 53.6 (C-18); 37.5 (C-20); 27.4 (C-16); 20.8 (C-17); 20.3 (C-19); 20.1 (C-21); 13.9 (C-22). Signals for C-9, C-11, and C-15 could not be determined from ^{13}C{^{1}H}-NMR, HSCQ or HMBC experiments. HR-MS (pos. ESI): m/z for [$C_{42}H_{44}ClN_2^+$]; calculated 611.31875, found 611.31843. HR-MS (neg. ESI): m/z for [I^-]; calculated 126.90502, found 126.90568. Elemental Analysis: Calculated: [C] 68.25% [H] 6.00% [N] 3.79% [Cl] 4.80% [I] 17.17%; Found: [C] 67.74% [H] 5.92% [N] 3.63% [Cl] 4.67% [I] 16.43%;

For the counterion exchange to PF_6^- the iodide salt of **10a-Cl** (1.00 g, 1.353 mmol, 1 eq) was dissolved in MeOH (125 ml, heated to 35–40 °C) and added dropwise to a solution of $NaPF_6$ (11.36 g, 67.643 mmol, 50 eq) in water (50 ml). The resulting suspension was stirred for 10 min and filtered over celite. The precipitate was treated as described for **Cy7P** to give the PF_6^- salt of **10a-Cl** as a black solid (0.81 g, 79%). d.p. 232 °C. NMR data are given above for the iodide salt. The PF_6^- salt showed broad signals in all common solvents (aggregation) and thus no correlations with the structure could be obtained. HR-MS (pos. ESI): m/z for [$C_{42}H_{44}ClN_2^+$]; calculated 611.31875, found 611.31901. HR-MS (neg. ESI): m/z for [F_6P^-]; calculated 144.96363, found 144.96459.

Elemental Analysis: Calculated: [C] 66.62% [H] 5.86% [N] 3.70% [F] 15.05% [P] 4.09% [Cl] 4.68%; Found: [C] 66.90% [H] 5.96% [N] 3.65% [F] 14.87% [P] 3.84% [Cl] 4.53%.

IR (cm^{-1}): 2955*w*, 2927*w*, 2868*w*, 1628*w*, 1577*w*, 1541*m*, 1501*m*, 1488*m*, 1455*m*, 1432*m*, 1406*m*, 1373*m*, 1353*s*, 1278*w*, 1226*m*, 1215*m*, 1191*w*, 1148*m*, 1101*m*, 1051*m*, 1018*m*, 970*m*, 923*w*, 886*w*, 829*s*, 815*s*, 784*m*, 759*m*, 730*m*, 646*w*, 622*w*, 611*w*.

2-[2-[2-chloro-3-[2-(1-octylbenz[*cd*]indol-2(1*H*)-ylidene)ethylidene]-1-cyclohexen-1-yl]ethenyl]-1-octyl-benz[*cd*]indolium hexafluorophosphate
(10b–Cl)

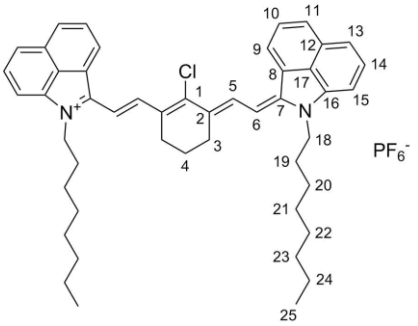

Chemical Formula: $C_{48}H_{56}ClF_6N_2P$
Molecular Weight: 841.40

To a solution of **S4** (2.45 mmol, 0.88 g, 1 eq) in acetic acid anhydride (2.5 ml) NEt_3 (2.5ml) was added slowly, raising the temperature to 40 °C; then the solution was stirred at this temperature for 10 min. Then a suspension of **12b** (4.91 mmol, 2.00 g, 2 eq) in acetic acid (10 ml) was added and the temperature was raised to 65 °C. After 30 min the solution was cooled to room temperature, and then it was added dropwise to water (20 ml), stirred for 30 min and filtered. The obtained black solid was dissolved in DCM and transferred to a separating funnel. It was washed with water (3x), then the combined organic layers were dried over Na_2SO_4 and concentrated to give the iodide salt of **10b-Cl** as a black solid (1.72 g, 85%).

The PF_6^-salt of **10b-Cl** was obtained by adding solution of the iodide salt of **10b-Cl** (2.09 mmol, 1.72 g, 1 eq) in acetone (40 ml) dropwise to a solution of KPF_6 (84.05 mmol, 15.47 g, 40 eq) in H_2O (100 ml). The precipitate was purified as described fo **Cy7P** to give the PF_6^-salt of **10b-Cl** as a black solid (1.19 g, 68%). d.p. 128 °C.

^{1}H-NMR ($CDCl_3$): 8.56 (*d*, *J*=13.8, 2H, H-5); 8.19 (*d*, *J*=7.0, 2H, H-9); 7.94 (*d*, *J*=7.8, 2H, H-11); 7.82 (*t*, *J*=7.4, 2H, H-10); 7.48 (*d*, *J*=8.2, 2H, H-13); 7.43 (*t*, *J*=7.6, 2H, H-14); 7.05 (*d*, *J*=7.0, 2H, H-15); 6.45 (*d*, *J*=13.8, 2H, H-6); 4.00 (*t*, *J*=6.6, 4H, H-18); 2.79 (*bs*, 4H, H-3); 2.05 (*bs*, 2H, H-4); 1.76 (*quint*, *J*=6.8, 4H, H-19); 1.42-1.35 (*m*, 4H, H-20); 1.32-1.20 (*m*, 16H, H-21, H-22, H-23, H-24); 0.86 (*t*, J=6.8, 6H, H-25). ^{13}C-NMR ($CDCl_3$): 153.5 (C-7), 149.2 (C-1), 142.2 (C-5), 141.0 (C-16), 132.4 (C-2), 131.3 (C-11), 130.3 (C-10), 130.0 (C-12), 129.7 (C-8), 129.4 (C-14), 128.0 (C-9), 125.1 (C-17), 123.3 (C-13), 109.8 (C-15), 107.9 (C-6), 44.6 (C-18), 31.9 (C-23), 29.8 (C-21/22), 29.5 (C-21/22), 29.2 (C-19), 27.1 (C-20), 26.9 (C-3), 22.7

(C-24), 21.0 (C-4), 14.2 (C-25). HR-MS (pos. ESI): m/z for [$C_{48}H_{56}ClN_2^+$]; calculated 695.41265, found 695.41171. IR (cm^{-1}): 3069*w*, 2921*m*, 2851*m*, 1633*w*, 1578*w*, 1537*m*, 1507*m*, 1490*m*, 1461*m*, 1431*m*, 1383*s*, 1358*s*, 1337*m*, 1272*m*, 1217*s*, 1185*m*, 1111*s*, 1084*s*, 1063*s*, 1035*s*, 898*m*, 830*s*, 816*s*, 766*m*, 758*m*, 686*m*, 615*w*.

1-Octyl-2-[2-[3-[2-(1-octylbenz[*cd*]indol-2(1*H*)-ylidene)ethylidene]-2-phenyl-1-cyclohexen-1-yl]ethenyl]-benz[*cd*]indolium hexafluorophosphate
(10b–Ph)

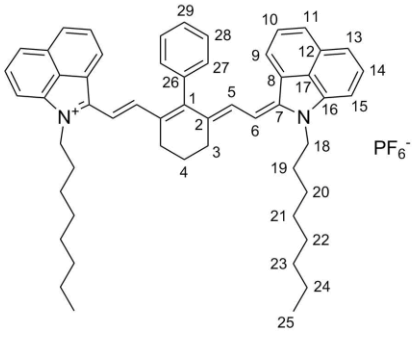

Chemical Formula: $C_{54}H_{61}F_6N_2P$
Molecular Weight: 883.06

12b (12.50 mmol, 5.09 g, 2 eq), **S5** (6.25 mmol, 2.50 g, 1 eq), and anhydrous NaOAc (15 mmol, 1.23 g, 2.4 eq) were dissolved in ethanol (anhydrous, 170 ml). The solution was heated to reflux (80 °C) for 4 h and then cooled in a refrigerator overnight. The formed precipitate was collected by filtration and washed with cold ethanol and Et_2O to obtain the iodide salt of **10b-Ph** as a black solid (3.44 g, 64%).

For the counterion exchange to PF_6^- a solution of the iodide salt of **10b-Ph** (2.31 mmol, 2.00 g, 1 eq) in a mixture of acetone (400 ml) and acetonitrile (200 ml) was added dropwise to a solution of KPF_6 (92.63 mmol, 17.05 g, 40 eq). The resulting suspension was stirred for 10 min and then filtered over celite. The obtained precipitate was dissolved in DCM, transferred to a separating funnel and washed with water (3x). The aqueous phase was then extracted with DCM (3x). The combined organic layers were dried over Na_2SO_4 and filtered over a plug of silica, which was washed with plenty of DCM. The solution was concentrated to give a crude product (1.54 g, 76%). For the final purification, the product was recrystallized from boiling ethyl acetate to give the pure PF_6^-salt of **10b-Ph** as a black solid (0.588 g, 29%). m.p. 189 °C. d.p. 284 °C.

^{1}H-NMR (acetone-d$_6$): 8.12 (*d*, *J*=8.0, 2H, H-11); 7.94 (*d*, *J*=13.6, 2H, H-5); 7.85 (*m*, 1H, H-29); 7.82 (*m*, 2H, H-28); 7.70 (*d*, *J*=8.2, 2H, H-13); 7.62 (*m*, 2H, H-14); 7.60 (*m*, 2H, H-27); 7.57 (*m*, 2H, H-10); 7.45 (*d*, *J*=7.2, 2H, H-15); 7.18 (*d*, *J*=7.2, 2H, H-9); 6.85 (*d*, *J*=14.0, 2H, H-6); 4.38 (*t*, *J*=7.3, 4H, H-18); 2.93 (*t*, *J*=5.3, 4H, H-3); 2.13 (*quint*, *J*=6.0, 2H, H-4); 1.95–1.88 (*m*, 4H, H-19); 1.52–1.45 (*m*, 4H, H-20); 1.43–1.36 (*m*, 4H, H-21); 1.34–1.25 (*m*, 12H, H-22, H-23 and H-24); 0.86 (*t*, *J*=6.9, 6H, H-25). ^{13}C-NMR (acetone-d$_6$): 161.9 (C-1), 154.4 (C-7), 146.9 (C-5), 142.3 (C-16), 139.8 (C-26), 137.5 (C-2), 132.1 (C-27), 131.8 (C-11), 131.1 (C-

12), 130.7 (C-8), 130.5 (C-14), 130.2 (C-10), 129.6 (C-28), 129.4 (C-29), 127.6 (C-9), 126.0 (C-17), 123.6 (C-13), 110.6 (C-15), 107.7 (C-6), 44.8 (C-18), 32.5 (C-23), 29.9 (C-21), 29.8 (C-22), 29.6 (C-19), 27.5 (C-20), 25.6 (C-3), 23.3 (C-24), 22.1 (C-4), 14.4 (C-25). HR-MS (pos. ESI): m/z for [$C_{54}H_{61}N_2^+$]; calculated 737.48293, found 737.48365. IR (cm^{-1}): 3056*w*, 2919*w*, 2852*w*, 1632*w*, 1579*w*, 1534s, 1506*m*, 1489*m*, 1457*m*, 1440*m*, 1426*m*, 1385*s*, 1356*s*, 1334*s*, 1292*m*, 1269*w*, 1250*m*, 1213*s*, 1184*m*, 1109*s*, 1080*s*, 1063*s*, 1021*s*, 898*m*, 858*m*, 830*m*, 814*m*, 796*m*, 759*m*, 679*m*, 617*w*.

7.1.2.4 Counterion Exchange[79]

2-[2-[2-Chloro-3-[2-(1-ethyl-1,3-dihydro-3,3-dimethyl-2*H*-indol-2-ylidene)ethylidene]-1-cyclohexen-1-yl]ethenyl]-1-ethyl-3,3-dimethyl-3*H*-indolium hexafluorophosphate
(Cy7P)

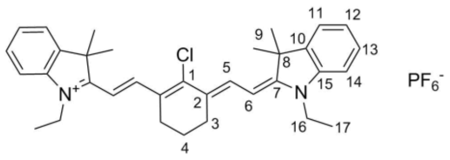

Chemical Formula: $C_{34}H_{40}ClF_6N_2P$
Molecular Weight: 657.12

NaPF$_6$ (15.9 g, 93.89 mmol, 40 eq) was dissolved in H_2O (22 ml). The iodide salt of ***8–Cl*** (1.50 g, 2.35 mmol, 1 eq) was dissolved in the minimal amount of methanol (50 ml) and added dropwise to the stirred PF_6^- solution. The resulting suspension was stirred for 10 min, then the precipitate was filtered, washed with water and dried on the filter. The green solid was dissolved in DCM, transferred to a separating funnel and washed with water (3x). The aq. phase was extracted with DCM (3x), then the combined organic layers were filtered through a plug of silica, which was washed with DCM. The solvent was removed *in vacuo* to give ***Cy7P*** as a crystalline bright green solid (1.45 g, 94% yield). d.p. 273 °C.

^{1}H-NMR (acetone-d$_6$): 8.46 (*d*, *J*=14.2, 2H, H-5); 7.63 (*d*, *J*= 7.3, 2H, H-11); 7.49-7.45 (*m*, 2H, H-13); 7.44-7.43 (*m*, 2H, H-14); 7.33 (*td*, *J*=7.2, 1.4, 2H, H-12); 6.44 (*d*, *J*=14.2, 2H, H-6); 4.35 (*q*, *J*=7.2, 4H, H-16); 2.77 (*t*, *J*=6.2, 4H, H-3); 1.94 (*quint*, J=6.3, 2H, H-4); 1.77 (*s*, 12H, H-9); 1.44 (*t*, *J*=7.2, 6H, H-17). ^{13}C-NMR (acetone-d$_6$): 173.4 (C-7), 150.2 (C-1), 145.0 (C-5), 142.9 (C-15), 142.4 (C-10), 129.6 (C-13), 127.4 (C-2), 126.2 (C-12), 123.4 (C-11), 111.9 (C-14), 101.9 (C-6), 50.3 (C-8), 40.1 (C-16), 28.0 (C-9), 26.9 (C-3), 21.6 (C-4), 12.5 (C-17). HR-MS (pos. ESI): m/z for [$C_{34}H_{40}ClN_2^+$]; calculated 511.28745, found 511.28751. HR-MS (neg. ESI): m/z for [F_6P^-]; calculated 144.96473, found 144.96486. Elemental Analysis: Calculated: [C] 62.15%, [H] 6.14%, [N] 4.26%, [F] 17.35%, [P] 4.71%, [Cl] 5.40%; Found: [C] 62.21%, [H] 6.26%, [N] 4.25%, [F] 17.19%, [P] 4.74%, [I] 0.07%. IR (cm^{-1}): 3078*w*, 2972*w*, 2923*w*, 2873*w*, 1614*w*, 1552*s*, 1509*m*, 1481*w*, 1454*m*, 1434*m*, 1416*s*, 1396*s*, 1366*s*, 1340*m*, 1314*m*, 1248*w*, 1250*s*, 1210*w*, 1183*m*, 1167*s*, 1152*s*, 1127*m*, 1105*s*, 1063*s*, 1034*s*, 1016*m*, 993*m*, 930*m*, 914*m*, 877*w*, 866*w*, 830*s*, 803*m*, 770*m*, 751*m*, 712*m*, 698*m*, 672*w*, 628*w*.

2-[2-[2-Chloro-3-[2-(1-ethyl-1,3-dihydro-3,3-dimethyl-2*H*-indol-2-ylidene)ethylidene]-1-cyclohexen-1-yl]ethenyl]-1-ethyl-3,3-dimethyl-3*H*-indolium (*OC*-6-11-Δ)-tris[3,4,5,6-tetrachloro-1,2-benzenediolato(2-)-κO^1, κO^2]phosphate(1-) (Cy7T)

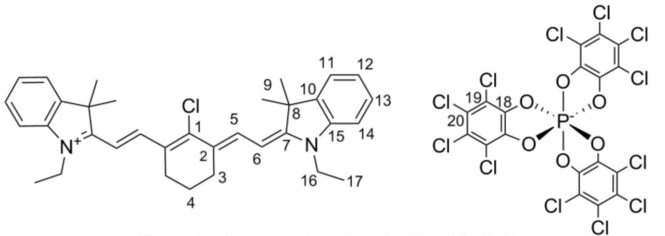

Chemical Formula: $C_{52}H_{40}Cl_{13}N_2O_6P$
Molecular Weight: 1280.72

The iodide salt of **8–Cl** (0.34 mmol, 0.22 g, 1 eq) and **S7** (0.34 mmol, 0.35 g, 1 eq) were weighed in a Schlenk flask and dissolved in dry DCM (35 ml, freshly distilled from CaH_2). The dark green solution was stirred under argon at room temperature for 17 h before it was filtered through a plug of silica to remove excess of the iodide salt. The solution was concentrated and the residue was recrystallized from MeOH/EtOAc to give **Cy7T** as a fine dark-green powder (250 mg, 57%). m.p. 182 °C. d.p. 258 °C.

^{1}H-NMR (DMSO-d_6): 8.26 (*d*, *J*=14.2, 2H, H-5); 7.62 (*d*, *J*=7.4, 2H, H-11); 7.46-7.43 (*m*, 2H, H-14); 7.43-7.41 (*m*, 2H, H-13); 7.28 (*m*, 2H, H-12); 6.32 (*d*, *J*=14.2, 2H, H-6); 4.25 (*q*, *J*=7.1, 4H, H-16); 2.71 (*t*, *J*=6.0, 4H, H-3); 1.85 (*quint*, *J*=6.0, 2H, H-4); 1.66 (*s*, 12H, H-9); 1.31 (*t*, *J*=7.1, 6H, H-17). ^{13}C-NMR (DMSO-d_6): 171.8 (C-7), 148.0 (C-1), 143.1 (C-5), 141.6 (C-15), 141.2 (C-10), 141.2 (C-18, $J_{C\text{-}P}$=6.6), 128.6 (C-13), 126.0 (C-2), 125.1 (C-12), 122.5 (C-11), 122.1 (C-20), 113.2 (C-19, $J_{C\text{-}P}$=19.7), 111.3 (C-14), 101.2 (C-6), 49.0 (C-8), 39.0 (C-16), 27.4 (C-9), 25.8 (C-3), 20.3 (C-4), 12.2 (C-17). HR-MS (pos. ESI): m/z for [$C_{34}H_{40}ClN_2^+$]; calculated 511.28745, found 511.28780. HR-MS (neg. ESI): m/z for [$C_{18}Cl_{12}O_6P^-$]; calculated 762.57003, found 762.56924. Elemental Analysis: Calculated: [C] 48.77%, [H] 3.15%, [N] 2.19%, [O] 7.50%, [P] 2.42%, [Cl] 35.99%; Found: [C] 48.66%, [H] 3.23%, [N] 2.31%, [O] 7.74%, [P] 2.36%, [Cl] 36.13%, [I] 0.12 %. IR (cm^{-1}): 2973*w*, 2927*w*, 2870*w*, 1585*w*, 1546*m*, 1505*m*, 1449*m*, 1430*m*, 1392*m*, 1365*m*, 1336*m*, 1315*w*, 1302*w*, 1286*w*, 1240*m*, 1208*m*, 1182*m*, 1167*s*, 1148*s*, 1125*m*, 1102*s*, 1087*m*, 1073*s*, 1057*s*, 1033*s*, 1015*s*, 1005*s*, 987*s*, 908*m*, 858*w*, 820*m*, 798*m*, 766*m*, 741*m*, 711*m*, 669*m*, 645*s*, 617*s*.

1-Ethyl-2-[3-(1-ethyl-1,3-dihydro-3,3-dimethyl-2*H*-indol-2-ylidene)-1-propen-1-yl]-3,3-dimethyl-3*H*-indolium hexafluorophosphate
(Cy3P)

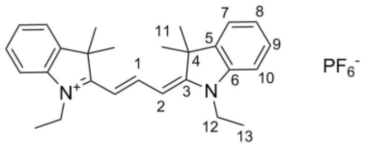

Chemical Formula: $C_{27}H_{33}F_6N_2P$
Molecular Weight: 530.54

NaPF$_6$ (30.2 g, 188.49 mmol, 50 eq) was dissolved in H_2O (60 ml). **S6** (1.99 g, 3.77 mmol, 1 eq) was dissolved in the minimal amount of methanol (50 ml) and added dropwise to the stirred PF$_6$ solution. The resulting suspension was stirred for 10 min, then the precipitate was filtered, washed with water and dried on the filter. The purple solid was dissolved in DCM and passed through a short plug of silica; the solution was concentrated and the residue was recrystallized from methanol to give **Cy3P** as a grey solid with metallic shine (1.12 g, 56 %). m.p. 235 °C, d.p. 281 °C.

^{1}H–NMR (acetone-d6): 8.59 (*t*, *J*=13.5, 1H, H-1); 7.63 (*d*, *J*=7.3, 2H, H-7); 7.50-7.46 (*m*, 2H, H-10); 7.46-7.43 (*m*, 2H, H-9); 7.35-7.31 (*m*, 2H, H-8); 6.61 (*d*, *J*=13.5, 2H, H-2); 4.27 (*q*, *J*=7.3, 4H, H-12); 1.81 (*s*, 12H, H-11); 1.43 (*t*, *J*=7.3, 6H, H-13). ^{13}C–NMR (acetone-d$_6$): 175.1 (C-3), 151.8 (C-1), 142.7 (C-6), 142.0 (C-5), 129.7 (C-9), 126.3 (C-8), 123.3 (C-7), 112.0 (C-10), 103.3 (C-2), 50.2 (C-4), 40.0 (C-12), 28.1 (C-11), 12.6 (C-13). HR–MS (pos. ESI): m/z for [$C_{27}H_{33}N_2^+$]; calculated 385.26383, found 385.26378. HR–MS (neg. ESI): m/z for [F_6P^-]; calculated 144.96473, found 144.96465. Elemental Analysis: calculated [C] 61.13 %, [H] 6.27 %, [N] 5.28 %, [F] 21.49 %, [P] 5.84 %; found [C] 61.07 %, [H] 6.32 %, [N] 5.30 %, [F] 21.45 %, [P] 5.69 %, [I] 0.01 %. IR (cm^{-1}): 3059*w*, 2992*w*, 2971*w*, 2933*w*, 2873*w*, 2831*w*, 1618*w*, 1602*w*, 1563*m*, 1555*m*, 1492*m*, 1456*m*, 1423*s*, 1384*m*, 1368*m*, 1341*m*, 1278*w*, 1257*m*, 1230*w*, 1195*s*, 1158*m*, 1131*m*, 1111*s*, 1076*s*, 1042*m*, 1020*m*, 965*w*, 945*m*, 926*m*, 872*w*, 825*s*, 811*s*, 777*m*, 754*m*, 696*w*, 678*m*, 648*w*.

1-Ethyl-2-[3-(1-ethyl-1,3-dihydro-3,3-dimethyl-2*H*-indol-2-ylidene)-1-propen-1-yl]-3,3-dimethyl-3*H*-indolium (*OC*-6-11-Δ)-tris[3,4,5,6-tetrachloro-1,2-benzenediolato(2-)-κO^1, κO^2]phosphate(1-)
(Cy3T)

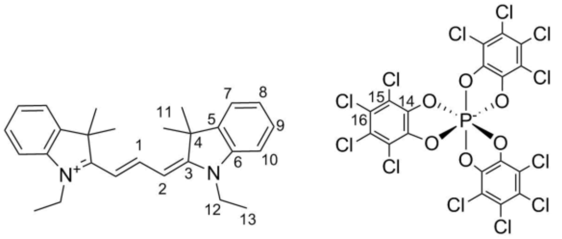

S6 (2.93 mmol, 1.50 g, 1 eq) and **S7** (2.93 mmol, 2.91 g, 1 eq) were weighed in a Schlenk flask and dissolved in dry DCM (180 ml, freshly distilled from CaH_2). The deep purple solution was stirred under argon at room temperature for 20 h before it was filtered through a plug of silica to remove excess **S2**. The solution was concentrated and the residue was recrystallized from ethanol to give **Cy3T** as dark-red needles with metallic shine (1.69 g, 50%). m.p. 197 °C, d.p. 302 °C.

^{1}H–NMR (DMSO-d_6): 8.35 (*t, J*=13.4, 1H, H-1); 7.64 (*d, J*=7.3, 2H, H-7); 7.48-7.45 (*m*, 2H, H-10); 7.45-7.42 (*m*, 2H, H-9); 7.32-7.28 (*m*, 2H, H-8); 6.52 (*d, J*=13.5, 2H, H-2); 4.16 (*q, J*=7.1, 4H, H-12); 1.69 (*s*, 12H, H-11); 1.32 (*t, J*=7.1, 6H, H-13). ^{13}C–NMR (DMSO-d_6): 173.5 (C-3), 149.9 (C-1), 141.4 (C-6), 141.2 (d, $J_{C\text{-}P}$=6.5, C-14), 140.7 (C-5), 128.7 (C-9), 125.2 (C-8), 122.6 (C-7), 122.2 (C-16), 113.2 (d, $J_{C\text{-}P}$=19.8, C-15), 111.3 (C-10), 102.3 (C-2), 48.9 (C-4), 39.0 (C-12), 27.4 (C-11), 12.3 (C-13). HR–MS (pos. ESI): m/z for [$C_{27}H_{33}N_2^+$]; calculated 385.26383, found 385.26355. HR–MS (neg. ESI): m/z for [$C_{18}Cl_{12}O_6P^-$]; calculated 762.57003, found 762.57033. Elemental Analysis: calculated [C] 46.83%, [H] 2.88%, [N] 2.43%, [O] 8.32%, [P] 2.68%, [Cl] 36.86%; found [C] 46.93%, [H] 2.98%, [N] 2.37%, [O] 8.39%, [P] 2.68%, [Cl] 36.79%. IR (cm^{-1}): 2974*w*, 2931*w*, 2873*w*, 1617*w*, 1595*w*, 1553*m*, 1482*w*, 1449*s*, 1426*s*, 1386*m*, 1368*m*, 1339*m*, 1300*w*, 1277*w*, 1248*m*, 1232*m*, 1194*s*, 1173*m*, 1155*m*, 1126*m*, 1111*m*, 1073*m*, 1043*w*, 1019*w*, 989*m*, 969*m*, 922*m*, 872*w*, 820*s*, 772*m*, 744*m*, 718*m*, 700*w*, 679*m*, 662*m*, 645*m*, 619*m*.

7.1.2.5 $S_{RN}1$ Reactions[61,243]

2-[2-[2-(Dimethylamino)-3-[2-(1-ethyl-1,3-dihydro-3,3-dimethyl-2*H*-indol-2-ylidene)ethylidene]-1-cyclohexen-1-yl]ethenyl]-1-ethyl-3,3-dimethyl-3*H*-indolium hexafluorophosphate
(8–NMe$_2$)

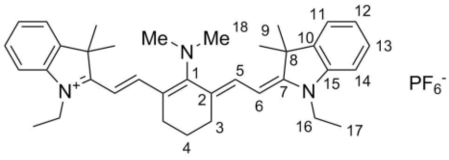

Chemical Formula: $C_{36}H_{46}F_6N_3P$
Molecular Weight: 665.75

A solution of dimethylamine (5.6M in EtOH, 16.7 ml, 93.8 mmol, 20 eq) was added to a stirred solution of **8–Cl** (3.00 g, 4.7 mmol, 1 eq) in DMF (200ml) under argon, leading to a color change from green to blue. After stirring the reaction mixture at 70 °C for 3 h the solvent was evaporated under reduced pressure. The blue oily residue was dissolved in DCM and washed with H_2O, and the aqueous phase was extracted with DCM (3x). The combined organic layers were dried over Na_2SO_4, concentrated under reduced pressure and dried in a vacuum oven (40 °C, 15 mbar) for 18 h to give the iodide salt of **8–NMe$_2$** as a dark green solid (2.74 g, 90%).

For the counterion exchange to PF_6^- the iodide salt of **8–NMe$_2$** (2.00 g, 3.08 mmol, 1 eq) was dissolved in acetone (250 ml) and added dropwise to a solution of KPF_6 (22.70 g, 123.5 mmol, 40 eq) in water (450 ml). The resulting suspension was stirred for 20 min and filtered. The precipitate was then treated as described for **Cy7P** to give the PF_6^-salt of **8–Ph** as green crystals (1.50 g, 73%). m.p. 226 °C, d.p. 258 °C.

^{1}H-NMR (acetone-d$_6$): 7.59 (*d*, *J*=13.1, 2H, H-5); 7.43 (*d*, *J*=7.3, 2H, H-11); 7.32 (*t*, *J*=8.0, 2H, H-13); 7.12 (*d*, *J*=8.0, 2H, H-14); 7.09 (*t*, *J*=7.7, 2H, H-12); 5.93 (*d*, *J*=13.1, 2H, H-6); 4.08 (*q*, *J*=7.1, 4H, H-16); 3.67 (*s*, 6H, H-18); 2.58 (*t*, *J*=6.6, 4H, H-3); 1.83 (*quint*, *J*=6.6, 2H, H-4); 1.64 (*s*, 12H, H-9); 1.33 (*t*, *J*=7.1, 6H, H-17). ^{13}C-NMR (acetone-d$_6$): 141.4 (C-5), 176.9 (C-1), 167.7 (C-7), 143.7 (C-15), 141.1 (C-10), 129.2 (C-13), 123.4 (C-12), 122.9 (C-11), 122.7 (C-2), 109.6 (C-14), 94.5 (C-6), 48.3 (C-8), 47.5 (C-18), 38.5 (C-16), 29.4 (C-9), 25.6 (C-3), 22.4 (C-4), 11.8 (C-17). HR-MS (pos. ESI): m/z for [$C_{36}H_{46}N_3^+$]; calculated 520.36862, found 520.36861. Elemental Analysis: calculated [C] 64.95%, [H] 6.96%, [N] 6.31%, [F] 17.12%, [P] 4.65%; found [C] 65.16%, [H] 6.95%, [N] 6.04%, [F] 17.01%, [P] 4.59%. IR (cm^{-1}): 3054*w*, 2956*w*, 2932*w*, 2870*w*, 1613*w*, 1601*w*, 1550*m*, 1540*m*, 1505*m*, 1485*m*, 1465*m*, 1454*m*, 1434*m*, 1363*m*, 1340*m*, 1313*w*, 1272*w*, 1254*w*, 1228*w*, 1197*w*, 1158*m*, 1122*m*, 1110*m*, 1090*m*, 1075*m*, 1067*m*, 1043*w*, 958*w*, 926*w*, 915*w*, 873*w*, 830*s*, 760*m*, 750*m*, 713*w*, 677*w*, 627*w*.

2-[2-[2-(Dimethylamino)-3-[2-(3-ethyl-1,3-dihydro-1,1-dimethyl-2H-benz[e]indol-2-ylidene)ethylidene]-1-cyclohexen-1-yl]ethenyl]-3-ethyl-1,1-dimethyl-1H-benz[e]indolium hexafluorophosphate

(9–NMe$_2$)

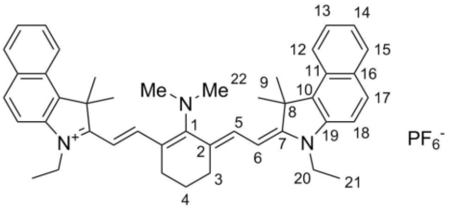

Chemical Formula: $C_{44}H_{50}F_6N_3P$
Molecular Weight: 765.87

The iodide salt of **9–NMe$_2$** was synthesized by stirring dimethylamine (5.6M in EtOH, 16.7 ml, 93.8 mmol, 20 eq), and **9–Cl** (4.00 g, 5.4 mmol, 1 eq) in DMF (270 ml) at 75 °C for 4 h (procedure and work-up as described for **8–NMe$_2$**) and was obtained as a green solid (3.88 g, 96%).

For the counterion exchange to PF_6^- the iodide salt of **9–NMe$_2$** (2.00 g, 2.67 mmol, 1 eq) was dissolved in acetonitrile (300 ml, heated to 40 °C) and added dropwise to a solution of KPF_6 (19.72 g, 107.03 mmol, 40 eq) in water (400 ml). The resulting suspension was stirred for 10 min and filtered over celite. The precipitate was then treated as described for **Cy7P** to give the PF_6^--salt of **9–NMe$_2$** as green crystals (1.17 g, 56%). d.p. 271 °C.

^{1}H-NMR (acetone-d$_6$): 8.19 (*d*, *J*=8.6, 2H, H-12); 8.01 (*m*, 2H, H-17); 7.99 (*m*, 2H, H-15); 7.76 (*d*, *J*=13.3, 2H, H-5); 7.58 (*m*, 2H, H-13); 7.55 (*m*, 2H, H-18); 7.42 (*m*, 2H, H-14); 6.03 (*d*, *J*=13.2, 2H, H-6); 4.24 (*q*, *J*=7.1, 4H, H-20); 3.70 (*s*, 6H, H-22); 2.62 (*t*, *J*=6.6, 4H, H-3); 1.97 (*s*, 12H, H-9); 1.87 (*quint*, *J*=6.6, 2H, H-4); 1.41 (*t*, *J*=7.1, 6H, H-21). ^{13}C-NMR (acetone-d$_6$): 175.9 (C-1), 170.1 (C-7), 141.8 (C-5), 141.3 (C-19), 132.5 (C-10), 132.0 (C-16), 131.1 (C-17), 130.9 (C-15), 129.4 (C-11), 128.2 (C-13), 124.6 (C-14), 123.0 (C-2), 122.7 (C-12), 111.3 (C-18), 94.6 (C-6), 50.4 (C-8), 47.5 (C-22), 38.9 (C-20), 28.9 (C-9), 25.5 (C-3), 22.6 (C-4), 12.2 (C-21). HR-MS (pos. ESI): m/z for [$C_{44}H_{50}N_3^+$]; calculated 620.39993, found 620.40019. IR (cm^{-1}): 2982*w*, 2935*w*, 2867*w*, 1623*w*, 1586*w*, 1551*m*, 1530*m*, 1511*m*, 1467*w*, 1438*m*, 1363*m*, 1352*m*, 1332*m*, 1292*m*, 1245*m*, 1231*m*, 1197*m*, 1163*m*, 1118*s*, 1104*s*, 1071*m*, 1037*m*, 1014*m*, 966*m*, 956*m*, 935*m*, 914*m*, 878*w*, 867*w*, 832*s*, 809*s*, 784*m*, 747*m*, 708*m*, 671*m*, 619*w*.

1-Ethyl-2-[2-[3-[2-(1-ethyl-1,3-dihydro-3,3-dimethyl-2*H*-indol-2-ylidene) ethylidene]-2-(hexahydro-1,3-dimethyl-2,4,6-trioxo-5-pyrimidinyl)-1-cyclohexen-1-yl]ethenyl]-3,3-dimethyl-3*H*-indolium, inner salt

(8–barb)

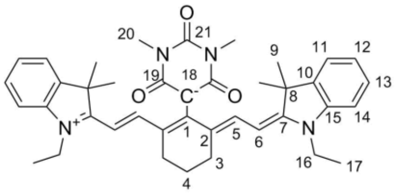

Chemical Formula: $C_{40}H_{46}N_4O_3$
Molecular Weight: 630.83

The iodide salt of **8–Cl** (0.323 g, 0.500 mmol, 1.0 eq) and 1,3-dimethylbarbituric acid **S8** (0.134 g, 0.850 mmol, 1.7 eq) were dissolved in a mixture of DCM (5 ml) and methanol (5 ml). NEt_3 (0.12 ml, 0.850 mmol, 1.7 eq) was added to the solution. The reaction mixture was heated to 50 °C (reflux) for 1 hour and then concentrated under reduced pressure. The crude product was purified by column chromatography (silica gel; started with DCM as the eluent, then gradually changed to DCM/MeOH 19:1) to give **8–barb** as a blue-green solid (0.240 g, 75%). Rf=0.39 (silica; DCM/MeOH 19:1). m.p. 251 °C, d.p. 277 °C.

^{1}H–NMR (DMSO-d$_6$): 7.96 (*d*, *J*=14.2, 2H, H-5); 7.51 (*d*, *J*=7.3, 2H, H-11); 7.33 (*t*, *J*=7.6, 2H, H-13); 7.26 (*d*, *J*=7.9, 2H, H-14); 7.13 (*t*, *J*=7.4, 2H, H-12); 6.06 (*d*, *J*=14.2, 2H, H-6); 4.09 (*q*, *J*=7.0, 4H, H-16); 3.14 (*s*, 6H, H-20); 2.56 (*broad t*, *J*=5.5, 4H, H-3); 1.83 (*broad quint*, *J*=5.5, 2H, H-4); 1.41 (*s*, 12H, H-9); 1.24 (*t*, *J*= 6.9, 6H, H-17). ^{13}C–NMR (DMSO-d$_6$): 169.5 (C-7), 164.6 (C-1), 160.3 (C-19), 153.1 (C-21), 146.6 (C-5), 142.0 (C-15), 140.7 (C-10), 131.4 (C-2), 128.3 (C-13), 123.7 (C-12), 122.4 (C-11), 110.0 (C-14), 98.6 (C-6), 83.1 (C-18), 48.1 (C-8), 38.2 (C-16), 27.5 (C-9), 26.9 (C-20), 24.4 (C-3), 21.0 (C-4), 11.8 (C-17). HR-MS (pos. ESI): m/z for [$C_{40}H_{47}N_4O_3^+$]; calculated 631.36427, found 631.36367. IR (cm^{-1}): 3050*w*, 2965*w*, 2926*w*, 2866*w*, 1670*m*, 1578*m*, 1540*s*, 1505*s*, 1485*m*, 1452*m*, 1428*m*, 1393*m*, 1363*s*, 1336*m*, 1315*m*, 1265*m*, 1248*m*, 1229*m*, 1206*m*, 1163*m*, 1151*s*, 1123*m*, 1098*s*, 1056*m*, 1034*s*, 1013*s*, 941*m*, 909*m*, 856*m*, 803*m*, 777*w*, 750*m*, 710*m*, 676*w*, 649*w*, 630*w*, 610*w*.

3-Ethyl-2-[2-[3-[2-(3-ethyl-1,3-dihydro-1,1-dimethyl-2*H*-benz[*e*]indol-2-ylidene) ethylidene]-2-(hexahydro-1,3-dimethyl-2,4,6-trioxo-5-pyrimidinyl)-1-cyclohexen-1-yl]ethenyl]-1,1-dimethyl-1*H*-benz[*e*]indolium, inner salt
(9–barb)

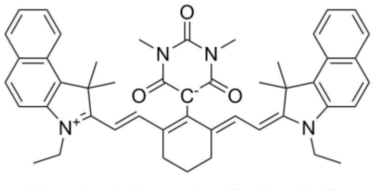

Chemical Formula: $C_{48}H_{50}N_4O_3$
Molecular Weight: 730.95

9–barb was purchased from FEW Chemicals recrystallized from MeOH for optical and electrochemical analysis and fabrication of thin films for solar cell devices.

7.1.2.6 Benz[cd]indolium Squaraine Dye[91]

2-[[2-Hydroxy-3-[(1-octylbenz[*cd*]indol-2(1*H*)-ylidene)methyl]-4-oxo-2-cyclobuten-1-ylidene]methyl]-1-octyl-benz[*cd*]indolium, inner salt
(SQ–870)

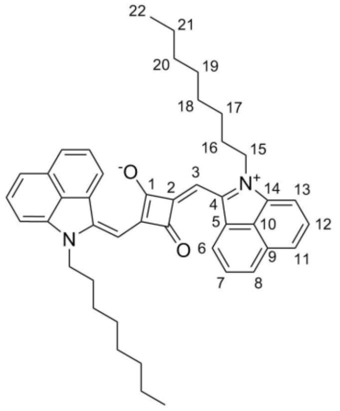

Chemical Formula: $C_{44}H_{48}N_2O_2$
Molecular Weight: 636.88

Squaric acid (0.28 g, 2.455 mmol, 1.0 eq) was dissolved in a mixture of toluene (35 ml) and 1-butanol (35 ml) at 120 °C (reflux). **12b** was added as a solid and the reaction mixture was kept at 120 °C (reflux) for 2 h, then it was concentrated under reduced pressure to give a black crude product. After recrystallization from EtOH, squaraine dye **SQ-870** was obtained as a black crystalline powder (1.08 g, 69%). d.p. 116 °C.

^{1}H–NMR ($CDCl_3$): 9.20 (*bs*, 2H, H-8); 7.94 (*d*, *J*=8.0, 2H, H-6); 7.83 (*t*, *J*=7.7, 2H, H-7); 7.55 (*d*, *J*=8.2, 2H, H-11); 7.48 (*t*, *J*=7.7, 2H, H-12); 7.03 (*d*, *J*=7.1, 2H, H-13); 6.37 (*bs*, 2H, H-3); 4.17 (*bs*, 4H, H-15); 1.89 (*quint*, *J*=7.5, 4H, H-16); 1.49-1.42 (*m*, 4H, H-17); 1.39-1.33 (*m*, 4H, H-19); 1.32-1.22 (*m*, 4H, H-21); 0.87 (*t*, *J*=6.8, 6H, H-22). ^{13}C–NMR ($CDCl_3$): 183.3 (C-1); 176.3 (C-2); 151.1 (C-4); 141.6 (C-14); 131.5 (C-8); 130.4 (C-5); 129.7 (C-7); 129.6 (C-6); 128.4 (C-12); 125.5 (C-10); 121.6 (C-11); 107.0 (C-13); 92.1 (C-3); 44.1 (C-15); 31.7 (C-

20); 29.4 (C-19); 29.1 (C-18); 28.9 (C-16); 27.2 (C-17); 22.6 (C-21); 14.1 (C-22). The signal for C-9 could not be determined from ^{13}C {^{1}H}-NMR, HSCQ or HMBC experiments. HR–MS (pos. ESI): m/z for [$C_{44}H_{49}N_2O_2^+$]; calculated 637.37886, found 637.37803. Elemental Analysis: Calculated: [C] 82.98% [H] 7.60% [N] 4.40% [O] 5.02%; Found: [C] 82.93% [H] 7.58% [N] 4.17% [O] 5.21%. IR (cm^{-1}): 3069*w*, 3028*w*, 2999*m*, 2948*m*, 2918*m*, 1606*m*, 1578*m*, 1484*s*, 1470*s*, 1422*s*, 1390*m*, 1347*m*, 1322*m*, 1316*m*, 1294*m*, 1274*w*, 1256*m*, 1241*m*, 1223*s*, 1194*m*, 1172*m*, 1150*m*, 1111*m*, 1078*m*, 1071*m*, 1058*m*, 1028*m*, 1002*m*, 995*m*, 976*m*, 902*w*, 883*w*, 871*w*, 837*w*, 820*m*, 805*w*, 775*m*, 746*m*, 725*m*, 683*w*, 660*w*, 633*w*, 618*w*.

7.1.3 Optical and Electrochemical Analysis

7.1.3.1 Optical Data in Solution

UV–Vis–NIR spectra (300–1100 nm) of the compounds in solution were recorded on a *Varian Cary 50 Scan* spectrophotometer in a 1.0 cm square cuvette. For extinction coefficient (ε) determination, several stock solutions were prepared (A ≈ 1) and then successively diluted to get at least three different concentrations; the value of ε was calculated by linear least-squares fitting of plots of absorbance vs. concentration; all fits gave R^2 values of ≥ 0.98. Emission spectra of homoabsorptive solutions (A ≈ 0.2) were recorded on a *HORIBA Jobin Yvon Fluorolog®–3* spectrofluorometer with a 450 W xenon lamp. Excitation wavelength was 525 nm for the trimethine dyes and 780 nm for the heptamethine dyes in all solvents. Normalized emission spectra of **Cy3P**, **Cy3T**, **Cy7P** and **Cy7T** in different solvents are shown in **Figure 7.1**.

Optical data for all compounds are given in **Table 7.1**, **Table 7.2**, and **Table 7.3**: Absorption maxima λ_{max} (nm); molar extinction coefficient ε (/10^3 L $mol^{-1}cm^{-1}$); integrated absorption coefficient $IAC = \int \varepsilon(\nu)d\nu$ (ν=frequency /s^{-1}) (/10^{18}); oscillator strength $f = 4.31 * 10^{-9} \int \varepsilon(\tilde{\nu})d\tilde{\nu}$ ($\tilde{\nu}$= wavenumbers/cm^{-1}); emission maximum λ_{em} (nm); stokes shift λ_s (nm); absorption onset at higher wavelength λ_{on} (nm); optical bandgap $E_{opt} = hc/\lambda_{on}$.

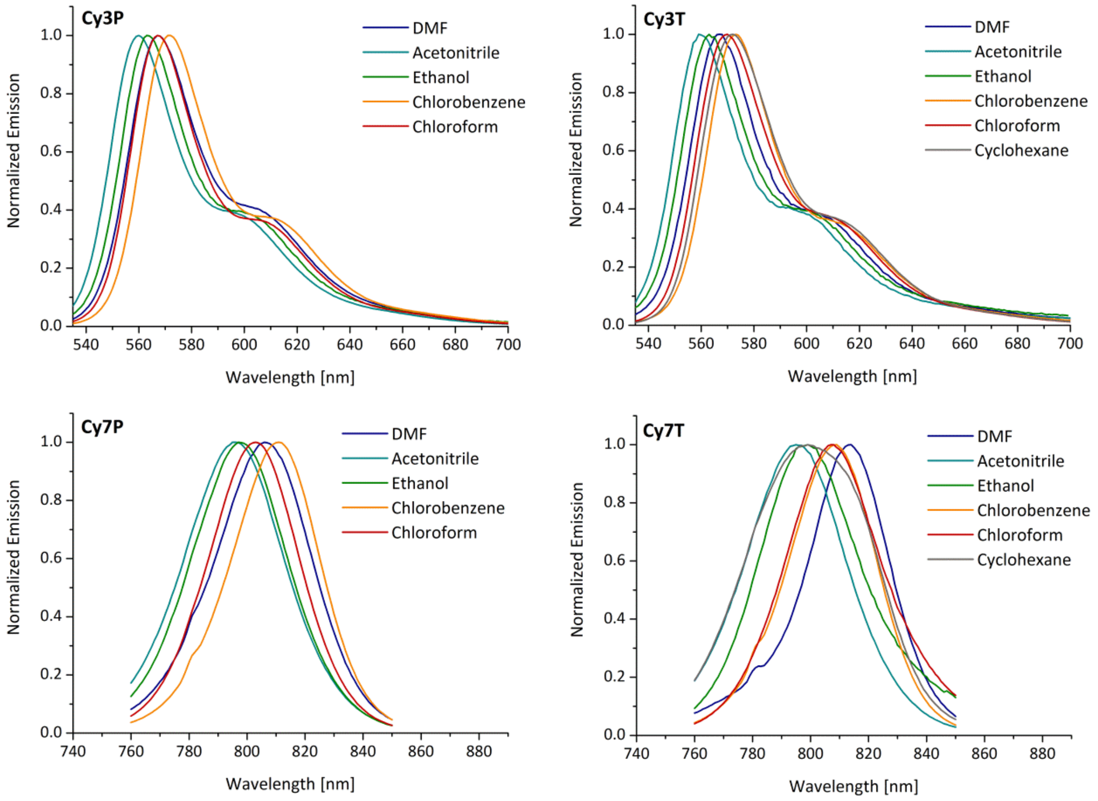

Figure 7.1: Normalized emission spectra of **Cy3P**, **Cy3T**, **Cy7P** and **Cy7T** in different solvents.

Table 7.1: Tabulated optical data of trimethine dyes **Cy3P** and **Cy7T** in different solvents. Acetonitrile (ACN), ethanol (EtOH), dimethylformamide (DMF), chloroform ($CHCl_3$), chlorobenzene (PhCl), cyclohexane (C_6H_{12}). Cy7P was not soluble in cylcohexane.

	solvent	λ_{max}	ε	$log(\varepsilon)$	IAC	f	λ_{em}	λ_s	λ_{on}	E_{opt}
Cy3P	ACN	544	176	5.25	9.78	1.40	560	16	563	2.20
	EtOH	548	137	5.14	7.60	1.09	563	15	568	2.18
	DMF	550	141	5.15	8.06	1.16	567	17	571	2.17
	$CHCl_3$	555	156	5.19	7.75	1.11	567	12	574	2.16
	PhCl	558	164	5.22	8.11	1.16	571	13	574	2.16
Cy3T	ACN	544	146	5.16	7.96	1.15	559	15	565	2.19
	EtOH	548	136	5.13	7.50	1.08	564	16	569	2.18
	DMF	550	124	5.09	6.87	0.99	567	17	573	2.16
	$CHCl_3$	555	129	5.11	6.65	0.95	570	15	577	2.15
	PhCl	557	135	5.13	7.01	1.01	574	17	578	2.15
	C_6H_{12}	558	133	5.13	6.34	0.91	572	14	578	2.15

Table 7.2: Tabulated optical data of heptamethine dyes **Cy7P** and **Cy7T** in different solvents. See **Table 7.1** for abbreviations.

	solvent	λ_{max}	ε	$log(\varepsilon)$	IAC	f	λ_{em}	λ_s	λ_{on}	E_{opt}
Cy7P	ACN	777	254	2.40	10.01	1.44	796	19	811	1.53
	EtOH	781	325	2.51	11.54	1.66	798	17	813	1.53
	DMF	788	243	2.39	10.10	1.46	806	18	823	1.51
	$CHCl_3$	788	340	2.53	10.26	1.48	803	15	813	1.53
	PhCl	795	305	2.48	9.16	1.32	811	16	826	1.50
Cy7T	ACN	777	242	2.38	9.74	1.40	795	18	815	1.52
	EtOH	781	260	2.42	9.07	1.31	799	18	811	1.53
	DMF	787	245	2.39	10.26	1.47	813	26	823	1.51
	$CHCl_3$	789	375	2.57	10.76	1.55	808	19	828	1.50
	PhCl	796	360	2.56	9.83	1.41	809	13	828	1.50
	C_6H_{12}	775	219	2.34	8.88	1.27	799	24	815	1.52

Table 7.3: Tabulated optical data of heptamethine dyes **8–10** and squaraine dye **SQ–870** in ethanol. The integrals for IAC and *f* of **10b-Cl** are lower because the peak exceeds the scanning range of the instrument.

	λ_{max}	ε	$log(\varepsilon)$	IAC	f	λ_{on}	E_{opt}
8-Cl	781	325	2.51	11.54	1.66	813	1.53
8-Ph	761	330	2.52	11.32	1.64	798	1.55
8-barb	758	278	2.44	9.99	1.45	795	1.56
8-NMe₂	664	88	1.95	10.57	1.53	785	1.58
9-Cl	821	298	2.47	11.51	1.65	855	1.45
9-Ph	798	295	2.47	10.88	1.59	832	1.49
9-barb	792	274	2.44	9.55	1.46	830	1.49
9-NMe₂	698	90	1.95	9.95	1.44	806	1.54
10b-Cl	1022	116	2.07	4.83	0.69	1070	1.16
10b-Ph	1003	216	2.33	7.65	1.10	1051	1.18
SQ870	867	142	2.15	5.36	0.77	907	1.37

7.1.3.2 Electrochemical Data

Cyclic voltammetry (CV) measurements were performed on a PGStat 30 potentiostat (Autolab) using a three cell electrode system (Au working electrode, Pt counter electrode and an Ag / AgCl reference electrode) in a 0.1 M solution of TBACl in DMF. The concentration of the dyes was 0.2–0.5 mM, the scan rate was 100 mV/s. For the trimethine dyes the oxidation was not reversible in DMF, and could not be used for calculations of oxidation potentials. For this reason, the cyclic voltammetry measurements for **Cy3T** and **Cy3P** have been also carried out in 2,2,2–trifluoroethanol (TFE) using a glassy carbon working electrode where reversible oxidation peaks could be found. When estimating the position of the anodic peak potential E_{pa}(ox) of the irreversible oxidation peak in DMF, the same value for the oxidation potential E^0_{ox} was obtained as from the measurement in TFE (after referencing to NHE). Heptamethine dyes **8–NMe$_2$** and **9–NMe$_2$** also gave non-symmetric oxidation peaks in DMF. Based on the findings from the trimethine dyes the anodic peak potential E_{pa}(ox) was estimated from the peak shape in order to calculate E^0_{ox} for these dyes. All other heptamethine dyes gave symmetric oxidation and reduction peaks. All potentials were referenced to NHE by adopting a potential of +0.72 V vs. NHE for Fc/Fc$^+$ in DMF or +0.69 V vs. NHE for Fc/Fc$^+$ in TFE and the energy level of NHE is situated 4.5 eV below the zero vacuum energy level. Cyclic voltammograms of all dyes are shown hereafter.

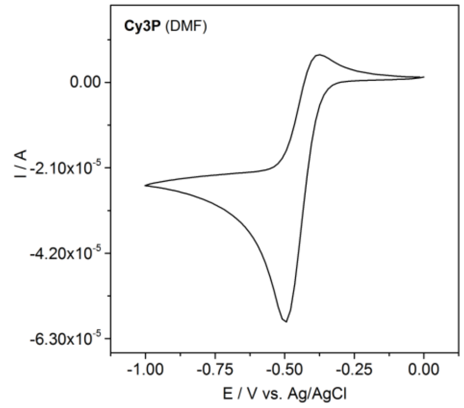

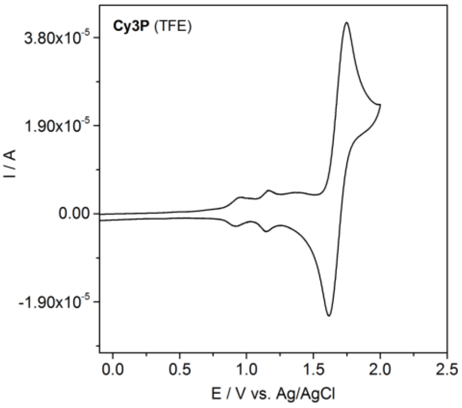

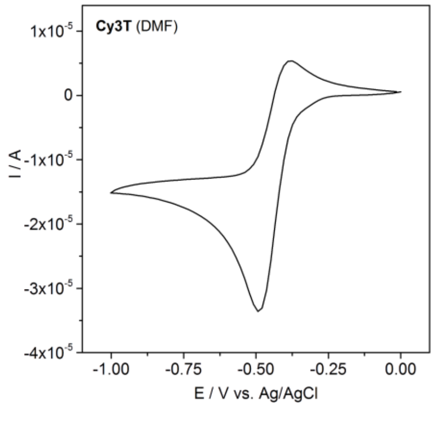

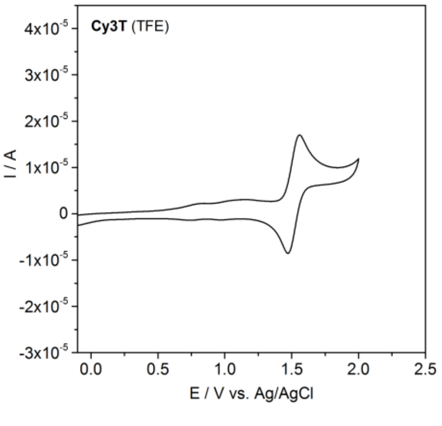

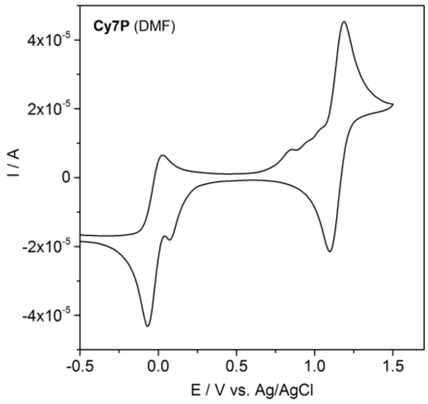
Cy7P (DMF)
4x10⁻⁵
2x10⁻⁵
0
-2x10⁻⁵
-4x10⁻⁵
I / A
-0.5
0.0
0.5
1.0
1.5
E / V vs. Ag/AgCl

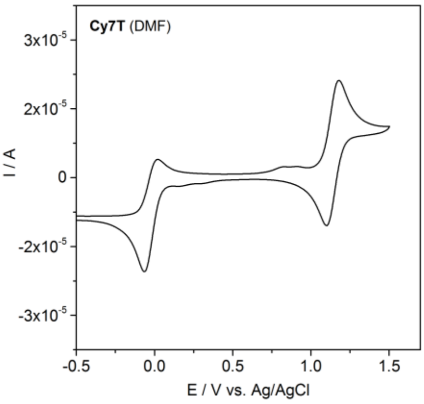
Cy7T (DMF)
3x10⁻⁵
2x10⁻⁵
0
-2x10⁻⁵
-3x10⁻⁵
I / A
-0.5
0.0
0.5
1.0
1.5
E / V vs. Ag/AgCl

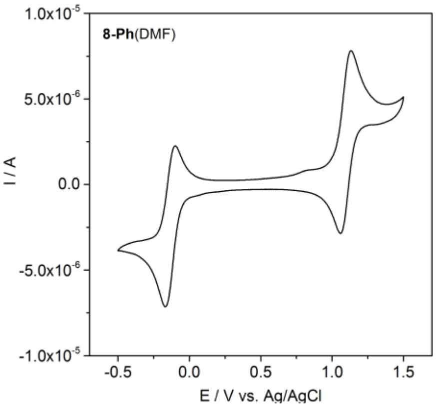
8-Ph(DMF)
1.0x10⁻⁵
5.0x10⁻⁶
0.0
-5.0x10⁻⁶
-1.0x10⁻⁵
I / A
-0.5
0.0
0.5
1.0
1.5
E / V vs. Ag/AgCl

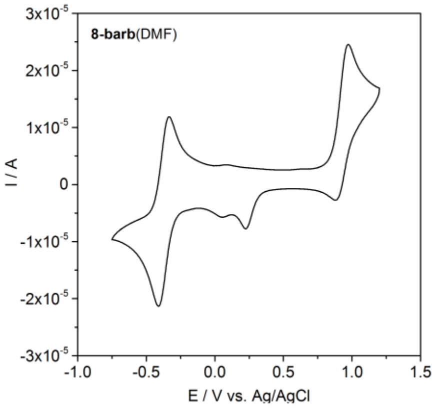
8-barb(DMF)
3x10⁻⁵
2x10⁻⁵
1x10⁻⁵
0
-1x10⁻⁵
-2x10⁻⁵
-3x10⁻⁵
I / A
-1.0
-0.5
0.0
0.5
1.0
1.5
E / V vs. Ag/AgCl

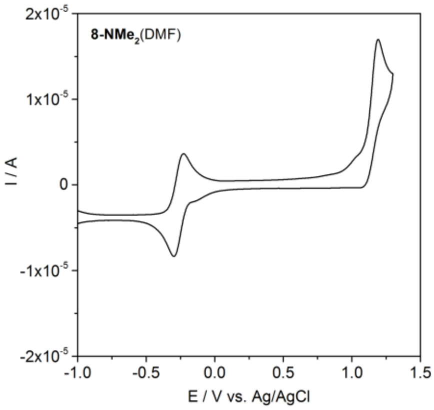
8-NMe₂(DMF)
2x10⁻⁵
1x10⁻⁵
0
-1x10⁻⁵
-2x10⁻⁵
I / A
-1.0
-0.5
0.0
0.5
1.0
1.5
E / V vs. Ag/AgCl

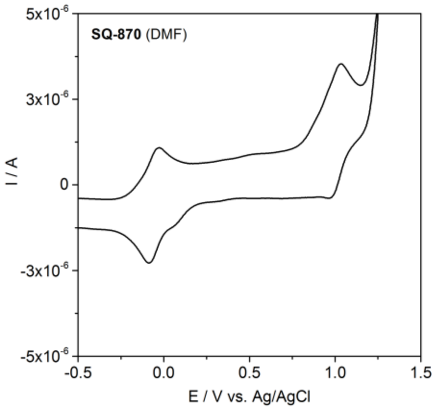
SQ-870 (DMF)
5x10⁻⁶
3x10⁻⁶
0
-3x10⁻⁶
-5x10⁻⁶
I / A
-0.5
0.0
0.5
1.0
1.5
E / V vs. Ag/AgCl

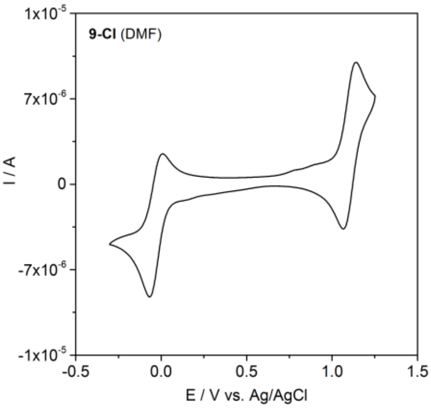
9-Cl (DMF)
1x10⁻⁵
7x10⁻⁶
0
-7x10⁻⁶
-1x10⁻⁵
I / A
-0.5
0.0
0.5
1.0
1.5
E / V vs. Ag/AgCl

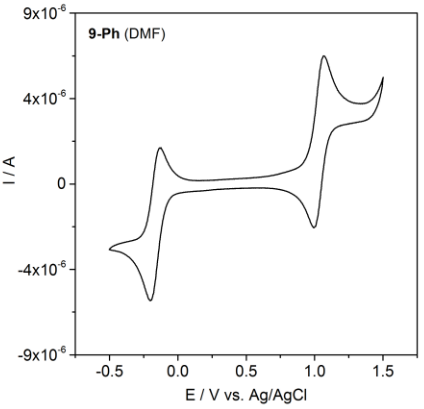
9-Ph (DMF)
9x10⁻⁶
4x10⁻⁶
0
-4x10⁻⁶
-9x10⁻⁶
I / A
-0.5
0.0
0.5
1.0
1.5
E / V vs. Ag/AgCl

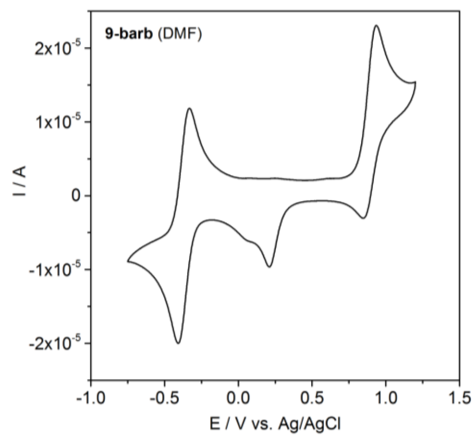
9-barb (DMF)
2x10^{-5}
1x10^{-5}
0
-1x10^{-5}
-2x10^{-5}
I / A
-1.0
-0.5
0.0
0.5
1.0
1.5
E / V vs. Ag/AgCl

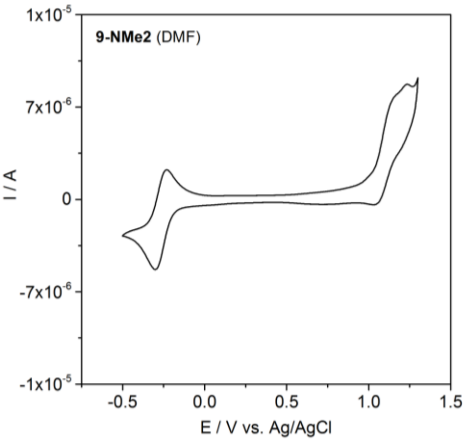
9-NMe2 (DMF)
1x10^{-5}
7x10^{-6}
0
-7x10^{-6}
-1x10^{-5}
I / A
-0.5
0.0
0.5
1.0
1.5
E / V vs. Ag/AgCl

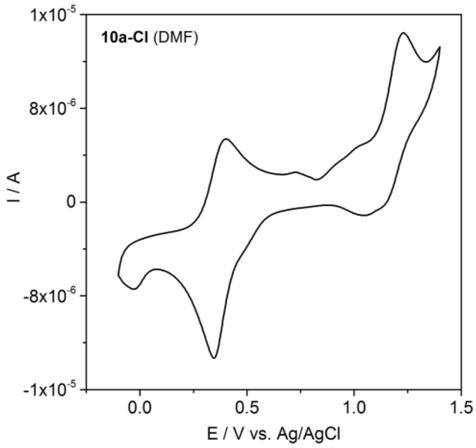
10a-Cl (DMF)
1x10^{-5}
8x10^{-6}
0
-8x10^{-6}
-1x10^{-5}
I / A
0.0
0.5
1.0
1.5
E / V vs. Ag/AgCl

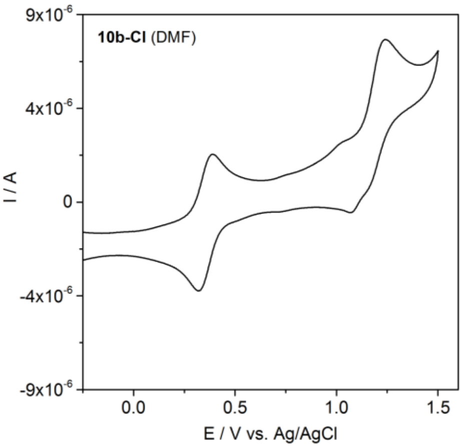
10b-Cl (DMF)
9x10^{-6}
4x10^{-6}
0
-4x10^{-6}
-9x10^{-6}
I / A
0.0
0.5
1.0
1.5
E / V vs. Ag/AgCl

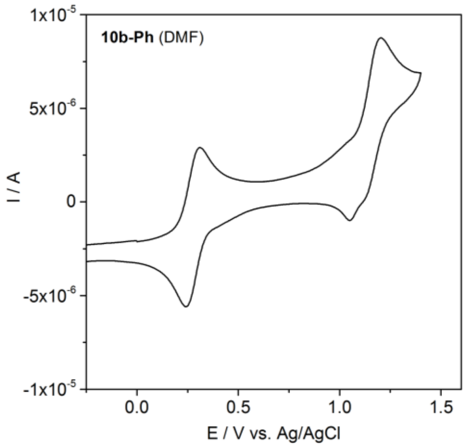
10b-Ph (DMF)
1x10^{-5}
5x10^{-6}
0
-5x10^{-6}
-1x10^{-5}
I / A
0.0
0.5
1.0
1.5
E / V vs. Ag/AgCl

7.2 Preparation and Analysis of Solar Cells and Thin Films

7.2.1 Organic Solar Cells and Bulk Heterojunction Blend Films

7.2.1.1 Semitransparent Organic Solar Cells[79]

These are the experimental details to chapter 3.1.3.

Bilayer solar cells were fabricated with **Cy7P** or **Cy7T** as electron donors and C_{60} as the electron acceptor. Cyanine layers were spin–cast from chlorobenzene solutions inside a nitrogen–filled glove box (< 1 ppm H_2O, < 6 ppm O_2). MoO_3 (Sigma Aldrich), C_{60} (SES Research, 99.9%) and Alq_3 (Sigma Aldrich, 99.995%) were deposited by thermal sublimation under vacuum at a pressure of 3 x 10^{-6} mbar. Ag (Cerac, 99.99%) was evaporated through a shadow mask to define eight solar cells on each substrate with active areas of 3.1 or 7.1 mm^2. For non-transparent cells, the Ag cathode thickness was 80 nm, for semitransparent cells, the electron-collecting electrode was composed of Ag (12 nm)/Alq_3 (60 nm).

Film thicknesses were determined by profilometry (*Ambios XP1*). Absorption spectra of thin films were measured on a *Varian Cary 50 Scan* spectrophotometer using a glass substrate as the baseline. For characterization, solar cells were mounted under N_2 into an air–tight homemade transfer box and measured outside the glove box. Current-voltage (J–V) characteristics were measured using 100 mW cm^{-2} simulated AM1.5G solar irradiation on a calibrated solar simulator from *Spectra Nova*. Solar cells were characterized via illumination through the anode side (glass/ITO) only. Short–circuit currents (J_{sc}) in **Table 7.4** are indicated from the solar simulator measurements. J_{sc} values were also measured directly outside under natural sunlight irradiation (96 mW cm^{-2}, measured with a radiant power meter from *LOT Oriel* using a calibrated thermopile probe). J_{sc} values from the two measurements agreed within 10%.

For solar cell fabrication, the C_{60} film thickness was fixed at 40 nm. This value corresponds to the exciton diffusion length of C_{60} (40 ± 5 nm).[96] The MoO_3 and Alq_3 buffer layer thicknesses were 5 nm and 2 nm, respectively.[56,244] The Ag (12 nm) / Alq_3-capping (60 nm) thick semitransparent electrode was chosen based on optical modeling results. The cyanine layer thicknesses were varied between 10 nm and 30 nm, and best solar cell performances were obtained for dye thicknesses of ≈ 20 nm.

Table 7.4: Experimental average visible transmittances (AVT, 450–670 nm) and performance data of cyanine (20 nm)/C_{60} (40 nm) bilayer solar cells. Mean values originate from # different devices with eight cells per device. The illumination intensity was 100 mW cm^{-2}.

device structure		V_{oc} / V	J_{sc} / mA cm^{-2}	*FF* %	η %	*AVT* %
ITO/MoO_3(5 nm)/**Cy7T**/C_{60}/Alq_3(2 nm)/Ag (80 nm)	#6	0.63	7.1	52.3	2.3	-
	best	0.61	7.5	61.4	2.8	-
ITO/MoO_3 (5 nm)/ **Cy7T** /C_{60}/Alq_3(2 nm)/Ag(12 nm)/Alq_3(60 nm)	#3	0.63	4.9	54.4	1.7	66
	best	0.63	6.4	54.0	2.2	66
ITO/MoO_3(5 nm)/ **Cy7P**/C_{60}/Alq_3(2 nm)/Ag (80 nm)	#3	0.38	5.7	64.3	1.4	-
	best	0.39	6.8	69.1	1.8	-
ITO/MoO_3 (5 nm)/ **Cy7P** /C_{60}/Alq_3(2 nm)/Ag(12 nm)/Alq_3(60 nm)	#3	0.37	3.6	59.0	0.8	62
	best	0.38	3.6	64.8	0.9	62

7.2.2 Perovskite Solar Cells

General

Solvents were purchased from commercial sources in p.a. grade and used as received. Fluorine doped tin oxide (FTO) glass substrates (TCO22-7 from *Solaronix*, 7 Ω square^{-1}, 2.5 cm × 2.5 cm) were patterned by etching with Zn powder and HCl (conc.). Then they were cleaned by sonication in a 20% solution of *Hellmanex*® (5 min), followed by rinsing in millipore water (3 x 5 min), acetone p. a. (5 min), and 2-propanol p. a. (5 min) and a UV–ozone treatment (5 min). Methylammonium iodide was prepared according to literature procedures[220,245] and carefully recrystallized from EtOH/Et_2O to remove residues of iodine.

Sequential Deposition (chapter 3.2.2.2.1)[121]

For the formation of a compact TiO_2 blocking layer, $TiCl_4$ (25 ml) was hydrolyzed in water (90 ml) at 0 °C and the resulting solution was spin–cast at 5000 rpm for 30 sec on cleaned FTO glass substrates and then heated at 140 °C for 10 min. A mesoporous TiO_2 layer was subsequently applied by spin coating a paste of TiO_2 nanoparticles (0.22% w/w *Ti-Nanoxide T/SP* from *Solaronix* diluted in ethanol) at 5000 rpm for 30 s followed by gradual heating to 380 °C for 10 min and then to 500 °C for 30 min in air. $CH_3NH_3PbI_3$ was deposited on these substrate according to the sequential method described by Burschka et al.[121] PbI_2 (0.460 g) was dissolved in DMF (1.000 ml) by stirring at 80 °C and the hot solution was spin–coated under ambient atmosphere at 6000 rpm (3000 rpm s^{-1}) for 90 sec, followed by heating at 80 °C for 5 min. This spin–coating process was repeated a second time on the same substrate to obtain a dark yellow PbI_2 film. Under ambient atmosphere, a solution of methylammonium iodide (24 mg) in 2-propanol (3.000 ml) was spread on the PbI_2 film (200 μl per substrate), and after a wait time of 30 sec the substrate was spun at 4000 rpm for 30 sec. For the cyanine HTM, a solution of **9–Cl** (8 mg) in chlorobenzene (1.000 ml) was spin–coated on the perovskite layer at 4000 rpm for 30 sec in a nitrogen–filled glovebox. For the reference solar cells using Spiro–OMeTAD as the HTM, $N^2,N^2,N^{2'},N^{2'},N^7,N^7,N^{7'},N^{7'}$-octakis(4-methoxyphenyl)-9,9'-Spirobi[9*H*-fluorene]-2,2',7,7'-tetramine (*Sigma–Aldrich*, 72.3 mg) was dissolved in chlorobenzene (1.000 ml) and mixed with the following additives: cobalt complex *FK102* (*Dyesol*, 29 μl of a stock solution of 300 mg/ml in dry acetonitrile); lithium bis(trifluoromethylsulfonyl)imide LiTFSI (*Sigma–Aldrich*, 18 μl of a stock solution of 520 mg/ml in dry acetonitrile); 4-*tert*-butylpyridine (*Sigma–Aldrich*, 29 μl). The resulting solution was spin–cast on the perovskite layer at 4000 rpm for 30 sec in a nitrogen–filled glovebox. The solar cells were finished by thermal evaporation of Au electrodes (70 nm) at $< 5 \times 10^{-6}$ mbar through a shadow mask.

Antisolvent Deposition (chapter 3.2.2.2.2)[134]

FTO substrates size was ≈ 1.2 cm × 2.5 cm. A TiO_2 compact layer (30 nm) was deposited on cleaned FTO substrates *via* spray pyrolysis at 450 °C from a precursor solution of titanium diisopropoxide bis(acetylacetonate) in anhydrous ethanol. A mesoporous TiO_2 layer was deposited by spin–coating for 20 s at 4000 rpm (2000 rpm s^{-1}) using 30 nm particle paste (Dyesol 30 NR-D) diluted in ethanol to achieve a 150–200 nm thick layer. After spin–coating, the substrates were sintered at 450 °C for 30 min under dry air flow. After cooling to 150 °C, the substrates were transferred into a dry box for the deposition of the perovskite films. The perovskite films were deposited from a precursor solution containing FAI (1 M), PbI_2 (1.1 M), MABr (0.2 M) and $PbBr_2$ (0.2 M) in anhydrous DMF/DMSO 4:1 (v:v). The precursor solution was spin–cast in a two–step program at 1000 and 6000 rpm. for 10 and 30 s, respectively. During the second step, 100 μl of chlorobenzene was poured on the spinning substrate 10 s before the end of the program. The substrates were then annealed at 100 °C for 1 h in a dry air–filled glovebox.

For the cyanine HTMs, a solution of **9–Cl** or **9–barb** in chlorobenzene (20 mM) was spin–cast on the perovskite layer in a nitrogen–filled glovebox at 4000 rpm for 20 sec. For the cyanine HTMs with additives the same relative additive concentration as described below for Spiro–OMeTAD was used. For the reference solar cells a Spiro–OMeTAD as the HTM, solution of $N^2,N^2,N^{2'},N^{2'},N^7,N^7,N^{7'},N^{7'}$-octakis(4-methoxyphenyl)-9,9'-Spirobi[9*H*-fluorene]-2,2',7,7'-tetramine (*Merck*) in chlorobenzene (70 mM), containing the additives listed hereafter, was spin–cast on the perovskite layer in a nitrogen–filled glovebox at 4000 rpm for 20 sec. Additives in mole percent relative to the HTM Spiro–OMeTAD or cyanine: lithium bis(trifluoromethylsulfonyl)imide (LiTFSI, *Sigma–Aldrich*) 0.5%; cobalt complex *FK209* (*Dyenamo*) 0.03%; 4-*tert*-butylpyridine (*Sigma–Aldrich*) 3.3%. The solar cells were finished by thermal evaporation of Au electrodes (70–80 nm) under high vacuum.

Solar Cell Characterization

Solar cells were characterized in ambient atmosphere. Current–voltage (J–V) characteristics were measured by a *Keithley* 2400 source/measure unit under simulated AM1.5G solar irradiation of 100 mW cm^{-2} from a calibrated solar simulator (*Spectra-Nova*). Cells were masked with a metal aperture of 0.138 cm^2 to define the active area. Current–voltage curves were recorded at a scanning rate of 0.1 V s^{-1}. The external quantum efficiency (EQE) of the devices was measured with a lock–in amplifier. The probing beam was generated by a chopped white light source (900 W, halogen lamp, 260 Hz) and a dual grating monochromator. The beam size was adjusted to ensure that the illuminated area was fully inside the cell area. A certified single crystalline silicon solar cell was used as the reference cell. The steady–state efficiency as a function of time was recorded using a maximum power point tracker, which adjusts the applied voltage in order to reach the maximum power point (perturb and observe algorithm). The starting voltage was set to be 0.1 V. Steady–state efficiencies were in agreement with the efficiencies obtained from the reverse scans (forward bias to short circuit current) of the current–voltage measurement.

7.2.3 Low–Dimensional Organic–Inorganic Hybrid Materials

7.2.3.1 2D–Perovskite Thin Films $(C_{12}H_{25}NH_3)_2PbI_4$

General

PbI_2 (99.99%, for perovskite precursor) was purchased from *TCI Chemicals*, DMF (dried, max. 0.003% H_2O, *SeccoSolv*®) and toluene (dried, max. 0.005% H_2O, *SeccoSolv*®) were purchased from *Merck Millipore* and used as received. Dodecylammonium iodide (DDAI) was prepared from dodecylamine and hydriodic acid by an adapted literature procedure[220,245] and purified by careful recrystallization from EtOH/Et_2O to obtain a colorless solid (yellow color indicates contamination with iodine). Elemental Analysis: Calculated: [C] 46.01% [H] 9.01% [N] 4.47% [I] 40.51%; Found: [C] 46.28% [H] 9.17% [N] 4.40% [I] 40.40. Glass substrates were *Menzel* microscope slides purchased from *Thermo Scientific*; Si–SiO_2 wafer substrates (100 nm thermally grown SiO_2 layer) were obtained from the *Center of MicroNanoTechnology* (CMI) at the *Ecole Polytechnique fédérale de Lausanne* (EPFL); OFET substrates were standard substrates with evaporated Au contacts on Si–SiO_2 (230 nm SiO_2) wafers from *Fraunhofer IPMS.*[237]

Scanning electron microscopy of cross–sections and surfaces of the samples were performed on a *Hitachi S-4800* field emission scanning electron microscope using an acceleration voltage of 7 kV and an emission current of 10 mA. To avoid charging effects the samples were coated with 5 nm of Pt by sputtering prior to the analysis.

X–ray diffraction (XRD) patterns were obtained using a θ–2θ scan on a *PANalytical X'Pert PRO* instrument (Cu–$K_{\alpha 1}$ radiation, $\lambda = 1.5406$ Å) from 3–40° (2θ) with a step interval of 0.017°. XRD scans were performed under ambient atmosphere and thus films were exposed to air during the measurement (for 2 h).

Spin–Casting of PbI_2 Films

For 29% (w/w) solution, PbI_2 (1.552 g) was suspended in DMF (2.000 ml) and stirred at 70 °C overnight to obtain a clear solution, which was filtered (pore size 5 μm) before use. Glass substrates (2.5 cm × 2.5 cm) or Fraunhofer OFET substrates (1.5 × 1.5 cm) were cleaned by sonicating in a 20% solution of *Hellmanex*® (5 min), followed by rinsing in millipore water (3 x 5 min), acetone p. a. (5 min) and 2-propanol p. a. (5 min) and UV–ozone treatment (5 min). PbI_2 solution (at 70 °C) was spin–cast on the clean glass slides at 6000 rpm (3000 rpm s^{-1}) for 50 sec in ambient atmosphere. Immediately after the spin–coating program was finished, the yellow–white films were transferred to a hotplate at the indicated temperature (40 °C, 50 °C, 60 °C or 70 °C) and heated for 5 min. Alternatively, the films were placed in a vial with a glass joint lid and placed in a refrigerator (5 °C) for 1h, or kept in ambient atmosphere (25 °C). After drying, a color change from yellow–white to dark yellow was observed; films dried at lower temperatures were opaque, while the heated films were transparent. Film thickness was ≈ 100 nm (determined by SEM). **Figure 7.2** shows the XRD spectrum of a film dried at 5 °C compared to the five most common polytypes of PbI_2. Polytype 6R shows the best match to the peaks that are not consistent with the main polytype 2H. *Note*: This procedure was found to be reproducible in ambient atmosphere only when the relative humidity (RH) was < 40%. At higher humidity, inconsistent PbI_2 films where obtained, with large particles or inhomogeneous transparency / opacity. When the spin–casting of PbI_2 films like described above was carried out inside a nitrogen–filled glovebox the film formation was reproducible.

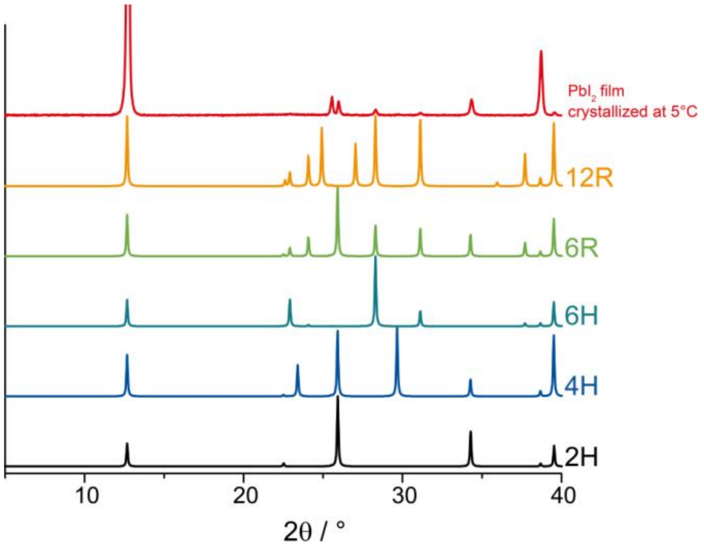

Figure 7.2: XRD spectrum of spin–coated PbI_2 film dried at 5 °C compared to calculated powder diffraction patterns of the five most common polytypes of PbI_2.[231,235]

Stability of PbI_2 Films in Air

It was found that PbI_2 films changed color from yellow to white when stored for a prolonged time in ambient air. **Figure 7.3** shows the XRD spectra of PbI_2 films stored at different conditions. After 8 months in ambient air (varying RH from 30–60%), full conversion of PbI_2 to Pb(OH)I was observed. After three days in ambient air (RH ≈ 30–40%) or inside a nitrogen–filled glovebox, PbI_2 films were still intact, after three days in a chamber filled with H_2O vapor, partial conversion to Pb(OH)I had occurred (peaks labelled with asterisks). Even though the conversion was only partial, and most of the film was still PbI_2 according to XRD, a drastic change in morphology was observed when characterizing the surfaces of the films using SEM (**Figure 7.4**). As a conclusion, PbI_2 precursor films were always stored inside a nitrogen–filled glovebox before intercalation.

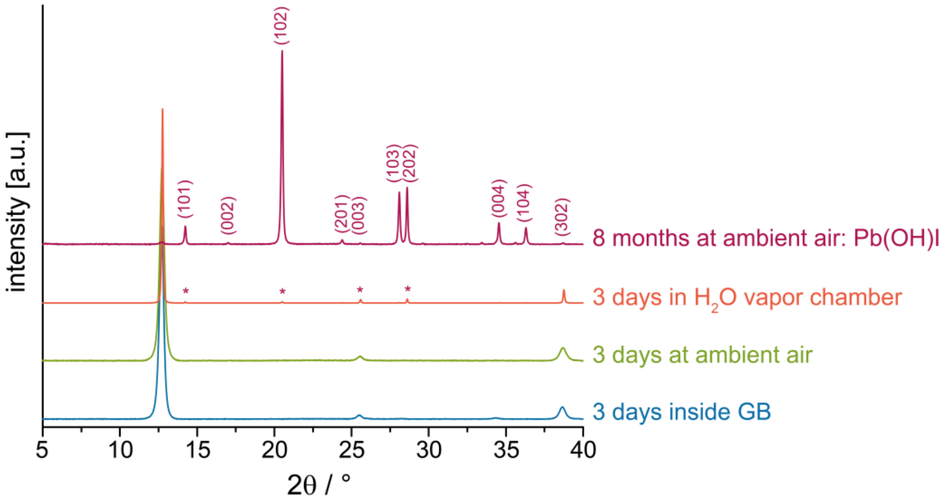

Figure 7.3. XRD patterns of spin–coated PbI_2 films stored under different conditions. From top to bottom: Eight months in ambient air (red), the film is fully converted to Pb(OH)I. Indexed according to reference ICSD–192169;[246] three days in a chamber filled with H_2O vapor (orange), partial conversion to Pb(OH)I (peaks labelled with asterisk); three days at ambient air (green); three days inside nitrogen–filled glovebox (GB) (blue).

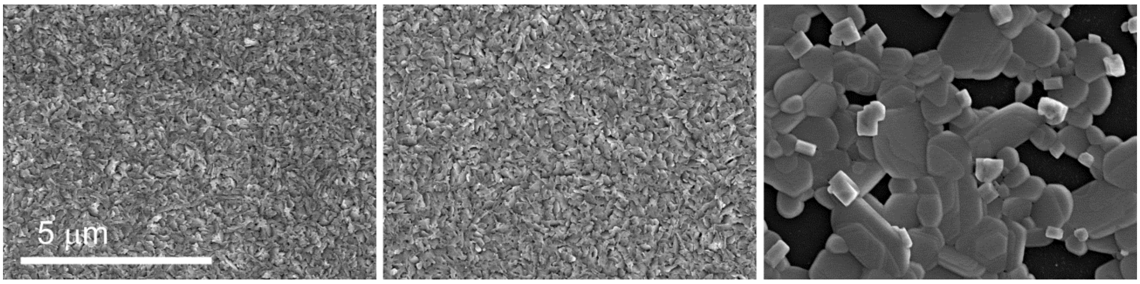

Figure 7.4. SEM images of PbI_2 films stored for three days under different conditions. From left to right: inside nitrogen–filled glovebox, at ambient air, in a chamber filled with H_2O vapor.

Intercalation of DDAI into PbI_2 to Form DDAP Thin Films

For a 0.58% (w/w) solution, dodecyl ammonium iodide (1.009 g) was dissolved in toluene (200 ml). For dip–coating, the solution was kept at a temperature of 30 °C, 40 °C, or 50 °C, as indicated. PbI_2 films were freshly prepared or stored inside a nitrogen–filled glovebox for a maximum of two days. Before dip–coating, the films were heated on a hotplate to the same temperature as the solution. Films were held with tweezers and dipped into the solution for exactly the indicated amount of time (30–120 sec), and then dipped into pure toluene (which was also kept at the same temperature) for 2–3 sec. The DDAP films were then dried on a hotplate at 30 °C, 40 °C, or 50 °C. The temperature of the dip–coating solution and washing solvent were strictly monitored to be at the indicated temperature ± 0.5 °C during the process. The dip–coating time had to be chosen carefully according to the temperature. Porous PbI_2 films (dried at 25 °C, see preparation of PbI_2 films) were fully converted after ≈ 60 sec (30 °C), ≈ 50 sec (40 °C) or ≈ 45 sec (50 °C). At longer reaction times films were damaged due to abrasion by the solvent.

Figure 7.5 shows SEM images of the surface (top) and cross–section (bottom) of a DDAP film prepared using the optimized conditions (from a porous precursor film at a dip–coating temperature of 50 °C). SEM images were recorded after the film was stored inside a nitrogen–filled glovebox for three weeks. The thickness was determined to be ≈ 1 µm according to cross–sectional SEM and profilometry.

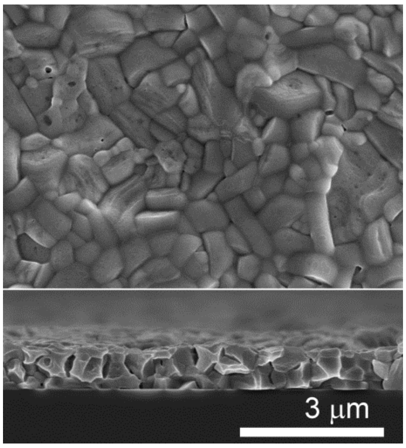

Figure 7.5. SEM images of surface (top) and cross–section (bottom) of a DDAP film prepared using optimized intercalation conditions on glass substrate.

Note on intercalation of water: Preliminary intercalation experiments on glass slides and Fraunhofer OFET substrates (results in **Figure 4.7**, **Figure 4.8** and **Figure 4.9**) were performed in ambient atmosphere. Depending on the RH on a given day, films were found to show an additional set of peaks (marked with † in **Figure 7.6**), with the basal peak at 3.38° 2θ (d = 26.08 Å). The basal peak of phase II of DDAP (002) is at 3.66° 2θ (d = 24.15 Å) and corresponds to the distance between the $[\mathrm{PbI}_4^-]$ sheets in the crystal structure. In the new set of peaks, that appears after prolonged exposure to ambient atmosphere, the spacing of the sheets is increased by ≈ 2 Å. This corresponds approximately to the size of a water molecule,[247] and thus it is likely that water from the atmosphere can intercalate into the structure to form a hydrate.

For device quality films (results in **Figure 4.11** and **Figure 4.12**), intercalation was performed inside a nitrogen–filled glovebox to avoid formation of the hydrate.

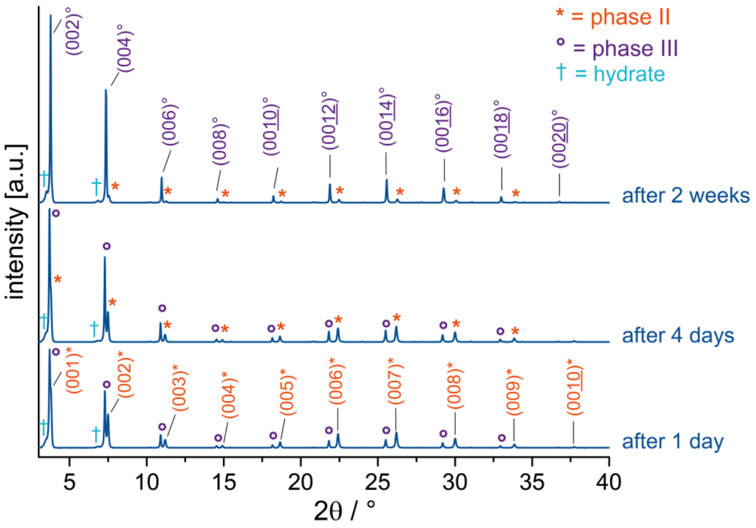

Figure 7.6. XRD patterns of a DDAP film prepared at 50 °C after different storage times, intensities as measured. Peaks are indexed according to Billing et al.[172] Phase II (orange, marked with *), phase III (purple, marked with °), hydrate (light blue, marked with †).

To study the relaxation from phase II to phase III in the films prepared at 50 °C, they were stored in a nitrogen–filled glovebox and repeatedly analyzed by XRD at ambient atmosphere (**Figure 7.6**). After one day, a large amount of phase II (marked with *) is present. After two weeks, there is still a small amount of phase II, but most of the crystals have relaxed to phase III (marked with °), and the overall intensity of the reflexes is increased. For a full conversion to phase III, films have to be stored for more than two weeks. Over time the peaks associated with the hydrate (marked with †) were found to increase in intensity, indicating that water from the atmosphere intercalated into the films (during XRD scans the films are exposed to air).

Optimization of DDAP Films for FET Devices

Annealed DDAP films were prepared on Si–SiO_2 wafer substrates (2.5 × 2.5 cm) inside a nitrogen–filled glovebox. The procedure and concentrations of the solutions for both steps were the same as described above for films on glass substrates. PbI_2 films were dried at room temperature and the dip–coating solution was at 50 °C. Before annealing, the substrate was broken into two halves; one was heated to 100 °C inside the glovebox and annealed at this temperature for 30 min and then let cool to room temperature slowly over the course of 1 h. The other half of the substrate was not annealed and used for comparison of the morphology before and after annealing. XRD spectra illustrating the (00ℓ) preferential orientation of crystallites are given in **Figure 7.7** (left). Spectra were measured 4 days after annealing and films are not fully relaxed to phase III yet.

Very thin PbI_2 (≈ 10 nm) and DDAP films (≈ 100 nm) were prepared on Si–SiO_2 wafer substrates (1.5 × 1.5 cm) inside a nitrogen–filled glovebox, according to the same procedure as described above for films on the glass substrates. However, the concentrations of the solutions were adjusted as follows. The PbI_2 spin–coating solution (29% w/w in DMF) was diluted 1:9 with DMF; the dip–coating solution of DDAI (0.58% w/w in toluene) was diluted 1:9 with toluene. PbI_2 films were dried at room temperature and the dip–coating solution was at 50 °C. Dip–coating time was varied and intercalation was found to be completed after 30 sec. XRD spectra illustrating the (00ℓ) preferential orientation of crystallites are given in **Figure 7.7** (right). Spectra were measured 4 days after preparation and films are not fully relaxed to phase III yet.

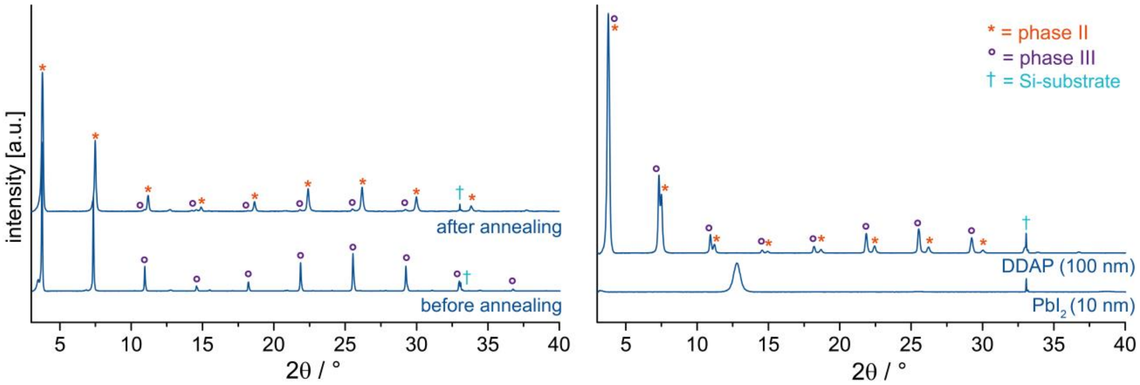

Figure 7.7. XRD spectra of DDAP film before and after annealing (left) and PbI_2 and DDAP films with reduced thickness (right). Phase II and III are labelled as in **Figure 7.6**. Peak labelled with † (light blue) corresponds to Si–substrate.

7.3 X–ray Crystal Structures

7.3.1 Crystal growth

Single crystals of **Cy7I**, **Cy7P** and **Cy7T** suitable for X–ray crystal structure determination were grown by vapor diffusion of Et_2O into a saturated solution of the respective cyanine salt in DCM.

A very thin needle of the hybrid compound **Cy7–PbI$_3$** was obtained by slow evaporation of a solution containing lead iodide (67 mM) and cyanine dye iodide salt **Cy7I** (**8–Cl**) (134 mM) in DMF over ≈ 2 weeks.

Crystal structure determination was carried out by the X–ray Crystallography Facility of the University of Zurich (Anthony Linden).

7.3.2 Definition of Terms

Function minimized: $\Sigma w(F_o{}^2 - F_c{}^2)^2$

where $w = [\sigma^2(F_o{}^2) + (aP)^2 + bP]^{-1}$ and $P = (F_o{}^2 + 2F_c{}^2)/3$

$F_o{}^2 = \mathrm{S(C - RB)/Lp}$

and $\sigma^2(F_o{}^2) = \mathrm{S^2(C + R^2B)/Lp^2}$

S = Scan rate

C = Total integrated peak count

R = Ratio of scan time to background counting time

B = Total background count

Lp = Lorentz-polarization factor

R-factors:

$R_{\mathrm{int}} = \Sigma|\langle F_o{}^2\rangle - F_o{}^2|/\Sigma F_o{}^2$ summed only over reflections for which more than one symmetry equivalent was measured

$R(F) = \Sigma||F_o| - |F_c||/\Sigma|F_o$ summed over all observed reflections.

$wR(F^2) = [\Sigma w(F_o{}^2 - F_c{}^2)^2/\Sigma w(F_o{}^2)^2]^{1/2}$ summed over all reflections.

Standard deviation of an observation of unit weight (goodness of fit):

$[\Sigma w(F_o{}^2 - F_c{}^2)^2/(\mathrm{N_o} - \mathrm{N_v})]^{1/2}$ where $\mathrm{N_o}$ = number of observations; $\mathrm{N_v}$ = number of variables

7.3.3 Crystal Structure Determination of **Cy7I** ($C_{34}H_{40}ClN_2^+$ I^-)

The structure of $C_{34}H_{40}ClN_2^+$ I^- (**Cy7I**) has been solved and refined successfully. The crystals were very thin fragile plates and it was difficult to isolate and mount a usable fragment without too much damage. The data are thus of modest quality, but the structure model is clear and unambiguous. The compound crystallizes in a polar space group and the absolute structure has been determined independently by the diffraction experiment.

Experimental

A crystal of $C_{34}H_{40}ClN_2^+$ I^-, obtained from CH_2Cl_2 / Et_2O, was mounted on a glass fiber and used for a low–temperature X–ray structure determination. All measurements were made on a *Rigaku Oxford Diffraction SuperNova* area-detector diffractometer[248] using Cu $K\alpha$ radiation (λ = 1.54184 Å) from a micro-focus X–ray source and an *Oxford Instruments Cryojet XL* cooler. The unit cell constants and an orientation matrix for data collection were obtained from a least-squares refinement of the setting angles of 7860 reflections in the range $7° < 2\theta < 153°$. A total of 2754 frames were collected using ω scans with κ offsets, 2.0–20.0 seconds exposure time and a rotation angle of 1601.0° per frame, and a crystal–detector distance of 60.0 mm.

Data reduction was performed with *CrysAlisPro*.[248] The intensities were corrected for Lorentz and polarization effects, and a numerical absorption correction[249] was applied. The space group was uniquely determined by the systematic absences. Equivalent reflections, other than Friedel pairs, were merged. The data collection and refinement parameters are given in **Table 7.5**. A view of the molecule is shown in **Figure 7.8**. Bond lengths, bond angles and torsion angles are given in **Table 7.9**, **Table 7.10** and **Table 7.11** respectively.

The structure was solved by dual space methods using *SHELXT-2014*,[250] which revealed the positions of all non-hydrogen atoms. The non-hydrogen atoms were refined anisotropically. All of the H-atoms were placed in geometrically calculated positions and refined by using a riding model where each H-atom was assigned a fixed isotropic displacement parameter with a value equal to $1.2U_{\mathrm{eq}}$ of its parent atom ($1.5U_{\mathrm{eq}}$ for the methyl groups). The refinement of the structure was carried out on F^2 by using full-matrix least-squares procedures, which minimised the function $\Sigma w(F_o^2 - F_c^2)^2$. The weighting scheme was based on counting statistics and included a factor to downweight the intense reflections. Plots of $\Sigma w(F_o^2 - F_c^2)^2$ versus $F_c/F_c(\mathrm{max})$ and resolution showed no unusual trends. A correction for secondary extinction was not applied. Refinement of the absolute structure parameter[251] yielded a value of -0.019(8), which confidently confirms that the refined model represents the true absolute structure. The seven largest peaks of residual electron density are between 0.64 and 1.36 e Å^{-3} and all lie within 1.2 Å of the iodide ion.

Neutral atom scattering factors for non-hydrogen atoms were taken from Maslen, Fox and O'Keefe,[241a] and the scattering factors for H-atoms were taken from Stewart, Davidson and Simpson.[252] Anomalous dispersion effects were included in F_C;[253] the values for f' and f'' were those of Creagh and McAuley.[241b] The values of the mass attenuation coefficients are those of Creagh and Hubbel.[241c] The *SHELXL-2014* program[254] was used for all calculations.

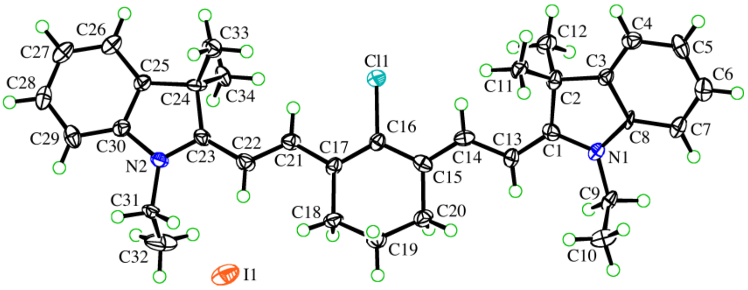

Figure 7.8. *ORTEP*[255] representation of the cation and anion in **Cy7I** (50% probability ellipsoids; H-atoms given arbitrary displacement parameters for clarity).

Table 7.5. Crystallographic Data for **Cy7I** ($C_{34}H_{40}ClN_2^+\ I^-$).

Crystallized from		CH_2Cl_2 / Et_2O
Empirical formula		$C_{34}H_{40}ClIN_2$
Formula weight [g mol^{-1}]		639.03
Crystal colour, habit		yellow, plate
Crystal dimensions [mm]		0.03 × 0.09 × 0.35
Temperature [K]		160(1)
Crystal system		orthorhombic
Space group		$P2_12_12_1$ (#19)
Z		4
Reflections for cell determination		7860
2θ range for cell determination [°]		7–153
Unit cell parameters	a [Å]	7.9571(3)
	b [Å]	11.6098(3)
	c [Å]	33.2904(11)
	α [°]	90
	β [°]	90
	γ [°]	90
	V [Å^3]	3075.38(17)
$F(000)$		1312
D_X [g cm^{-3}]		1.380
μ(Cu $K\alpha$) [mm^{-1}]		9.153
Scan type		ω
$2\theta_{(\max)}$ [°]		154.0
Transmission factors (min; max)		0.143; 1.000
Total reflections measured		17773
Symmetry independent reflections		5760
R_{int}		0.047
Reflections with $I > 2\sigma(I)$		5147
Reflections used in refinement		5760
Parameters refined		349
Final	$R(F)$ [$I > 2\sigma(I)$ reflections]	0.0654
	$wR(F^2)$ (all data)	0.1501
Weights:	$w = [\sigma^2(F_o^2) + (0.0177P)^2 + 29.1457P]^{-1}$ where $P = (F_o^2 + 2F_c^2)/3$	
Goodness of fit		1.076
Final $\Delta_{\max}/\sigma$		0.000
$\Delta\rho$ (max; min) [e Å^{-3}]		1.36; -0.99
$\sigma(d_{(C-C)})$ [Å]		0.012 – 0.016

7.3.4 Crystal Structure Determination of **Cy7P** ($C_{34}H_{40}ClN_2^+ PF_6^-$)

The structure of $C_{34}H_{40}ClN_2^+ PF_6^-$ (**Cy7P**) has been solved and refined successfully. The asymmetric unit contains four cations and four anions. The cations generally have very similar conformations with only small differences in most torsion angles. The major differences are that one cation has a the terminal methyl group of one ethyl substituent rotated by approximately 180° relative to its orientation in the other three cations, and that another cation has the opposite half-chair puckering of the central six-membered ring compared with the other cations. No additional crystallographic symmetry could be found in the structure, although the structure is pseudo-centrosymmetric with an 83% fit of the atoms to the additional symmetry element; the differences between the conformations of the cations are breaking the additional symmetry. The crystals are non-merohedral twins resulting from a rotation of 180° about [103]. The twin matrix is 1 0 0 / 0 -1 0 / 0.6363 0 1 and the major twin fraction is 0.5668(10). All reflections from both twin components were integrated and included in the refinement. Note that the precision of the geometric parameters is somewhat lower than normal and this should be taken into consideration if these parameters are being compared.

Experimental

A crystal of $C_{34}H_{40}ClN_2^+ PF_6^-$ was mounted on a glass fiber and used for a low-temperature X-ray structure determination. All measurements were made on an *Agilent Technologies SuperNova* area-detector diffractometer[256] using Mo $K\alpha$ radiation (λ = 0.71073 Å) from a micro-focus X-ray source and an *Oxford Instruments Cryojet XL* cooler. The unit cell constants and an orientation matrix for data collection were obtained from a least-squares refinement of the setting angles of 8185 reflections in the range $4° < 2\theta < 55°$. A total of 1504 frames were collected using ω scans with κ offsets, 30.0 seconds exposure time and a rotation angle of 0.5° per frame, and a crystal-detector distance of 115.0 mm.

Data reduction was performed with *CrysAlisPro*.[256] The intensities were corrected for Lorentz and polarization effects, and an empirical absorption correction using spherical harmonics[256] was applied. The space group was determined from the systematic absences, packing considerations, a statistical analysis of intensity distribution, and the successful solution and refinement of the structure. Equivalent reflections were not merged. The data collection and refinement parameters are given in **Table 7.6**. A view of the molecule is shown in **Figure 7.9**. Bond lengths, bond angles and torsion angles are given in **Table 7.12**, **Table 7.13**, and **Table 7.14**, respectively.

The structure was solved by direct methods using *SHELXS-2013*,[257] which revealed the positions of all non-hydrogen atoms. The crystals are non-merohedral twins resulting from a rotation of 180° about [103]. The twin matrix is 1 0 0 / 0 -1 0 / 0.6363 0 1 and the major twin fraction is 0.5668(10). All reflections from both twin components were integrated; a total of 6609 and 7249 non-overlapping reflections from twin components 1 and 2, respectively, plus 4785 reflections from both twin components that were overlapping by more than 80%. The non-hydrogen atoms were refined anisotropically. All of the H-atoms were placed in geometrically calculated positions and refined by using a riding model where each H-atom was assigned a fixed isotropic displacement parameter with a value equal to $1.2U_{eq}$ of its parent atom ($1.5U_{eq}$ for the methyl groups). The refinement of the structure was carried out on F^2 by using full-matrix least-squares procedures, which minimised the function $\Sigma w(F_o^2 - F_c^2)^2$. The weighting scheme was based on counting statistics and included a factor to downweight the intense reflections. Plots of $\Sigma w(F_o^2 - F_c^2)^2$ versus F_c/F_c(max) and resolution showed no unusual trends. A correction for secondary extinction was not applied. Refinement of the absolute structure parameter[258,259] yielded a value of 0.42(6).

Neutral atom scattering factors for non-hydrogen atoms were taken from Maslen, Fox and O'Keefe,[241a] and the scattering factors for H-atoms were taken from Stewart, Davidson and Simpson.[252] Anomalous dispersion effects were included in F_c;[253] the values for f' and f'' were those of Creagh and McAuley.[241b] The values of the mass attenuation coefficients are those of Creagh and Hubbel.[241c] The *SHELXL-2013* program[257] was used for all calculations.

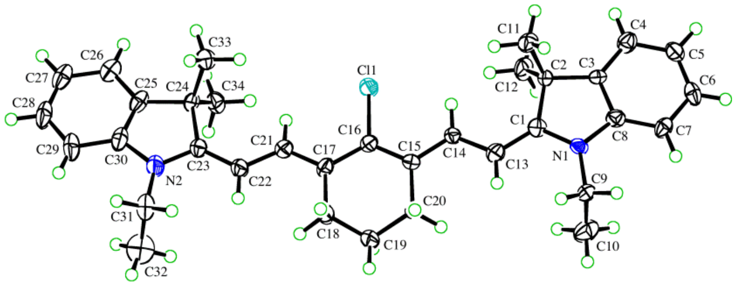

Figure 7.9. *ORTEP*[255] representation of one of the cations in **Cy7P** (50% probability ellipsoids; H-atoms given arbitrary displacement parameters for clarity).

Table 7.6. Crystallographic Data for **Cy7P** ($C_{34}H_{40}ClN_2^+$ PF_6^-).

Crystallized from		CH_2Cl_2 / Et_2O
Empirical formula		$C_{34}H_{40}ClF_6N_2P$
Formula weight [g mol^{-1}]		657.12
Crystal colour, habit		pale-green, needle
Crystal dimensions [mm]		0.10 × 0.10 × 0.40
Temperature [K]		160(1)
Crystal system		monoclinic
Space group		*Pn* (#7)
Z		8
Reflections for cell determination		8185
2θ range for cell determination [°]		4–55
Unit cell parameters	*a* [Å]	8.4401(3)
	b [Å]	24.4463(15)
	c [Å]	31.1399(11)
	α [°]	90
	β [°]	94.948(3)
	γ [°]	90
	V [Å^3]	6401.1(5)
F(000)		2752
D_X [g cm^{-3}]		1.364
μ(Mo $K\alpha$) [mm^{-1}]		0.231
Scan type		ω
$2\theta_{(\max)}$ [°]		55.8
Transmission factors (min; max)		0.654; 1.000
Total reflections measured		15439
Reflections with $I > 2\sigma(I)$		13362
Reflections used in refinement		15439
Parameters refined; restraints		1610; 2
Final	$R(F)$ [$I > 2\sigma(I)$ reflections]	0.0559
	$wR(F^2)$ (all data)	0.1467
Weights:	$w = [\sigma^2(F_o^2) + (0.0924P)^2 + 3.8130P]^{-1}$ where $P = (F_o^2 + 2F_c^2)/3$	
Goodness of fit		1.010
Final $\Delta_{\max}/\sigma$		0.000
$\Delta\rho$ (max; min) [e Å^{-3}]		0.51; -0.63
$\sigma(d_{(C-C)})$ [Å]		0.009 – 0.014

7.3.5 Crystal Structure Determination of **Cy7T** ($C_{34}H_{40}ClN_2^+$ $C_{18}C1_{12}O_6P^-$ $\cdot 1.5Et_2O$)

The structure of $C_{34}H_{40}ClN_2^+$ $C_{18}C1_{12}O_6P^-$ $\cdot 1.5Et_2O$ (**Cy7T**) has been solved and refined successfully. The asymmetric unit contains one cation, one anion and some disordered solvent molecules, which from the distribution of electron density peaks are estimated to be Et_2O. The solvent molecules could not be modelled sufficiently well, so their contribution to the diffraction data was removed by using the *SQUEEZE* procedure (see below). One methylene group in the cyclohexene ring of the cation is disordered over two positions, which can be rationalized as alternate positions of the flap of the envelope conformation of the ring.

Experimental

A crystal of $C_{34}H_{40}ClN_2^+$ $C_{18}C1_{12}O_6P^-$ $\cdot 1.5Et_2O$, obtained from diethyl ether / dichloromethane, was mounted on a glass fiber and used for a low–temperature X-ray structure determination. All measurements were made on an *Agilent Technologies SuperNova* area-detector diffractometer[256] using Cu $K\alpha$ radiation (λ = 1.54184 Å) from a micro–focus X–ray source and an *Oxford Instruments Cryojet XL* cooler. The unit cell constants and an orientation matrix for data collection were obtained from a least–squares refinement of the setting angles of 15347 reflections in the range $5° < 2\theta < 149°$. A total of 2236 frames were collected using ω scans with κ offsets, 3.0–27.0 seconds exposure time and a rotation angle of 1.0° per frame, and a crystal–detector distance of 55.0 mm.

Data reduction was performed with *CrysAlisPro*.[256] The intensities were corrected for Lorentz and polarization effects, and a numerical absorption correction[249] was applied. The space group was determined from packing considerations, a statistical analysis of intensity distribution, and the successful solution and refinement of the structure. Equivalent reflections were merged. The data collection and refinement parameters are given in **Table 7.7**. A view of the molecule is shown in **Figure 7.10**. Bond lengths, bond angles and torsion angles are given in **Table 7.15**, **Table 7.16** and **Table 7.17**, respectively.

The structure was solved by direct methods using *SHELXS97*,[257] which revealed the positions of all non–hydrogen atoms. The asymmetric unit contains one cation, one anion and some disordered solvent molecules, which from the distribution of electron density peaks are estimated to be Et_2O. The disorder of the solvent molecules could not be modelled adequately, so their contribution to the diffraction data was removed by using the *SQUEEZE* procedure[260] of the program *PLATON*.[261] Each unit cell contains one centrosymmetric cavity of 465 Å^3. The electron count in the cavity was calculated to be approximately 111 e, which can be an underbound. Three molecules of Et_2O per cavity contribute 126 e, so this assumption has been used in the calculation of the empirical formula, formula weight, density, linear absorption coefficient and $F(000)$. Based on the assumption, the ratio of cation:anion:solvent in the structure is 1:1:1.5.

One methylene group in the cyclohexene ring of the cation is disordered over two positions. Two positions were defined for this methylene group and the site occupation factor of the major conformation refined to 0.752(12). Similarity restraints were applied to the chemically equivalent bond lengths the disordered C-atom. The non-hydrogen atoms were refined anisotropically. All of the H-atoms were placed in geometrically calculated positions and refined by using a riding model where each H-atom was assigned a fixed isotropic displacement parameter with a value equal to $1.2U_{eq}$ of its parent atom ($1.5U_{eq}$ for the methyl groups). The refinement of the structure was carried out on F^2 by using full-matrix least-squares procedures, which minimised the function $\Sigma w(F_o^2 - F_c^2)^2$. The weighting scheme was based on counting statistics and included a factor to downweight the intense reflections. Plots of $\Sigma w(F_o^2 - F_c^2)^2$ versus $F_c/F_c(\max)$ and resolution showed no unusual trends. A correction for secondary extinction was not applied.

Neutral atom scattering factors for non-hydrogen atoms were taken from Maslen, Fox and O'Keefe,[241a] and the scattering factors for H-atoms were taken from Stewart, Davidson and Simpson.[252] Anomalous dispersion effects were included in F_c;[253] the values for f' and f'' were those of Creagh and McAuley.[241b] The values of the mass attenuation coefficients are those of Creagh and Hubbel.[241c] The *SHELXL97* program[257] was used for all calculations.

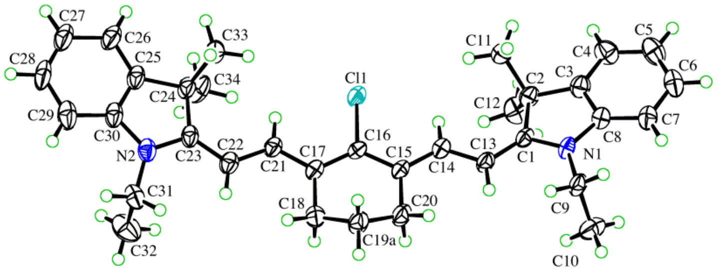

Figure 7.10. *ORTEP*[255] representation of the cation in **Cy7T** (50% probability ellipsoids; H-atoms given arbitrary displacement parameters for clarity).

Table 7.7. Crystallographic Data for **Cy7T** ($C_{34}H_{40}ClN_2^+$ $C_{18}C1_{12}O_6P^-$ $\cdot 1.5Et_2O$).

Crystallized from		CH_2Cl_2 / Et_2O
Empirical formula		$C_{58}H_{55}Cl_{13}N_2O_{7.5}P$
Formula weight [g mol^{-1}]		1391.86
Crystal colour, habit		yellow-green, needle
Crystal dimensions [mm]		0.03 × 0.04 × 0.45
Temperature [K]		160(1)
Crystal system		triclinic
Space group		$\bar{P}$ 1 (#2)
Z		2
Reflections for cell determination		15347
2θ range for cell determination [°]		5–149
Unit cell parameters	a [Å]	12.8224(3)
	b [Å]	14.2116(3)
	c [Å]	18.3477(4)
	α [°]	98.9303(18)
	β [°]	107.070(2)
	γ [°]	101.931(2)
	V [Å^3]	3042.62(12)
$F(000)$		1426
D_X [g cm^{-3}]		1.519
μ(Cu $K\alpha$) [mm^{-1}]		6.105
Scan type		ω
$2\theta_{(\max)}$ [°]		149.1
Transmission factors (min; max)		0.435; 1.159
Total reflections measured		39423
Symmetry independent reflections		12155
R_{int}		0.105
Reflections with $I > 2\sigma(I)$		9250
Reflections used in refinement		12155
Parameters refined; restraints		683; 6
Final	$R(F)$ [$I > 2\sigma(I)$ reflections]	0.0643
	$wR(F^2)$ (all data)	0.1825
Weights:	$w = [\sigma^2(F_o^2) + (0.1175P)^2]^{-1}$ where $P = (F_o^2 + 2F_c^2)/3$	
Goodness of fit		1.000
Final $\Delta_{\max}/\sigma$		0.001
$\Delta\rho$ (max; min) [e Å^{-3}]		0.70; -0.73
$\sigma(d_{(C-C)})$ [Å]		0.004 – 0.007

7.3.6 Crystal Structure Determination of **Cy7-PbI$_3$** (($C_{34}H_{40}ClN_2^+$)$_n$[PbI_3^-]$_n$·2n(DMF))

The structure of ($C_{34}H_{40}ClN_2^+$)$_n$[PbI_3^-]$_n$·2n(DMF) (**Cy7-PbI$_3$**) has been solved and refined successfully. The asymmetric unit contains one organic cation, one PbI_3^- fragment of a [PbI_3^-]$_n$ chain and two DMF molecules. The DMF molecules could be somewhat disordered, but no attempt has been made to model the disorder. A test refinement using the *SQUEEZE* procedure of *PLATON*[262] to account for the solvent, instead of modelling these molecules, did not yield significantly improved results, so the solvent molecules were retained in the final refinement model.

The available crystals were extremely thin needles, and even then, the chosen crystal was not a perfect single crystal. The reconstructed synthetic precession images showed there was at least one other set of reflections from another crystal orientation. However, these reflections could be ignored without unduly affecting the quality of the used reflection data. The size of the crystal necessitated the use of Cu *K*α radiation to gain sufficient diffraction intensity, despite the presence of Pb– and I–atoms, but again, after absorption corrections, this did not unduly affect the quality of the data.

The anions form columns, which run parallel to the [001] direction, with the cations and DMF molecules dispersed between the columns. Each pair of Pb(II) ions within the columns is bridged by three iodide ions.

Experimental

A crystal of ($C_{34}H_{40}ClN_2^+$)$_n$[PbI_3^-]$_n$·2n(DMF), obtained from DMF, was mounted on a glass fibre and used for a low–temperature X–ray structure determination. All measurements were made on an *Agilent Technologies SuperNova* area–detector diffractometer[248] using Cu *K*α radiation (λ = 1.54184 Å) from a micro–focus X–ray source and an *Oxford Instruments Cryojet XL* cooler. The unit cell constants and an orientation matrix for data collection were obtained from a least–squares refinement of the setting angles of 13827 reflections in the range $7° < 2\theta < 152°$. A total of 1790 frames were collected using ω scans with κ offsets, 10.0–30.0 seconds exposure time and a rotation angle of 0.5° per frame, and a crystal–detector distance of 55.0 mm.

Data reduction was performed with *CrysAlisPro*.[248] The intensities were corrected for Lorentz and polarization effects, and an empirical absorption correction using spherical harmonics[248] was applied. The space group was uniquely determined by the systematic absences. Equivalent reflections were merged. The data collection and refinement parameters are given in **Table 7.8**. A view of the molecule is shown in **Figure 7.11**. Bond lengths, bond angles and torsion angles are given in **Table 7.18**, **Table 7.19** and **Table 7.20**, respectively.

The structure was solved by dual space methods using *SHELXT-2014*,[250] which revealed the positions of all non-hydrogen atoms. The non-hydrogen atoms were refined anisotropically. All of the H-atoms were placed in geometrically calculated positions and refined by using a riding model where each H-atom was assigned a fixed isotropic displacement parameter with a value equal to $1.2U_{eq}$ of its parent atom ($1.5U_{eq}$ for the methyl groups). The refinement of the structure was carried out on F^2 by using full-matrix least-squares procedures, which minimised the function $\Sigma w(F_o{}^2 - F_c{}^2)^2$. The weighting scheme was based on counting statistics and included a factor to downweight the intense reflections. Plots of $\Sigma w(F_o{}^2 - F_c{}^2)^2$ versus F_c/F_c(max) and resolution showed no unusual trends. A correction for secondary extinction was not applied.

Neutral atom scattering factors for non-hydrogen atoms were taken from Maslen, Fox and O'Keefe,[241a] and the scattering factors for H–atoms were taken from Stewart, Davidson and Simpson.[252] Anomalous dispersion effects were included in F_c;[253] the values for f' and f'' were those of Creagh and McAuley.[241b] The values of the mass attenuation coefficients are those of Creagh and Hubbel.[241c] The *SHELXL–2014* program[254] was used for all calculations.

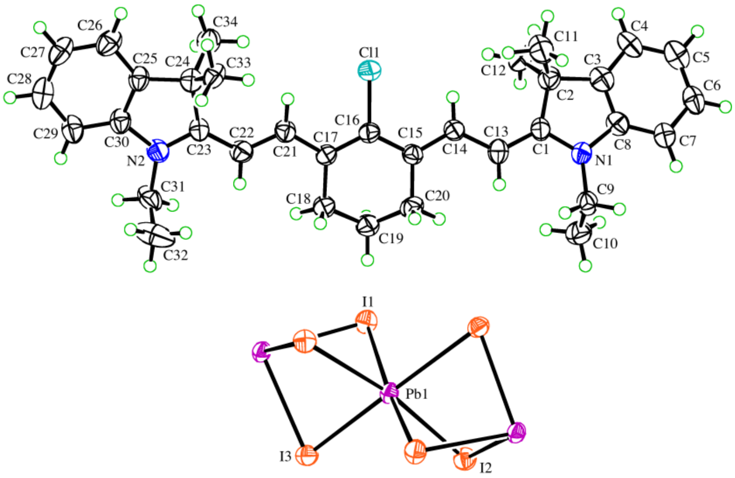

Figure 7.11. *ORTEP*[255] representation of the cation and part of the anionic chain in **Cy7-PbI$_3$** (50% probability ellipsoids; H-atoms given arbitrary displacement parameters for clarity).

Table 7.8. Crystallographic Data for **Cy7-PbI$_3$** $(C_{34}H_{40}ClN_2^{+})_n[PbI_3^{-}]_n \cdot 2n(DMF)$.

Crystallized from		DMF
Empirical formula		$C_{40}H_{54}ClI_3N_4O_2Pb$
Formula weight [g mol^{-1}]		1246.21
Crystal colour, habit		green, needle
Crystal dimensions [mm]		0.02 × 0.03 × 0.12
Temperature [K]		160(1)
Crystal system		monoclinic
Space group		$P2_1/c$ (#14)
Z		4
Reflections for cell determination		13827
2θ range for cell determination [°]		7–152
Unit cell parameters	a [Å]	16.3649(7)
	b [Å]	33.5729(10)
	c [Å]	8.0898(3)
	α [°]	90
	β [°]	97.210(4)
	γ [°]	90
	V [Å^3]	4409.5(3)
$F(000)$		2384
D_x [g cm^{-3}]		1.877
μ(Cu $K\alpha$) [mm^{-1}]		24.771
Scan type		ω
$2\theta_{(\max)}$ [°]		155.0
Transmission factors (min; max)		0.469; 1.000
Total reflections measured		45548
Symmetry independent reflections		9174
R_{int}		0.101
Reflections with $I > 2\sigma(I)$		7351
Reflections used in refinement		9174
Parameters refined		470
Final	$R(F)$ [$I > 2\sigma(I)$ reflections]	0.0519
	$wR(F^2)$ (all data)	0.1324
Weights:	$w = [\sigma^2(F_o^2) + (0.0456P)^2 + 23.44P]^{-1}$ where $P = (F_o^2 + 2F_c^2)/3$	
Goodness of fit		1.054
Final $\Delta_{\max}/\sigma$		0.001
$\Delta\rho$ (max; min) [e Å^{-3}]		1.67; -1.50
$\sigma(d_{(C-C)})$ [Å]		0.012 – 0.018

7.3.7 Bond Lengths, Bond Angles and Torsion Angles

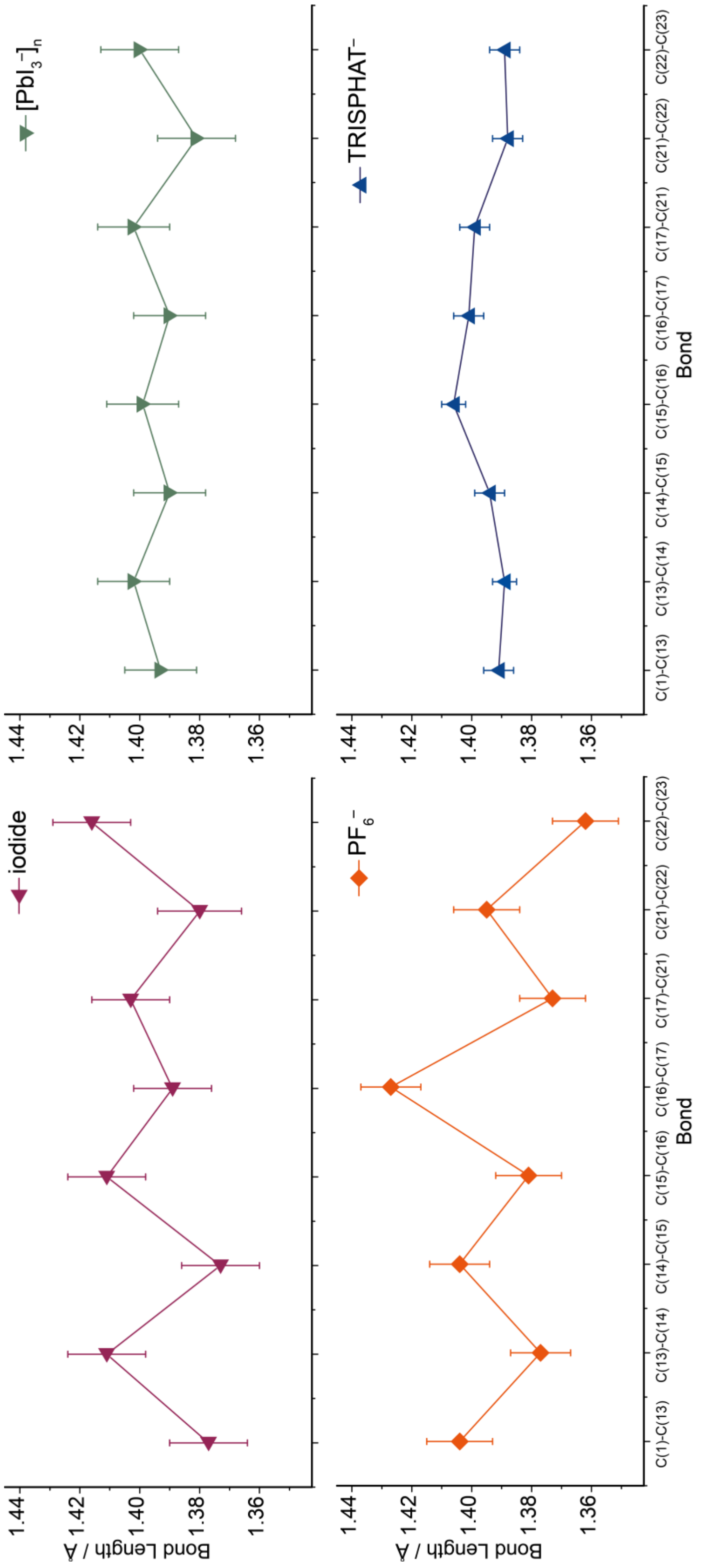

Figure 7.12. C–C bond lengths in the polymethine chain of cyanine cations with different counterions for visualization of the bond length alternation. Iodide (**Cy7I**), PF$_6^-$ (**Cy7P**), TRISPHAT$^-$ (**Cy7T**) and [PbI$_3^-$]$_n$ (**Cy7–PbI$_3$**).

Table 7.9. Bond lengths (Å) in **Cy7I** with standard uncertainties in parentheses.

Cl(1)	-C(16)	1.756(9)	C(15)	-C(16)	1.411(13)
N(1)	-C(1)	1.362(12)	C(15)	-C(20)	1.511(13)
N(1)	-C(8)	1.401(12)	C(16)	-C(17)	1.389(13)
N(1)	-C(9)	1.468(12)	C(17)	-C(21)	1.403(13)
N(2)	-C(23)	1.337(12)	C(17)	-C(18)	1.501(12)
N(2)	-C(30)	1.414(12)	C(18)	-C(19)	1.511(14)
N(2)	-C(31)	1.477(11)	C(19)	-C(20)	1.514(15)
C(1)	-C(13)	1.377(13)	C(21)	-C(22)	1.380(14)
C(1)	-C(2)	1.534(13)	C(22)	-C(23)	1.416(13)
C(2)	-C(3)	1.490(13)	C(23)	-C(24)	1.527(12)
C(2)	-C(11)	1.531(14)	C(24)	-C(25)	1.509(14)
C(2)	-C(12)	1.547(13)	C(24)	-C(34)	1.527(13)
C(3)	-C(4)	1.381(14)	C(24)	-C(33)	1.532(13)
C(3)	-C(8)	1.384(12)	C(25)	-C(26)	1.396(13)
C(4)	-C(5)	1.380(15)	C(25)	-C(30)	1.406(13)
C(5)	-C(6)	1.382(16)	C(26)	-C(27)	1.360(16)
C(6)	-C(7)	1.394(15)	C(27)	-C(28)	1.390(15)
C(7)	-C(8)	1.387(13)	C(28)	-C(29)	1.379(15)
C(9)	-C(10)	1.511(14)	C(29)	-C(30)	1.378(13)
C(13)	-C(14)	1.411(13)	C(31)	-C(32)	1.515(15)
C(14)	-C(15)	1.373(13)			

Table 7.10. Bond angles (°) in **Cy7I** with standard uncertainties in parentheses.

C(1)	-N(1)	-C(8)	111.2(7)	C(17)	-C(16)	-C(15)	126.2(8)
C(1)	-N(1)	-C(9)	125.3(8)	C(17)	-C(16)	-Cl(1)	117.5(7)
C(8)	-N(1)	-C(9)	123.4(8)	C(15)	-C(16)	-Cl(1)	116.3(7)
C(23)	-N(2)	-C(30)	111.7(8)	C(16)	-C(17)	-C(21)	122.0(9)
C(23)	-N(2)	-C(31)	125.8(8)	C(16)	-C(17)	-C(18)	118.5(8)
C(30)	-N(2)	-C(31)	122.5(8)	C(21)	-C(17)	-C(18)	119.5(9)
N(1)	-C(1)	-C(13)	122.8(9)	C(17)	-C(18)	-C(19)	112.9(8)
N(1)	-C(1)	-C(2)	108.0(8)	C(18)	-C(19)	-C(20)	111.7(8)
C(13)	-C(1)	-C(2)	129.2(9)	C(15)	-C(20)	-C(19)	111.8(8)
C(3)	-C(2)	-C(11)	111.6(8)	C(22)	-C(21)	-C(17)	125.3(9)
C(3)	-C(2)	-C(1)	101.7(8)	C(21)	-C(22)	-C(23)	125.0(9)
C(11)	-C(2)	-C(1)	113.4(8)	N(2)	-C(23)	-C(22)	121.5(9)
C(3)	-C(2)	-C(12)	109.4(8)	N(2)	-C(23)	-C(24)	110.3(8)
C(11)	-C(2)	-C(12)	110.8(8)	C(22)	-C(23)	-C(24)	128.0(9)
C(1)	-C(2)	-C(12)	109.6(8)	C(25)	-C(24)	-C(34)	111.7(8)
C(4)	-C(3)	-C(8)	118.5(9)	C(25)	-C(24)	-C(23)	100.2(8)
C(4)	-C(3)	-C(2)	131.7(9)	C(34)	-C(24)	-C(23)	111.4(8)
C(8)	-C(3)	-C(2)	109.8(8)	C(25)	-C(24)	-C(33)	109.2(8)
C(5)	-C(4)	-C(3)	120.2(10)	C(34)	-C(24)	-C(33)	111.1(8)
C(4)	-C(5)	-C(6)	120.7(10)	C(23)	-C(24)	-C(33)	112.7(8)
C(5)	-C(6)	-C(7)	120.5(10)	C(26)	-C(25)	-C(30)	117.9(9)
C(8)	-C(7)	-C(6)	117.5(10)	C(26)	-C(25)	-C(24)	131.7(9)
C(3)	-C(8)	-C(7)	122.7(9)	C(30)	-C(25)	-C(24)	110.3(8)
C(3)	-C(8)	-N(1)	109.0(8)	C(27)	-C(26)	-C(25)	119.6(10)
C(7)	-C(8)	-N(1)	128.3(9)	C(26)	-C(27)	-C(28)	121.1(10)
N(1)	-C(9)	-C(10)	112.9(8)	C(29)	-C(28)	-C(27)	121.6(10)
C(1)	-C(13)	-C(14)	124.6(9)	C(30)	-C(29)	-C(28)	116.7(10)
C(15)	-C(14)	-C(13)	126.2(9)	C(29)	-C(30)	-C(25)	123.2(10)
C(14)	-C(15)	-C(16)	124.4(9)	C(29)	-C(30)	-N(2)	129.5(9)
C(14)	-C(15)	-C(20)	120.4(9)	C(25)	-C(30)	-N(2)	107.3(8)
C(16)	-C(15)	-C(20)	115.2(8)	N(2)	-C(31)	-C(32)	111.2(9)

Table 7.11. Torsion angles (°) in **Cy7I** with standard uncertainties in parentheses.

C(8)	-N(1)	-C(1)	-C(13)	-172.6(9)	Cl(1)	-C(16)	-C(17)	-C(18)	-176.6(7)
C(9)	-N(1)	-C(1)	-C(13)	4(1)	C(16)	-C(17)	-C(18)	-C(19)	19(1)
C(8)	-N(1)	-C(1)	-C(2)	6(1)	C(21)	-C(17)	-C(18)	-C(19)	-161.4(9)
C(9)	-N(1)	-C(1)	-C(2)	-178.0(8)	C(17)	-C(18)	-C(19)	-C(20)	-48(1)
N(1)	-C(1)	-C(2)	-C(3)	-6(1)	C(14)	-C(15)	-C(20)	-C(19)	144.8(9)
C(13)	-C(1)	-C(2)	-C(3)	172(1)	C(16)	-C(15)	-C(20)	-C(19)	-34(1)
N(1)	-C(1)	-C(2)	-C(11)	-126.1(9)	C(18)	-C(19)	-C(20)	-C(15)	56(1)
C(13)	-C(1)	-C(2)	-C(11)	52(1)	C(16)	-C(17)	-C(21)	-C(22)	-173(1)
N(1)	-C(1)	-C(2)	-C(12)	109.6(9)	C(18)	-C(17)	-C(21)	-C(22)	7(2)
C(13)	-C(1)	-C(2)	-C(12)	-72(1)	C(17)	-C(21)	-C(22)	-C(23)	179(1)
C(11)	-C(2)	-C(3)	-C(4)	-56(1)	C(30)	-N(2)	-C(23)	-C(22)	-178.8(9)
C(1)	-C(2)	-C(3)	-C(4)	-177(1)	C(31)	-N(2)	-C(23)	-C(22)	-1(2)
C(12)	-C(2)	-C(3)	-C(4)	67(1)	C(30)	-N(2)	-C(23)	-C(24)	-4(1)
C(11)	-C(2)	-C(3)	-C(8)	125.5(9)	C(31)	-N(2)	-C(23)	-C(24)	174.0(9)
C(1)	-C(2)	-C(3)	-C(8)	4(1)	C(21)	-C(22)	-C(23)	-N(2)	-178(1)
C(12)	-C(2)	-C(3)	-C(8)	-111.5(9)	C(21)	-C(22)	-C(23)	-C(24)	7(2)
C(8)	-C(3)	-C(4)	-C(5)	1(1)	N(2)	-C(23)	-C(24)	-C(25)	3(1)
C(2)	-C(3)	-C(4)	-C(5)	-177.6(9)	C(22)	-C(23)	-C(24)	-C(25)	178(1)
C(3)	-C(4)	-C(5)	-C(6)	0(2)	N(2)	-C(23)	-C(24)	-C(34)	-115(1)
C(4)	-C(5)	-C(6)	-C(7)	-1(2)	C(22)	-C(23)	-C(24)	-C(34)	60(1)
C(5)	-C(6)	-C(7)	-C(8)	0(1)	N(2)	-C(23)	-C(24)	-C(33)	119(1)
C(4)	-C(3)	-C(8)	-C(7)	-1(1)	C(22)	-C(23)	-C(24)	-C(33)	-66(1)
C(2)	-C(3)	-C(8)	-C(7)	177.5(8)	C(34)	-C(24)	-C(25)	-C(26)	-66(1)
C(4)	-C(3)	-C(8)	-N(1)	179.9(8)	C(23)	-C(24)	-C(25)	-C(26)	176(1)
C(2)	-C(3)	-C(8)	-N(1)	-1(1)	C(33)	-C(24)	-C(25)	-C(26)	58(1)
C(6)	-C(7)	-C(8)	-C(3)	1(1)	C(34)	-C(24)	-C(25)	-C(30)	116.2(9)
C(6)	-C(7)	-C(8)	-N(1)	179.1(9)	C(23)	-C(24)	-C(25)	-C(30)	-2(1)
C(1)	-N(1)	-C(8)	-C(3)	-3(1)	C(33)	-C(24)	-C(25)	-C(30)	-120.5(9)
C(9)	-N(1)	-C(8)	-C(3)	-179.3(8)	C(30)	-C(25)	-C(26)	-C(27)	0(2)
C(1)	-N(1)	-C(8)	-C(7)	178.3(9)	C(24)	-C(25)	-C(26)	-C(27)	-178(1)
C(9)	-N(1)	-C(8)	-C(7)	2(1)	C(25)	-C(26)	-C(27)	-C(28)	0(2)
C(1)	-N(1)	-C(9)	-C(10)	-87(1)	C(26)	-C(27)	-C(28)	-C(29)	0(2)
C(8)	-N(1)	-C(9)	-C(10)	88(1)	C(27)	-C(28)	-C(29)	-C(30)	1(2)
N(1)	-C(1)	-C(13)	-C(14)	-176.0(9)	C(28)	-C(29)	-C(30)	-C(25)	-1(1)
C(2)	-C(1)	-C(13)	-C(14)	6(2)	C(28)	-C(29)	-C(30)	-N(2)	178.1(9)
C(1)	-C(13)	-C(14)	-C(15)	-174(1)	C(26)	-C(25)	-C(30)	-C(29)	1(1)
C(13)	-C(14)	-C(15)	-C(16)	-173.7(9)	C(24)	-C(25)	-C(30)	-C(29)	179.6(9)
C(13)	-C(14)	-C(15)	-C(20)	7(2)	C(26)	-C(25)	-C(30)	-N(2)	-178.5(9)
C(14)	-C(15)	-C(16)	-C(17)	-174(1)	C(24)	-C(25)	-C(30)	-N(2)	0(1)
C(20)	-C(15)	-C(16)	-C(17)	5(1)	C(23)	-N(2)	-C(30)	-C(29)	-177.3(9)
C(14)	-C(15)	-C(16)	-Cl(1)	6(1)	C(31)	-N(2)	-C(30)	-C(29)	5(2)
C(20)	-C(15)	-C(16)	-Cl(1)	-175.4(7)	C(23)	-N(2)	-C(30)	-C(25)	2(1)
C(15)	-C(16)	-C(17)	-C(21)	-176.6(9)	C(31)	-N(2)	-C(30)	-C(25)	-175.5(8)
Cl(1)	-C(16)	-C(17)	-C(21)	4(1)	C(23)	-N(2)	-C(31)	-C(32)	-82(1)
C(15)	-C(16)	-C(17)	-C(18)	3(2)	C(30)	-N(2)	-C(31)	-C(32)	95(1)

Table 7.12. Bond lengths (Å) in **Cy7P** with standard uncertainties in parentheses.

Cl(1)	-C(16)	1.743(8)
N(1)	-C(1)	1.344(9)
N(1)	-C(8)	1.391(10)
N(1)	-C(9)	1.480(9)
N(2)	-C(23)	1.371(10)
N(2)	-C(30)	1.404(11)
N(2)	-C(31)	1.517(12)
C(1)	-C(13)	1.404(11)
C(1)	-C(2)	1.536(10)
C(2)	-C(3)	1.500(10)
C(2)	-C(11)	1.523(10)
C(2)	-C(12)	1.525(11)
C(3)	-C(8)	1.380(10)
C(3)	-C(4)	1.387(11)
C(4)	-C(5)	1.393(12)
C(5)	-C(6)	1.388(12)
C(6)	-C(7)	1.381(11)
C(7)	-C(8)	1.399(11)
C(9)	-C(10)	1.513(11)
C(13)	-C(14)	1.377(10)
C(14)	-C(15)	1.404(10)
C(15)	-C(16)	1.381(11)
C(15)	-C(20)	1.502(10)
C(16)	-C(17)	1.427(10)
C(17)	-C(21)	1.373(11)
C(17)	-C(18)	1.517(11)
C(18)	-C(19)	1.464(12)
C(19)	-C(20)	1.512(11)
C(21)	-C(22)	1.395(11)
C(22)	-C(23)	1.362(11)
C(23)	-C(24)	1.544(11)
C(24)	-C(34)	1.516(12)
C(24)	-C(25)	1.516(10)
C(24)	-C(33)	1.527(11)
C(25)	-C(26)	1.366(12)
C(25)	-C(30)	1.382(13)
C(26)	-C(27)	1.394(12)
C(27)	-C(28)	1.382(14)
C(28)	-C(29)	1.378(13)
C(29)	-C(30)	1.394(11)
C(31)	-C(32)	1.424(14)
Cl(2)	-C(56)	1.747(8)
N(3)	-C(41)	1.344(9)
N(3)	-C(48)	1.437(9)
N(3)	-C(49)	1.463(9)
N(4)	-C(63)	1.369(10)
C(83)	-C(88)	1.384(11)
C(83)	-C(84)	1.389(11)
C(84)	-C(85)	1.377(13)
C(85)	-C(86)	1.376(13)
C(86)	-C(87)	1.360(12)
C(87)	-C(88)	1.392(10)
C(89)	-C(90)	1.502(12)
C(93)	-C(94)	1.366(10)
C(94)	-C(95)	1.399(10)
C(95)	-C(96)	1.393(10)
C(95)	-C(100)	1.517(10)
C(96)	-C(97)	1.410(10)
C(97)	-C(101)	1.363(10)
C(97)	-C(98)	1.506(11)
C(98)	-C(99)	1.502(11)
C(99)	-C(100)	1.511(10)
C(101)	-C(102)	1.421(10)
C(102)	-C(103)	1.389(11)
C(103)	-C(104)	1.519(12)
C(104)	-C(105)	1.505(10)
C(104)	-C(114)	1.536(12)
C(104)	-C(113)	1.542(11)
C(105)	-C(106)	1.374(11)
C(105)	-C(110)	1.404(12)
C(106)	-C(107)	1.388(12)
C(107)	-C(108)	1.355(14)
C(108)	-C(109)	1.395(13)
C(109)	-C(110)	1.404(11)
C(111)	-C(112)	1.553(11)
Cl(4)	-C(136)	1.740(8)
N(7)	-C(121)	1.370(9)
N(7)	-C(128)	1.407(9)
N(7)	-C(129)	1.459(10)
N(8)	-C(143)	1.343(9)
N(8)	-C(150)	1.418(9)
N(8)	-C(151)	1.460(9)
C(121)	-C(133)	1.363(11)
C(121)	-C(122)	1.543(10)
C(122)	-C(123)	1.504(10)
C(122)	-C(131)	1.532(11)
C(122)	-C(132)	1.535(11)
C(123)	-C(124)	1.385(11)
C(123)	-C(128)	1.387(11)
C(124)	-C(125)	1.373(12)
C(125)	-C(126)	1.395(13)
C(126)	-C(127)	1.388(12)

N(4)	-C(70)	1.409(10)	C(127)	-C(128)	1.386(10)
N(4)	-C(71)	1.460(12)	C(129)	-C(130)	1.484(12)
C(41)	-C(53)	1.415(10)	C(133)	-C(134)	1.411(10)
C(41)	-C(42)	1.495(10)	C(134)	-C(135)	1.367(10)
C(42)	-C(43)	1.533(10)	C(135)	-C(136)	1.444(10)
C(42)	-C(52)	1.536(10)	C(135)	-C(140)	1.519(10)
C(42)	-C(51)	1.539(10)	C(136)	-C(137)	1.364(11)
C(43)	-C(44)	1.364(11)	C(137)	-C(141)	1.432(9)
C(43)	-C(48)	1.372(10)	C(137)	-C(138)	1.500(10)
C(44)	-C(45)	1.374(12)	C(138)	-C(139)	1.523(9)
C(45)	-C(46)	1.391(12)	C(139)	-C(140)	1.515(11)
C(46)	-C(47)	1.375(11)	C(141)	-C(142)	1.372(10)
C(47)	-C(48)	1.383(10)	C(142)	-C(143)	1.421(10)
C(49)	-C(50)	1.504(10)	C(143)	-C(144)	1.512(10)
C(53)	-C(54)	1.377(10)	C(144)	-C(145)	1.507(10)
C(54)	-C(55)	1.395(10)	C(144)	-C(153)	1.512(11)
C(55)	-C(56)	1.426(10)	C(144)	-C(154)	1.546(10)
C(55)	-C(60)	1.500(10)	C(145)	-C(146)	1.372(11)
C(56)	-C(57)	1.394(11)	C(145)	-C(150)	1.402(10)
C(57)	-C(61)	1.381(11)	C(146)	-C(147)	1.436(12)
C(57)	-C(58)	1.492(12)	C(147)	-C(148)	1.358(13)
C(58)	-C(59)	1.527(12)	C(148)	-C(149)	1.394(11)
C(59)	-C(60)	1.515(10)	C(149)	-C(150)	1.363(10)
C(61)	-C(62)	1.412(11)	C(151)	-C(152)	1.553(12)
C(62)	-C(63)	1.380(11)	P(1)	-F(5)	1.569(5)
C(63)	-C(64)	1.529(11)	P(1)	-F(3)	1.578(6)
C(64)	-C(65)	1.500(10)	P(1)	-F(6)	1.583(6)
C(64)	-C(73)	1.533(11)	P(1)	-F(1)	1.585(6)
C(64)	-C(74)	1.537(11)	P(1)	-F(4)	1.585(5)
C(65)	-C(66)	1.378(12)	P(1)	-F(2)	1.594(5)
C(65)	-C(70)	1.394(12)	P(2)	-F(9)	1.567(7)
C(66)	-C(67)	1.393(12)	P(2)	-F(7)	1.569(7)
C(67)	-C(68)	1.373(13)	P(2)	-F(10)	1.593(6)
C(68)	-C(69)	1.384(12)	P(2)	-F(8)	1.597(6)
C(69)	-C(70)	1.394(11)	P(2)	-F(11)	1.597(6)
C(71)	-C(72)	1.518(13)	P(2)	-F(12)	1.600(5)
Cl(3)	-C(96)	1.750(8)	P(3)	-F(18)	1.575(6)
N(5)	-C(81)	1.334(9)	P(3)	-F(17)	1.581(6)
N(5)	-C(88)	1.395(10)	P(3)	-F(14)	1.582(6)
N(5)	-C(89)	1.475(9)	P(3)	-F(15)	1.595(5)
N(6)	-C(103)	1.371(10)	P(3)	-F(13)	1.596(5)
N(6)	-C(110)	1.380(10)	P(3)	-F(16)	1.605(6)
N(6)	-C(111)	1.446(11)	P(4)	-F(24)	1.564(6)
C(81)	-C(93)	1.408(10)	P(4)	-F(20)	1.571(5)
C(81)	-C(82)	1.508(10)	P(4)	-F(22)	1.582(7)
C(82)	-C(83)	1.533(10)	P(4)	-F(19)	1.594(6)
C(82)	-C(91)	1.533(11)	P(4)	-F(23)	1.601(6)
C(82)	-C(92)	1.541(10)	P(4)	-F(21)	1.609(6)

Table 7.13. Bond angles (°) in **Cy7P** with standard uncertainties in parentheses.

C(1)	-N(1)	-C(8)	111.6(6)	C(94)	-C(95)	-C(100)	119.1(6)
C(1)	-N(1)	-C(9)	125.4(7)	C(95)	-C(96)	-C(97)	125.2(7)
C(8)	-N(1)	-C(9)	122.8(6)	C(95)	-C(96)	-Cl(3)	117.8(6)
C(23)	-N(2)	-C(30)	111.2(8)	C(97)	-C(96)	-Cl(3)	116.9(6)
C(23)	-N(2)	-C(31)	125.9(7)	C(101)	-C(97)	-C(96)	123.1(7)
C(30)	-N(2)	-C(31)	122.8(7)	C(101)	-C(97)	-C(98)	120.8(7)
N(1)	-C(1)	-C(13)	121.5(7)	C(96)	-C(97)	-C(98)	116.1(7)
N(1)	-C(1)	-C(2)	108.3(6)	C(99)	-C(98)	-C(97)	111.9(7)
C(13)	-C(1)	-C(2)	130.2(7)	C(98)	-C(99)	-C(100)	112.0(6)
C(3)	-C(2)	-C(11)	110.6(6)	C(99)	-C(100)	-C(95)	112.2(6)
C(3)	-C(2)	-C(12)	110.5(6)	C(97)	-C(101)	-C(102)	125.0(8)
C(11)	-C(2)	-C(12)	111.3(6)	C(103)	-C(102)	-C(101)	123.9(8)
C(3)	-C(2)	-C(1)	100.9(6)	N(6)	-C(103)	-C(102)	121.6(8)
C(11)	-C(2)	-C(1)	109.0(7)	N(6)	-C(103)	-C(104)	109.1(7)
C(12)	-C(2)	-C(1)	114.2(6)	C(102)	-C(103)	-C(104)	129.2(8)
C(8)	-C(3)	-C(4)	120.7(7)	C(105)	-C(104)	-C(103)	101.4(7)
C(8)	-C(3)	-C(2)	109.6(7)	C(105)	-C(104)	-C(114)	111.2(7)
C(4)	-C(3)	-C(2)	129.7(7)	C(103)	-C(104)	-C(114)	113.0(7)
C(3)	-C(4)	-C(5)	117.2(8)	C(105)	-C(104)	-C(113)	107.8(6)
C(6)	-C(5)	-C(4)	121.9(8)	C(103)	-C(104)	-C(113)	110.3(7)
C(7)	-C(6)	-C(5)	121.0(8)	C(114)	-C(104)	-C(113)	112.5(7)
C(6)	-C(7)	-C(8)	116.8(7)	C(106)	-C(105)	-C(110)	120.4(8)
C(3)	-C(8)	-N(1)	108.9(7)	C(106)	-C(105)	-C(104)	131.0(8)
C(3)	-C(8)	-C(7)	122.3(7)	C(110)	-C(105)	-C(104)	108.6(7)
N(1)	-C(8)	-C(7)	128.7(7)	C(105)	-C(106)	-C(107)	119.1(10)
N(1)	-C(9)	-C(10)	110.7(7)	C(108)	-C(107)	-C(106)	120.6(8)
C(14)	-C(13)	-C(1)	122.6(7)	C(107)	-C(108)	-C(109)	122.5(8)
C(13)	-C(14)	-C(15)	124.0(7)	C(108)	-C(109)	-C(110)	116.8(9)
C(16)	-C(15)	-C(14)	122.2(7)	N(6)	-C(110)	-C(105)	109.8(7)
C(16)	-C(15)	-C(20)	119.1(7)	N(6)	-C(110)	-C(109)	129.7(9)
C(14)	-C(15)	-C(20)	118.7(7)	C(105)	-C(110)	-C(109)	120.5(8)
C(15)	-C(16)	-C(17)	125.4(7)	N(6)	-C(111)	-C(112)	113.9(8)
C(15)	-C(16)	-Cl(1)	118.2(6)	C(121)	-N(7)	-C(128)	111.3(6)
C(17)	-C(16)	-Cl(1)	116.3(6)	C(121)	-N(7)	-C(129)	125.1(6)
C(21)	-C(17)	-C(16)	124.3(8)	C(128)	-N(7)	-C(129)	123.4(6)
C(21)	-C(17)	-C(18)	120.6(7)	C(143)	-N(8)	-C(150)	110.5(6)
C(16)	-C(17)	-C(18)	114.9(7)	C(143)	-N(8)	-C(151)	128.1(7)
C(19)	-C(18)	-C(17)	112.5(8)	C(150)	-N(8)	-C(151)	121.2(6)
C(18)	-C(19)	-C(20)	113.7(8)	C(133)	-C(121)	-N(7)	122.4(7)
C(15)	-C(20)	-C(19)	112.7(7)	C(133)	-C(121)	-C(122)	129.5(7)
C(17)	-C(21)	-C(22)	125.9(8)	N(7)	-C(121)	-C(122)	108.1(6)
C(23)	-C(22)	-C(21)	125.8(8)	C(123)	-C(122)	-C(131)	110.5(6)
C(22)	-C(23)	-N(2)	124.3(8)	C(123)	-C(122)	-C(132)	110.7(7)
C(22)	-C(23)	-C(24)	127.6(7)	C(131)	-C(122)	-C(132)	112.3(7)
N(2)	-C(23)	-C(24)	108.1(7)	C(123)	-C(122)	-C(121)	101.3(6)
C(34)	-C(24)	-C(25)	110.4(6)	C(131)	-C(122)	-C(121)	110.7(6)

C(34)	-C(24)	-C(33)	111.9(7)	C(132)	-C(122)	-C(121)	110.9(7)
C(25)	-C(24)	-C(33)	109.0(7)	C(124)	-C(123)	-C(128)	119.4(7)
C(34)	-C(24)	-C(23)	112.3(7)	C(124)	-C(123)	-C(122)	130.6(8)
C(25)	-C(24)	-C(23)	101.2(7)	C(128)	-C(123)	-C(122)	110.0(7)
C(33)	-C(24)	-C(23)	111.5(6)	C(125)	-C(124)	-C(123)	119.5(8)
C(26)	-C(25)	-C(30)	119.8(8)	C(124)	-C(125)	-C(126)	120.1(8)
C(26)	-C(25)	-C(24)	130.6(9)	C(127)	-C(126)	-C(125)	122.0(8)
C(30)	-C(25)	-C(24)	109.5(7)	C(128)	-C(127)	-C(126)	116.2(8)
C(25)	-C(26)	-C(27)	119.2(9)	C(127)	-C(128)	-C(123)	122.8(7)
C(28)	-C(27)	-C(26)	119.6(9)	C(127)	-C(128)	-N(7)	128.2(8)
C(29)	-C(28)	-C(27)	122.9(8)	C(123)	-C(128)	-N(7)	108.9(6)
C(28)	-C(29)	-C(30)	115.6(10)	N(7)	-C(129)	-C(130)	112.4(8)
C(25)	-C(30)	-C(29)	122.9(9)	C(121)	-C(133)	-C(134)	125.2(7)
C(25)	-C(30)	-N(2)	109.6(7)	C(135)	-C(134)	-C(133)	124.8(7)
C(29)	-C(30)	-N(2)	127.4(10)	C(134)	-C(135)	-C(136)	123.2(7)
C(32)	-C(31)	-N(2)	109.8(9)	C(134)	-C(135)	-C(140)	121.1(7)
C(41)	-N(3)	-C(48)	109.2(6)	C(136)	-C(135)	-C(140)	115.6(7)
C(41)	-N(3)	-C(49)	127.3(7)	C(137)	-C(136)	-C(135)	123.8(7)
C(48)	-N(3)	-C(49)	123.5(6)	C(137)	-C(136)	-Cl(4)	119.8(6)
C(63)	-N(4)	-C(70)	110.5(7)	C(135)	-C(136)	-Cl(4)	116.3(6)
C(63)	-N(4)	-C(71)	127.1(7)	C(136)	-C(137)	-C(141)	120.7(7)
C(70)	-N(4)	-C(71)	122.3(7)	C(136)	-C(137)	-C(138)	120.8(6)
N(3)	-C(41)	-C(53)	119.8(7)	C(141)	-C(137)	-C(138)	118.4(6)
N(3)	-C(41)	-C(42)	111.5(7)	C(137)	-C(138)	-C(139)	111.7(6)
C(53)	-C(41)	-C(42)	128.6(7)	C(140)	-C(139)	-C(138)	110.6(6)
C(41)	-C(42)	-C(43)	100.6(6)	C(139)	-C(140)	-C(135)	110.2(6)
C(41)	-C(42)	-C(52)	109.6(7)	C(142)	-C(141)	-C(137)	124.3(7)
C(43)	-C(42)	-C(52)	109.9(6)	C(141)	-C(142)	-C(143)	122.8(7)
C(41)	-C(42)	-C(51)	115.1(7)	N(8)	-C(143)	-C(142)	120.6(7)
C(43)	-C(42)	-C(51)	110.7(7)	N(8)	-C(143)	-C(144)	110.0(6)
C(52)	-C(42)	-C(51)	110.5(6)	C(142)	-C(143)	-C(144)	129.4(6)
C(44)	-C(43)	-C(48)	119.6(7)	C(145)	-C(144)	-C(143)	102.1(6)
C(44)	-C(43)	-C(42)	131.0(7)	C(145)	-C(144)	-C(153)	110.3(7)
C(48)	-C(43)	-C(42)	109.3(7)	C(143)	-C(144)	-C(153)	114.5(7)
C(43)	-C(44)	-C(45)	119.3(8)	C(145)	-C(144)	-C(154)	110.2(6)
C(44)	-C(45)	-C(46)	120.1(8)	C(143)	-C(144)	-C(154)	107.9(6)
C(47)	-C(46)	-C(45)	121.7(8)	C(153)	-C(144)	-C(154)	111.5(7)
C(46)	-C(47)	-C(48)	116.0(7)	C(146)	-C(145)	-C(150)	120.7(7)
C(43)	-C(48)	-C(47)	123.2(7)	C(146)	-C(145)	-C(144)	131.1(8)
C(43)	-C(48)	-N(3)	109.1(7)	C(150)	-C(145)	-C(144)	108.2(6)
C(47)	-C(48)	-N(3)	127.7(7)	C(145)	-C(146)	-C(147)	116.6(8)
N(3)	-C(49)	-C(50)	112.5(6)	C(148)	-C(147)	-C(146)	120.7(8)
C(54)	-C(53)	-C(41)	124.6(7)	C(147)	-C(148)	-C(149)	122.7(8)
C(53)	-C(54)	-C(55)	124.4(8)	C(150)	-C(149)	-C(148)	116.2(8)
C(54)	-C(55)	-C(56)	122.4(7)	C(149)	-C(150)	-C(145)	123.0(7)
C(54)	-C(55)	-C(60)	120.0(7)	C(149)	-C(150)	-N(8)	127.8(7)
C(56)	-C(55)	-C(60)	117.6(7)	C(145)	-C(150)	-N(8)	109.1(6)
C(57)	-C(56)	-C(55)	125.0(7)	N(8)	-C(151)	-C(152)	108.5(6)

C(57)	-C(56)	-Cl(2)	118.3(6)	F(5)	-P(1)	-F(3)	89.2(3)
C(55)	-C(56)	-Cl(2)	116.7(6)	F(5)	-P(1)	-F(6)	179.4(4)
C(61)	-C(57)	-C(56)	122.9(8)	F(3)	-P(1)	-F(6)	90.2(4)
C(61)	-C(57)	-C(58)	120.7(7)	F(5)	-P(1)	-F(1)	90.4(4)
C(56)	-C(57)	-C(58)	116.3(7)	F(3)	-P(1)	-F(1)	91.7(4)
C(57)	-C(58)	-C(59)	112.5(8)	F(6)	-P(1)	-F(1)	89.8(4)
C(60)	-C(59)	-C(58)	109.7(7)	F(5)	-P(1)	-F(4)	90.3(4)
C(55)	-C(60)	-C(59)	114.2(7)	F(3)	-P(1)	-F(4)	177.5(4)
C(57)	-C(61)	-C(62)	124.3(8)	F(6)	-P(1)	-F(4)	90.3(4)
C(63)	-C(62)	-C(61)	124.4(8)	F(1)	-P(1)	-F(4)	90.8(4)
N(4)	-C(63)	-C(62)	121.3(8)	F(5)	-P(1)	-F(2)	89.7(4)
N(4)	-C(63)	-C(64)	108.6(7)	F(3)	-P(1)	-F(2)	87.8(3)
C(62)	-C(63)	-C(64)	130.1(8)	F(6)	-P(1)	-F(2)	90.1(3)
C(65)	-C(64)	-C(63)	102.1(7)	F(1)	-P(1)	-F(2)	179.4(4)
C(65)	-C(64)	-C(73)	111.7(7)	F(4)	-P(1)	-F(2)	89.8(3)
C(63)	-C(64)	-C(73)	112.1(7)	F(9)	-P(2)	-F(7)	94.3(5)
C(65)	-C(64)	-C(74)	107.9(7)	F(9)	-P(2)	-F(10)	177.0(5)
C(63)	-C(64)	-C(74)	110.3(7)	F(7)	-P(2)	-F(10)	88.3(4)
C(73)	-C(64)	-C(74)	112.1(7)	F(9)	-P(2)	-F(8)	89.1(4)
C(66)	-C(65)	-C(70)	119.5(8)	F(7)	-P(2)	-F(8)	176.6(5)
C(66)	-C(65)	-C(64)	131.5(8)	F(10)	-P(2)	-F(8)	88.3(4)
C(70)	-C(65)	-C(64)	109.0(7)	F(9)	-P(2)	-F(11)	89.5(4)
C(65)	-C(66)	-C(67)	119.1(9)	F(7)	-P(2)	-F(11)	89.5(4)
C(68)	-C(67)	-C(66)	120.4(8)	F(10)	-P(2)	-F(11)	89.1(4)
C(67)	-C(68)	-C(69)	122.1(8)	F(8)	-P(2)	-F(11)	90.7(3)
C(68)	-C(69)	-C(70)	116.6(9)	F(9)	-P(2)	-F(12)	91.4(4)
C(65)	-C(70)	-C(69)	122.2(8)	F(7)	-P(2)	-F(12)	90.8(4)
C(65)	-C(70)	-N(4)	109.5(7)	F(10)	-P(2)	-F(12)	90.1(4)
C(69)	-C(70)	-N(4)	128.3(8)	F(8)	-P(2)	-F(12)	88.9(3)
N(4)	-C(71)	-C(72)	111.2(9)	F(11)	-P(2)	-F(12)	179.1(4)
C(81)	-N(5)	-C(88)	111.8(6)	F(18)	-P(3)	-F(17)	178.0(4)
C(81)	-N(5)	-C(89)	127.5(7)	F(18)	-P(3)	-F(14)	92.0(4)
C(88)	-N(5)	-C(89)	120.5(6)	F(17)	-P(3)	-F(14)	89.7(4)
C(103)	-N(6)	-C(110)	110.6(7)	F(18)	-P(3)	-F(15)	90.3(3)
C(103)	-N(6)	-C(111)	125.7(7)	F(17)	-P(3)	-F(15)	88.8(4)
C(110)	-N(6)	-C(111)	123.6(7)	F(14)	-P(3)	-F(15)	89.5(4)
N(5)	-C(81)	-C(93)	121.9(7)	F(18)	-P(3)	-F(13)	89.2(4)
N(5)	-C(81)	-C(82)	110.2(7)	F(17)	-P(3)	-F(13)	89.1(3)
C(93)	-C(81)	-C(82)	127.9(7)	F(14)	-P(3)	-F(13)	178.8(4)
C(81)	-C(82)	-C(83)	100.2(6)	F(15)	-P(3)	-F(13)	90.2(3)
C(81)	-C(82)	-C(91)	115.8(6)	F(18)	-P(3)	-F(16)	89.6(4)
C(83)	-C(82)	-C(91)	110.1(7)	F(17)	-P(3)	-F(16)	91.4(4)
C(81)	-C(82)	-C(92)	108.9(6)	F(14)	-P(3)	-F(16)	91.1(4)
C(83)	-C(82)	-C(92)	110.3(6)	F(15)	-P(3)	-F(16)	179.4(4)
C(91)	-C(82)	-C(92)	111.0(7)	F(13)	-P(3)	-F(16)	89.3(3)
C(88)	-C(83)	-C(84)	120.2(8)	F(24)	-P(4)	-F(20)	90.0(4)
C(88)	-C(83)	-C(82)	109.0(7)	F(24)	-P(4)	-F(22)	92.2(4)
C(84)	-C(83)	-C(82)	130.8(8)	F(20)	-P(4)	-F(22)	90.1(3)

C(85)	-C(84)	-C(83)	117.2(8)	F(24)	-P(4)	-F(19)	91.0(4)
C(86)	-C(85)	-C(84)	121.9(8)	F(20)	-P(4)	-F(19)	178.7(4)
C(87)	-C(86)	-C(85)	121.9(8)	F(22)	-P(4)	-F(19)	89.1(4)
C(86)	-C(87)	-C(88)	116.7(8)	F(24)	-P(4)	-F(23)	178.8(4)
C(83)	-C(88)	-C(87)	122.1(8)	F(20)	-P(4)	-F(23)	90.5(3)
C(83)	-C(88)	-N(5)	108.6(7)	F(22)	-P(4)	-F(23)	88.8(4)
C(87)	-C(88)	-N(5)	129.3(7)	F(19)	-P(4)	-F(23)	88.4(3)
N(5)	-C(89)	-C(90)	109.5(7)	F(24)	-P(4)	-F(21)	90.2(4)
C(94)	-C(93)	-C(81)	124.8(7)	F(20)	-P(4)	-F(21)	89.8(3)
C(93)	-C(94)	-C(95)	125.7(7)	F(22)	-P(4)	-F(21)	177.6(4)
C(96)	-C(95)	-C(94)	122.3(7)	F(19)	-P(4)	-F(21)	90.9(3)
C(96)	-C(95)	-C(100)	118.6(7)	F(23)	-P(4)	-F(21)	88.8(3)

Table 7.14. Torsion angles (°) in **Cy7P** with standard uncertainties in parentheses.

C(8)	-N(1)	-C(1)	-C(13)	170.8(7)	C(88)	-N(5)	-C(81)	-C(93)	-176.2(7)
C(9)	-N(1)	-C(1)	-C(13)	-4(1)	C(89)	-N(5)	-C(81)	-C(93)	9(1)
C(8)	-N(1)	-C(1)	-C(2)	-8.9(8)	C(88)	-N(5)	-C(81)	-C(82)	4.9(9)
C(9)	-N(1)	-C(1)	-C(2)	176.1(7)	C(89)	-N(5)	-C(81)	-C(82)	-170.0(7)
N(1)	-C(1)	-C(2)	-C(3)	7.3(8)	N(5)	-C(81)	-C(82)	-C(83)	-5.0(8)
C(13)	-C(1)	-C(2)	-C(3)	-172.3(8)	C(93)	-C(81)	-C(82)	-C(83)	176.1(8)
N(1)	-C(1)	-C(2)	-C(11)	-109.1(7)	N(5)	-C(81)	-C(82)	-C(91)	-123.4(7)
C(13)	-C(1)	-C(2)	-C(11)	71(1)	C(93)	-C(81)	-C(82)	-C(91)	58(1)
N(1)	-C(1)	-C(2)	-C(12)	125.8(7)	N(5)	-C(81)	-C(82)	-C(92)	110.6(7)
C(13)	-C(1)	-C(2)	-C(12)	-54(1)	C(93)	-C(81)	-C(82)	-C(92)	-68(1)
C(11)	-C(2)	-C(3)	-C(8)	111.8(8)	C(81)	-C(82)	-C(83)	-C(88)	3.6(8)
C(12)	-C(2)	-C(3)	-C(8)	-124.5(7)	C(91)	-C(82)	-C(83)	-C(88)	126.1(7)
C(1)	-C(2)	-C(3)	-C(8)	-3.4(8)	C(92)	-C(82)	-C(83)	-C(88)	-111.0(8)
C(11)	-C(2)	-C(3)	-C(4)	-70(1)	C(81)	-C(82)	-C(83)	-C(84)	-175.3(9)
C(12)	-C(2)	-C(3)	-C(4)	54(1)	C(91)	-C(82)	-C(83)	-C(84)	-53(1)
C(1)	-C(2)	-C(3)	-C(4)	175.1(8)	C(92)	-C(82)	-C(83)	-C(84)	70(1)
C(8)	-C(3)	-C(4)	-C(5)	0(1)	C(88)	-C(83)	-C(84)	-C(85)	1(1)
C(2)	-C(3)	-C(4)	-C(5)	-178.4(8)	C(82)	-C(83)	-C(84)	-C(85)	179.7(8)
C(3)	-C(4)	-C(5)	-C(6)	1(1)	C(83)	-C(84)	-C(85)	-C(86)	0(1)
C(4)	-C(5)	-C(6)	-C(7)	-2(1)	C(84)	-C(85)	-C(86)	-C(87)	-1(1)
C(5)	-C(6)	-C(7)	-C(8)	2(1)	C(85)	-C(86)	-C(87)	-C(88)	-0(1)
C(4)	-C(3)	-C(8)	-N(1)	179.9(7)	C(84)	-C(83)	-C(88)	-C(87)	-2(1)
C(2)	-C(3)	-C(8)	-N(1)	-1.4(9)	C(82)	-C(83)	-C(88)	-C(87)	179.0(7)
C(4)	-C(3)	-C(8)	-C(7)	0(1)	C(84)	-C(83)	-C(88)	-N(5)	177.9(7)
C(2)	-C(3)	-C(8)	-C(7)	178.8(7)	C(82)	-C(83)	-C(88)	-N(5)	-1.1(9)
C(1)	-N(1)	-C(8)	-C(3)	6.7(9)	C(86)	-C(87)	-C(88)	-C(83)	2(1)
C(9)	-N(1)	-C(8)	-C(3)	-178.2(7)	C(86)	-C(87)	-C(88)	-N(5)	-178.2(8)
C(1)	-N(1)	-C(8)	-C(7)	-173.6(8)	C(81)	-N(5)	-C(88)	-C(83)	-2.3(9)
C(9)	-N(1)	-C(8)	-C(7)	2(1)	C(89)	-N(5)	-C(88)	-C(83)	172.9(7)
C(6)	-C(7)	-C(8)	-C(3)	-1(1)	C(81)	-N(5)	-C(88)	-C(87)	177.5(8)
C(6)	-C(7)	-C(8)	-N(1)	179.1(7)	C(89)	-N(5)	-C(88)	-C(87)	-7(1)
C(1)	-N(1)	-C(9)	-C(10)	83.9(9)	C(81)	-N(5)	-C(89)	-C(90)	96.1(9)
C(8)	-N(1)	-C(9)	-C(10)	-90.6(9)	C(88)	-N(5)	-C(89)	-C(90)	-78.3(9)
N(1)	-C(1)	-C(13)	-C(14)	-175.7(8)	N(5)	-C(81)	-C(93)	-C(94)	176.3(8)
C(2)	-C(1)	-C(13)	-C(14)	4(1)	C(82)	-C(81)	-C(93)	-C(94)	-5(1)
C(1)	-C(13)	-C(14)	-C(15)	172.9(8)	C(81)	-C(93)	-C(94)	-C(95)	-174.1(8)
C(13)	-C(14)	-C(15)	-C(16)	-178.6(8)	C(93)	-C(94)	-C(95)	-C(96)	172.7(8)
C(13)	-C(14)	-C(15)	-C(20)	3(1)	C(93)	-C(94)	-C(95)	-C(100)	-6(1)
C(14)	-C(15)	-C(16)	-C(17)	-178.1(8)	C(94)	-C(95)	-C(96)	-C(97)	175.9(8)
C(20)	-C(15)	-C(16)	-C(17)	1(1)	C(100)	-C(95)	-C(96)	-C(97)	-6(1)
C(14)	-C(15)	-C(16)	-Cl(1)	4(1)	C(94)	-C(95)	-C(96)	-Cl(3)	-3(1)
C(20)	-C(15)	-C(16)	-Cl(1)	-176.9(6)	C(100)	-C(95)	-C(96)	-Cl(3)	175.7(6)
C(15)	-C(16)	-C(17)	-C(21)	-177.9(8)	C(95)	-C(96)	-C(97)	-C(101)	175.3(8)
Cl(1)	-C(16)	-C(17)	-C(21)	-0(1)	Cl(3)	-C(96)	-C(97)	-C(101)	-6(1)
C(15)	-C(16)	-C(17)	-C(18)	8(1)	C(95)	-C(96)	-C(97)	-C(98)	-2(1)
Cl(1)	-C(16)	-C(17)	-C(18)	-174.8(7)	Cl(3)	-C(96)	-C(97)	-C(98)	176.7(6)
C(21)	-C(17)	-C(18)	-C(19)	150.5(9)	C(101)	-C(97)	-C(98)	-C(99)	-144.6(8)
C(16)	-C(17)	-C(18)	-C(19)	-35(1)	C(96)	-C(97)	-C(98)	-C(99)	33(1)

C(17)	-C(18)	-C(19)	-C(20)	54(1)	C(97)	-C(98)	-C(99)	-C(100)	-56(1)
C(16)	-C(15)	-C(20)	-C(19)	18(1)	C(98)	-C(99)	-C(100)	-C(95)	48(1)
C(14)	-C(15)	-C(20)	-C(19)	-163.4(9)	C(96)	-C(95)	-C(100)	-C(99)	-18(1)
C(18)	-C(19)	-C(20)	-C(15)	-46(1)	C(94)	-C(95)	-C(100)	-C(99)	160.6(7)
C(16)	-C(17)	-C(21)	-C(22)	-170.6(8)	C(96)	-C(97)	-C(101)	-C(102)	173.8(8)
C(18)	-C(17)	-C(21)	-C(22)	4(1)	C(98)	-C(97)	-C(101)	-C(102)	-9(1)
C(17)	-C(21)	-C(22)	-C(23)	174.4(9)	C(97)	-C(101)	-C(102)	-C(103)	178.5(8)
C(21)	-C(22)	-C(23)	-N(2)	-174.0(9)	C(110)	-N(6)	-C(103)	-C(102)	173.0(7)
C(21)	-C(22)	-C(23)	-C(24)	5(2)	C(111)	-N(6)	-C(103)	-C(102)	-5(1)
C(30)	-N(2)	-C(23)	-C(22)	-176.1(9)	C(110)	-N(6)	-C(103)	-C(104)	-5.8(9)
C(31)	-N(2)	-C(23)	-C(22)	8(2)	C(111)	-N(6)	-C(103)	-C(104)	175.9(7)
C(30)	-N(2)	-C(23)	-C(24)	5(1)	C(101)	-C(102)	-C(103)	-N(6)	172.2(7)
C(31)	-N(2)	-C(23)	-C(24)	-170.7(8)	C(101)	-C(102)	-C(103)	-C(104)	-9(1)
C(22)	-C(23)	-C(24)	-C(34)	58(1)	N(6)	-C(103)	-C(104)	-C(105)	5.5(8)
N(2)	-C(23)	-C(24)	-C(34)	-123.4(8)	C(102)	-C(103)	-C(104)	-C(105)	-173.2(8)
C(22)	-C(23)	-C(24)	-C(25)	175.2(9)	N(6)	-C(103)	-C(104)	-C(114)	124.6(7)
N(2)	-C(23)	-C(24)	-C(25)	-5.7(9)	C(102)	-C(103)	-C(104)	-C(114)	-54(1)
C(22)	-C(23)	-C(24)	-C(33)	-69(1)	N(6)	-C(103)	-C(104)	-C(113)	-108.6(7)
N(2)	-C(23)	-C(24)	-C(33)	110.1(8)	C(102)	-C(103)	-C(104)	-C(113)	73(1)
C(34)	-C(24)	-C(25)	-C(26)	-60(1)	C(103)	-C(104)	-C(105)	-C(106)	177.4(9)
C(33)	-C(24)	-C(25)	-C(26)	64(1)	C(114)	-C(104)	-C(105)	-C(106)	57(1)
C(23)	-C(24)	-C(25)	-C(26)	-178.8(9)	C(113)	-C(104)	-C(105)	-C(106)	-67(1)
C(34)	-C(24)	-C(25)	-C(30)	124.0(8)	C(103)	-C(104)	-C(105)	-C(110)	-3.3(8)
C(33)	-C(24)	-C(25)	-C(30)	-112.8(8)	C(114)	-C(104)	-C(105)	-C(110)	-123.7(8)
C(23)	-C(24)	-C(25)	-C(30)	4.9(9)	C(113)	-C(104)	-C(105)	-C(110)	112.6(8)
C(30)	-C(25)	-C(26)	-C(27)	-0(1)	C(110)	-C(105)	-C(106)	-C(107)	0(1)
C(24)	-C(25)	-C(26)	-C(27)	-176.3(8)	C(104)	-C(105)	-C(106)	-C(107)	179.5(8)
C(25)	-C(26)	-C(27)	-C(28)	0(1)	C(105)	-C(106)	-C(107)	-C(108)	-1(1)
C(26)	-C(27)	-C(28)	-C(29)	1(1)	C(106)	-C(107)	-C(108)	-C(109)	2(1)
C(27)	-C(28)	-C(29)	-C(30)	-1(1)	C(107)	-C(108)	-C(109)	-C(110)	-2(1)
C(26)	-C(25)	-C(30)	-C(29)	-0(1)	C(103)	-N(6)	-C(110)	-C(105)	3.7(9)
C(24)	-C(25)	-C(30)	-C(29)	176.6(8)	C(111)	-N(6)	-C(110)	-C(105)	-178.1(7)
C(26)	-C(25)	-C(30)	-N(2)	-179.2(8)	C(103)	-N(6)	-C(110)	-C(109)	-176.3(8)
C(24)	-C(25)	-C(30)	-N(2)	-2(1)	C(111)	-N(6)	-C(110)	-C(109)	2(1)
C(28)	-C(29)	-C(30)	-C(25)	1(1)	C(106)	-C(105)	-C(110)	-N(6)	179.5(8)
C(28)	-C(29)	-C(30)	-N(2)	179.7(9)	C(104)	-C(105)	-C(110)	-N(6)	0.1(9)
C(23)	-N(2)	-C(30)	-C(25)	-2(1)	C(106)	-C(105)	-C(110)	-C(109)	-1(1)
C(31)	-N(2)	-C(30)	-C(25)	174.1(8)	C(104)	-C(105)	-C(110)	-C(109)	-179.9(8)
C(23)	-N(2)	-C(30)	-C(29)	179.4(9)	C(108)	-C(109)	-C(110)	-N(6)	-178.6(8)
C(31)	-N(2)	-C(30)	-C(29)	-5(2)	C(108)	-C(109)	-C(110)	-C(105)	1(1)
C(23)	-N(2)	-C(31)	-C(32)	-97(1)	C(103)	-N(6)	-C(111)	-C(112)	89(1)
C(30)	-N(2)	-C(31)	-C(32)	88(1)	C(110)	-N(6)	-C(111)	-C(112)	-89(1)
C(48)	-N(3)	-C(41)	-C(53)	172.2(7)	C(128)	-N(7)	-C(121)	-C(133)	173.1(8)
C(49)	-N(3)	-C(41)	-C(53)	-8(1)	C(129)	-N(7)	-C(121)	-C(133)	-3(1)
C(48)	-N(3)	-C(41)	-C(42)	-6.7(9)	C(128)	-N(7)	-C(121)	-C(122)	-5.5(9)
C(49)	-N(3)	-C(41)	-C(42)	173.1(7)	C(129)	-N(7)	-C(121)	-C(122)	178.9(7)
N(3)	-C(41)	-C(42)	-C(43)	5.8(9)	C(133)	-C(121)	-C(122)	-C(123)	-172.0(8)
C(53)	-C(41)	-C(42)	-C(43)	-172.9(8)	N(7)	-C(121)	-C(122)	-C(123)	6.5(8)
N(3)	-C(41)	-C(42)	-C(52)	-109.9(7)	C(133)	-C(121)	-C(122)	-C(131)	-55(1)
C(53)	-C(41)	-C(42)	-C(52)	71(1)	N(7)	-C(121)	-C(122)	-C(131)	123.6(7)

N(3)	-C(41)	-C(42)	-C(51)	124.8(7)	C(133)	-C(121)	-C(122)	-C(132)	71(1)
C(53)	-C(41)	-C(42)	-C(51)	-54(1)	N(7)	-C(121)	-C(122)	-C(132)	-111.0(7)
C(41)	-C(42)	-C(43)	-C(44)	172.9(9)	C(131)	-C(122)	-C(123)	-C(124)	59(1)
C(52)	-C(42)	-C(43)	-C(44)	-72(1)	C(132)	-C(122)	-C(123)	-C(124)	-66(1)
C(51)	-C(42)	-C(43)	-C(44)	51(1)	C(121)	-C(122)	-C(123)	-C(124)	176.4(9)
C(41)	-C(42)	-C(43)	-C(48)	-2.8(9)	C(131)	-C(122)	-C(123)	-C(128)	-122.7(8)
C(52)	-C(42)	-C(43)	-C(48)	112.7(8)	C(132)	-C(122)	-C(123)	-C(128)	112.3(8)
C(51)	-C(42)	-C(43)	-C(48)	-124.9(7)	C(121)	-C(122)	-C(123)	-C(128)	-5.4(9)
C(48)	-C(43)	-C(44)	-C(45)	-3(1)	C(128)	-C(123)	-C(124)	-C(125)	-1(1)
C(42)	-C(43)	-C(44)	-C(45)	-178.0(8)	C(122)	-C(123)	-C(124)	-C(125)	176.8(9)
C(43)	-C(44)	-C(45)	-C(46)	4(1)	C(123)	-C(124)	-C(125)	-C(126)	-0(1)
C(44)	-C(45)	-C(46)	-C(47)	-3(1)	C(124)	-C(125)	-C(126)	-C(127)	2(1)
C(45)	-C(46)	-C(47)	-C(48)	1(1)	C(125)	-C(126)	-C(127)	-C(128)	-1(1)
C(44)	-C(43)	-C(48)	-C(47)	1(1)	C(126)	-C(127)	-C(128)	-C(123)	-0(1)
C(42)	-C(43)	-C(48)	-C(47)	176.9(7)	C(126)	-C(127)	-C(128)	-N(7)	-179.5(8)
C(44)	-C(43)	-C(48)	-N(3)	-177.1(7)	C(124)	-C(123)	-C(128)	-C(127)	1(1)
C(42)	-C(43)	-C(48)	-N(3)	-0.9(9)	C(122)	-C(123)	-C(128)	-C(127)	-177.0(7)
C(46)	-C(47)	-C(48)	-C(43)	0(1)	C(124)	-C(123)	-C(128)	-N(7)	-179.1(7)
C(46)	-C(47)	-C(48)	-N(3)	177.7(7)	C(122)	-C(123)	-C(128)	-N(7)	2.5(9)
C(41)	-N(3)	-C(48)	-C(43)	4.7(9)	C(121)	-N(7)	-C(128)	-C(127)	-178.5(8)
C(49)	-N(3)	-C(48)	-C(43)	-175.1(7)	C(129)	-N(7)	-C(128)	-C(127)	-3(1)
C(41)	-N(3)	-C(48)	-C(47)	-172.9(8)	C(121)	-N(7)	-C(128)	-C(123)	2.0(9)
C(49)	-N(3)	-C(48)	-C(47)	7(1)	C(129)	-N(7)	-C(128)	-C(123)	177.7(7)
C(41)	-N(3)	-C(49)	-C(50)	88(1)	C(121)	-N(7)	-C(129)	-C(130)	89(1)
C(48)	-N(3)	-C(49)	-C(50)	-92.0(8)	C(128)	-N(7)	-C(129)	-C(130)	-86(1)
N(3)	-C(41)	-C(53)	-C(54)	-174.1(8)	N(7)	-C(121)	-C(133)	-C(134)	175.0(7)
C(42)	-C(41)	-C(53)	-C(54)	5(1)	C(122)	-C(121)	-C(133)	-C(134)	-7(1)
C(41)	-C(53)	-C(54)	-C(55)	173.7(8)	C(121)	-C(133)	-C(134)	-C(135)	177.2(8)
C(53)	-C(54)	-C(55)	-C(56)	-177.4(8)	C(133)	-C(134)	-C(135)	-C(136)	170.6(8)
C(53)	-C(54)	-C(55)	-C(60)	1(1)	C(133)	-C(134)	-C(135)	-C(140)	-6(1)
C(54)	-C(55)	-C(56)	-C(57)	-174.8(8)	C(134)	-C(135)	-C(136)	-C(137)	177.6(8)
C(60)	-C(55)	-C(56)	-C(57)	7(1)	C(140)	-C(135)	-C(136)	-C(137)	-5(1)
C(54)	-C(55)	-C(56)	-Cl(2)	3(1)	C(134)	-C(135)	-C(136)	-Cl(4)	-2(1)
C(60)	-C(55)	-C(56)	-Cl(2)	-175.2(6)	C(140)	-C(135)	-C(136)	-Cl(4)	175.3(6)
C(55)	-C(56)	-C(57)	-C(61)	179.8(8)	C(135)	-C(136)	-C(137)	-C(141)	178.3(7)
Cl(2)	-C(56)	-C(57)	-C(61)	2(1)	Cl(4)	-C(136)	-C(137)	-C(141)	-2(1)
C(55)	-C(56)	-C(57)	-C(58)	3(1)	C(135)	-C(136)	-C(137)	-C(138)	-4(1)
Cl(2)	-C(56)	-C(57)	-C(58)	-175.5(8)	Cl(4)	-C(136)	-C(137)	-C(138)	175.2(6)
C(61)	-C(57)	-C(58)	-C(59)	147.9(8)	C(136)	-C(137)	-C(138)	-C(139)	-19(1)
C(56)	-C(57)	-C(58)	-C(59)	-35(1)	C(141)	-C(137)	-C(138)	-C(139)	158.7(7)
C(57)	-C(58)	-C(59)	-C(60)	57(1)	C(137)	-C(138)	-C(139)	-C(140)	50.4(9)
C(54)	-C(55)	-C(60)	-C(59)	-161.2(8)	C(138)	-C(139)	-C(140)	-C(135)	-59.5(8)
C(56)	-C(55)	-C(60)	-C(59)	17(1)	C(134)	-C(135)	-C(140)	-C(139)	-145.9(7)
C(58)	-C(59)	-C(60)	-C(55)	-48(1)	C(136)	-C(135)	-C(140)	-C(139)	36.9(9)
C(56)	-C(57)	-C(61)	-C(62)	-174.7(8)	C(136)	-C(137)	-C(141)	-C(142)	175.1(8)
C(58)	-C(57)	-C(61)	-C(62)	2(1)	C(138)	-C(137)	-C(141)	-C(142)	-3(1)
C(57)	-C(61)	-C(62)	-C(63)	175.1(9)	C(137)	-C(141)	-C(142)	-C(143)	-174.3(7)
C(70)	-N(4)	-C(63)	-C(62)	-175.9(8)	C(150)	-N(8)	-C(143)	-C(142)	-178.6(7)
C(71)	-N(4)	-C(63)	-C(62)	3(1)	C(151)	-N(8)	-C(143)	-C(142)	7(1)
C(70)	-N(4)	-C(63)	-C(64)	4(1)	C(150)	-N(8)	-C(143)	-C(144)	2.4(8)

C(71)	-N(4)	-C(63)	-C(64)	-176.5(8)	C(151)	-N(8)	-C(143)	-C(144)	-172.4(7)
C(61)	-C(62)	-C(63)	-N(4)	-172.6(8)	C(141)	-C(142)	-C(143)	-N(8)	173.4(7)
C(61)	-C(62)	-C(63)	-C(64)	7(1)	C(141)	-C(142)	-C(143)	-C(144)	-8(1)
N(4)	-C(63)	-C(64)	-C(65)	-4.6(9)	N(8)	-C(143)	-C(144)	-C(145)	-4.0(8)
C(62)	-C(63)	-C(64)	-C(65)	175.5(9)	C(142)	-C(143)	-C(144)	-C(145)	177.2(8)
N(4)	-C(63)	-C(64)	-C(73)	-124.3(7)	N(8)	-C(143)	-C(144)	-C(153)	-123.2(7)
C(62)	-C(63)	-C(64)	-C(73)	56(1)	C(142)	-C(143)	-C(144)	-C(153)	58(1)
N(4)	-C(63)	-C(64)	-C(74)	110.0(8)	N(8)	-C(143)	-C(144)	-C(154)	112.1(7)
C(62)	-C(63)	-C(64)	-C(74)	-70(1)	C(142)	-C(143)	-C(144)	-C(154)	-67(1)
C(63)	-C(64)	-C(65)	-C(66)	-178(1)	C(143)	-C(144)	-C(145)	-C(146)	-175.6(9)
C(73)	-C(64)	-C(65)	-C(66)	-58(1)	C(153)	-C(144)	-C(145)	-C(146)	-54(1)
C(74)	-C(64)	-C(65)	-C(66)	66(1)	C(154)	-C(144)	-C(145)	-C(146)	70(1)
C(63)	-C(64)	-C(65)	-C(70)	3.3(9)	C(143)	-C(144)	-C(145)	-C(150)	4.1(8)
C(73)	-C(64)	-C(65)	-C(70)	123.3(8)	C(153)	-C(144)	-C(145)	-C(150)	126.2(7)
C(74)	-C(64)	-C(65)	-C(70)	-112.9(9)	C(154)	-C(144)	-C(145)	-C(150)	-110.3(7)
C(70)	-C(65)	-C(66)	-C(67)	0(1)	C(150)	-C(145)	-C(146)	-C(147)	-1(1)
C(64)	-C(65)	-C(66)	-C(67)	-178.4(9)	C(144)	-C(145)	-C(146)	-C(147)	178.8(8)
C(65)	-C(66)	-C(67)	-C(68)	-2(1)	C(145)	-C(146)	-C(147)	-C(148)	1(1)
C(66)	-C(67)	-C(68)	-C(69)	2(1)	C(146)	-C(147)	-C(148)	-C(149)	-1(1)
C(67)	-C(68)	-C(69)	-C(70)	-0(1)	C(147)	-C(148)	-C(149)	-C(150)	1(1)
C(66)	-C(65)	-C(70)	-C(69)	2(1)	C(148)	-C(149)	-C(150)	-C(145)	-1(1)
C(64)	-C(65)	-C(70)	-C(69)	-179.4(8)	C(148)	-C(149)	-C(150)	-N(8)	-175.9(7)
C(66)	-C(65)	-C(70)	-N(4)	-179.9(8)	C(146)	-C(145)	-C(150)	-C(149)	1(1)
C(64)	-C(65)	-C(70)	-N(4)	-1(1)	C(144)	-C(145)	-C(150)	-C(149)	-179.0(7)
C(68)	-C(69)	-C(70)	-C(65)	-2(1)	C(146)	-C(145)	-C(150)	-N(8)	176.8(7)
C(68)	-C(69)	-C(70)	-N(4)	-179.7(9)	C(144)	-C(145)	-C(150)	-N(8)	-3.0(8)
C(63)	-N(4)	-C(70)	-C(65)	-2(1)	C(143)	-N(8)	-C(150)	-C(149)	176.1(8)
C(71)	-N(4)	-C(70)	-C(65)	178.7(8)	C(151)	-N(8)	-C(150)	-C(149)	-9(1)
C(63)	-N(4)	-C(70)	-C(69)	176.1(9)	C(143)	-N(8)	-C(150)	-C(145)	0.4(9)
C(71)	-N(4)	-C(70)	-C(69)	-3(1)	C(151)	-N(8)	-C(150)	-C(145)	175.6(7)
C(63)	-N(4)	-C(71)	-C(72)	-95(1)	C(143)	-N(8)	-C(151)	-C(152)	97.0(9)
C(70)	-N(4)	-C(71)	-C(72)	84(1)	C(150)	-N(8)	-C(151)	-C(152)	-77.4(9)

Table 7.15. Bond lengths (Å) in **Cy7T** with standard uncertainties in parentheses.

Cl(1)	-C(16)	1.756(3)	Cl(2)	-C(36)	1.718(3)
N(1)	-C(1)	1.344(4)	Cl(3)	-C(37)	1.726(3)
N(1)	-C(8)	1.406(5)	Cl(4)	-C(38)	1.719(3)
N(1)	-C(9)	1.471(4)	Cl(5)	-C(39)	1.711(3)
N(2)	-C(23)	1.355(5)	Cl(6)	-C(42)	1.715(4)
N(2)	-C(30)	1.418(5)	Cl(7)	-C(43)	1.736(4)
N(2)	-C(31)	1.462(5)	Cl(8)	-C(44)	1.733(4)
C(1)	-C(13)	1.391(5)	Cl(9)	-C(45)	1.710(4)
C(1)	-C(2)	1.531(4)	Cl(10)	-C(48)	1.713(3)
C(2)	-C(3)	1.512(5)	Cl(11)	-C(49)	1.718(3)
C(2)	-C(12)	1.530(5)	Cl(12)	-C(50)	1.719(3)
C(2)	-C(11)	1.560(5)	Cl(13)	-C(51)	1.725(3)
C(3)	-C(4)	1.383(5)	P(1)	-O(2)	1.699(2)
C(3)	-C(8)	1.388(5)	P(1)	-O(6)	1.710(2)
C(4)	-C(5)	1.396(6)	P(1)	-O(1)	1.714(2)
C(5)	-C(6)	1.377(7)	P(1)	-O(4)	1.720(2)
C(6)	-C(7)	1.394(6)	P(1)	-O(5)	1.724(2)
C(7)	-C(8)	1.389(5)	P(1)	-O(3)	1.725(2)
C(9)	-C(10)	1.507(5)	O(1)	-C(35)	1.349(4)
C(13)	-C(14)	1.389(4)	O(2)	-C(40)	1.353(4)
C(14)	-C(15)	1.394(5)	O(3)	-C(41)	1.348(4)
C(15)	-C(16)	1.406(4)	O(4)	-C(46)	1.352(4)
C(15)	-C(20)	1.515(5)	O(5)	-C(47)	1.348(4)
C(16)	-C(17)	1.401(5)	O(6)	-C(52)	1.349(4)
C(17)	-C(21)	1.399(5)	C(35)	-C(36)	1.381(5)
C(17)	-C(18)	1.508(5)	C(35)	-C(40)	1.389(4)
C(18)	-C(19b)	1.515(5)	C(36)	-C(37)	1.406(4)
C(18)	-C(19a)	1.524(4)	C(37)	-C(38)	1.384(5)
C(19a)	-C(20)	1.514(4)	C(38)	-C(39)	1.400(5)
C(19b)	-C(20)	1.520(5)	C(39)	-C(40)	1.374(5)
C(21)	-C(22)	1.388(5)	C(41)	-C(42)	1.378(5)
C(22)	-C(23)	1.389(5)	C(41)	-C(46)	1.396(5)
C(23)	-C(24)	1.523(5)	C(42)	-C(43)	1.389(6)
C(24)	-C(25)	1.508(5)	C(43)	-C(44)	1.396(7)
C(24)	-C(33)	1.528(5)	C(44)	-C(45)	1.400(5)
C(24)	-C(34)	1.544(5)	C(45)	-C(46)	1.371(5)
C(25)	-C(30)	1.380(6)	C(47)	-C(48)	1.369(5)
C(25)	-C(26)	1.395(6)	C(47)	-C(52)	1.398(4)
C(26)	-C(27)	1.409(6)	C(48)	-C(49)	1.413(4)
C(27)	-C(28)	1.370(7)	C(49)	-C(50)	1.383(5)
C(28)	-C(29)	1.396(7)	C(50)	-C(51)	1.404(5)
C(29)	-C(30)	1.392(5)	C(51)	-C(52)	1.380(4)
C(31)	-C(32)	1.514(6)			

Table 7.16. Bond angles (°) in **Cy7T** with standard uncertainties in parentheses.

C(1)	-N(1)	-C(8)	112.1(3)	O(1)	-P(1)	-O(4)	89.55(11)
C(1)	-N(1)	-C(9)	126.2(3)	O(2)	-P(1)	-O(5)	88.33(11)
C(8)	-N(1)	-C(9)	121.7(3)	O(6)	-P(1)	-O(5)	91.01(11)
C(23)	-N(2)	-C(30)	111.3(3)	O(1)	-P(1)	-O(5)	178.37(11)
C(23)	-N(2)	-C(31)	125.2(3)	O(4)	-P(1)	-O(5)	91.37(11)
C(30)	-N(2)	-C(31)	123.1(3)	O(2)	-P(1)	-O(3)	88.08(11)
N(1)	-C(1)	-C(13)	122.7(3)	O(6)	-P(1)	-O(3)	178.08(11)
N(1)	-C(1)	-C(2)	108.6(3)	O(1)	-P(1)	-O(3)	92.74(11)
C(13)	-C(1)	-C(2)	128.7(3)	O(4)	-P(1)	-O(3)	90.56(11)
C(3)	-C(2)	-C(12)	110.1(3)	O(5)	-P(1)	-O(3)	88.61(11)
C(3)	-C(2)	-C(1)	101.5(3)	C(35)	-O(1)	-P(1)	110.90(19)
C(12)	-C(2)	-C(1)	111.4(3)	C(40)	-O(2)	-P(1)	111.5(2)
C(3)	-C(2)	-C(11)	109.2(3)	C(41)	-O(3)	-P(1)	111.57(19)
C(12)	-C(2)	-C(11)	111.5(3)	C(46)	-O(4)	-P(1)	111.2(2)
C(1)	-C(2)	-C(11)	112.8(3)	C(47)	-O(5)	-P(1)	111.02(19)
C(4)	-C(3)	-C(8)	119.6(4)	C(52)	-O(6)	-P(1)	111.34(19)
C(4)	-C(3)	-C(2)	131.2(3)	O(1)	-C(35)	-C(36)	126.7(3)
C(8)	-C(3)	-C(2)	109.2(3)	O(1)	-C(35)	-C(40)	112.9(3)
C(3)	-C(4)	-C(5)	118.1(4)	C(36)	-C(35)	-C(40)	120.4(3)
C(6)	-C(5)	-C(4)	121.5(4)	C(35)	-C(36)	-C(37)	118.0(3)
C(5)	-C(6)	-C(7)	121.4(4)	C(35)	-C(36)	-Cl(2)	121.5(2)
C(8)	-C(7)	-C(6)	116.3(4)	C(37)	-C(36)	-Cl(2)	120.5(2)
C(3)	-C(8)	-C(7)	123.2(3)	C(38)	-C(37)	-C(36)	120.9(3)
C(3)	-C(8)	-N(1)	108.6(3)	C(38)	-C(37)	-Cl(3)	119.8(3)
C(7)	-C(8)	-N(1)	128.2(3)	C(36)	-C(37)	-Cl(3)	119.3(3)
N(1)	-C(9)	-C(10)	111.5(3)	C(37)	-C(38)	-C(39)	120.4(3)
C(14)	-C(13)	-C(1)	123.2(3)	C(37)	-C(38)	-Cl(4)	120.3(3)
C(13)	-C(14)	-C(15)	125.8(3)	C(39)	-C(38)	-Cl(4)	119.3(3)
C(14)	-C(15)	-C(16)	121.6(3)	C(40)	-C(39)	-C(38)	118.0(3)
C(14)	-C(15)	-C(20)	120.6(3)	C(40)	-C(39)	-Cl(5)	120.1(3)
C(16)	-C(15)	-C(20)	117.8(3)	C(38)	-C(39)	-Cl(5)	121.9(3)
C(17)	-C(16)	-C(15)	125.4(3)	O(2)	-C(40)	-C(39)	125.7(3)
C(17)	-C(16)	-Cl(1)	117.4(2)	O(2)	-C(40)	-C(35)	112.4(3)
C(15)	-C(16)	-Cl(1)	117.2(3)	C(39)	-C(40)	-C(35)	121.9(3)
C(21)	-C(17)	-C(16)	121.7(3)	O(3)	-C(41)	-C(42)	126.1(3)
C(21)	-C(17)	-C(18)	121.0(3)	O(3)	-C(41)	-C(46)	112.7(3)
C(16)	-C(17)	-C(18)	117.2(3)	C(42)	-C(41)	-C(46)	121.2(3)
C(17)	-C(18)	-C(19b)	115.1(7)	C(41)	-C(42)	-C(43)	118.1(4)
C(17)	-C(18)	-C(19a)	111.2(3)	C(41)	-C(42)	-Cl(6)	119.6(3)
C(20)	-C(19a)	-C(18)	111.2(4)	C(43)	-C(42)	-Cl(6)	122.3(3)
C(18)	-C(19b)	-C(20)	111.4(5)	C(42)	-C(43)	-C(44)	120.8(3)
C(19a)	-C(20)	-C(15)	112.0(3)	C(42)	-C(43)	-Cl(7)	119.4(3)
C(15)	-C(20)	-C(19b)	112.7(7)	C(44)	-C(43)	-Cl(7)	119.8(3)
C(22)	-C(21)	-C(17)	126.7(3)	C(43)	-C(44)	-C(45)	120.6(3)
C(21)	-C(22)	-C(23)	122.7(3)	C(43)	-C(44)	-Cl(8)	120.3(3)
N(2)	-C(23)	-C(22)	123.3(3)	C(45)	-C(44)	-Cl(8)	119.1(3)

N(2)	-C(23)	-C(24)	108.6(3)	C(46)	-C(45)	-C(44)	118.0(4)
C(22)	-C(23)	-C(24)	128.0(3)	C(46)	-C(45)	-Cl(9)	119.6(3)
C(25)	-C(24)	-C(23)	101.9(3)	C(44)	-C(45)	-Cl(9)	122.3(3)
C(25)	-C(24)	-C(33)	110.2(3)	O(4)	-C(46)	-C(45)	125.8(3)
C(23)	-C(24)	-C(33)	114.2(3)	O(4)	-C(46)	-C(41)	113.1(3)
C(25)	-C(24)	-C(34)	109.1(3)	C(45)	-C(46)	-C(41)	121.2(3)
C(23)	-C(24)	-C(34)	109.9(3)	O(5)	-C(47)	-C(48)	126.1(3)
C(33)	-C(24)	-C(34)	111.1(4)	O(5)	-C(47)	-C(52)	112.8(3)
C(30)	-C(25)	-C(26)	120.4(3)	C(48)	-C(47)	-C(52)	121.0(3)
C(30)	-C(25)	-C(24)	109.5(3)	C(47)	-C(48)	-C(49)	118.4(3)
C(26)	-C(25)	-C(24)	130.1(4)	C(47)	-C(48)	-Cl(10)	120.4(2)
C(25)	-C(26)	-C(27)	117.6(4)	C(49)	-C(48)	-Cl(10)	121.2(3)
C(28)	-C(27)	-C(26)	120.6(4)	C(50)	-C(49)	-C(48)	120.7(3)
C(27)	-C(28)	-C(29)	122.5(4)	C(50)	-C(49)	-Cl(11)	119.8(3)
C(30)	-C(29)	-C(28)	116.1(4)	C(48)	-C(49)	-Cl(11)	119.4(3)
C(25)	-C(30)	-C(29)	122.7(4)	C(49)	-C(50)	-C(51)	120.2(3)
C(25)	-C(30)	-N(2)	108.7(3)	C(49)	-C(50)	-Cl(12)	120.6(3)
C(29)	-C(30)	-N(2)	128.6(4)	C(51)	-C(50)	-Cl(12)	119.2(3)
N(2)	-C(31)	-C(32)	111.0(4)	C(52)	-C(51)	-C(50)	118.8(3)
O(2)	-P(1)	-O(6)	93.79(11)	C(52)	-C(51)	-Cl(13)	119.2(3)
O(2)	-P(1)	-O(1)	90.79(11)	C(50)	-C(51)	-Cl(13)	122.0(3)
O(6)	-P(1)	-O(1)	87.67(11)	O(6)	-C(52)	-C(51)	126.1(3)
O(2)	-P(1)	-O(4)	178.61(11)	O(6)	-C(52)	-C(47)	113.1(3)
O(6)	-P(1)	-O(4)	87.57(11)	C(51)	-C(52)	-C(47)	120.8(3)

Table 7.17. Torsion angles (°) in **Cy7T** with standard uncertainties in parentheses.

C(8)	-N(1)	-C(1)	-C(13)	-179.8(3)	O(6)	-P(1)	-O(2)	-C(40)	98.6(2)
C(9)	-N(1)	-C(1)	-C(13)	-0.9(5)	O(1)	-P(1)	-O(2)	-C(40)	10.9(2)
C(8)	-N(1)	-C(1)	-C(2)	0.6(4)	O(5)	-P(1)	-O(2)	-C(40)	-170.5(2)
C(9)	-N(1)	-C(1)	-C(2)	179.6(3)	O(3)	-P(1)	-O(2)	-C(40)	-81.8(2)
N(1)	-C(1)	-C(2)	-C(3)	-1.1(4)	O(2)	-P(1)	-O(3)	-C(41)	-172.5(2)
C(13)	-C(1)	-C(2)	-C(3)	179.4(3)	O(1)	-P(1)	-O(3)	-C(41)	96.8(2)
N(1)	-C(1)	-C(2)	-C(12)	116.0(3)	O(4)	-P(1)	-O(3)	-C(41)	7.3(2)
C(13)	-C(1)	-C(2)	-C(12)	-63.5(5)	O(5)	-P(1)	-O(3)	-C(41)	-84.1(2)
N(1)	-C(1)	-C(2)	-C(11)	-117.7(3)	O(6)	-P(1)	-O(4)	-C(46)	170.7(2)
C(13)	-C(1)	-C(2)	-C(11)	62.8(5)	O(1)	-P(1)	-O(4)	-C(46)	-101.6(2)
C(12)	-C(2)	-C(3)	-C(4)	64.6(5)	O(5)	-P(1)	-O(4)	-C(46)	79.7(2)
C(1)	-C(2)	-C(3)	-C(4)	-177.4(4)	O(3)	-P(1)	-O(4)	-C(46)	-8.9(2)
C(11)	-C(2)	-C(3)	-C(4)	-58.1(5)	O(2)	-P(1)	-O(5)	-C(47)	-101.6(2)
C(12)	-C(2)	-C(3)	-C(8)	-116.9(3)	O(6)	-P(1)	-O(5)	-C(47)	-7.8(2)
C(1)	-C(2)	-C(3)	-C(8)	1.2(4)	O(4)	-P(1)	-O(5)	-C(47)	79.8(2)
C(11)	-C(2)	-C(3)	-C(8)	120.5(3)	O(3)	-P(1)	-O(5)	-C(47)	170.3(2)
C(8)	-C(3)	-C(4)	-C(5)	0.5(6)	O(2)	-P(1)	-O(6)	-C(52)	95.8(2)
C(2)	-C(3)	-C(4)	-C(5)	179.0(4)	O(1)	-P(1)	-O(6)	-C(52)	-173.5(2)
C(3)	-C(4)	-C(5)	-C(6)	0.2(6)	O(4)	-P(1)	-O(6)	-C(52)	-83.9(2)
C(4)	-C(5)	-C(6)	-C(7)	-0.5(7)	O(5)	-P(1)	-O(6)	-C(52)	7.4(2)
C(5)	-C(6)	-C(7)	-C(8)	-0.1(6)	P(1)	-O(1)	-C(35)	-C(36)	-173.2(3)
C(4)	-C(3)	-C(8)	-C(7)	-1.1(6)	P(1)	-O(1)	-C(35)	-C(40)	8.7(3)
C(2)	-C(3)	-C(8)	-C(7)	-179.9(3)	O(1)	-C(35)	-C(36)	-C(37)	175.7(3)
C(4)	-C(3)	-C(8)	-N(1)	177.8(3)	C(40)	-C(35)	-C(36)	-C(37)	-6.3(5)
C(2)	-C(3)	-C(8)	-N(1)	-0.9(4)	O(1)	-C(35)	-C(36)	-Cl(2)	-5.5(5)
C(6)	-C(7)	-C(8)	-C(3)	0.9(5)	C(40)	-C(35)	-C(36)	-Cl(2)	172.5(2)
C(6)	-C(7)	-C(8)	-N(1)	-177.9(3)	C(35)	-C(36)	-C(37)	-C(38)	6.3(5)
C(1)	-N(1)	-C(8)	-C(3)	0.2(4)	Cl(2)	-C(36)	-C(37)	-C(38)	-172.5(3)
C(9)	-N(1)	-C(8)	-C(3)	-178.8(3)	C(35)	-C(36)	-C(37)	-Cl(3)	-171.4(2)
C(1)	-N(1)	-C(8)	-C(7)	179.1(3)	Cl(2)	-C(36)	-C(37)	-Cl(3)	9.9(4)
C(9)	-N(1)	-C(8)	-C(7)	0.0(5)	C(36)	-C(37)	-C(38)	-C(39)	-0.5(5)
C(1)	-N(1)	-C(9)	-C(10)	93.9(4)	Cl(3)	-C(37)	-C(38)	-C(39)	177.2(3)
C(8)	-N(1)	-C(9)	-C(10)	-87.2(4)	C(36)	-C(37)	-C(38)	-Cl(4)	179.9(3)
N(1)	-C(1)	-C(13)	-C(14)	171.3(3)	Cl(3)	-C(37)	-C(38)	-Cl(4)	-2.4(4)
C(2)	-C(1)	-C(13)	-C(14)	-9.3(6)	C(37)	-C(38)	-C(39)	-C(40)	-5.3(5)
C(1)	-C(13)	-C(14)	-C(15)	-175.3(3)	Cl(4)	-C(38)	-C(39)	-C(40)	174.3(2)
C(13)	-C(14)	-C(15)	-C(16)	172.8(3)	C(37)	-C(38)	-C(39)	-Cl(5)	175.7(3)
C(13)	-C(14)	-C(15)	-C(20)	-7.9(5)	Cl(4)	-C(38)	-C(39)	-Cl(5)	-4.7(4)
C(14)	-C(15)	-C(16)	-C(17)	177.5(3)	P(1)	-O(2)	-C(40)	-C(39)	172.8(3)
C(20)	-C(15)	-C(16)	-C(17)	-1.7(5)	P(1)	-O(2)	-C(40)	-C(35)	-8.0(3)
C(14)	-C(15)	-C(16)	-Cl(1)	-3.0(4)	C(38)	-C(39)	-C(40)	-O(2)	-175.5(3)
C(20)	-C(15)	-C(16)	-Cl(1)	177.7(3)	Cl(5)	-C(39)	-C(40)	-O(2)	3.5(5)
C(15)	-C(16)	-C(17)	-C(21)	177.5(3)	C(38)	-C(39)	-C(40)	-C(35)	5.4(5)
Cl(1)	-C(16)	-C(17)	-C(21)	-2.0(4)	Cl(5)	-C(39)	-C(40)	-C(35)	-175.6(2)
C(15)	-C(16)	-C(17)	-C(18)	-2.2(5)	O(1)	-C(35)	-C(40)	-O(2)	-0.5(4)
Cl(1)	-C(16)	-C(17)	-C(18)	178.4(3)	C(36)	-C(35)	-C(40)	-O(2)	-178.8(3)
C(21)	-C(17)	-C(18)	-C(19b)	158.9(7)	O(1)	-C(35)	-C(40)	-C(39)	178.7(3)
C(16)	-C(17)	-C(18)	-C(19b)	-21.4(8)	C(36)	-C(35)	-C(40)	-C(39)	0.4(5)

C(21)	-C(17)	-C(18)	-C(19a)	-148.8(4)	P(1)	-O(3)	-C(41)	-C(42)	176.8(3)
C(16)	-C(17)	-C(18)	-C(19a)	30.8(5)	P(1)	-O(3)	-C(41)	-C(46)	-3.9(3)
C(17)	-C(18)	-C(19a)	-C(20)	-55.8(5)	O(3)	-C(41)	-C(42)	-C(43)	-178.4(3)
C(19b)	-C(18)	-C(19a)	-C(20)	49.5(7)	C(46)	-C(41)	-C(42)	-C(43)	2.3(5)
C(17)	-C(18)	-C(19b)	-C(20)	47(2)	O(3)	-C(41)	-C(42)	-Cl(6)	3.7(5)
C(19a)	-C(18)	-C(19b)	-C(20)	-49.3(8)	C(46)	-C(41)	-C(42)	-Cl(6)	-175.6(3)
C(18)	-C(19a)	-C(20)	-C(15)	52.1(5)	C(41)	-C(42)	-C(43)	-C(44)	0.1(6)
C(18)	-C(19a)	-C(20)	-C(19b)	-49.2(7)	Cl(6)	-C(42)	-C(43)	-C(44)	177.9(3)
C(14)	-C(15)	-C(20)	-C(19a)	157.0(4)	C(41)	-C(42)	-C(43)	-Cl(7)	179.9(3)
C(16)	-C(15)	-C(20)	-C(19a)	-23.7(5)	Cl(6)	-C(42)	-C(43)	-Cl(7)	-2.3(5)
C(14)	-C(15)	-C(20)	-C(19b)	-150.8(7)	C(42)	-C(43)	-C(44)	-C(45)	-1.0(6)
C(16)	-C(15)	-C(20)	-C(19b)	28.5(7)	Cl(7)	-C(43)	-C(44)	-C(45)	179.2(3)
C(18)	-C(19b)	-C(20)	-C(19a)	49.6(8)	C(42)	-C(43)	-C(44)	-Cl(8)	179.5(3)
C(18)	-C(19b)	-C(20)	-C(15)	-50(1)	Cl(7)	-C(43)	-C(44)	-Cl(8)	-0.4(5)
C(16)	-C(17)	-C(21)	-C(22)	-179.2(3)	C(43)	-C(44)	-C(45)	-C(46)	-0.4(6)
C(18)	-C(17)	-C(21)	-C(22)	0.4(6)	Cl(8)	-C(44)	-C(45)	-C(46)	179.1(3)
C(17)	-C(21)	-C(22)	-C(23)	174.0(3)	C(43)	-C(44)	-C(45)	-Cl(9)	-179.3(3)
C(30)	-N(2)	-C(23)	-C(22)	176.3(3)	Cl(8)	-C(44)	-C(45)	-Cl(9)	0.2(5)
C(31)	-N(2)	-C(23)	-C(22)	-10.9(5)	P(1)	-O(4)	-C(46)	-C(45)	-171.2(3)
C(30)	-N(2)	-C(23)	-C(24)	-1.9(4)	P(1)	-O(4)	-C(46)	-C(41)	8.5(3)
C(31)	-N(2)	-C(23)	-C(24)	170.9(3)	C(44)	-C(45)	-C(46)	-O(4)	-177.4(3)
C(21)	-C(22)	-C(23)	-N(2)	-175.4(3)	Cl(9)	-C(45)	-C(46)	-O(4)	1.5(5)
C(21)	-C(22)	-C(23)	-C(24)	2.5(6)	C(44)	-C(45)	-C(46)	-C(41)	2.9(5)
N(2)	-C(23)	-C(24)	-C(25)	1.7(4)	Cl(9)	-C(45)	-C(46)	-C(41)	-178.2(3)
C(22)	-C(23)	-C(24)	-C(25)	-176.4(3)	O(3)	-C(41)	-C(46)	-O(4)	-3.0(4)
N(2)	-C(23)	-C(24)	-C(33)	120.5(3)	C(42)	-C(41)	-C(46)	-O(4)	176.4(3)
C(22)	-C(23)	-C(24)	-C(33)	-57.6(5)	O(3)	-C(41)	-C(46)	-C(45)	176.7(3)
N(2)	-C(23)	-C(24)	-C(34)	-113.8(3)	C(42)	-C(41)	-C(46)	-C(45)	-3.9(5)
C(22)	-C(23)	-C(24)	-C(34)	68.1(5)	P(1)	-O(5)	-C(47)	-C(48)	-173.5(3)
C(23)	-C(24)	-C(25)	-C(30)	-1.0(4)	P(1)	-O(5)	-C(47)	-C(52)	6.2(3)
C(33)	-C(24)	-C(25)	-C(30)	-122.6(4)	O(5)	-C(47)	-C(48)	-C(49)	-179.0(3)
C(34)	-C(24)	-C(25)	-C(30)	115.2(4)	C(52)	-C(47)	-C(48)	-C(49)	1.3(5)
C(23)	-C(24)	-C(25)	-C(26)	178.3(4)	O(5)	-C(47)	-C(48)	-Cl(10)	-0.4(5)
C(33)	-C(24)	-C(25)	-C(26)	56.7(5)	C(52)	-C(47)	-C(48)	-Cl(10)	179.9(2)
C(34)	-C(24)	-C(25)	-C(26)	-65.5(5)	C(47)	-C(48)	-C(49)	-C(50)	-0.7(5)
C(30)	-C(25)	-C(26)	-C(27)	0.4(6)	Cl(10)	-C(48)	-C(49)	-C(50)	-179.3(2)
C(24)	-C(25)	-C(26)	-C(27)	-178.9(4)	C(47)	-C(48)	-C(49)	-Cl(11)	-179.6(2)
C(25)	-C(26)	-C(27)	-C(28)	0.5(6)	Cl(10)	-C(48)	-C(49)	-Cl(11)	1.8(4)
C(26)	-C(27)	-C(28)	-C(29)	-0.7(7)	C(48)	-C(49)	-C(50)	-C(51)	0.4(5)
C(27)	-C(28)	-C(29)	-C(30)	-0.0(6)	Cl(11)	-C(49)	-C(50)	-C(51)	179.3(2)
C(26)	-C(25)	-C(30)	-C(29)	-1.1(6)	C(48)	-C(49)	-C(50)	-Cl(12)	-178.2(2)
C(24)	-C(25)	-C(30)	-C(29)	178.3(3)	Cl(11)	-C(49)	-C(50)	-Cl(12)	0.7(4)
C(26)	-C(25)	-C(30)	-N(2)	-179.5(3)	C(49)	-C(50)	-C(51)	-C(52)	-0.6(5)
C(24)	-C(25)	-C(30)	-N(2)	-0.0(4)	Cl(12)	-C(50)	-C(51)	-C(52)	178.0(2)
C(28)	-C(29)	-C(30)	-C(25)	0.9(6)	C(49)	-C(50)	-C(51)	-Cl(13)	180.0(2)
C(28)	-C(29)	-C(30)	-N(2)	178.9(4)	Cl(12)	-C(50)	-C(51)	-Cl(13)	-1.4(4)
C(23)	-N(2)	-C(30)	-C(25)	1.2(4)	P(1)	-O(6)	-C(52)	-C(51)	175.4(3)
C(31)	-N(2)	-C(30)	-C(25)	-171.7(3)	P(1)	-O(6)	-C(52)	-C(47)	-5.3(3)
C(23)	-N(2)	-C(30)	-C(29)	-176.9(4)	C(50)	-C(51)	-C(52)	-O(6)	-179.6(3)
C(31)	-N(2)	-C(30)	-C(29)	10.1(6)	Cl(13)	-C(51)	-C(52)	-O(6)	-0.2(4)

C(23)	-N(2)	-C(31)	-C(32)	-82.7(5)	C(50)	-C(51)	-C(52)	-C(47)	1.2(5)
C(30)	-N(2)	-C(31)	-C(32)	89.2(4)	Cl(13)	-C(51)	-C(52)	-C(47)	-179.4(2)
O(2)	-P(1)	-O(1)	-C(35)	-11.1(2)	O(5)	-C(47)	-C(52)	-O(6)	-0.6(4)
O(6)	-P(1)	-O(1)	-C(35)	-104.9(2)	C(48)	-C(47)	-C(52)	-O(6)	179.1(3)
O(4)	-P(1)	-O(1)	-C(35)	167.5(2)	O(5)	-C(47)	-C(52)	-C(51)	178.7(3)
O(3)	-P(1)	-O(1)	-C(35)	77.0(2)	C(48)	-C(47)	-C(52)	-C(51)	-1.5(5)

Table 7.18. Bond lengths (Å) in **Cy7-PbI$_3$** with standard uncertainties in parentheses.

Pb(1)	-I(3)	3.1987(7)	C(15)	-C(20)	1.506(12)
Pb(1)	-I(2)	3.2154(6)	C(16)	-C(17)	1.390(12)
Pb(1)	-I(3')	3.2283(6)	C(17)	-C(21)	1.402(12)
Pb(1)	-I(1)	3.2330(6)	C(17)	-C(18)	1.504(12)
Pb(1)	-I(2")	3.2804(6)	C(18)	-C(19)	1.521(12)
Pb(1)	-I(1')	3.3052(7)	C(19)	-C(20)	1.502(14)
Cl(1)	-C(16)	1.778(9)	C(21)	-C(22)	1.381(13)
N(1)	-C(1)	1.365(11)	C(22)	-C(23)	1.400(13)
N(1)	-C(8)	1.401(12)	C(23)	-C(24)	1.526(12)
N(1)	-C(9)	1.459(12)	C(24)	-C(25)	1.503(12)
N(2)	-C(23)	1.338(12)	C(24)	-C(34)	1.534(13)
N(2)	-C(30)	1.418(12)	C(24)	-C(33)	1.550(12)
N(2)	-C(31)	1.461(12)	C(25)	-C(26)	1.388(13)
C(1)	-C(13)	1.393(12)	C(25)	-C(30)	1.398(13)
C(1)	-C(2)	1.509(13)	C(26)	-C(27)	1.396(16)
C(2)	-C(12)	1.531(14)	C(27)	-C(28)	1.385(17)
C(2)	-C(11)	1.533(13)	C(28)	-C(29)	1.390(15)
C(2)	-C(3)	1.538(14)	C(29)	-C(30)	1.387(13)
C(3)	-C(8)	1.359(14)	C(31)	-C(32)	1.505(18)
C(3)	-C(4)	1.365(14)	O(1)	-C(35)	1.20(2)
C(4)	-C(5)	1.393(16)	N(3)	-C(35)	1.34(3)
C(5)	-C(6)	1.382(16)	N(3)	-C(37)	1.43(2)
C(6)	-C(7)	1.385(14)	N(3)	-C(36)	1.44(3)
C(7)	-C(8)	1.403(13)	O(2)	-C(38)	1.25(3)
C(9)	-C(10)	1.521(13)	N(4)	-C(38)	1.30(2)
C(13)	-C(14)	1.402(12)	N(4)	-C(39)	1.435(18)
C(14)	-C(15)	1.390(12)	N(4)	-C(40)	1.445(19)
C(15)	-C(16)	1.399(12)			

Symmetry operators for primed atoms:

' x, 0.5–y, 0.5+z, " x, 0.5–y, –0.5+z

Table 7.19. Bond angles (°) in **Cy7-PbI$_3$** with standard uncertainties in parentheses.

I(3)	-Pb(1)	-I(2)	89.669(17)
I(3)	-Pb(1)	-I(3')	101.39(2)
I(2)	-Pb(1)	-I(3')	85.028(17)
I(3)	-Pb(1)	-I(1)	84.852(17)
I(2)	-Pb(1)	-I(1)	99.456(17)
I(3')	-Pb(1)	-I(1)	172.402(19)
I(3)	-Pb(1)	-I(2")	84.450(17)
I(2)	-Pb(1)	-I(2")	170.91(2)
I(3')	-Pb(1)	-I(2")	89.336(17)
I(1)	-Pb(1)	-I(2")	86.940(16)
I(3)	-Pb(1)	-I(1')	173.950(18)
I(2)	-Pb(1)	-I(1')	86.813(16)
I(3')	-Pb(1)	-I(1')	83.222(17)
I(1)	-Pb(1)	-I(1')	90.868(18)
I(2")	-Pb(1)	-I(1')	99.618(16)
Pb(1)	-I(1)	-Pb(1")	76.433(13)
Pb(1)	-I(2)	-Pb(1')	77.024(12)
Pb(1)	-I(3)	-Pb(1")	78.010(14)
C(1)	-N(1)	-C(8)	110.2(8)
C(1)	-N(1)	-C(9)	125.4(8)
C(8)	-N(1)	-C(9)	124.3(8)
C(23)	-N(2)	-C(30)	111.2(8)
C(23)	-N(2)	-C(31)	127.1(8)
C(30)	-N(2)	-C(31)	121.8(8)
N(1)	-C(1)	-C(13)	121.7(9)
N(1)	-C(1)	-C(2)	109.3(8)
C(13)	-C(1)	-C(2)	129.0(9)
C(1)	-C(2)	-C(12)	113.6(8)
C(1)	-C(2)	-C(11)	108.8(9)
C(12)	-C(2)	-C(11)	111.4(9)
C(1)	-C(2)	-C(3)	101.2(8)
C(12)	-C(2)	-C(3)	110.9(8)
C(11)	-C(2)	-C(3)	110.5(8)
C(8)	-C(3)	-C(4)	121.6(10)
C(8)	-C(3)	-C(2)	108.4(9)
C(4)	-C(3)	-C(2)	130.0(10)
C(3)	-C(4)	-C(5)	118.0(11)
C(6)	-C(5)	-C(4)	120.9(10)
C(5)	-C(6)	-C(7)	120.9(10)
C(6)	-C(7)	-C(8)	117.0(10)
C(3)	-C(8)	-N(1)	110.7(9)
C(3)	-C(8)	-C(7)	121.5(9)
N(1)	-C(8)	-C(7)	127.7(9)
N(1)	-C(9)	-C(10)	112.7(8)
C(1)	-C(13)	-C(14)	126.3(9)
C(15)	-C(14)	-C(13)	124.3(8)
C(14)	-C(15)	-C(16)	124.0(8)
C(14)	-C(15)	-C(20)	120.4(8)
C(16)	-C(15)	-C(20)	115.6(8)
C(17)	-C(16)	-C(15)	126.3(8)
C(17)	-C(16)	-Cl(1)	117.1(6)
C(15)	-C(16)	-Cl(1)	116.5(7)
C(16)	-C(17)	-C(21)	122.8(8)
C(16)	-C(17)	-C(18)	118.1(8)
C(21)	-C(17)	-C(18)	119.2(8)
C(17)	-C(18)	-C(19)	113.0(8)
C(20)	-C(19)	-C(18)	112.2(8)
C(19)	-C(20)	-C(15)	110.9(8)
C(22)	-C(21)	-C(17)	123.8(8)
C(21)	-C(22)	-C(23)	126.4(9)
N(2)	-C(23)	-C(22)	121.8(8)
N(2)	-C(23)	-C(24)	109.5(8)
C(22)	-C(23)	-C(24)	128.8(8)
C(25)	-C(24)	-C(23)	101.8(7)
C(25)	-C(24)	-C(34)	110.2(8)
C(23)	-C(24)	-C(34)	113.8(7)
C(25)	-C(24)	-C(33)	110.3(7)
C(23)	-C(24)	-C(33)	110.2(8)
C(34)	-C(24)	-C(33)	110.3(8)
C(26)	-C(25)	-C(30)	119.8(9)
C(26)	-C(25)	-C(24)	131.2(9)
C(30)	-C(25)	-C(24)	108.9(8)
C(25)	-C(26)	-C(27)	117.8(10)
C(28)	-C(27)	-C(26)	122.0(10)
C(27)	-C(28)	-C(29)	120.6(10)
C(30)	-C(29)	-C(28)	117.4(10)
C(29)	-C(30)	-C(25)	122.5(9)
C(29)	-C(30)	-N(2)	128.8(9)
C(25)	-C(30)	-N(2)	108.7(8)
N(2)	-C(31)	-C(32)	112.9(9)
C(35)	-N(3)	-C(37)	119(2)
C(35)	-N(3)	-C(36)	127(2)
C(37)	-N(3)	-C(36)	114(2)
O(1)	-C(35)	-N(3)	127(3)
C(38)	-N(4)	-C(39)	122.1(18)
C(38)	-N(4)	-C(40)	121.0(16)
C(39)	-N(4)	-C(40)	116.9(13)
O(2)	-C(38)	-N(4)	125(2)

Symmetry operators for primed atoms:

' x, 0.5–y, 0.5+z, " x, 0.5–y, –0.5+z

Table 7.20. Torsion angles (°) in **Cy7-PbI$_3$** with standard uncertainties in parentheses.

C(8)	-N(1)	-C(1)	-C(13)	173.4(8)	C(21)	-C(17)	-C(18)	-C(19)	165.2(9)
C(9)	-N(1)	-C(1)	-C(13)	-2(1)	C(17)	-C(18)	-C(19)	-C(20)	46(1)
C(8)	-N(1)	-C(1)	-C(2)	-5(1)	C(18)	-C(19)	-C(20)	-C(15)	-57(1)
C(9)	-N(1)	-C(1)	-C(2)	179.7(8)	C(14)	-C(15)	-C(20)	-C(19)	-145.0(8)
N(1)	-C(1)	-C(2)	-C(12)	123.2(9)	C(16)	-C(15)	-C(20)	-C(19)	37(1)
C(13)	-C(1)	-C(2)	-C(12)	-55(1)	C(16)	-C(17)	-C(21)	-C(22)	174.1(9)
N(1)	-C(1)	-C(2)	-C(11)	-112.1(9)	C(18)	-C(17)	-C(21)	-C(22)	-6(1)
C(13)	-C(1)	-C(2)	-C(11)	70(1)	C(17)	-C(21)	-C(22)	-C(23)	-179.5(9)
N(1)	-C(1)	-C(2)	-C(3)	4.3(9)	C(30)	-N(2)	-C(23)	-C(22)	-179.0(8)
C(13)	-C(1)	-C(2)	-C(3)	-173.7(9)	C(31)	-N(2)	-C(23)	-C(22)	1(2)
C(1)	-C(2)	-C(3)	-C(8)	-3(1)	C(30)	-N(2)	-C(23)	-C(24)	1(1)
C(12)	-C(2)	-C(3)	-C(8)	-123.3(9)	C(31)	-N(2)	-C(23)	-C(24)	-179.0(9)
C(11)	-C(2)	-C(3)	-C(8)	113(1)	C(21)	-C(22)	-C(23)	-N(2)	172.3(9)
C(1)	-C(2)	-C(3)	-C(4)	175(1)	C(21)	-C(22)	-C(23)	-C(24)	-7(2)
C(12)	-C(2)	-C(3)	-C(4)	54(1)	N(2)	-C(23)	-C(24)	-C(25)	0(1)
C(11)	-C(2)	-C(3)	-C(4)	-70(1)	C(22)	-C(23)	-C(24)	-C(25)	179.7(9)
C(8)	-C(3)	-C(4)	-C(5)	-3(2)	N(2)	-C(23)	-C(24)	-C(34)	-118.4(9)
C(2)	-C(3)	-C(4)	-C(5)	-179.7(9)	C(22)	-C(23)	-C(24)	-C(34)	61(1)
C(3)	-C(4)	-C(5)	-C(6)	2(2)	N(2)	-C(23)	-C(24)	-C(33)	117.1(9)
C(4)	-C(5)	-C(6)	-C(7)	-2(2)	C(22)	-C(23)	-C(24)	-C(33)	-63(1)
C(5)	-C(6)	-C(7)	-C(8)	2(2)	C(23)	-C(24)	-C(25)	-C(26)	-176(1)
C(4)	-C(3)	-C(8)	-N(1)	-177.8(9)	C(34)	-C(24)	-C(25)	-C(26)	-55(1)
C(2)	-C(3)	-C(8)	-N(1)	0(1)	C(33)	-C(24)	-C(25)	-C(26)	67(1)
C(4)	-C(3)	-C(8)	-C(7)	3(2)	C(23)	-C(24)	-C(25)	-C(30)	-1(1)
C(2)	-C(3)	-C(8)	-C(7)	-179.5(8)	C(34)	-C(24)	-C(25)	-C(30)	120.3(9)
C(1)	-N(1)	-C(8)	-C(3)	3(1)	C(33)	-C(24)	-C(25)	-C(30)	-117.7(9)
C(9)	-N(1)	-C(8)	-C(3)	178.8(8)	C(30)	-C(25)	-C(26)	-C(27)	2(2)
C(1)	-N(1)	-C(8)	-C(7)	-177.6(9)	C(24)	-C(25)	-C(26)	-C(27)	177(1)
C(9)	-N(1)	-C(8)	-C(7)	-2(2)	C(25)	-C(26)	-C(27)	-C(28)	-2(2)
C(6)	-C(7)	-C(8)	-C(3)	-2(1)	C(26)	-C(27)	-C(28)	-C(29)	1(2)
C(6)	-C(7)	-C(8)	-N(1)	178.4(9)	C(27)	-C(28)	-C(29)	-C(30)	0(2)
C(1)	-N(1)	-C(9)	-C(10)	87(1)	C(28)	-C(29)	-C(30)	-C(25)	0(2)
C(8)	-N(1)	-C(9)	-C(10)	-89(1)	C(28)	-C(29)	-C(30)	-N(2)	-177(1)
N(1)	-C(1)	-C(13)	-C(14)	178.9(8)	C(26)	-C(25)	-C(30)	-C(29)	-1(2)
C(2)	-C(1)	-C(13)	-C(14)	-3(2)	C(24)	-C(25)	-C(30)	-C(29)	-176.3(9)
C(1)	-C(13)	-C(14)	-C(15)	175.6(9)	C(26)	-C(25)	-C(30)	-N(2)	177.0(9)
C(13)	-C(14)	-C(15)	-C(16)	173.4(8)	C(24)	-C(25)	-C(30)	-N(2)	1(1)
C(13)	-C(14)	-C(15)	-C(20)	-5(1)	C(23)	-N(2)	-C(30)	-C(29)	176(1)
C(14)	-C(15)	-C(16)	-C(17)	176.0(9)	C(31)	-N(2)	-C(30)	-C(29)	-4(2)
C(20)	-C(15)	-C(16)	-C(17)	-6(1)	C(23)	-N(2)	-C(30)	-C(25)	-1(1)
C(14)	-C(15)	-C(16)	-Cl(1)	-1(1)	C(31)	-N(2)	-C(30)	-C(25)	178.5(9)
C(20)	-C(15)	-C(16)	-Cl(1)	177.5(6)	C(23)	-N(2)	-C(31)	-C(32)	84(1)
C(15)	-C(16)	-C(17)	-C(21)	174.4(9)	C(30)	-N(2)	-C(31)	-C(32)	-96(1)
Cl(1)	-C(16)	-C(17)	-C(21)	-9(1)	C(37)	-N(3)	-C(35)	-O(1)	178(3)
C(15)	-C(16)	-C(17)	-C(18)	-6(1)	C(36)	-N(3)	-C(35)	-O(1)	0(5)
Cl(1)	-C(16)	-C(17)	-C(18)	171.0(7)	C(39)	-N(4)	-C(38)	-O(2)	-1(5)
C(16)	-C(17)	-C(18)	-C(19)	-15(1)	C(40)	-N(4)	-C(38)	-O(2)	179(3)

Anna C. Véron

Curriculum Vitae

Personal Information

Born	28th May 1988 in Bregenz, Austria
Nationality	Austrian and Swiss
Languages	German (native), English (fluent), Portuguese, French and Swedish (basic)

Education

PhD	**Swiss Federal Laboratories for Materials Science and Technology (Empa)**, Dübendorf, Switzerland and University of Zurich, Zurich, Switzerland PhD program at the Graduate School of Chemical and Molecular Sciences Zurich Thesis Title: “Near–Infrared Absorbing Cyanine Dyes and Organic–Inorganic Perovskites for Electronic Applications” Research Advisors: Prof. Dr. Frank A. Nüesch, Prof. Dr. Jay S. Siegel and Prof. Dr. Kim K. Baldridge Graduation **2017**
MSc	**University of Zurich**, Zurich, Switzerland Master of Science in Chemistry Thesis Title: “Ruthenium(II) Tris(bipyridine) Complexes Containing Alternating Pyridine–Thiophene Units”, Grade: 6.0 (scale 6.0) Research Advisor: PD Dr. Nathaniel S. Finney Graduation **2012**
BSc	**University of Zurich**, Zurich, Switzerland Bachelor of Science in Chemistry Graduation **2010**
high school	**Bundesgymnasium Blumenstraße,** Bregenz, Austria Graduation **2006** with distinction

Research Experience

2012–present	Research as a PhD Student in Organic, Physical and Materials Chemistry
2011–2012	Research as a Master Student in Organic Chemistry
2009, 2010	Undergraduate Research Internships in Inorganic Chemistry in the groups of Prof. Dr. Bernhard Spingler and Dr. Koushik Venkatesan
2009	Summer Internship in Synthetic Organic Chemistry in the group of PD Dr. Nathaniel S. Finney

Teaching Experience at the University of Zurich

2014	Teaching Assistant in “General Practical Course in Chemistry“
2011	Teaching Assistant in “General and Inorganic Chemistry for Biology Students”
2007–2011	Tutor in “General Practical Course in Chemistry“

Contribution to Scientific Conferences

Poster Presentations	2013: 1st Nanotechnology for Next Generation High Efficiency Photovoltaics conference in Cargèse, France
	2013, 2014, 2015: Empa PhD Students' Symposium, Dübendorf, Switzerland Best Poster Award in 2015
Oral Presentations	2015: XIV Brazilian MRS Meeting, Rio de Janeiro, Brazil 2013: XII Brazilian MRS Meeting, Campos do Jordão, Brazil

List of Publications

First Author or Contributing Equally

- Véron, A. C.; Nüesch, F.A. One–Dimensional Organic–Inorganic Hybrid Perovskite Photonic Crystals incorporating NIR Active Cyanine Cations. *Manuscript in preparation*.

- Makha, M.; Fernandes, S. L.; Jenatsch, S.; Offermans, T.; Schleuniger, J.; Tisserant, J.-N.; Véron, A. C.; Hany, R. A Transparent, Solvent-Free Laminated Top Electrode for Perovskite Solar Cells. *Sci. Technol. Adv. Mater.* **2016**, *17* (1), 260–266.

- Véron, A. C.; Zhang, H.; Linden, A.; Nüesch, F.; Heier, J.; Hany, R.; Geiger, T. NIR-Absorbing Heptamethine Dyes with Tailor-Made Counterions for Application in Light to Energy Conversion. *Org. Lett.* **2014**, *16* (4), 1044–1047

- Véron, A. C.; Felber, M.; Blacque, O.; Spingler, B. Conformational Flexibility of Palladium BINAP Complexes Explored by X-Ray Analyses and DFT Studies. *Polyhedron* **2013**, *52*, 102–105.

Further Co–Authored Publications

- Hany, R.; Makha, M.; Testa, P.; Anantharaman, S.; Heier, J.; Jenatsch, S.; Leclaire, N.; Tisserant, J-N; Véron, A. C.; Wang, L.; Nüesch, F. A. Ternary semitransparent organic solar cells with a laminated top electrode. *Sci. Technol. Adv. Mater.* **2017**, *18* (1), 68–75.

- Tesfay, H.; Bronze-Uhle, E. S.; Batagin-Neto, A.; C. Véron, A.; Geiger, T.; Yohannes, T.; Megerssa, N.; F.O. Graeff, C. Study of Heptamethine Iodide and Heptamethine PF_6 Solutions in Different Solvents for the Measurement of Low Doses of X-Ray & Gamma Radiation. *Curr. Phys. Chem.* **2016**, *5* (4), 308–317.

- Zhang, H.; Niesen, B.; Hack, E.; Jenatsch, S.; Wang, L.; Véron, A. C.; Makha, M.; Schneider, R.; Arroyo, Y.; Hany, R.; Nüesch, F. Cyanine Tandem and Triple-Junction Solar Cells. *Org. Electron.* **2016**, *30*, 191–199.

- Jenatsch, S.; Wang, L.; Bulloni, M.; Véron, A. C.; Ruhstaller, B.; Altazin, S.; Nüesch, F.; Hany, R. Doping Evolution and Junction Formation in Stacked Cyanine Dye Light-Emitting Electrochemical Cells. *ACS Appl. Mater. Interfaces* **2016**, *8* (10), 6554–6562.

- Fernandes, S. L.; Véron, A. C.; Neto, N. F. A.; Nüesch, F. A.; Dias da Silva, J. H.; Zaghete, M. A.; Graeff, C. F. de O. Nb_2O_5 Hole Blocking Layer for Hysteresis-Free Perovskite Solar Cells. *Mater. Lett.* **2016**, *181*, 103–107.

- Zhang, H.; Jenatsch, S.; De Jonghe, J.; Nüesch, F.; Steim, R.; Véron, A. C.; Hany, R. Transparent Organic Photodetector Using a Near-Infrared Absorbing Cyanine Dye. *Sci. Rep.* **2015**, *5*, 9439.

- Jenatsch, S.; Geiger, T.; Heier, J.; Kirsch, C.; Nüesch, F.; Paracchino, A.; Rentsch, D.; Ruhstaller, B.; Véron, A. C.; Hany, R. Influence of Chemically P-Type Doped Active Organic Semiconductor on the Film Thickness versus Performance Trend in cyanine/C 60 Bilayer Solar Cells. *Sci. Technol. Adv. Mater.* **2015**, *16* (3), 35003.

- Jenatsch, S.; Hany, R.; Véron, A. C.; Neukom, M.; Züfle, S.; Borgschulte, A.; Ruhstaller, B.; Nüesch, F. Influence of Molybdenum Oxide Interface Solvent Sensitivity on Charge Trapping in Bilayer Cyanine Solar Cells. *J. Phys. Chem. C* **2014**, *118* (30), 17036–17045.

- Heier, J.; Peng, C.; Véron, A. C.; Hany, R.; Geiger, T.; Nüesch, F. A.; Vismara, M. V. G.; Graeff, C. F. O. Cyanine Dyes in Solid State Organic Heterojunction Solar Cells. *Proc. SPIE* **2014**, *9184*.

- Geiger, T.; Schoger, I.; Rentsch, D.; Véron, A. C.; Oswald, F.; Meyer, T.; Nüesch, F. Unsymmetrical Heptamethine Dyes for NIR Dye-Sensitized Solar Cells. *Int. J. Photoenergy* **2014**, *2014*, 1–10.